Technische Universität München
TUM School of Engineering and Design

Engineering smart biopolymer-based materials for drug delivery applications

Ceren KIMNA

Vollständiger Abdruck der von der TUM School of Engineering and Design der Technischen Universität München zur Erlangung einer

Doktorin der Ingenieurwissenschaften (Dr.-Ing.)

genehmigten Dissertation.

Vorsitz: Prof. Dr. techn. Jan Torgersen

Prüfer*innen der Dissertation:

1. Prof. Dr. rer. nat. Oliver Lieleg
2. Prof. Dr. Petra Mela
3. Prof. Dr. Olivia M. Merkel

Die Dissertation wurde am 22.09.2022 bei der Technischen Universität München eingereicht und durch die TUM School of Engineering and Design am 17.03.2023 angenommen.

“I could be bounded in a nutshell and count myself a king of infinite space.” Shakespeare

to those who encouraged me to never give up chasing my curiosity…

Summary

Medication-oriented treatment constitutes a significant part of current medical interventions. Although there is great effort to develop new drugs, most strategies fail or are insufficient due to problems arising during drug administration, mainly due to the biological barriers that the active component faces and the disease-associated heterogeneity of the biological targets. In this thesis, conceptual biomaterial designs for smart drug delivery systems were developed to address these problems.

First, considering that most administration routes include drug transportation in complex biological environments, drug delivery mechanisms were designed to meet the requirements of specific tissues. In particular, to overcome the intrinsic barriers of the ocular system that limit the topical delivery of therapeutically active molecules to the posterior eye, nanoparticles with intermediate levels of mucoadhesivity were developed. Here, by modulating the net charge of the nanoparticles, improved drug transport across the corneal barrier (when compared to aqueous solutions of free drug molecules) was successfully accomplished. The second study focused on unidirectional drug delivery to wet tissue wounds. To tackle this challenge, it was necessary to manage additional conflicting properties as promoting wound closure and preventing unwanted tissue adhesions with one material often requires contradictory physical properties, *e.g.*, adhesion and lubrication. Here, this problem was addressed by generating asymmetrically designed double-layer films where distinct functions were canalized towards the opposing sides of the film. Once deployed, the bilayer films exhibited strong adhesion to wet tissues and released the integrated therapeutics exclusively toward the tissue side. At the same time, the outer surface of the films acted as a shield against tribological stress, pathogenic attacks, as well as cellular immune recognition. Finally, when their tasks were completed, the bilayer films decomposed on the applied surface and neither left any traces nor induced alterations on the tissue microtopography, which eliminated the necessity for a secondary (removal) operation.

The second part of this thesis focuses on the design of delivery mechanisms that can be initiated by (patho)physiological conditions. This is a crucial aspect as, without a rational release mechanism, the delivery of drugs not only lacks control over the (therapeutic) level of a drug dose at the desired location but also exposes off-target locations to a certain level of drugs, and this can induce adverse effects. Thus, several strategies were employed to use selected trigger conditions (*e.g.*, a change in ionic concentration, high wall shear stress) to initiate drug release. First, synthetic DNA stabilized nanoparticle clusters were embedded into a host hydrogel system to release different nanoparticle species in a sequential manner. This release cascade was initiated by exposing the system to physiological salt concentrations. As the liberation of one nanoparticle species was designed to trigger the release of the next nanoparticle variant through selective base pairing reactions, a release avalanche with a tunable duration was achieved. Moreover, it was demonstrated that enriching the reservoir hydrogel with biopolymers can be utilized to obtain

charge-selective release properties towards small molecules – without interfering with the DNA-based release cascade. As a strategy focusing on implant-associated post-surgery infections, a multi-layered surface coating that responds to two different stimuli was developed. This approach combined different molecular mechanisms, including a transient compaction of macromolecules and a controlled disassembly of sacrificial layers by releasing a mediating molecule from thermos-responsive liposomes. As a result, two antibiotic doses were liberated in response to two independent stimuli as they can occur *in vivo, e.g.*, as a consequence of an implantation and inflammation process. In the third study of this chapter, a mechanosensitive drug release strategy was designed to address different severity levels of a stenotic blood vessel occlusion. The nanogels prepared in this context exhibited a tunable disintegration behavior, and they released the encapsulated drugs upon exposure to microscopic shear stress as induced by stenotic constrictions. By implementing logical release mechanisms as presented here, which are initiated by pre-defined trigger conditions, a known drug dose could be delivered to the point of care either at the correct location or at the right time.

In the last chapter, intracellular release mechanisms controlled by strand displacement reactions were developed. Synthetic DNA-stabilized mucin nanoparticles were designed to deliver therapeutics across the cellular membrane and release them when reaching the cytosol of cells containing the trigger DNA strands. The on-demand release was achieved by using the diverse chemistry and conformational flexibility of mucin glycoproteins in combination with the high specificity of selective DNA hybridization. Then, this strategy was developed further by inducing a conformational change of mucin nanoparticles by opening the stabilizing DNA crosslinks through hybridization with a specific, intracellular microRNA sequence that is overexpressed in certain pathological conditions such as cancer. With this last upgrade, the nanoparticulate system obtained a control mechanism, where a cell receives the medication only “if it asks for help”. Importantly, those nanoparticles could receive an additional surface coating or could be chemically modified to be selectively taken up by target cells without interfering with the conformational change mechanism. Finally, those DNA-stabilized nanoparticles were reengineered to play a dual role: first, dedicated synthetic DNA strands stabilized the nanoparticles until a certain level of target miRNA triggered the nanoparticle dispersal. Then, the nanoparticles released a silencing oligonucleotide into the target cytosol that depletes the targeted cellular miRNA, thus, enabling apoptosis in cancer cells (and in those cells only).

The design mechanisms in this thesis bridge material science, biology, and nanomedicine and will help customizing healthcare approaches for individuals. The paradigm introduced here can be used as a theoretical and technical platform to design novel generations of drug delivery strategies for more effective and personalized therapy routes.

Table of Contents

1. Introduction

Although they can come with severe drawbacks both in the short- and long-term, local, or overall deviations of drug concentration from the therapeutically required dose are inevitable in many medication-based therapies. For example, overdosing a drug can lead to the development of adverse effects, which can cause significant side effects at both, target, and off-target locations. These side effects can cause dysregulation of the healthy metabolic processes, and can even lead to significant toxic effects, preventing the treatment progression as it is the case for most cancer chemotherapies. In a different scenario where drugs are underdosed, subtherapeutic drug concentrations might lead to low efficacy; moreover, continuously exposing the target to such low drug concentrations can eventually initiate severe problems such as antibiotic resistance. Therefore, while passively or actively maintaining a therapeutic drug concentration at the target site, minimizing the off-target accumulation of the drug is the ultimate goal of all drug delivery systems.

An efficient local or temporal delivery of pharmaceutically active agents to target cells or tissues and preventing off-target effects is not unlike the transportation of goods – one needs an appropriate cargo carrier, accurate mapping, a feasible route, punctuality, and proof of delivery [1]. In biological routes, these challenges become even more evident: physical, chemical, and biological barriers or dysregulated, mostly not uncovered paths (resulting from such pathological conditions) often lead to a partial loss of the cargo (and thus a loss of its therapeutic functionality) before reaching the target site. Thus, targeted drug delivery mechanisms are developed with the aim to engineer specific, efficient, and smart therapy approaches to provide a foundation to support three main pillars: benchside, bedside, and community [2].

To obtain an efficient drug delivery mechanism, a meticulous evaluation of the pathological micro-and macroenvironment, the cargo and its mode of action, and the carrier material is required; and many boundary conditions brought about by the physiology may impose contradictory demands. For example, on the cellular scale, a positive charge of the carrier material is mostly undesired to avoid the disruption of the plasma membrane integrity. However, at the same time, such a cationic charge state would be preferred for endosomal escape [3,4]. On the tissue level, good protein adsorption is demanded in certain cases such as osseointegration; yet, to ensure hemocompatibility of a foreign material, protein adsorption needs to be prevented [5]. From both perspectives, good interactions between the carrier and the cargo (*i.e.*, active pharmaceutical ingredients) are favorable to achieve high encapsulation efficiencies. However, once navigated to the target location or in the presence of a pathological trigger, the cargo should also be able to efficiently leave the carrier matrix. Overall, the design principles employed to drug delivery mechanisms should be kept as simple as possible to not hamper their scale-up for translation from bench to bedside.

Thus, the development of smart drug delivery strategies requires the combined perspectives of natural scientists and engineers to identify the biological obstacles and convert them into a mass transfer problem. To fulfill all these demands and to combine them in one pot, generating carrier matrices that exhibit strong interactions with drugs to deliver such cargos in a sustained way has been, for a long time, the preferred approach. These controlled drug delivery systems increased the patient comfort and compliance over many decades and reduced the need for a follow-up care. Examples include ocular inserts, subdermal reservoir implants, and periodontal pocket fillers [6]. Although the development of these systems has led to great advances in medical care, many drugs still need to be delivered *via* improved ways to ensure their safety and efficiency at the optimal dose. Therefore, recent smart drug delivery mechanisms aim for precisely managing the delivery of a required dose to the target at the desired time in order to provide people with better drug treatments and to improve the global healthcare.

1.1. Signature conditions that distinguish biological targets from off-target locations

In complete analogy to batch processes used for manufacturing fine chemicals, outlining the problem at the macro level is the first stage of planning a delivery mechanism. Then, the microlevel scheduling is the following phase, where each obstacle and phase are evaluated individually to satisfy the delivery demands [7]. To design a rational mechanism that can be implemented in a biological environment, the pathological environment and its signature conditions distinguishing the target from the healthy environment needs to be well-identified. In this context, designing a delivery system responsive to a signature stimulus is, if successful, undoubtedly a significant improvement in the quality of a treatment strategy. A wide range of signature conditions in biological systems can be implemented in a material design to initiate a cargo release at the desired location.

To achieve this goal, complex strategies were developed that employ, *e.g.*, changes in intracellular pH [8,9], enzyme levels [10,11], or redox conditions [12,13] as release triggers. Of course, the main challenge in all those approaches is to identify a suitable trigger that satisfies two demands: first, the condition needs to be highly specific for the disease to be treated (to ensure that healthy cells remain unaffected); second, the delivery of sufficiently high drug doses to the target cells has to be guaranteed so that therapeutic drug levels can be obtained. **Table 1** lists some well-known endogenous signature conditions related to different pathological states, and the mechanism of implementation of those conditions into the stimuli-responsive materials.

In addition to obtaining a stimuli-responsive targeted release, some environmental conditions are exploited to retain the drug cargo within the matrix during storage conditions. For example, drug release from drug-resin complexes can be initiated by an equilibrium exchange reaction when placed in contact with a solution containing certain ions. During storage, the drug-resin complex can be maintained by keeping the complex in a liquid, free of the counterions of these resins. After oral administration, the ions present in the saliva or the gastrointestinal fluids shift the ion equilibrium and promote drug release to elicit a therapeutic effect [14].

Table 1. Endogenous signature conditions affiliated with local pathological conditions and the underlying mechanism to leverage these conditions to obtain stimuli-responsive systems.

Trigger	Associated condition	Underlying mechanism	Ref.
Redox conditions	Cancer, cellular internalization	Cleavage of disulfide or diselenide bonds	15,16
Glucose concentration	Hypo- or hyperglycemia	Change in conformation, degree of ionization	17,18
Enzyme level	Presence of pathogens, tumor, wound	Enzymatic cleavage of crosslinks, catalysis of enzyme	19-21
Temperature	Inflammation, infection, infarction, cancer	Phase transition	22,23
Shear stress	Venous occlusion	Physical degradation	24,25
pH level	Tumor tissue, sub-cellular compartments, inflammation, presence of pathogens	Conformational/solubility changes of the ionizable groups	26
Dysregulated gene expression	Cancer, Hepatitis C, systemic diseases	Base complementarity, gel to sol transition, suppression/restoration of the target oligonucleotide	27-30
Dysregulated protein expression	Cardiovascular disease, cancer	Ligand-receptor interactions	31,32

In addition to the endogenous markers listed above, externally controlled triggers can also be used for targeted delivery approaches. For example, magnetically, ultrasound, light, and electrically - controlled systems are widely used for a local activation of chemotherapeutics, and some strategies in this field were already commercialized [33,34]. However, these systems follow different design aspects, which this thesis does not aim to cover.

Although these stimuli-responsive systems mostly offer very promising results *in vitro*, the choice of a triggering mechanism should be done very carefully since the same condition can be present in different malignant and/or healthy conditions *in vivo*. For example, a low pH can be associated with a tumor microenvironment but is also expected in some healthy body fluids such as the gastric juice. Accordingly, understanding the detailed interplay between target, material and trigger mechanism is the essential element in the decision-making process (**Fig. 1.1**).

1.2. Caveats when designing smart drug delivery systems

As the new generation of therapeutics (*e.g.*, monoclonal antibodies, targeting peptides, nucleic acids) started to get commercialized in the last decade, delivery strategies and carrier material designs were adapted to reflect the changing drug delivery needs. In principle, drug carriers can be formed on different scales, varying from nanoparticulate systems (*e.g.*, nanoparticles, micelleplexes, polymersomes) to macroscopic materials (*e.g.*, microneedles, brush coatings, hydrogels). Alternatively, biological entities such as red blood cells [35], microalgae [36] , macrophages [37], and cyanobacteria biomass [38] can be used to shuttle drugs to the desired location. Although the current paradigm in the delivery system design is to alter the chemical and material properties of the carrier to meet the requirements of the cargo molecule [39], also the target location

and the respective boundary conditions are elements that, indeed, play a crucial role in the success of the designed carrier system. Defining proper boundary conditions requires an in-depth analysis of the barriers to be overcome (from administration to the target location) as well as the respective clearance mechanisms. Of course, the barriers to be considered change with the target: At the tissue/organ level, the tissue stroma, different hemodynamic flow conditions, and organ-specific barriers are the main challenges that a drug carrier encounters. However, at the cellular level, molecular interactions with the glycocalyx, internalization mechanisms, and escape from endosomal and lysosomal compartments play an essential role for the delivery success [40]. Additionally, defining those boundaries becomes more challenging when considering the physical deviations and the heterogeneity of the biological targets. For instance, Sykes *et al.* [41] showed that changes in the tumor pathophysiology and volume can significantly affect the uptake, permeation and retention of nanoparticles *in vivo*. Again, this finding highlighted that, rather than developing a universal nanoparticle design, a case-specific design is required to improve the targeted delivery efficiency.

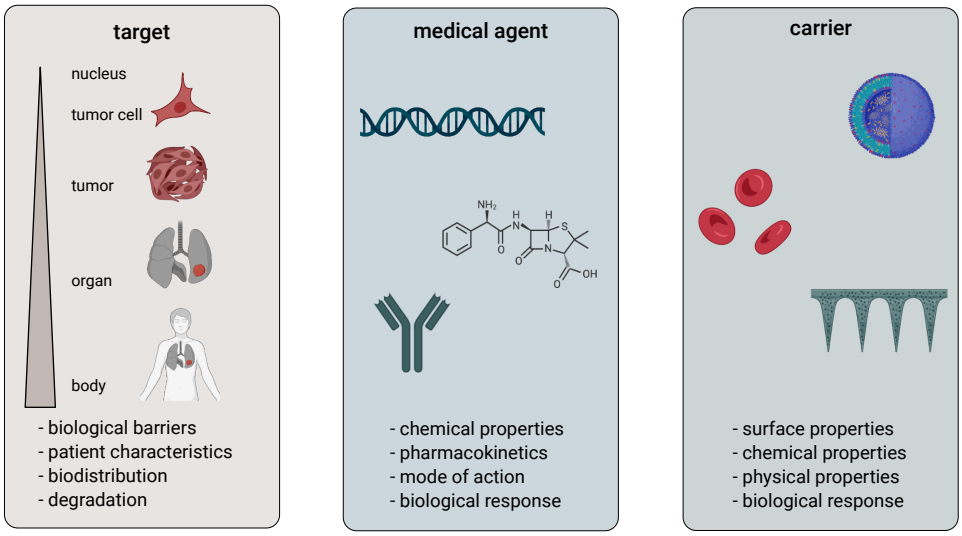

Figure 1.1: The interplay between the target scale, medical agent, and the carrier material; and the considerations brought about by these subjects define the boundary conditions when designing a drug delivery mechanism.

After deciding on the material type and the form of a carrier, its material properties must be well characterized and adjusted to meet general and case-specific requirements. Although some aspects such as stability and off-target distribution are common checkpoints for most delivery applications, different aspects become important depending on the carrier size and type. For instance, shape, size, and surface charge play crucial roles in the stability, bioavailability, and toxicity of nanosized materials, all contributing to the disparate fate of those nanomaterials [42-45]. Importantly, all those properties (together with the surface chemistry) contribute to the formation of a protein corona, and the resulting biological coating can lead to mononuclear phagocyte

sequestration and a reduction in delivery specificity [46]. Thus, the structure of the interface between the nanoparticle and its environment (*i.e.*, the target and biological milieu) at the molecular level is critical in determining the biological fate of the system.

Selecting an ideal administration route can help reducing the number of barriers that can hamper the delivery efficiency. For example, inhalable systems can improve the delivery and the therapeutic efficacy in the lungs compared to intravenous administration where the carrier would have to pass the reticuloendothelial system [47]. However, further characterizations are necessary to ensure that the carrier material matches the requirements of the selected administration routes. Mucoadhesion, hemocompatibility, injectability, and inhalability are some examples of specific requirements brought about by the selection of an administration route.

Additionally, different challenges arise from different classes of therapeutics (*e.g.*, small molecules, proteins and peptides, antibodies, nucleic acids, live-cell therapies), and thus play an important role in identifying feasible options for the targeted delivery of these agents [48]. For example, although it does not generate a crucial problem for small drug molecules, degradation by ubiquitous nuclease in the body is considered a main problem for nucleic acid therapeutics. To avoid this problem, chemical alterations are applied at specific locations of the nucleotide sequence, sugar rings, or at the termini of nucleic acids to improve their interactions with target cells [49]. In this thesis, instead of modifying drugs, the focus is to develop a controllable interface between the drug and its microenvironment to modulate the interactions between the drug, the carrier, and the environment as well as to fulfill certain case-specific requirements and to use endogenous markers to trigger drug release events.

As briefly outlined here, the complete design of a drug carrier material is ratheras a multicollinear problem than a stepwise process. Nevertheless, optimization is crucial to fulfill (sometimes opposing) demands for successful drug delivery. As stated above, strong interactions between the drug and the carrier material increase the loading capacity and unwanted drug leakage, whereas weakened interactions at the target are important to obtain a high release efficiency. A similar compromise is also required to ensure both, safety and efficacy.

In this thesis, smart drug delivery mechanisms were developed to generate a tunable or programmable interface between the target environment and the therapeutics (**Fig. 1.2**). Accordingly, the designed drug delivery mechanisms are grouped into three major categories based on the underlying strategies: The first chapter explains materials explicitly adapted to the physiological characteristics of the delivery point. The second chapter describes innovative platforms leveraging the pathophysiological environment of the point of care to activate the delivery of the cargo molecules. Finally, the third chapter focuses on complex autonomous systems initiated by specific signature conditions at the molecular level.

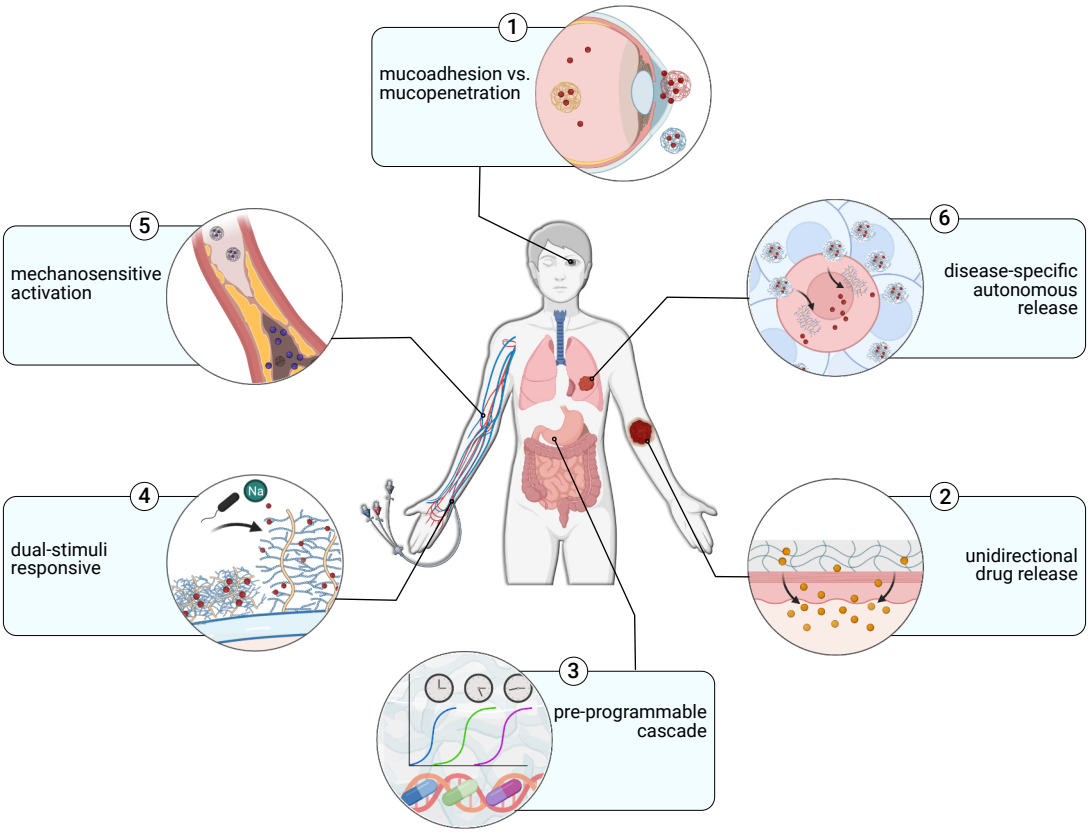

Figure 1.2: A systematic view of the mechanisms developed throughout this thesis to deliver therapeutics to its targets in a programmable manner. The term “programmable” refers to obtain a control over delivery destination (number **1, 2, 4, 5**), time (**3, 4**), or autonomous initiation at the target (**6**).

2. Materials and methods

2.1. Building blocks

In this thesis, smart drug delivery strategies were developed by constructing macro- to nano-scale materials using functional (macro)molecules. The material properties (and the modifications applied to these materials), as well as the measurement techniques are discussed in this section.

Probe particles

The architecture and the efficiency of the strand displacement-guided release cascade mechanism were tested by monitoring the liberation of commercially available probe nanoparticles (NPs). Here, branched polyethyleneimine-functionalized silver nanoparticles (AgNP, 100 nm, Sigma Aldrich), gold nanoparticles (AuNP, 5 nm, Sigma Aldrich), and the avidin coated Fe_2O_3 nanoparticles (20 nm, Nanomag®-D-spio avidin, Micromod Partikeltechnologie, Rostock, Germany) were selected as probe particles to monitor DNA-triggered cascade release mechanisms. These particle types were chosen to avoid any overlap in the detection spectra and to identify the release of individual components in a mixture (**Fig. A2**).

Mucin

Mucin is a large glycoprotein that is the main structural component of mucus. Physiologically, mucins can be classified as secreted gel-forming mucins, secreted non-gel forming mucins, and cell-associated mucins anchored to cellular membranes by a transmembrane domain. Depending on their location and classification, mucins can carry vital functions such as lubrication, protection against pathogens and micro/nanoparticles, and regulation of molecular uptake [50-52]. These diverse functionalities are made possible by their unique chemical structure carrying a hydrophilic core (glycosylated central region) and hydrophobic moieties (non-glycosylated termini). In detail, mucin macromolecules have an O-glycosylated backbone edged by cysteine regions and von-Willebrand factor-like domains at the termini that carry both anionic and cationic motifs. The protein backbone has a molecular weight of over 0.5 MDa, which including the glycosylation reaches values around a few MDa. The oligomerization due to disulfide bond formations by C-terminal cysteine knots and the carbohydrates increases mucin's overall molecular weight up to 50 MDa [53].

Thus, these properties that mucins hold make them ideal macromolecules for implementing specific functions to biomaterials and obtaining control in various processes, including the transport and adsorption of molecules. However, to ensure a certain level of functionality and to prevent unwanted structural alterations, Marczynski *et al.* [54] identified that the use of high-quality mucins is essential. Therefore, porcine gastric mucins were manually purified as described previously for further use as building blocks with slight modifications (**Fig. A1***)* [55]. Several additional changes were applied to purified mucins to conjugate desired molecules (*e.g.,* fluorescent molecules, oligonucleotides), or to immobilize them onto surfaces.

Mucin modifications

To enable mucin-based multilayer formation or to detect mucin-based nanomaterials, manually purified mucins were fluorescently labeled (with carboxy modified ATTO390, ATTO488, or ATTO594, ATTO-TEC GmbH, Siegen, Germany) *via* carbodiimide coupling. Stock solutions of these dyes were prepared by dissolving them to a concentration of c_{Stock} = 10.0 mg/mL in either ultrapure water (for ATTO488, ATTO594) or DMSO (for ATTO390). Dye solutions were diluted to a concentration of c_{ATTO} = 1.0 mg/mL in 1 mL of 10 mM 2-(N-Morpholino)ethanesulfonic acid hemisodium salt buffer (MES; pH = 5). Afterwards, 5 mM EDC and 5 mM sulfo-NHS were added to this solution, and the mixture was allowed to incubate under shaking in the dark at RT for 3 h. In parallel, 40 mg of purified mucins were solubilized in 19 mL PBS (10 mM, pH = 7). Then, both solutions were mixed thoroughly (V_{final} = 20 mL), and again allowed to react at RT for 3 h, avoiding light. To remove unbound dye molecules, the mixture was dialyzed (Spectrum™ Spectra/Por™ Float-A-Lyzer™ G2, MWCO: 300 kDa, Carl Roth) against ddH_2O for 2 days. The labeled mucins were lyophilized and stored at – 80 °C until further use.

Oligonucleotides were conjugated to mucin glycoproteins through disulfide bond formation between thiol-modified DNA molecules and cysteine side chains of mucin glycoproteins. To do so, DNA sequences were obtained from Integrated DNA Technologies (IDT, Munchen, Germany) with the modification "Thio-Modifier C6 S-S linker" at the 5' end, and stored in 0.1 mM EDTA containing 10 mM dithiothreitol (DTT). Before use, DTT was removed using an illustra-NAP-5 column (GE Healthcare, Freiburg, Germany). Next, purified mucins were dissolved to a concentration of 10 mg/mL in ddH_2O, and oligonucleotides were added to this mucin solution with a final single-stranded DNA (ssDNA) concentration of 100 µM. The mucin/ssDNA solution was stirred at 4 °C overnight to allow mucin-ssDNA conjugation.

Mucin glycoproteins were functionalized with folic acid for specific cell targeting *via* folate receptors. Folic acid was conjugated to carboxyl groups of mucin using carbodiimide chemistry. The folic acid conjugation to mucin glycoproteins was verified spectroscopically at 358 nm, and the conjugation efficiency was calculated using a folic acid standard curve (**Fig. A3**).

Mucin immobilization onto surfaces

Covalent conjugation of mucins on polydimethylsiloxane (PDMS) substrates was performed as previously described by Winkeljann *et al.* [56]. To do so, prepolymer and the curing agent (Sylgard 184, Dow Corning, Midland, MI, USA) were mixed in a 10:1 w/w ratio, allowed to degas under vacuum for 1 h, and 300 µL of the mixture was poured into each cuvette. After curing at 60 °C overnight, cuvettes were treated with O_2 plasma (Femto Model 1 base unit type B, Diener electronic, Ebhausen, Germany; 0.4 mbar, 30 W for 90 s) to replace the methoxy groups on the PDMS surface with hydroxyl groups. This step was essential to obtain an appropriate substrate for the covalent attachment of silane molecules. The latter silanization was performed by adding 0.1 % (w/v) N-[3-trimethoxysiyl]propylethylenediamine triacetic trisodium salt (TMS-EDTA, abcr GmbH, Karlsruhe, Germany) dissolved in 10 mM acetate buffer (pH = 4.5) to cuvettes and allowed to react for 5 h. Next, samples were washed with ethanol to remove the unbound residues and

incubated at 60 °C to stabilize the silane bonds on PDMS. As a next step, carboxyl groups of the silanes were activated by 5 mM EDC and 5 mM sulfo-NHS dissolved in 100 mM MES buffer (pH = 5.0) for 30 min. Finally, mucin macromolecules were coupled to the surface by replacing the EDC/NHS solution with 0.1 % (w/v) mucin solution dissolved in PBS (pH = 8.0). The occurring reaction between the amine groups of the mucins and carboxyl groups of the activated silanes was allowed to take place at 4 °C overnight to form a stable covalent bond.

Hyaluronic acid

Hyaluronic acid (hyaluronan, HA) is a linear anionic polysaccharide composed of disaccharide repeats of N-acetylglucosamine and glucuronic acid. As an essential component of mammals' extracellular matrix (ECM), HA maintains the viscoelasticity of liquid connective tissues such as the synovial and eye vitreous fluid. Importantly, as a highly hydrated macromolecule, it functions as a lubricant for the body's movable parts, such as joints. Due to its biocompatibility and biodegradability, hyaluronic acid and its derivatives are highly preferred in clinically used medical products [57]. Especially in skin tissue engineering, HA-based biomaterials are widely chosen since they are immunoneutral and can condition intracellular signals responsible for cell proliferation and migration, thus promoting wound healing [58].

In this work, hyaluronic acid sodium salt from Streptococcus Equi (Alfa Aesar, Ward Hill, MA, USA) was conjugated with dopamine molecules to generate an adhesive layer for unidirectional drug delivery on wet tissue wounds. The conjugation was established between the amine groups of dopamine and carboxyl groups of hyaluronic acid to keep the hydroxyl groups of dopamine available for hydrogen bond formation (thus, adhesion with the wet tissue surface). In brief, HA was solubilized to a concentration of 1 % (w/v) in MES buffer (10 mM, pH = 5). Afterwards, 5 mM EDC and 5 mM sulfo-NHS were added to this solution and stirred for 3 h. Next, the solution was mixed with 1 % (w/v) dopamine hydrochloride (Sigma Aldrich) dissolved in PBS (pH = 8.0) at a 1:1 (v/v) ratio. After stirring overnight, the solution was dialyzed against ddH_2O at 4 °C for two days and subsequently freeze-dried. The catechol functionalization was proved spectroscopically at 280 nm, and the degree of functionalization was calculated using a standard curve (**Fig. A3**).

Chitosan and alginate

Chitosan is a cationic polymer obtained by partial deacetylation of chitin, which is the second most abundant polysaccharide in nature. Chitosan is a linear copolymer composed of N-acetyl-D glucosamine and D-glucosamine units in different grades depending upon the degree of acetylated motifs. It is derived from natural sources such as the exoskeleton of insects, crustaceans, and some fungi. Due to its versatile biological activities (*e.g.*, biocompatible, biodegradable, antimicrobial, mucoadhesive) and ease of processing to obtain different materials (hydrogels, membranes, particles, fibers, and scaffolds), chitosan is one of the most used biopolymers in biomedical applications [59].

Alginate is an anionic heteropolysaccharide that is composed of 1,4-linked β-D-mannuronic acid and 1,4 α-l-guluronic acid residues. It naturally occurs in the cell wall of algae and certain bacteria.

Owing to its biocompatibility and physicochemical properties (especially gel-forming capability in presence of divalent cations), alginate and its derivatives are used in various biomedical applications such as bioink production, wound dressing, or drug delivery [60].

Both chitosan and alginate in their pristine forms are not suitable for obtaining a stable network to be used under physiological conditions where the material is immersed chiefly or in touch with a liquid environment and is exposed to ions, enzymes, and different pH levels. Thus, several stabilization strategies (covalent or non-covalent crosslinking and use of reinforcement agents) are employed for those polymer networks. In this thesis, high molecular weight chitosan (Sigma-Aldrich) and Na-alginate (Sigma-Aldrich) were mixed in different ratios (alginate: chitosan of 2:1, 1:1, or 1:2 (w/w)) to form nanoparticles with tunable mucoadhesion properties. In brief, 2% (w/v) chitosan was dissolved in 90% acetic acid, and 2% (w/v) alginate was dissolved in water. To prepare drug loaded nanoparticles, Timolol maleate (Sigma Aldrich) was dissolved in an alginate solution with a drug to final polymer ratio of 1:20 (w/w). The alginate solution was then added to the chitosan solution and stirred at RT for 48 h. The final (drug loaded) solution was fed to an electrospraying unit (voltage: 25 kV; flow rate: 2 – 10 mL/h; needle tip to collector distance: 5 – 15 cm) to form nanoparticles.

Poly(ethylene glycol) diacrylate

Poly(ethylene glycol)-diacrylate (PEG-DA) is a derivative of poly(ethylene glycol) (PEG) comprising repeating ethylene oxide units and polymerizable methylene end groups. It is a flexible, non-elastomeric polymer that has been widely used in microfluidics due to its resistance to nonspecific adsorption, low background fluorescence, and water stability [61,62]. Additionally, it is a nontoxic material that enables (concentration-dependent) control over the mechanical properties of the final material. Thus, it is used in different biomedical settings such as hydrogels for tissue osteogenesis [63], films for wound dressing [64], and freely circulating nanoparticles [65].

In this work, nanoparticles with tunable mechanical properties were fabricated to address different levels of stenosis for atherosclerosis treatment. To do so, PEGDA-based materials (*i.e.*, macroscopic gels and nanoparticles) with a tunable elasticity were fabricated *via* free-radical polymerization. To generate nanoparticles, PEGDA was first emulsified in a continuous oil phase (water-in-oil emulsification) as described by Anselmo *et al.* [65]. Additionally, to increase nanoparticle matrix–anionic drug interactions, 2-aminoethyl methacrylate hydrochloride (Sigma Aldrich) was added to the water phase to a final concentration of 42 mM.

2.2. Oligonucleotide design

In addition to being the hereditary information carrier in nature, due to their unique physical and chemical properties, DNA molecules are one of the essential tools for nanomedicine and (nano)material science. To form nucleic acid polymers, nucleotides are joined by phosphodiester bonds between the 5’ and 3’ carbon atoms of adjacent sugar rings. DNA base pairs are composed of two chains, running in opposite directions (oriented with opposite chemical polarities), and

held together by a specific pairing of purine nucleotides with pyrimidine nucleotides (Watson-Crick base pairing). The linear sequence of nucleotides is commonly described using a one-letter code representing the base sequences (adenine, thymine, guanine, cytosine) beginning with the 5' end of the chain. Adenine and thymine (A-T) base pairs are connected by two H-bonds, guanine and cytosine (G-C) pairs by three. Thus, slightly higher hybridization energy is observed for C-G rich sequences. The two strands of the DNA double helix are held together by hydrogen bonds between complementary base pairs.

When two complementary DNA oligomers form a duplex by hybridization, the hybridization reaction is second order, and the reverse reaction where the duplex dissociation spontaneously takes place is first order (**Fig. 2.1**).

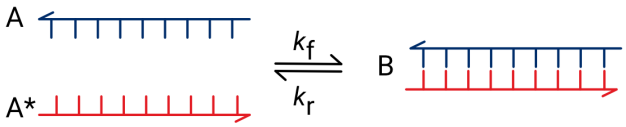

Figure 2.1: DNA hybridization and dissociation reaction. Left hand side shows two single stranded, fully complementary sequences that are forming the duplex B.

The equilibrium concentration of reactants and the product (duplex) is determined by the equilibrium constant (K) as

$$K = \frac{k_f}{k_r} = \frac{[B]}{[A][A^*]} \tag{2.1.}$$

where the k_f denotes the forward reaction rate constant, and k_r denotes the reverse rate constant. The equilibrium constant K is related to the standard Gibbs free energy change (ΔG°) of the reaction as described with van't Hoff equation as

$$K = e^{-\Delta G^\circ / RT} \tag{2.2.}$$

where R is the ideal gas constant and T is the absolute temperature. The stacking interactions between two bases of the same strand contribute strongly to the total energy gain of the hybridization reaction, and it depends on which bases are stacked. Therefore, the nearest neighbor model was found to allow for a precise prediction of the free energy ΔG° [66].

The free energy change can be predicted at different temperature, T:

$$\Delta G^\circ(T) = (\Delta H^\circ - T\Delta S^\circ) \tag{2.3.}$$

where T is the absolute temperature, ΔH° is the change in enthalpy, and ΔS° is the change in entropy.* The stability of the oligonucleotide constructs is strongly dependent on the ambient

* Note that the *Eq.* 2.3. assumes that ΔCp° is zero, which means that ΔH° and ΔS° are assumed to be temperature independent.

temperature. The melting temperature of the product is defined as the temperature where the half of the duplex is dissociated, and can be calculated as

$$T_m = -\frac{\Delta G^\circ}{R\ln\frac{[B]_{initial}}{2}} \quad (2.4.)$$

By using the nearest neighbor model, one can calculate not only the thermodynamic properties of the strand hybridization process, but also the thermal stability (melting temperature), and the energy associated with the hybridization of the DNA strands [67].

The forward reaction rate is dependent on temperature and the osmolarity of the environment. When electrostatic repulsion is screened, *e.g.*, in high ionic strength buffer conditions, duplex formation is strongly promoted due to ion cloud generated around DNA structures, thus weakening the strong repulsion of negatively charged phosphate backbones. Therefore, typical hybridization environments contain a high salt content [68]. Software tools can predict the formation of secondary structures from the base sequence for given sequences at envisioned concentration and environmental conditions. Thus, synthetically obtained DNA oligonucleotides can be used as building blocks to generate precisely designed materials [69].

After Ned Seeman and his colleagues' discovery of 4-way DNA arm junctions and their ability to connect networks through sticky ends, the generation of nano- to microstructures made of DNA has been explored exponentially [70]. Current DNA nanotechnology applications can be classified into two major compartments: First, structural DNA nanotechnology which focuses on the construction of static structures, and second,, dynamic DNA nanotechnology, where dynamic reaction networks based on DNA hybridization are designed [71]. However, obtaining a precisely controlled, functional DNA nanotool for a biomedical application requires the use of a simple design that relies on solid principles. In the projects that this thesis emphasizes, single-stranded oligonucleotides without secondary structures at the working conditions were designed to crosslink glycoproteins and/or to form nanoparticle aggregates to obtain precise control over their state, *e.g.,* reversible condensation and aggregation. Polynucleotides were designed using the software OligoAnalyzer 3.1 [72] and NUPACK [73] and obtained from Integrated DNA Technologies (IDT, München, Germany) in HPLC purified quality. The minimum free energy of the nucleotides was calculated according to nearest-neighbor empirical parameters. Gibbs free energy (ΔG°) values were calculated by considering the longest possible stretch of complementary bases.

All oligonucleotides were dissolved in RNase-free EDTA (0.1 mM, pH = 8.0, Thermo Fisher), and their concentration was adjusted to 100 µM using a NanoDrop 200c spectrometer (Thermo Fisher). Oligonucleotide solutions were stored at -20 °C until further use. To enable strong interactions with gold nanoparticles and mucin glycoproteins, oligonucleotides with a thiol modification were used. The latter sequences were obtained in their oxidized form, where the sulfur atoms were protected with disulfide bridges. Thus, these bonds were reduced by storing the oligonucleotides in 0.1 mM EDTA containing 10 mM reducing agent (*i.e.*, dithiothreitol, DTT) to release thiol groups by chemical reduction. DTT was immediately removed before use by passing the solution through

an illustra™ NAP™-5 column (GE Healthcare). Base pairing reactions and the conjugation to macromolecules were further analyzed with agarose gel and SDS-PAGE electrophoresis techniques.

2.3. Nanocarrier fabrication techniques

In the following, different nanocarrier fabrication techniques used in this thesis are explained in detail.

2.3.1. DNA-guided cluster formation

Probe particles were stabilized (using non-covalent and covalent interactions) with synthetic, single-stranded DNA sequences through the formation of NP/DNA micro aggregates, where the release of a single DNA strand can initiate the strand displacement cascade and, accordingly, allow for the liberation of nanoparticles.

Electrostatic stabilization

Branched polyethyleneimine (bPEI) coated silver nanoparticles (AgNPs) were selected to form electrostatically stable structures with DNA strands since the PEI coating carries primary, secondary, and tertiary amine groups interacting with the negatively charged phosphate backbone of DNA strands. To induce their microaggregation, AgNPs dispersed in ddH_2O (200 µL) were incubated with 50 µL DNA solution (c = 100 µM, Rhodamine Green modified) under constant shaking at RT for 12 h. Then, the supernatant of the microaggregates was removed, and the AgNP/DNA clusters were embedded in an agarose gel by instantly pipetting warm agarose solution in and out. The cluster-embedded agarose was placed into a fresh cuvette and set at 4 °C for solidification. The dispersal was initiated by incubating the aggregates (or the aggregate embedded agarose layer) with 150 mM NaCl solution which can break up the electrostatic interactions between oligonucleotides and the Ag NPs *via* Debye screening effects that weaken the electrostatic interactions.

Avidin – biotin interactions

The second type of cluster was generated using short cross-linking DNA strands (bridge DNA, bDNA) connecting two longer DNA strands that are attached to the NP surface (particle DNA, pDNA). Particle DNA strands were attached to the NP surface through avidin-biotin interactions. The avidin-biotin complex is the strongest non-covalent, rapidly occurring interaction between a protein and ligand with a K_d value of $\approx 10^{13} - 10^{15}$ M^{-1} [74]. In short, 100 µM of biotinylated DNA and bridge DNA strands were mixed and incubated at RT for 12 h. The DNA construct solution was then added to the Fe_2O_3 NP solution to obtain a 0.5 mg/mL final NP concentration.

Thiol-gold interactions

AuNP clusters were generated by coating gold nanoparticles with thiolated, single-stranded DNA oligonucleotides that contain partially self-complementary domains (crosslinker DNA, crDNA). Using this strategy, multiple DNA strands on each AuNP surface can induce the spontaneous formation of AgNP microaggregates since these strands have partial self-complementary regions. To do so, first, 10 µM of crDNA strands were incubated with 100 µM of (tris(2-carboxyethyl)phosphine) (TCEP; Carl Roth) at RT for 1h and the AuNPs were added. The concentration of DNA was adjusted to 1.5 nmol/mL of AuNPs. To induce AuNP aggregation, the NaCl concentration of the AuNP/DNA mixture was gradually increased to 1 M. The concentration was increased with increments of 50 mM, followed by 10 s of sonication, and 20 min of incubation. The resulting aggregate was incubated at RT for 4 h and washed thrice (10000·g for 20 min) to remove unbound agents.

The resulting aggregates were separately dissolved in 75 µL of 2 % (v/v) agarose solutions (Type IX-A, ultra-low gelling temperature agarose, Sigma Aldrich), and poured into cuvettes (UV-cuvette semi-micro, Brand, Werheim, Germany) in the order of AgNP and AuNP (for 2 layered hydrogels) or AgNP, Fe_2O_3NP, AuNP (for three-layered hydrogels). After each layer deposition, cuvettes were placed at 4 °C for 20 min to solidify the agarose hydrogel.

2.3.2. One-step condensation

Mucins were condensed as described in Yan *et al.* [75] but with slight modifications. After successful conjugation of DNA strands, mucins were incubated with the corresponding drug solutions for 4 h. Next, 250 µL of (drug-containing) mucin/DNA complexes (c_{Mucin} = 10 mg/mL) were added to 1 mL of glycerol solution (30 or 60 % v/v) to enable nanoparticle formation. To coat mucin nanoparticles with a cationic polymer, particles were subjected to a second condensation step. Here, a 30 % (v/v) glycerol solution containing either chitosan (chitosan 90/20, Heppe Medical Chitosan, Halle, Germany) or poly(L-lysine) (PLL, Sigma Aldrich) was added to the mucin nanoparticle/glycerol mixture with a final concentration of the cationic polymer of 0.05 mg/mL. Mixtures were dialyzed against 150 mM of NaCl solution to remove glycerol, excess coating substance, or unbound oligonucleotides.

2.3.3. Electrospraying

Electrospraying (electrohydrodynamic atomization) is a liquid atomization technique to form nano- to microparticles by employing electrical forces. In brief, an electric potential is applied to the polymer solution (containing the cargo molecule), fed to the nozzle tip with a constant flow rate, and atomized into droplets, which are deposited onto a collector surface. In detail, when the Coulombic force competing with the cohesion force in the droplet dominates, the surface tension gets relieved, and particle formation occurs. The point of breakdown (from solution to droplets) is called Rayleigh limit (L_R), and it also denotes the point where the surface tension is overcome by the applied electrostatic field [76]. Processing parameters (flow rate, distance, voltage), solution properties, and ambient conditions influence the resulting particle characteristics [77]. This

technique makes it possible to obtain a high yield of nanoparticles and high encapsulation efficiency by avoiding the limitations associated with harsh temperature and solvent conditions that can harm sensitive pharmaceutically active ingredients [78]. Depending on the molecular weight, chain entanglements, and the properties of the selected solvent, nanofibers can be produced with the same setting (electrospinning). When repulsive forces are more significant than the surface tension, the droplet elongates to form a cone (Taylor cone) and elongates to form a fiber jet [77]. To generate nanoparticles with tunable mucoadhesion properties, chitosan/alginate polyelectrolyte complex solutions with different chitosan to alginate ratios (2:1, 1:1, and 1:2 w/w) were electrosprayed to form nanoparticles carrying the drug timolol maleate (Sigma Aldrich). After preliminary screening based on homogeneity of the formed particles, process parameters were selected as follows: flowrate, 2 – 10 mL/h; voltage, 10 kV; distance, 10 cm. In a similar setting, to generate a non-adhesive and lubricant layer to form bilayer Janus films, polyvinyl alcohol (PVA, fully hydrolyzed, ca. 140,000 g/mol, Sigma Aldrich) and mucin solution were processed at 0.03 mL/h flow rate, 12 kV voltage, and 15 cm distance to obtain a nanofibrous mat.

2.3.4. Lipid film hydration

Liposomes are vesicular self-closed structures formed by one or several concentric lipid bilayers with an aqueous inner compartment. Due to their structural arrangement, they can entrap hydrophilic agents in their internal compartment and hydrophobic agents in their membrane. Liposomes' size, charge, and surface properties can be tuned by varying the lipid composition. Furthermore, the phase transition temperature, which indicates the point where the lipid bilayer becomes leaky, can be adjusted by tuning the components and their ratio. In this work, thermoresponsive liposomes are generated to release components as a response to temperature elevation. Therefore, a 0.25 mM lipid mixture composed of 6 % (mol/mol) 1,2-dioleoyl-3-trimethyl-ammonium-propane (DOTAP) and 94 % (mol/mol) 2,3-dipalmitoyl-sn-glycero-3-phosphocholine (DPPC) (both obtained from Avanti Polar Lipids, Alabaster, AL, USA) was dissolved in chloroform and placed under the fume hood overnight. The formed lipid layer was suspended in 0.5 mL of either ddH_2O or N-acetyl-D-glucosamine solution (GlcNAc, Carl Roth, 100 mM), and placed in an ultrasonic bath for 5 min subjected to 3 freeze-thaw cycles. The size of the liposomes was homogenized using a mini extruder (Avanti Polar Lipids) equipped with a 0.2 µm polycarbonate membrane. To remove unentrapped GlcNAc, liposomes were dialyzed against ddH_2O using a dialysis tube (MWCO: 6 – 8 kDa, Carl Roth), and they were stored at 4 °C until further use.

2.3.5. Water-in-oil emulsion

Thermodynamically, liquid droplets dispersed in another immiscible fluid can readily coalesce, and the mixture undergoes rapid phase separation. The water-in-oil emulsion technique uses a continuous oil phase to emulsify water-soluble polymer-cargo mixtures to form nanodroplets. In this study, PEGDA nanodroplets were generated by this technique, followed by free radical polymerization to crosslink droplets to form nanogels. In brief, 10 – 40 % (v/v) PEGDA (Mn = 700

g/mol, Sigma-Aldrich, Schnelldorf, Germany) was solubilized in ddH_2O and emulsified into a cyclohexane phase containing surfactants (Tween 80, 6.7 mg/mL and Span 80, 20 mg/mL) to create an energy barrier against droplet coalescence and stabilize the emulsion. The volume of the continuous oil phase was adjusted to obtain a uniform nanoparticle size at each polymer concentration. The size of the formed PEGDA droplets was homogenized by ultrasonication for 15 min. Next, a photoinitiator (2-hydroxy-2-methylpropiophenone, 35 mM, Sigma-Aldrich) was added, and the PEGDA droplets were photocrosslinked with a 365 nm long-wave UV lamp for 15 min (≈ 10 mW/cm^2, M365L2, Thorlabs GmbH, Bergkirchen, Germany). The cyclohexane and surfactant phase was replaced with ddH_2O or PBS buffer by several washing steps (3 times with cyclohexane and 5 times with the corresponding buffer, each at 7000·*g* for 19 min). To enable enhanced interactions with the highly negatively charged cargo molecule (*i.e.*, heparin), 2-aminoethyl methacrylate hydrochloride (Sigma Aldrich) was added to the water phase with a final concentration of 7 mg/mL, and the particles were prepared as described above.

2.4. Macroscopic multilayer coatings and films

Based on the requirements brought about by the required administration strategy (*e.g.*, number of doses, delivery direction, etc.) and the environmental conditions, biopolymer-based multilayers were generated.

Multilayer mucin coatings

Mucin multilayer coatings were generated to obtain a two-step drug release mechanism that responds to two distinct stimuli, *i.e.,* contact with physiologically relevant salt concentrations (150 mM NaCl) and temperature elevation. First, mucins were covalently immobilized onto PDMS surfaces, and the formed mucin layer was later either condensed or used as a base layer for deposition of multilayers. Similar to condensed mucin nanoparticles, either ionic or DNA-crosslinking was applied to stabilize the mucin brush coatings to entrap drug molecules.

Condensation mechanisms

Two-step condensation was applied to initiate the ionic stabilization of (drug-loaded) mucin layers. First, 30 % (v/v) glycerol was added onto the surface-bound mucin layer, and further stabilized with the addition of 100 mM $MgCl_2$ dissolved in 30 % glycerol solution. The system was allowed to incubate for 2 h and then washed with ddH_2O. The encapsulation efficiency was determined by exposing the condensed layer to a trypsin solution (50 µg/mL) for 12 h. On-demand decondensation of mucin layers was triggered by adding 2 mL of 150 mM NaCl solution. The second stabilization strategy was achieved by DNA-mediated condensation. In short, thiol-modified crosslinker DNA strands were used to crosslink the mucin macromolecules in presence of model drugs. Next, the DNA-mucin conjugates were condensed by adding a 30 % (v/v) glycerol solution and incubation for 4 h. Condensed layers were subjected to multiple washing steps with ddH_2O to remove the excessive glycerol and non-trapped drug molecules. On-demand

conformational change of the condensed mucins was initiated by the addition of 20 µL of 100 µM displacement DNA (dDNA) solution.

Multilayer deposition

The design of mucin multilayers can be divided into 3 main steps:

i. First, a non-condensed mucin base layer (including 0.5 mg/mL tetracycline hydrochloride, TCL) was incubated with lectin solution (*Triticum vulgaris* lectin, Medicago, 0.2 mg/ml) for 1 h. Due to favorable interaction of lectins with sialic acid and glycan groups of mucins, they can be used as a crosslinker for layer-by-layer deposition of mucin layers [79].

ii. After washing with HEPES buffer twice, cuvettes were filled with a mucin solution (1 mg/ml) containing 4 % (v/v) *N*-acetyl-D-glucosamine (GlcNAc) loaded thermoresponsive liposomes and incubated for 1 h to form the bottom layer. To connect the bottom and the top layer, dopamine hydrochloride solution (Sigma Aldrich, 50 mM, dissolved in 50 mM Tris buffer, pH = 8.5) was added to the cuvettes and incubated for 2 h.

iii. After the removal of this solution, a mucin solution containing 0.5 mg/mL TCL was added to the layers and ionically stabilized as described above.

All the unbound drug molecules were removed with several washing steps with ddH_2O, and the samples were stored at 37 °C. Two-step antibiotic release was initiated by first exposing the multilayers to physiologically relevant salt concentrations (150 mM NaCl, release from the top layer), and second by increasing the incubation temperature to 40 °C (release from the bottom layer).

Bilayer Janus films

Janus films were generated to strategically cluster different functions to opposing surfaces of the bilayer films. As a bottom layer, dopamine-conjugated hyaluronic acid (d-HA) film was generated by the solvent casting method. In brief, d-HA was solubilized in ddH_2O (10 mg/mL) and poured into custom-made polycarbonate well plates. Depending on the desired application, rectangular (1 cm x 3 cm) or circular (d = 1 or 2 cm) molds were used. Then, the solution in the wells was degassed under a vacuum and left to dry at RT for 2 days. The top layer was generated by electrospraying a PVA/mucin solution onto a pre-formed d-HA film. First, 500 mg of PVA was solubilized in ddH_2O (5 mL) at 80 °C for 1 h and was allowed to cool down to RT. Next, 25 g of mucin was solubilized in ddH_2O (5 mL) and gradually added to the PVA solution. The parameters of the electrospinning were selected as follows: voltage, 15 kV; distance between collector and syringe, 10 cm; flow rate, 0.03 mL/min. The final bilayer structure was exposed to glutaraldehyde vapor (GA; 25 % aqueous solution, Sigma Aldrich) for 12 h to form covalent bonds between hydroxyl groups of both layers and aldehyde groups of the crosslinker.

2.5. Dynamic light scattering and zeta potential

During dynamic light scattering (DLS) measurements, particles are illuminated with laser light (λ = 658 nm from a single-frequency laser diode that provides 40 mW). The dynamic fluctuation in the scattered light is quantified. Due to Brownian motion, dispersed particles move continuously while randomly colliding with the surrounding molecules. The speed of the particles can be related to their size: smaller particles move faster than larger ones, and this relation is defined in the Stokes-Einstein equation with the assumption of spherical geometry and liquid with a low Reynolds number [80]. The diffusion coefficient, *D*, of the particle's Brownian motion is proportional to the particle's mobility:

$$D = \frac{k_B T}{6\pi\eta r} \tag{2.5.}$$

where D denotes the diffusion coefficient, k_B: Boltzmann constant, *T*: absolute temperature, η: dynamic viscosity and r: the hydrodynamic radius of a spherical particle. Thus, DLS is an important micro- and nanoparticle characterization tool that gives information about hydrodynamic size, stability, conformational change, degradation, and phase transition temperature of nanoparticulate objects.

Another important nanoparticle characteristic is defined with zeta potential, the electrokinetic potential. If the solid-body surface of a material is brought into contact with an electrolyte solution, it undergoes a change in the charge distribution at the interface. Ions closer to the particle proximity are strongly bound on their surface to a distance that generates the Stern layer (**Fig. 2.2**). Ions after that point are loosely bound to those located at the Stern layer, which overall generates the diffuse layer. This phenomenon is called "the electrical double layer (EDL)", and it exists around each particle. The thickness of the EDL is represented by the Debye length which depends on the ionic strength, and thus, on the concentration, charge, and valency of the ions. Within this definition, an internal boundary exists where the ions located at the Stern layer and to an extent of the diffuse layer move with the particles. The EDL model distinguishes between a stationary immobile and diffuse mobile layer of counterions that compensate for the surface charge. After one point, any ion will stay in its location, and will not be affected by particle movement. This boundary is called the slipping plane. The electrophoretic potential at the slipping plane is called ζ-potential [80].

The zeta potential of particles dispersed in liquid is measured by the electrophoretic light scattering (ELS) technique. Therefore, samples are placed into a micro-electrophoresis system equipped with electrodes to which potential is applied at either end. Particles move towards the oppositely charged electrode and their velocity is measured and expressed in unit field strength as their electrophoretic mobility. Then, the Henry equation is applied to relate the electrophoretic mobility to the zeta potential:

$$U_E = \frac{2\varepsilon\xi}{3\eta} f(\kappa a) \tag{2.6.}$$

where U_E is the electrophoretic mobility, ε is dielectric constant, ξ is zeta potential, η is viscosity, and f(κa)is Henry's function.

For aqueous dispersions that exhibit H^+ and OH^- as major ionic constituents, zeta potential value is strongly affected by pH and the ionic strength. Importantly, the zeta potential decreases with increasing ionic strength due to a compression of the electrochemical double layer at high ionic strength. A common approach in drug delivery research is to correlate the absolute zeta potential value with the colloidal stability. However, the colloidal stability not only depends on electrostatic repulsive forces but also van der Waals attractive forces, thus, it is also possible to reach a highly stable nanoparticulate system with a low zeta potential value [81]. Steric interactions and the dispersant-particle dynamics must be considered in detail for stability assessments.

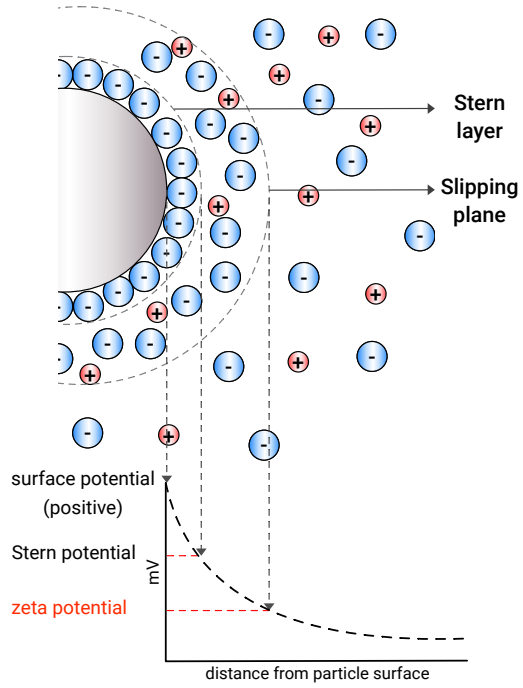

Figure 2.2: Simplified illustration of the electrical double layer at the surface of a (positively charged) model nanoparticle in an aqueous solution. The potential at the slipping plane is defined as the zeta potential of the nanoparticle, which brings detailed insight into the particle behavior (*e.g.*, dispersion, aggregation, flocculation, etc.) in a colloidal system.

Nanocarriers developed in this thesis were characterized in terms of their hydrodynamic size and zeta potential using a Litesizer™ 500 (Anton Paar). The temperature was either set to the target value or a temperature ramp was applied to detect dynamic size changes. For some particular cases, transmittance, intensity trace, and the polydispersity index (PDI) values were also recorded as further indicators for colloidal behavior (*e.g.,* aggregation, degradation, phase transition) and the broadness of the size distribution.

2.6. Systems used for the detection of released objects

Based on the application area, drug carrier type, and the drug release mechanism, several strategies were applied to detect the released objects (*e.g.*, drug molecules, fluorescence molecules, probe nanoparticles) spectrophotometrically.

Release from multilayers

Release of molecules was detected from the cuvettes where the multilayers (made of either agarose or mucin) were generated on-site (**Fig. 2.3**). For these experiments, the overall height of the gels was adjusted to avoid any interference with the light sent to the cuvette by the UV spectrometer, so that the detection of released objects could be individually monitored without external effects such as shaking or dilution. By employing time-lapse measurements, the release of objects from the reservoirs that they are embedded in, and their free diffusion to the corresponding media were monitored.

Release from dispersions

In the settings where the carrier matrix is dispersed in a liquid (*e.g.*, nanoparticle dispersions), dialysis tubes were selected as semi-permeable reservoirs to conduct drug release experiments. First, the (drug carrying) nanoparticle dispersion with a known volume and concentration was placed into dialysis tubes (donor compartment). Dialysis tubes were selected by considering the largest molecular weight cut-off that does not cause loss of the desired molecular species to retain inside the donor. Next, dialysis tubes were placed into a beaker containing drug-free buffer with a known volume (**Fig. 2.3**). Since the dialysis tubes do not interact with diffused objects, the setting allows for the detection of freely diffusing molecules that are liberated from the carrier matrices.

Unidirectional release

Permeable supports are useful tools to monitor the diffusion of nanocarriers and encapsulated agents over film-like materials or cellular monolayers. The unidirectional drug release tests were performed by placing the drug-loaded films into permeable polycarbonate inserts (BRANDplates® insert system, mesh size: 0.4 µm, Brand, Wertheim, Germany) with the drug loaded side facing downwards (**Fig. 2.3**). In the configuration where the inserts are placed into well plates, drug liberation into either side of the films can be separately determined.

Transmembrane permeation

Transmembrane permeation of molecules can be measured by placing a membrane in between acceptor and donor compartments of Franz diffusion cells, Valia-Chein cells, or Ussing chambers. In this work, *ex vivo* transcorneal permeation experiments were conducted using an Ussing chamber setup. First, the cornea of freshly excised pig eyeballs was excised along with 2–4 mm of scleral tissue and gently washed with cold saline solution twice. The isolated cornea was mounted in an Ussing chamber so that the epithelial surface faces the donor compartment (**Fig. 2.3**). The donor compartment was filled either with a drug solution or a nanoparticle dispersion that contains the same concentration of drugs. The receptor chamber was filled with the similar buffer that is used for the donor chamber.

The amount of drug entrapped in and on the corneal tissue was quantified at the end of each permeation experiment. Briefly, cornea samples were first gently washed with PBS to remove remaining loosely bound drugs on the surface and then placed in methanol at RT overnight. The drug amount in the methanol extraction liquor was quantified spectroscopically.

The drug flux (J_s) across the corneal barrier per unit area was calculated at the steady state by linear regression analysis of *ex vivo* permeation data following the relationship:

$$J_s = \frac{Q}{A \cdot t} \tag{2.7.}$$

where J_s denotes the drug flux (μg/(cm^2·h)), Q is the drug amount that passes through the membrane (μg), A is the area available for permeation (cm^2), and *t* is the time of the experiment (h).

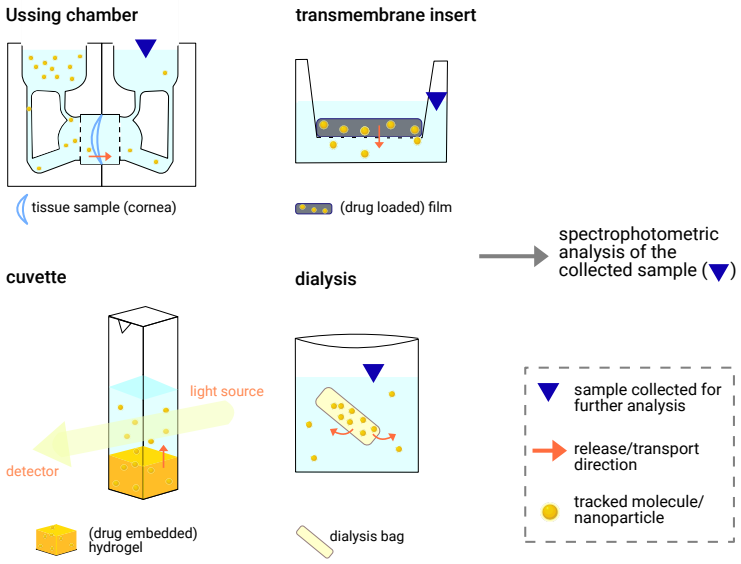

Figure 2.3: Setups used to monitor the release of probe nanoparticles or cargo molecules from the materials developed in this thesis.

The experimental setup (*e.g.*, cuvettes, dialysis setup, Ussing chamber) was placed into an incubator operating under constant shaking (40 rpm) and controlled temperature (37 °C). In predetermined time intervals, a fixed volume of a sample from the receptor side was withdrawn and replaced with a fresh buffer. The drug concentration of those samples was then assessed spectrophotometrically (specord210 spectral photometer, Analytikjena, Jena, Germany). The absorbance of the samples was measured where the corresponding drug has the maximum absorbance peak in its spectra. To correlate the absorbance with the concentration, the absorbance values of serially diluted drug solutions were measured, and a calibration curve equation was obtained (**Fig. A2-4**). To determine the encapsulation efficiency and cumulative release, the following equations were used:

$$\text{Encapsulation efficiency (\%)} = \frac{\text{amount of drug encapsulated in carriers (mg)}}{\text{initial drug feed (mg)}} \cdot 100 \quad (2.8.)$$

$$\text{Loading capacity (μg/mg NPs)} = \frac{\text{entrapped drug in NPs (μg)}}{\text{nanoparticle weight (mg)}} \quad (2.9)$$

$$\text{Cumulative release (\%)} = \frac{\text{amount of released drug (mg)}}{\text{amount of total drug in carriers (mg)}} \cdot 100 \quad (2.10.)$$

Similarly, adsorption and/or depletion of molecules, as well as the degradation of building blocks can be assessed by tracking corresponding molecules spectrophotometrically.

2.7. Mechanical characterization

An ideal elastic material after being exposed to a mechanical stress completely returns to its original geometry. On the other hand, a completely viscous material continuously deforms under constant load. However, most of the materials neither exhibit purely elastic or purely viscous character. This behavior is usually referred to viscoelastic material and described by a complex modulus $G^*(\omega)$ which can be separated into a real and an imaginary part.

$$G^*(\omega) = G'(\omega) + i \cdot G''(\omega) \quad (2.11.)$$

The real part $G'(\omega)$ describes the elastic response of a material whereas the imaginary part $G''(\omega)$ describes its viscous properties:

$$G'(\omega) = \frac{\sigma_0}{\gamma_0} \cdot \cos(\delta) \quad (2.12.)$$

$$G''(\omega) = \frac{\sigma_0}{\gamma_0} \cdot \sin(\delta) \quad (2.13.)$$

where and denote the amplitude of shear stress and the shear strain, respectively. The phase shift between the deformation of the material and its stress response is denoted with δ, which is dependent on the angular frequency ω of the stimulation. Mechanical characterization of the materials developed in the frame of this thesis was performed using a research-grade shear rheometer (MCR302, Anton Paar, Graz, Austria). Depending on the test type, different commercial measurement systems as well as custom made sample holders were used.

2.7.1. Viscoelastic properties

Viscosity measurements

Viscosity measurements were performed with a cone-plate measuring setup (CP50–1) in a rotational manner. 570 µL of a sample was pipetted into the measuring gap. Measurements were conducted at fixed temperatures (20°C or 37 °C) and a solvent trap was installed to avoid sample

dehydration. The shear-dependent viscosity of the solutions was determined for shear rates between $\dot{\gamma}$ = 10 s^{-1} and 1000 s^{-1}.

Frequency sweep

The viscoelastic properties of hydrogels were determined using a plate-plate measuring system (PP25, Anton Paar). 250 µL of the sample was placed onto the bottom plate and the measuring head was lowered to the measuring position. After an equilibration time of 30 s, a logarithmic frequency spectrum (oscillation frequencies f = 10 – 0.1 s^{-1}) of the viscoelastic moduli was recorded in a strain-controlled mode (γ = 1 %).

The gelation behavior of PEGDA hydrogels during crosslinking was assessed by recording the storage and loss modulus over a time span of 5 min in a torque-controlled manner (M = 0.5 µNm) at a constant oscillation frequency of f = 1 Hz. At t = 1 min, the sample was exposed to UV light (distance ≈ 5 cm) through the transparent bottom plate for 2 min. For these measurements, a transparent bottom plate (P-PTD200/GL, Anton Paar) was selected. An intermittent test was conducted to determine the deformation response of the crosslinked material at a constant torque level of M = 1 µNm and a fixed oscillation frequency of f = 1 Hz. Subsequently, a second frequency spectrum (f = 10 – 0.01 s^{-1}) was recorded with a constant strain level (determined as the average deformation recorded during the intermittent test).

Large Amplitude Oscillatory Shear (LAOS) measurements

At low mechanical loads, where Hooke's law applies a linear relationship between stress and strain is observed. When the mechanical load is increased, either strain weakening or strain hardening sets in, and Hooke's law is not applicable anymore [82]. The critical point is the point where the material leaves the linear response regime, and strain weakening can set in. In the non-linear viscoelastic regime, G' and G" are dependent on the strain amplitude, and the measurement signal cannot be detected as sinusoidal. At the non-linear regime, the material failure can set in, and the material cannot be determined as viscoelastic anymore. Thus, to detect the onset points for the non-linear material response of hydrogels, large amplitude oscillatory shear (LAOS) measurements were performed. The understanding of rheological behavior in both linear and nonlinear regimes gives a full notion of the rheological properties of the tested material [83]. In these measurements, the oscillatory strain applied to the samples is logarithmically increased (γ = 0.1 to 1000 %) while tracking the storage and loss moduli at a constant oscillation frequency of f = 1 Hz. All measurements were conducted at 37 °C using a humidity trap to prevent any solvent evaporation. The point where the material failure can take place was determined at the first point which significantly differs from the first measurement point.

2.7.2. Tensile and adhesion tests

The tensile properties of the macroscopic films were tested under uniaxial tension by fixing them at either end in custom-made sample holders. One clamp was fixed to the central shaft of the rheometer using a commercial adapter (D-CP/PP 7, Anton Paar); the second clamp was mounted onto the bottom plate (P-PTD 200, Anton Paar). The measurement head of the rheometer was

lifted at a constant speed of 10 µm/s until the film was ruptured, and the resulting normal force data were recorded at a sampling rate of 1 s^{-1}.

To determine the adhesion/detachment performance of the films, hydrated *ex vivo* tissue samples (eyeball, cartilage, tongue, intestine) were placed into a custom-made sample holder mounted to a commercial bottom plate (T-PTD 200, Anton Paar). Then, the adhesion/detachment tests were conducted in a humidified atmosphere at a constant temperature of 37 °C. The film sample was fixed to the measuring shaft of the rheometer by attaching the custom-made clamp to a commercial adapter (D-CP/PP 7, Anton Paar). The measuring head of the rheometer was lowered until one side of the bilayer film was brought into contact with the tissue (contact area ≈ 64 mm^2) for 10 s. Afterwards, the measuring head was lifted at a constant speed of 10 µm/s, and the resulting normal force was recorded at a measuring point density of 1 s^{-1} until the measured force dropped to zero. The adhesion energy was calculated from the force-distance plot by calculating the area under the force-distance curve.

2.8. *In vitro* cell culture studies

In the frame of this thesis, immortalized mouse embryonic fibroblasts (NIH/3T3) and human epithelial cells (HeLa) were used to assess the biological activity of the fabricated materials. NIH/3T3 cells were cultured in Dulbecco's modified Eagle medium (DMEM; Sigma Aldrich) supplemented with 10 % fetal bovine serum (FBS; Sigma Aldrich) and 1 % penicillin/streptomycin. HeLa cells were cultured in minimum essential medium (MEM; Sigma Aldrich) containing 10 % (v/v) FBS, 2 mM L-glutamine solution (Sigma-Aldrich), and 1 % (v/v) nonessential amino acid solution (Sigma-Aldrich). Cultured cells were incubated at 37 °C in a humidified atmosphere and 5 % CO_2.

Fluorescence staining of cellular sub-compartments

For a visualization of cells or their sub-compartments, several staining techniques were employed. The cell nuclei were stained with 4,6-diamino-2-phenylindole (DAPI; Ex/Em: 340/488 nm; Sigma Aldrich) by incubating cells with 300 nM DAPI solution prepared in PBS for 30 min. The endosomal escape of (fluorescently labeled) nanoparticles was determined with colocalization experiments. Therefore, one-fourth of the cell culture medium was replaced with nanoparticle dispersion containing 1 µL of endosome marker FM 4-64 (10 µg/mL in ddH_2O, Ex/Em: 515/640 nm; Invitrogen T1330). Cells were incubated for 24 h, washed twice, fixed with 4% formaldehyde, and imaged for analysis. To detect individual cell types in 3D co-culture models, cell trackers were used which remain in cells through several generations but do not getting transferred to adjacent cells in a population. To do so, dispersed cells were incubated either with 25 µM CellTracker™ Blue CMAC Dye (Ex/Em: 353/466 nm; Thermo Fisher) or 1 µM CellTracker™ Red CMTPX Dye (Ex/Em: 577/602 nm; Thermo Fisher) that were dissolved in serum-free medium at 37 °C for 30 min, centrifuged to remove excess dye, and resuspended in dye-free medium.

Cytotoxicity assessment

The *in vitro* cytotoxicity of materials fabricated in this thesis and their degradation byproducts were assessed with one-step Live/Dead staining (direct) and indirect WST-1 cytotoxicity tests. For direct detection, cells were stained with a solution containing two fluorescent dyes that can separately label live and dead cells. Calcein acetoxymethyl (calcein-AM, Ex/Em: 496/516 nm; ThermoFisher) is a membrane-permeant and non-fluorescent molecule until ubiquitous intracellular esterases remove ester groups and render the molecule fluorescent. In contrast, ethidium homodimer-1 dye (EthD-1, Ex/Em: 493/528 nm; ThermoFisher) enters damaged membranes of dead cells and binds to their nucleic acids with high affinity. After incubating with Live/Dead solution for 30 min, cells were imaged using a fluorescence microscope.

Stained cells that do not require Z-stacking were imaged using an inverted epifluorescence microscope (DMi8, Leica, Wetzlar, Germany) using either LED405 filter cube (Ex. = 375 – 435, DC = 455, Em. = 592 – 668, Leica) or FITC filter cube (Ex. = 460 – 500, DC = 505, Em. = 592 – 668, Leica). Images were acquired with a digital camera (Orca Flash 4.0 C11440, Hamamatsu, Japan) using the software Leica Application Suite X. For the samples where the z-stacking was required, a confocal microscope (Stellaris 8 Falcon, Leica) equipped with tunable White Light Laser (WLL) and Diode 405 laser was used.

The number of viable cells in culture is proportional to the total mitochondrial dehydrogenase activity. The indirect WST-1 assay is based on the cleavage of the tetrazolium salt WST-1 to formazan by cellular mitochondrial dehydrogenases. To assess the cytotoxicity of the degradation products of the materials prepared here, an indirect (following the ISO-10993 standards), or direct cytotoxicity test was applied [84]. For the indirect cytotoxicity tests, materials were incubated in corresponding media at 4 °C overnight, and sterile filtered to be used as a culture medium for the cells seeded with a density of 5000 cells/well to 96-well tissue culture well plates. For the direct cytotoxicity assessments, nanoparticle dispersions (in sterile culture medium) were replaced with the culture medium. After desired incubation time, the cytotoxicity of the material extracts was assessed with colorimetric WST-1 assay (Roche) at 450 nm following the manufacturer's protocol.

Flow cytometry

A flow cytometer equipped with a 488 nm argon-ion laser (15 mW) was used to detect the cellular internalization of (Atto-488 labeled) nanoparticles over 1 h, 4 h, and 24 h (BD FACSCalibur, OS X, BD Biosciences, San Jose, CA). Per sample 10,000 events were recorded and analyzed using CellQuest software (BD Biosciences). In these measurements, membrane-bound nanoparticles in the population were quenched with trypan blue. In cases where the endogenous trigger is not significantly present in off-target cells, nanoparticles were externally triggered by delivering the trigger DNA to the cells using a transfection reagent following the manufacturer's protocol (INTERFERin®, Polyplus Transfection, Illkirch, France).

The responsible mechanism for the uptake of (Atto-488 labeled) nanoparticles was determined by incubating NPs with the cells with blocked uptake pathways for 2 h (200,000 cells/well). To do so,

those cells were pre-incubated with one of the following inhibitors for 1 h: 7 µg/mL chlorpromazine (clathrin-mediated endocytosis inhibitor; Sigma Aldrich), 1 µg/mL filipin (caveolae-mediated uptake inhibitor; Sigma Aldrich), or 50 µM amiloride (a specific inhibitor for the Na^+/H^+ exchange during macropinocytosis; Sigma Aldrich). As a control group, cells that are not incubated with any of those inhibitors were used.

To detect cellular apoptosis, Annexin V/PI double staining kit (eBioscience™, Annexin V Apoptosis Detection Kit FITC; Thermo Fisher Scientific) was used. The Annexin V fluorescent signal corresponds to cellular apoptosis (which can be detected with FL1 laser; 488 nm, 530/30 nm) whereas propidium iodide (PI) signal (which can be detected with FL2 laser; 488 nm, 585/42 nm) corresponds to necrotic or late apoptotic cells, characterized by the loss of plasma integrity. To determine whether cells undergo an apoptotic pathway upon incubation with mucin NPs, target and off-target cells (100,000 cells/well) were incubated with mucin NP variants for 4 h. Experiments were conducted following the manufacturer's protocol and 10,000 events/sample were recorded under medium flow. The plotted data (PI vs. Annexin V) were divided in four regions to specify: *i*) viable cells (PI/Annexin V -/-); *ii*) early apoptotic cells (PI/Annexin V -/+); *iii*) late apoptotic cells (PI/Annexin V +/+); and *iv*) necrotic cells (PI/Annexin V +/-). The results were analyzed using the software CellQuest (BD Biosciences).

Fractionation Techniques

To determine whether drugs/drug carriers are trapped in the cellular membrane or internalized, cells incubated with nanocarriers were subjected to lysis to fractionate the cytosol and membrane parts. To do so, trypsinized and centrifuged cells (200,000 cells/well in 12 well plates) were resuspended in 100 µL of lysis buffer (20 mM HEPES, 10 mM KCl, 2 mM $MgCl_2$, 1 mM EDTA, 1 mM EGDA, pH = 7.2) and incubated on ice for 15 min. Next, samples were centrifuged at 20,800·*g* at 4 °C for 45 min. Supernatants (cytosol fraction) and sedimented pellets that are dissolved in lysis buffer (membrane fraction) were analyzed spectroscopically to determine their cargo content.

The miRNA elevation levels were determined by the qPCR technique. To do so, corresponding cells were cultivated up to > 75% confluency, trypsinized, and suspended in PBS. miRNA was isolated from the cells (≈ 10^6) following the instructions of the kit (High Pure miRNA Isolation Kit, F. Hoffmann – La Roche AG, Basel, Switzerland) and the concentration was measured using a NanoDrop 2000c spectrometer (Thermo Fisher). Per 20 µL reaction, 200 ng of isolated RNA was reverse transcribed into single-stranded cDNA using the High-Capacity cDNA Reverse Transcription Kit (Thermo Fisher). Stem-loop primers (Invitrogen, Thermo Fisher Scientific) specific for miR-21 as well as U6 (*i.e.*, the housekeeping gene) were designed as specified by Chen *et al.* [85] (**Table A1**). miR-21 expression level of the different cells was quantified using real-time polymerase chain reaction (RT-PCR). The reaction was carried out using KiCqStart® SYBR® Green qPCR ReadyMix™ (Sigma-Aldrich) and an "Mx3005P Real-Time PCR System" (Agilent Technologies, Inc., Santa Clara, CA, USA) according to the manufacturer's specifications. The primers (Invitrogen, Thermo Fisher Scientific) used for RT-PCR reactions were designed according to Xu *et al.* [86] and Zhang *et al.* [87] (**Table A1**). U6 was used as an internal control to normalize the

expression level of target miRNAs. The relative expression of miR-21 was calculated using the $2^{-\Delta Ct}$ method with $\Delta Ct = Ct_{miR\text{-}21} - Ct_{U6}$.

2.9. Statistical analysis and graphical representation

In this thesis, GraphPad Prism (Prism 9, GraphPad Software, San Diego, CA, USA) software was used for data plotting and statistical analyses. Before each analysis, the normal distribution of the measured values was confirmed with the Shapiro-Wilk or the Kolmogorow-Smirnow-Lilliefors tests. A Student's *t*-test was performed for normally distributed populations with homogeneous variances, whereas a Welch's *t*-test was used in case of unequal variances. One-way ANOVA and Tukey's multiple comparison test were conducted for the comparison between multiple samples. If not stated otherwise, the statistical level of significance was set to $p < 0.05$ and marked with an asterisk. Schematic representations were created using the software Affinity Designer (v. 1.10.03; Serif Ltd., Nottingham, UK) and BioRender.com.

3. Delivery mechanisms adapted to complex physiological environments

When designing a drug transport system, one of the first aspects to consider is the selection of a carrier material. Either a covalent or non-covalent interaction should be ensured between the carrier and the desired cargo to enable the entrapment of the latter. After this stage, the physiological environment that the carrier material will encounter during the route of delivery has to be evaluated. The performance of the delivery mechanism is strongly dependent on the dynamic conditions of the physiological environments they confront (*e.g.*, changes in chemical compositions, dynamic regeneration of boundaries, mechanical challenges, etc.). Thus, one additional role of a drug carrier material is to balance the conflicting requirements brought about by the complex physiological environments to ensure the therapeutic function of the carrier material under challenging circumstances. Accordingly, each carrier material should be designed with respect to the physicochemical properties of the apparent physiological environment. In this chapter of the thesis, delivery mechanisms that are adapted to meet the requirements of specific physiological environments are explored.

3.1. Nanoparticles with tunable mucoadhesion properties [†]

Mucosal systems are of particular interest in the field of drug delivery as they cover a significant fraction of the human body surfaces that putative drug carriers can come in contact with. They range from ocular surfaces, the lung, and the cervix to the gastrointestinal tract. In the last decade, a great deal of work has been conducted to understand the underlying principles of molecular transport across these mucosal barriers [88]. As a result, designing drug delivery systems by considering the boundary conditions of mucosal barriers bears a significant potential for the pharmaceutical industry [89].

To a large extent, the capacity of therapeutically active ingredients to trespass mucosal layers is limited by the binding interactions taking place at the mucus barrier – and mucin glycoproteins are the components primarily responsible for this effect. As introduced in the *Materials and methods* section, mucin macromolecules contain a zwitterionic protein backbone that is densely decorated with sugar residues, and many of these glycans carry sialic acid or sulfate groups, leading to the overall polyanionic character of mucin glycoproteins [53]. Accordingly, binding interactions between the mucin network and therapeutically active substances are highly dominated by electrostatic forces. To achieve increased retention/permeation properties and to gain control over such electrostatic interactions, most pharmaceutical formulations contain excipients with defined physicochemical properties.

[†] This section follows in part the publication: Kimna *et al.* Materials Science and Engineering C (2021).

Among other functions, the mucus layer on the wet epithelium acts as a trap to remove foreign substances such as allergens and pathogens, thus, the transport of "desired" substances through the mucosal layers requires the development of a well-controlled delivery system. Consequently, two main strategies were put forward to enable drug delivery to – and across mucosal barriers: Agents that chemically or physically disrupt the mucosa (*i.e*, mucolytics), and mucoadhesive formulations where the carriers exhibit strong binding interactions with mucus. For the latter, using cationic drug carriers has been suggested as the most promising strategy to increase the residence time of the drugs on mucosal surfaces [90-95]. It has been shown that particles carrying a positive net charge are prone to be trapped within the mucus layer due to the strong Coulomb interactions with the anionic glycans of the mucins [96]. However, the high level of mucoadhesion brought about by such particulate systems might be undesirable as these particles can be washed away together with with the mucus during mucus renewal.

Furthermore, inert materials that are firmly bound to the mucus may hamper biological functions of mucins in the mucosal barrier, and limit the diffusive entry of molecules [97,98]. In contrast, strongly anionic particles are not desirable either as they do not offer a sufficient retention time in mucus. Indeed, they are prone to be repelled by mucins, resulting in very low bioavailability. Overall, owing to these drawbacks, topical administration of drugs/drug carriers to the mucosa is generally very inefficient with a reported target delivery success rate of only < 5 % [99,100]. Especially for corneal applications (when the intraocular compartment is targeted), the bioavailability of the administrated drugs is limited by their interactions with membrane-tethered mucins. Thus, at the same time, a high level of mucin – drug interactions is required as the fast mucus replenishment on the ocular surface combined with the continuous tear drainage would lead to an immediate removal of the drugs. Vice versa, a substantial accumulation at the mucus/lumen interface comes with the risk of concentration-associated toxicity. Therefore, efficient transport of drugs across the ocular mucosal barrier remains as an unmet demand.

In this part of the thesis, nanoparticle carrier matrices were developed for their application on corneal surfaces, and the effect of nanoparticle (NP) properties on the corneal penetration behavior were investigated (**Fig. 3.1 A**). In detail, due to their favorable structural stability and biocompatibility [101-104], two well-characterized, biologically originated polymers carrying opposite charges, *i.e.*, chitosan (CS) and alginate (A) were chosen as NP-forming matrices. The pK_a values were reported for primary amines of chitosan as ≈ 6.5 (depending on the degree of N-deacetylation), and for carboxyl groups of alginate as ≈ 3.5, suggesting strong ionic interactions of these polymers in the pH interval of 4 – 6 [105]. Accordingly, three polymer blends were prepared to investigate three different charge regimes: net anionic (CS/A = 1:2), approximately neutral (CS/A = 1:1) and net cationic (CS/A = 2:1). Particles were produced using the electrospraying technique to avoid harsh physical and chemical conditions that can potentially alter the biopolymer characteristics, and to obtain particles in a dried state that allows for a longer storage time. All CS/A NP variants showed a monomodal size distribution (PDI: 0.10 - 0.41) in the hydrodynamic

diameter range of 240 - 380 nm (**Fig. 3.1 B**), which is way below the reported irritation limit for ocular administration [106-108].

Owing to the carboxylate groups present in the alginate dominated matrix, the zeta potential of CS/A = 1:2 NPs was determined as - 14.5 ± 6.1 mV. In contrast, the CS/A 2:1 NPs showed a positive zeta potential value of + 4.3 ± 2.5 mV (due to the primary amines present on each chitosan monomeric repeating unit (**Fig. 3.1 C**)).

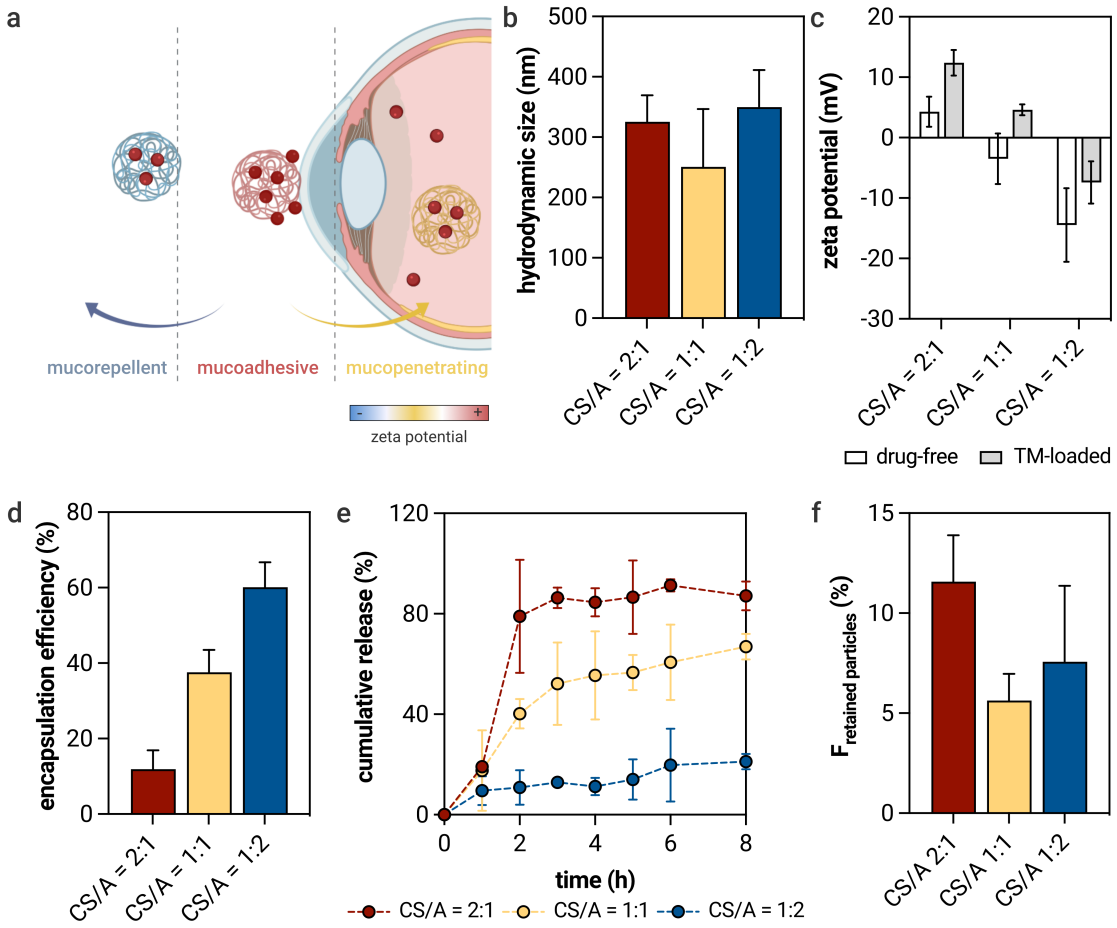

Figure 3.1: Nanoparticles with tunable zeta potential allow for control over mucoadhesion properties (**A**). Hydrodynamic size of the NPs in simulated tear fluid (STF) (**B**). Zeta potential of drug-free and TM-loaded NPs at pH = 7.4 (**C**). TM encapsulation efficiency of the particles (**D**). Cumulative TM release profiles of NPs at *in vitro* sink conditions (**E**). Fraction of the NPs retained on the mucin-coated surfaces (**F**). Data represent mean values, and the error bars show the standard deviation as obtained from $n \geq 4$ independent samples.

Further, the blend made from an equal polymer ratio turned out to be slightly negative (-3.5 ± 4.2 mV). In fact, this value seems reasonable considering the molecular weight of the charged

monomers and the deacetylation degree of chitosan as given by the vendor (≥ 75%) - theoretically, the CS/A 1:1 formulation should reach charge neutrality at a deacetylation degree of 78.5 %.

One possible application scenario in which ocular transmucosal delivery would be highly beneficial is the treatment of glaucoma, a disease usually caused by an abnormally high pressure in the posterior eye. Timolol maleate (TM) is an FDA-approved drug, which lowers the ocular pressure inside the eye by binding to beta-adrenergic receptors and blocking the endogenous adrenergic stimulation, thus preventing the production of aqueous humor [109]. The bioavailability of one dose of a commercial TM formulation is typically ≈ 1-2 %, therefore, multiple topical administrations per day (using a 0.125 % formulation) are required to reach the therapeutic need of 2.5 µg/day [110]. Although this application route can supply a therapeutic concentration of TM in the vitreous humor, significant side effects may occur from the large fraction of TM that fails to reach its target.

Therefore, in this study, TM was chosen as a cargo molecule for nanoparticle loading and for transmucosal transport assessments. TM has a predominantly cationic character in the physiological pH range of the ocular environment. Accordingly, for all three NP variants, incorporation of TM into the NP-forming matrix resulted in a shift of the NP zeta potential value towards the positive regime. In detail, the zeta potential values for the drug loaded NPs were strongly cationic (CS/A = 2:1, ζ = + 12.4 ± 2 mV), weakly cationic (CS/A = 1:1, ζ = + 4.6 ± 1 mV) and anionic (CS/A = 1:2, ζ = - 7.4 ± 4 mV) (**Fig. 3.1 C**). In agreement with the expected electrostatic interactions with the matrix, TM encapsulation efficiency was strongly dependent on the polymer blend ratio: NPs prepared from the alginate-dominated blend showed the highest encapsulation efficiency (60 ± 7 %). Consistently, the TM encapsulation efficiency decreased with decreasing alginate content in the NPs: encapsulation efficiencies were calculated as 38 ± 6 % for CS/A = 1:1, and 12 ± 5 % for CS/A = 2:1 (**Fig. 3.1 D**). After identifying the TM encapsulation efficiencies of the three NP variants, the release of TM from the NPs into simulated tear fluid was studied under full immersion conditions. The NP variants were observed to have very different release profiles: NPs carrying the highest positive net charge enabled the liberation of ≈ 80 % of the entrapped TM within the first 2 h (aided by electrostatic repulsion, (**Fig. 3.1 E**)). In contrast, only ≈ 10 % of the encapsulated TM was released from anionic CS/A 1:2 NPs in the same interval. A good compromise regarding the release rate was achieved with the weakly charged NPs. Here, the amount of anionic chitosan present in the NPs was sufficient to encapsulate the cationic TM with reasonable efficiency, whereas the cationic NP component ensured a sustained release. In other words, CS/A = 1:1 NPs provided efficient TM release over several hours while preventing an undesired burst release.

In a physiological setting, the most promising route of administration for this particle formulation would be the topical ocular application of a NP dispersion. To achieve a high bioavailability on-site (*i.e.*, in the vitreous gel), the loss of NPs should be minimized, and the majority of applied NPs should pass through the tear film and the corneal barriers, respectively. However, before the corneal barrier, secreted mucins (rapidly cleared) and membrane-associated mucins (slowly

cleared, forming a dense glycocalyx layer) form a challenging obstacle for allergens and pathogens, but also for the therapeutics [111]. Thus, diffusion kinetics play a vital role since the secreted mucins are cleared from the ocular surface within minutes (due to the blinking and tear drainage). Based on the Smoluchowski and Stokes-Einstein relations (see **Appendix A4.1.**), the theoretical diffusion time of NPs in a size range obtained in this study can be simply estimated: Considering the average thickness of the surface-bound mucin layers (*i.e.*, < 1 µm [112]), for example, the CS/A 1:1 formulation should require less than a minute to cross this barrier. When considering the comparably longer turnover rate of the surface-bound ocular mucus (*i.e.*, 5 – 7.7 min [113]), NP diffusion should not to be a limiting factor.

Additionally, the peripheral ocular mucus represents a more complex barrier with a higher thickness of 3 – 30 µm [114]. Thus, purely diffusive transport through this layer would take several minutes; however, other interactions (*e.g.*, electrostatic interactions or forced mixing driven by the blinking process) can strongly affect the fate of the NPs. To gain a better understanding of NP interactions with mucins, the mucoadhesive performance of (fluorescently labeled) NPs was tested by detecting the fraction of NPs attaching to surface-bound mucins. To probe these interactions, purified porcine gastric mucins were used as MUC5AC is the most prevalent secreted ocular mucin isoform in healthy tear fluid [111]. It was observed that the relative binding affinity of the strongly cationic CS:A = 2:1 NP species was higher than that of NPs generated from the other two polymer blends (**Fig. 3.1 F**). Notably, the anionic NP species (CS:A = 1:2) showed a higher binding affinity than the weakly cationic NP (CS:A = 1:1) sample. This finding agrees with previous observations that uncharged molecules and particles show the lowest binding propensity towards mucin glycoproteins [115,116]. This can be rationalized by attractive electrostatic interactions between anionic NPs and positively charged amino acid residues present in the mucin termini, as well as between cationic NPs and anionic motifs (*i.e.*, sialic acids and sulfate residues) of the mucin backbone [117].

Next, to gain a deeper understanding of the drug transport performance of NPs at a corneal barrier, *ex vivo* transcorneal permeation experiments were performed using an Ussing chamber. Such tests allow for the detection of the TM fraction that successfully crosses the corneal barrier. Due to their good drug loading and release performance, CS/A 1:1 NPs were chosen for these tests, and the findings were compared with those obtained for a TM solution of similar drug concentration. When the TM solution was placed into the donor chamber, only ≈ 65 % of the possible maximum TM concentration was detected in the receptor compartment (**Fig. 3.2 A**). However, the CS/A 1:1 carrier matrix was successful in transporting ≈ 89 % of the theoretical maximum amount of TM to the receptor chamber. In addition, the calculated permeability parameter also indicated a strong permeation enhancer effect of the carrier matrix (P_{NP} = 15 ± 1 mm/h) compared to the free TM solution (P_{TM} = 2 ± 1 mm/h) (**Fig. 3.2 B**).

When the *ex vivo* permeation studies were completed, the cornea samples were removed from the Ussing chamber for further examination. It was found that the corneal hydration levels remained in the non-pathological range (> 75 %), indicating that the cornea was not damaged by the NP

treatment [118] (**Fig. 3.2 C**). Next, cornea samples were dissected to determine the amount of TM retained in the tissue. A significant amount of free TM was retained at the corneal barrier (≈ 35 % of the TM feed), whereas the NP matrix could reduce this unwanted accumulation to ≈ 11 % (**Fig. 3.2 D**).

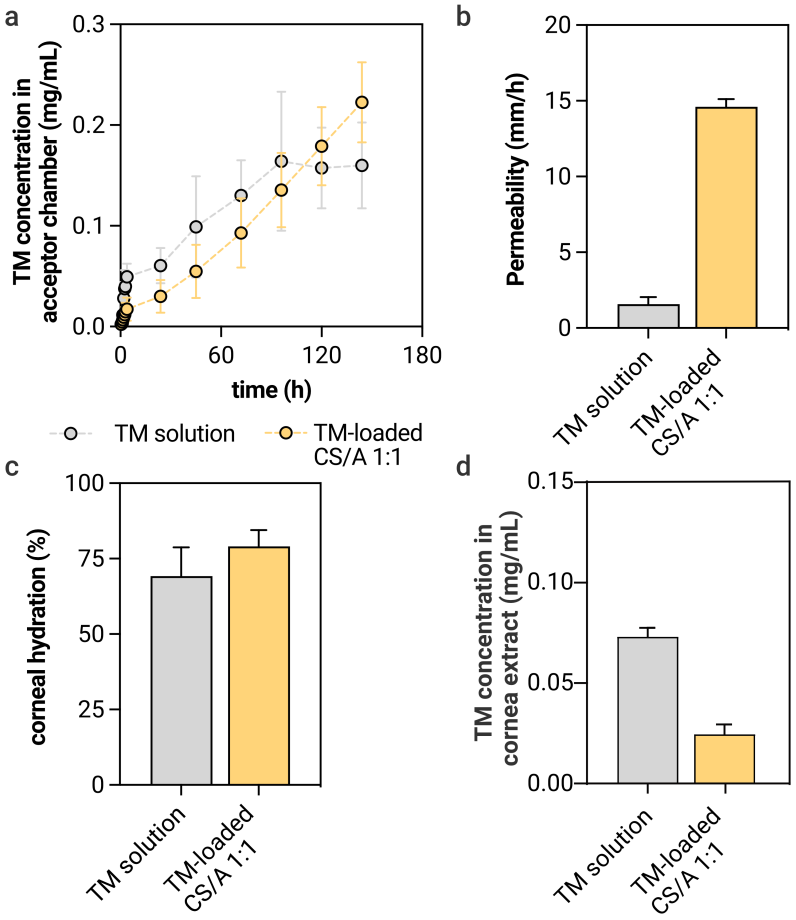

Figure 3.2: TM concentration at the receptor compartment of the Ussing chamber (**A**). Permeability parameter calculated for the free TM solution and the nanoparticle formulation (**B**). TM concentration detected in the corneal tissue liquor (**C**). Hydration levels of the cornea samples after the timespan of the *ex vivo* permeation experiments (**D**). Data represent mean values, and the error bars show the standard deviation as obtained from n = 5 independent samples.

The higher accumulation of free TM molecules on the cornea compared to encapsulated TM is likely to be attributed to the cationic nature of the drug: the corneal glycocalyx with surface-bound mucins facilitates electrostatic binding interactions with the cationic TM molecules. However, such attractive electrostatic interactions might help to reduce drug flushing from the precorneal segment through the tear fluid, and excessively strong binding results in drug accumulation rather than increasing the penetration. Thus, slightly cationic carriers offer a good trade-off between

mucoadhesion and barrier penetration. Recently, Cheng *et al.* [119] investigated the effect of alginate coating on strongly cationic NPs on mucosal transport efficiency, and their results were also in complete agreement with the picture depicted here: by tuning the zeta potential of the particles, they were able to increase the transport rate of the entrapped drugs (*i.e.*, insulin) across the intestinal mucosal barrier.

In other words, modulating the net charge of biopolymer-based drug carrier particles alters not only their drug encapsulation efficiency and drug release profiles, but also their mucoadhesivity. By adjusting the polymer composition, it was possible to change those properties of NPs that are responsible for the desired functionality (mucoadhesion vs. mucopenetration). In the case of TM delivery, an accumulation of the cargo drug on the corneal surface is undesired. However, for other ophthalmologic (*e.g.*, corneal wounds or infections) or gastrointestinal treatments, increasing the residence time of the drug/drug carrier on the mucosal surface can be favorable. This can be the case if a therapeutic action is desired on the mucosal surface – which is possible with NPs with a tunable mucoadehsion/mucopenetration profile such as those developed here.

3.2. Multifunctional bilayer films for unidirectional drug release into wound tissue ‡

In the previous section, a nanoparticulate system with tunable intrinsic properties was proposed to regulate the permeability propensity in (ocular) mucosal barriers. In other biological environments where the material is exposed to different tissues and biological fluids, adjusting the material properties to meet environmental conditions (*i.e.*, biofluid flux, hemorheological changes) may become even more challenging. A prominent example of such a complex environment is the wet epithelial wound tissue: while promoting wound closure, a battle must be won against external factors (*e.g.*, bacterial colonization, mechanical weathering) that may adversely affect the healing process. On the side facing the wound, good interaction with proteins/cells is imperative for a successful tissue adhesion, but this is not desired on the opposite side to avoid biofouling. In addition, the release of therapeutic molecules should be canalized to the point of care to prevent drug loss to the surrounding; this creates another asymmetric demand. Further, considering the drawbacks of unwanted adhesions to the surrounding tissues, a one-sided adhesion performance would be one of the most important properties such a system needs to have.

In this part of the thesis, a Janus-type bilayer film (JF) with asymmetric functionalities was developed to cope with various tasks required at the interface between a wet epithelial wound and healthy tissue. JF layers were made from different biopolymers to manage the conflicting functions that are needed on the opposing surfaces of the film. The bottom layer is composed of hyaluronic acid (HA) to benefit from its superior ability to support cellular proliferation and migration [58]. To achieve wet-adhesive behavior, HA was modified with dopamine *via* carbodiimide coupling: catechol-type molecules such as dopamine can engage in a variety of unspecific, non-covalent

‡ This section follows in part the publication: Kimna *et al.* Advanced Functional Materials (2022).

interactions that enable adhesion to a wide range of surfaces, including wet tissues [120,121]. At the molecular scale, different interactions (*e.g.*, physical interactions, Michael addition, and Schiff-base reactions [122,123]) can occur between the catechol group of dopamine and other chemical motifs found in epithelial tissues. Here, dopamine-modified hyaluronic acid (d-HA) films were prepared with varying geometries and served as a base layer for the second layer comprising electrospun PVA/mucin nanofibers (**Fig. 3.3 A**). Mucin was selected as a key component of this layer as mucin-based coatings have previously been shown to suppress biofouling evets. Thus, it should be able to protect wet wound tissue from bacterial contamination. To facilitate electrospinning of mucins, PVA was added as a structural reinforcing agent.

When cross-sectional and top views of the JFs were analyzed with SEM, an isotropic distribution of bead-free nanofibers (180 ± 50 nm) was detected (**Fig. 3.3 B**). The final JF structure was not adhesive in its dry state (the envisioned storage condition), and could be easily handled to be applied onto the desired surface.

Prior to investigating the functionalities brought about by the asymmetrical design of the material, the JFs were characterized in terms of their physical properties. First, the degradation lifetime of the JFs was tested under full immersion conditions by simultaneously monitoring the fluorescence intensity of labeled mucins (red line) and the absorbance signal of dopamine (grey line) (**Fig. 3.3 C**). At *in vitro* sink conditions, the bottom layer (d-HA) was largely disintegrated within the first 2 days whereas the degradation of the mucin component from the top layer was delayed by ≈ 2 days.

Additionally, similar degradation profiles were obtained when JFs were immersed in different media that mimic tear fluid (STF), intestinal fluid (SIF), or saliva (HSM) (**Fig. A5**). However, it can be speculated that this degradation behavior might vary depending on the physical conditions the film is exposed to. For example, when applied onto a dynamic surface such as an eyeball, movements of the eyeball and eyelid load may shorten this lifespan, whereas a skin wound on a relatively static location may delay the decomposition of JFs. Overall, the delayed degradation behavior of the top layer observed in the tested conditions should be very helpful for protecting the wound site from undesired mechanical challenges.

To circumvent an *on-site* dilution effect (due to certain characteristics of dynamic biological environments such as mucus turnover and/or biofluid flow), the selected model drug (broad spectrum antibiotic tetracycline hydrochloride, TCL) was loaded only to the bottom layer of JFs, and its release was examined using a semi-permeable insert setup. When the drug-free PVA/mucin layer of JF was facing the semi-permeable membrane, the drug amount detected in the acceptor chamber was negligible (cumulative release of < 2 % after 6 h) (**Fig. 3.3 D**, left). Thus, the PVA/mucin layer can prevent the undesired diffusion of embedded molecules loaded to the bottom layer. In contrast, when the JFs were placed with the drug-loaded side facing the membrane, a highly efficient (88 ± 7 %), unidirectional drug release from the attached surface was achieved (**Fig. 3.3 D,** right). In detail, the drug release profile reached a plateau at (72 ± 12 %) after ≈ 6 h, which was in line with the degradation behavior of the d-HA layer.

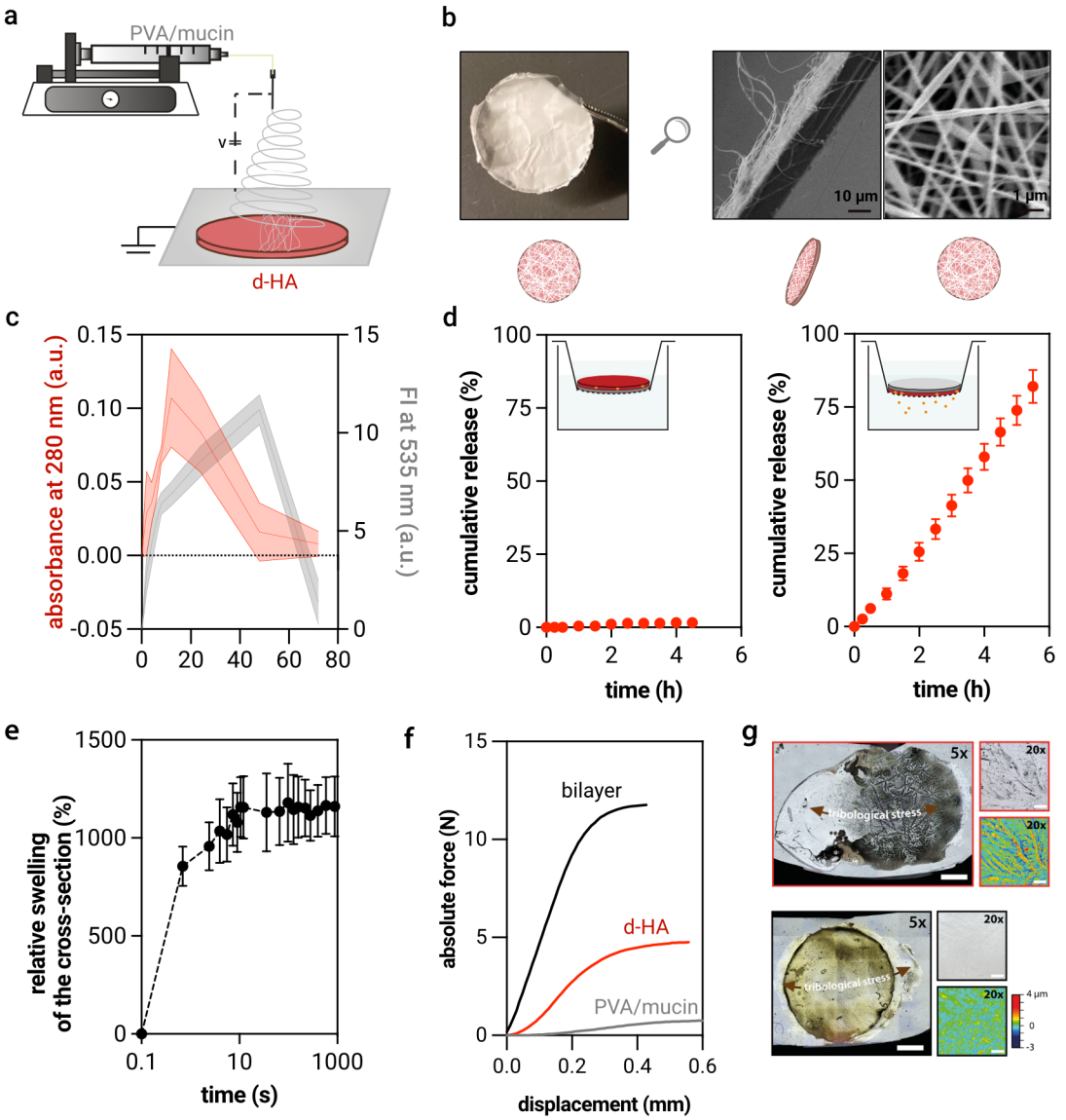

Figure 3.3 Schematic representation of the JF production (**A**). Photograph of the top side and SEM micrographs showing side and top views of the JF (**B**). Degradation profile of individual layers when placed into PBS (**C**). Cumulative drug release from JFs when the layer facing the acceptor chamber is PVA/mucin (left) and drug loaded d-HA (right) (**D**). Relative swelling profile of the cross-section of the JFs (n = 7) (**E**). The error bars denote the standard error of the mean. Representative stretching force – displacement curves of individual layers and the bilayer films (**F**). Morphology of d-HA monolayer (top) and bilayer films (bottom) upon exposure to tribological stress (**G**). Images in grey scales represent combined laser confocal/light microscopy pictures; colored images represent topographical images. Scale bars in 5x and 20x images depict 2 mm and 0.1 mm, respectively. If not stated otherwise, data shown represent mean values, error bars denote the standard deviation as obtained from $n \geq 3$ independent samples.[§]

§ I acknowledge Maria G. Bauer for conducting drug release from the control group, swelling experiments, and tribological damage assessments.

Drug release from swellable matrices such as d-HA is mainly governed by drug diffusion through the gel matrix; in such systems, swelling occurs in form of a glassy – rubbery transition of the polymer as the buffer penetrates into the matrix [124]. In this setup, the release of drug molecules from the d-HA matrix was also driven by the hygroscopic nature of HA, which results in a very high swelling capacity (≈ 1100 % after ≈ 10 s) (**Fig. 3.3 E**). Considering its potential application in a wet wound environment, d-HA may actively absorb the exudate, thereby reducing the risk of bacterial infection and promoting the wound healing process [125]. In this state, hydration of the d-HA side of the JF initiates one-sided swelling, thus increasing the diffusional path length of the loaded drug molecules. Therefore, it is hypothesized that unidirectional drug release from the d-HA layer can be initiated by fluid penetration into the dry matrix, and three following aspects are relevant: (*i*) swelling during the transition between the glassy polymer state and its rubbery state due to the hydration of the matrix; (*ii*) chemical potential driven mass transfer of the drug molecules to the surrounding fluid; (*iii*) erosion (degradation) taking place at the boundary between the matrix and the aqueous environment.

The supporting function of the PVA/mucin layer was also reflected in the mechanical properties of the JFs: when tested in the dried state, the monolayer d-HA films exhibited a relatively low stretching resistance and weak integrity (**Fig. 3.3 F**). The maximum rupture force detected for the individual d-HA and PVA/mucin layers were (4.6 ± 2.0) N, and (1.1 ± 0.5) N, respectively. However, when the individual layers were covalently crosslinked *via* glutaraldehyde exposure, JFs showed a maximum rupture force of (9 ± 3) N, which is ≈ 2-fold higher than that of d-HA monolayers. Furthermore, the structural fortification achieved by the deposition of the PVA/mucin layer onto d-HA protected JFs from mechanical stress: after application of tribological stress using an oscillatory tribology setup, a clear optical difference was observed between d-HA layers and JFs (**Fig. 3.3 G**): d-HA monolayers spread by (43 ± 8) %, while JFs remained stable and showed reduced spreading of (10 ± 8) % only.

After characterizing the material properties, several *in vitro* evaluations were conducted to investigate the biological response to JFs. First, cellular attachment to either side of the bilayer film was investigated using immortalized human epithelial cells (HeLa) as a model cell line. It was found that the cell density on the d-HA surface was similar to that of the control group (tissue culture plates; TCP) (**Fig. 3.4 A**). In contrast, a remarkably reduced cell count was achieved on the PVA/mucin surface; this is in line with previous studies which showed the cell-repellent function of mucin-coated surfaces [126-128]. Therefore, the mucin-containing top layer of the film has the potential to protect a wounded tissue area from unwanted cellular overgrowth potentially reducing the risk of fibrous encapsulation [129]. Furthermore, when JFs were placed onto a scratched cellular monolayer, the d-HA layer did not physically limit the cellular migration to the cavity created underneath (**Fig. 3.4 B**)

Although HA coatings have been shown to contribute to bacterial inhibition in the early stages of bacterial attack [130,131], dopamine conjugation was observed to counteract this effect due to its highly adhesive properties: both *Gr*(+) and *Gr*(-) bacteria (*i.e.*, *S. aureus* and *E. coli*, respectively)

adhered equally well to d-HA films and control (TCP) surfaces (**Fig. 3.4 C**). In contrast, the PVA/mucin side reduced the adhesion of *S. aureus* moderately; however, this effect was significantly stronger for *E. coli*. This finding was crucial because bacterial colonization on the material surface can critically complicate the wound healing process, and may result in longer treatment time, and can even cause severe infections [132].

During tissue repair and remodeling, macrophages are polarized to M1 and M2 types: M1-type macrophages participate in pro-inflammatory responses and play a central role in the host defense against infections; in contrast, the M2 type is associated with anti-inflammatory reactions, tissue remodeling, and fibrosis [133]. Once a foreign material is implanted into the body, immunological responses are initiated in a cascade-like manner. Starting with the acute response and the innate recognition of the foreign material, the subsequent chronic immune response can eventually lead to rejection of the implant [134]. To prevent unwanted immune response such as fibrotic encapsulation, materials with reduced protein adsorption profiles are developed [135]. Here, preliminary tests performed with fluorescently labeled proteins showed that the PVA/mucin layer exhibits reduced protein adsorption compared to the TCP surface and d-HA layer (**Fig. A6**).

To gain better insights into the immunological response towards JFs, the cytokine expression patterns were evaluated for both surfaces. The asymmetrical design of the bilayer film was important here as well: when macrophages were seeded onto the d-HA surface, pro-inflammatory markers, *i.e.*., tumor necrosis factor-α (TNF-α) and interleukin-6 (IL-6), were expressed at levels in the similar order of magnitude as those obtained for cells seeded onto TCP (**Fig. 3.4 D**). Furthermore, after 72 h, expression of the interleukin-1 receptor antagonist (IL-1Ra) – a type of anti-inflammatory cytokine – was ≈ 4.4 times higher on the surface of d-HA than on TCP. Indeed, previous studies reported that HA-rich materials promote the transformation of macrophages from a pro-inflammatory to a reparative phenotype [136-138].

In contrast, when macrophages were seeded onto the PVA/mucin layer, cytokine expression levels were up to two orders of magnitude lower than the results found with d-HA and TCP surfaces. This result was in agreement with previous studies investigating the short- and long-term response of macrophages seeded onto mucin-based materials: there, mucin-based gels were shown to have a broad dampening effect on the cytokine expression in macrophages, both *in vitro* and *in vivo* [129,139]. Consequently, the upper PVA/mucin layer of JFs could generate a stealth effect to help the material avoiding immune recognition, which may help preventing both acute inflammation reactions and fibrous encapsulation. Taken together, cytokine expression patterns after macrophage incubation on d-HA or PVA/mucin surfaces suggested that the immune responses at the wound – healthy tissue interface can be modulated by JFs in a favorable manner.

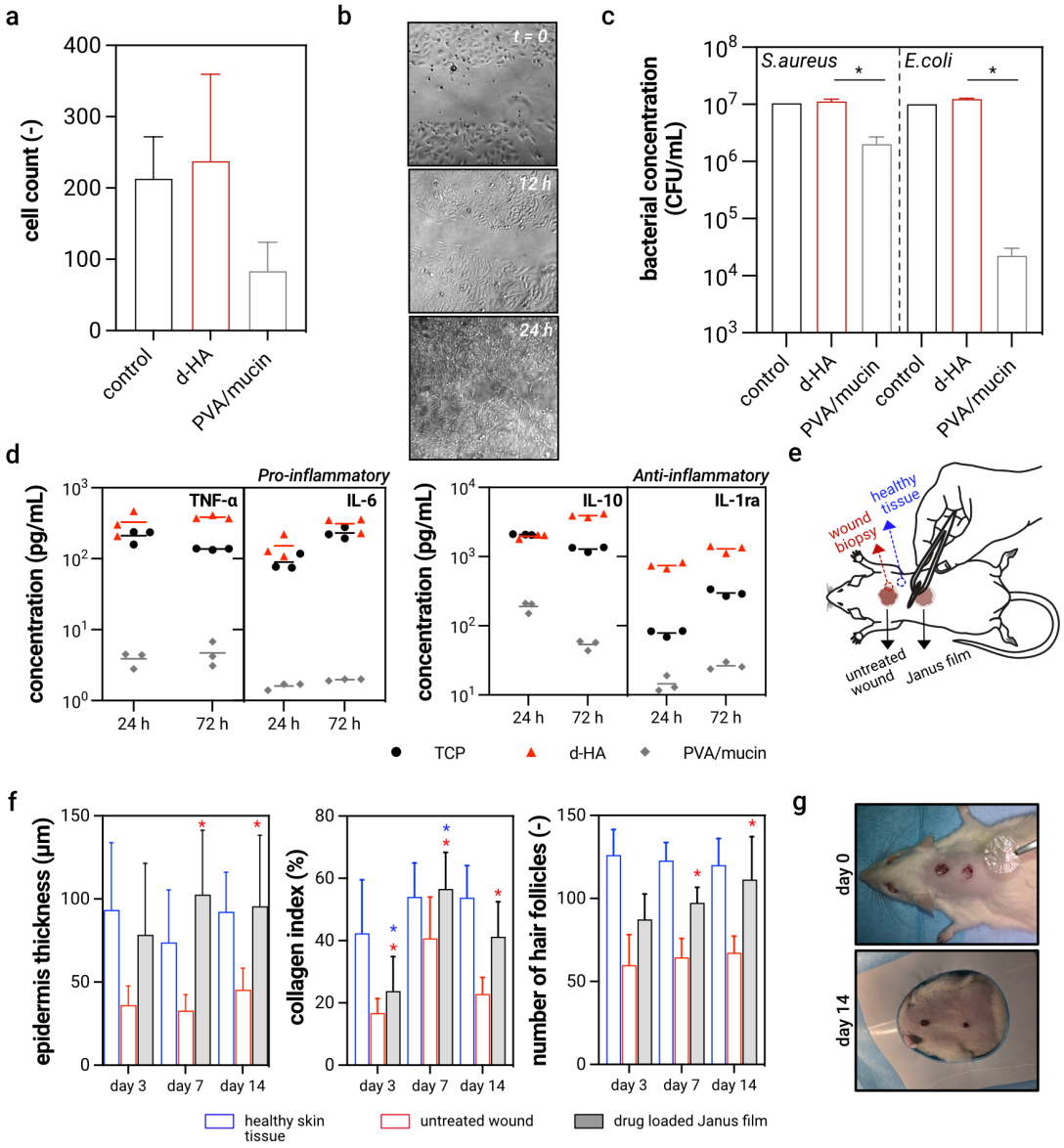

Figure 3.4: Number of cells after cultivated on surfaces of the JF (*n* = 5) (**A**). Representative light microscopy images showing the cellular migration under JF during 24 h (**B**). Detected CFU values for *S. aureus* and *E. coli* on surfaces of the JF (*n* = 5) (**C**). Expression levels of pro- and anti-inflammatory cytokines in monocyte-derived macrophages when cultivated on surfaces of the JF (**D**). Horizontal lines represent the mean values (*n* = 3). Schematic representation of the *in vivo* wound healing tests enabling the direct comparison of healing progress between untreated and JF-treated wounds (**E**). Quantitative evaluation of the histological sections acquired at the 3rd, 7th and 14th days of post-treatment (*N* = 6 animals per group, 10 histological images were analyzed per animal) (**F**). Representative images acquired before and after (14th day) the experimental procedure showing that the JF-treated wounds (right) became smaller than control wounds (left) (**G**). Data shown represent mean values, error bars denote the standard deviation. **

** I acknowledge Theresa M. Lutz and Salma Mansi for their contribution to *in vitro* cell culture experiments; Dr. Enes Akyuz, Dr. Zuleyha Doganyigit and Dr. Percin Karakol for the *in vivo* experiments.

In the next step, the wound healing performance of the JFs was investigated *in vivo* with Sprague-Dawley rats (**Fig. A7**). In detail, two circular wounds (Ø = 1 cm) were created on the dorsal side of each animal ($N = 7$) and only one of them received a JF-treatment (**Fig. 3.4 E**). No additional fixation was required as JFs adhered to the wound surface instantly. Biopsies were taken at the 3rd, 7th and 14th post-operative days, and were stained with haematoxylin & eosin (H&E) and Masson's trichrome for qualitative and quantitative assessments. For the latter, histological images were statistically analyzed in terms of epidermis thickness, number of hair follicles, and collagen index (**Fig. 3.4 F**). Notably, after 14 days, wounds treated with JFs were no longer distinguishable from healthy skin in terms of the analyzed parameters. Macroscopic observations also supported that, when compared to untreated wounds, JF-treated wounds showed accelerated wound closure (**Fig. 3.4 G**). When considering that the JFs did not contain a stimulant such as tissue inductive factors, JFs can be competitive to other materials tested for wet adhesive applications [140-143]. Another advantage brought about by JFs is that full wound closure was promoted without any need for a secondary intervention – the JFs degraded on site.

To investigate the adhesive properties of JFs on wet tissue surfaces, controlled adhesion tests were performed on different porcine tissue samples *ex vivo*. Briefly, JFs were brought into contact with the specimen (*i.e.*, porcine cornea, tongue, intestine, and cartilage) and then retracted at a constant rate while monitoring the required normal force (**Fig. 3.5 A**). Accordingly, the area under the obtained force – displacement curves indicates the adhesion energy between JF and the respective tissue sample. As seen in the exemplary force–displacement curves acquired with porcine eyeball samples, in spite of its good adhesive properties, a d-HA layer easily ruptured during the detachment tests as it forms an unstable gel upon contact with wet tissue (**Fig. 3.5 B**). However, this issue was remedied with JFs as they can withstand higher stretching forces during the detachment test and can be detached from tissues without rupturing. When the adhesion energies obtained on different tissues were calculated, the highest value was obtained on tongue samples ($\approx 4 \times 10^{-3}$ mJ/mm^2), followed by moderate levels on intestine and eye samples ($\approx 2.4 \times 10^{-3}$ mJ/mm^2 and $\approx 1.7 \times 10^{-3}$ mJ/mm^2, respectively) and cartilage samples ($\approx 1.3 \times 10^{-3}$ mJ/mm^2) (**Fig. 3.5 C**). This agrees well with previous findings obtained using a similar strategy to achieve tissue adhesion [140,144]. Moreover, adhesion energies with a similar order of magnitude were recently reported for bulk hydrogels employing polydopamine for adhesion promotion [144]. Other studies exploring bulk hydrogels as tissue adhesives were able to achieve even higher adhesion strengths [145,146], but aimed at the long-term fixation of mechanically highly stressed tissues such as tendons [147] rather than short-term wound healing.

In some sensitive tissues, the residues left after the application of a wound dressing might cause irritation and cab adversely affect the patient's comfort. To test whether the degradation products of JFs lead to any change in the topography of sensitive tissue surfaces, JFs were placed onto porcine eyeball samples and incubated for 3 days under full immersion conditions. Before and after JF treatment, the microtopography of each cornea sample was examined using confocal laser scanning microscopy. Image analysis showed that the JF treatment as well as the degradation

products produced during film decomposition did not cause microtopographical changes on the cornea samples (**Fig. 3.5 E**).

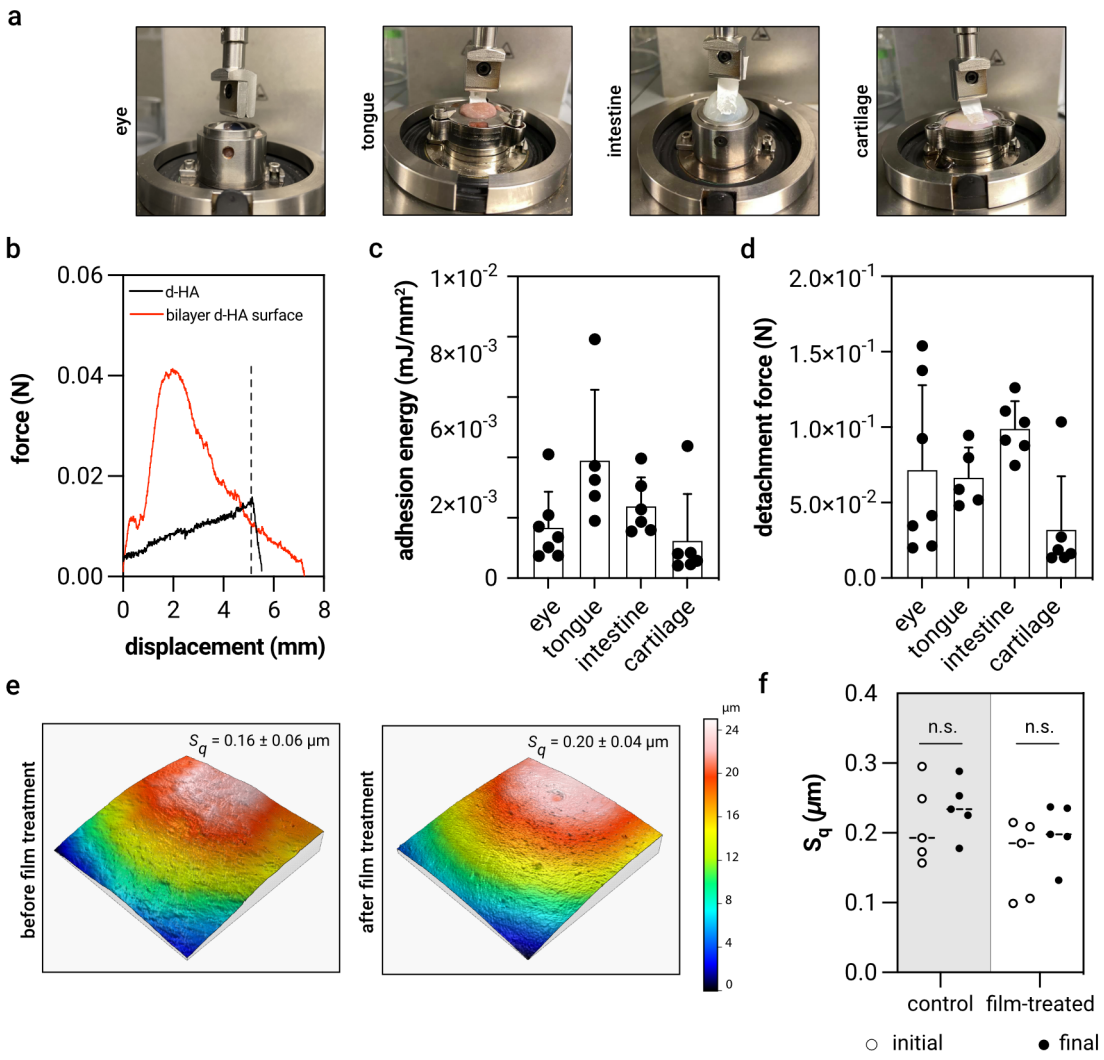

Figure 3.5: *Ex vivo* detachment test setup with different *ex vivo* tissue (porcine eye, tongue, intestine, and cartilage) samples (**A**). Exemplary force – displacement curves obtained by applying d-HA and JF (d-HA side facing the tissue) samples onto porcine eyeballs (**B**). Adhesion energy values obtained when the JFs (d-HA facing down) were applied to different tissue samples ($n \geq 5$) (**C**). Detachment forces obtained when the JFs (d-HA facing down) were applied to different tissue samples ($n \geq 5$) (**D**). Topographical 3D image of exemplary cornea samples before (left) and after 3 days of JF treatment (right) (**E**). The topographical parameter S_q that the surface structure of untreated (grey background) and JF-treated (white background) eyeball samples does not differ after 3 days of testing under full immersion conditions (**F**). Horizontal lines represent the mean values, open and closed circles represent the average value of individual measurements (n = 5) conducted per sample. Data shown represent mean values, error bars denote the standard deviation.

The roughness parameter S_q[††] was found statistically non-significant when each eye was evaluated before and after JF treatment (**Fig. 3.5 F**). Furthermore, a set of additional surface parameters that can define small pits and very fine scratches (*e.g.*, the surface area development, the isotropy of the surface; **Fig. A8**) also confirmed that no alterations were detected in the topography of the corneal tissue samples. Together, these results demonstrated that JFs as well as their degradation products do not damage the tissue surface.

Thus, by leveraging the different functionalities of biological macromolecules, it was made possible to control the mechanical and biological performances on different surfaces of an asymmetrically designed single material. The approach used here can serve as a foundation for the development of new materials designed for specific scenarios. For example, the material lifetime can be easily adjusted by changing either the molecular weight or the cathecol functionalization degree of HA, or by changing the supporting material component (*i.e.*, PVA) in the upper layer. Instead of wet wound tissue management, JFs may also serve as a powerful tool for regenerative medicine, *e.g.*, in mosaicplasty operations or during reconstructive surgery on non-articular cartilage surfaces to canalize important signaling molecules such as hormones, cytokines and growth factors to the point-of-care. Furthermore, JFs could be used as an interface material between implanted material, or wearable surface and host tissue to prevent biofouling and modulate immune reactions. For example, a modified JF carrying multiple drug releasing layers can supply sustained release of antimicrobial agents at the interface of a wearable monitor and the skin. Such an application might extend the lifetime of wearable monitors that analyze epidermally retrievable bliofluids (*e.g.*, sweat) by overcoming biofouling which causes rapid and irreversible signal degradation, thereby removing one of the major barriers to the commercialization of such materials.

[††] The root mean square value (S_q) is calculated according to ISO 25178-2 and is defined as the standard deviation of the measured height *z* in the *xy*-plane of the analyzed area.

4. Delivery mechanisms initiated by (patho)physiological conditions

To develop a material capable of releasing the required dose of drugs at the point of care, an in-depth characterization of the delivery system should be performed under both, storage and biologically relevant conditions. If the system does not offer a controlled liberation of the cargo molecules, premature initiation of the drug release may lead to undesirable consequences such as delivering a sub-therapeutical level of the active ingredient, off-target side effects. Such issues can eventually lead to treatment failure. Therefore, good stability and good cargo retaining efficiency of the designed drug reservoirs under off-target conditions must be ensured.

To achieve such precise control, an ideal drug carrier material should offer an activation mechanism to minimize undesired effects and to maximize the treatment efficiency. Such a controlled system can not only increase the treatment success of individual patients but also offer an essential contribution to combating global health problems such as antimicrobial resistance (AMR). According to the World Health Organization (WHO) estimate, 350 million deaths could be caused by AMR by 2050; excessive use of antibiotics due to a lack of local dose control is one of the major reasons for the development of AMR.

Furthermore, when considering multiple administrations of several different drugs, the implementation of controlled mechanisms can take the drug administration management out of the patients' hands and thus, can reduce the risk of treatment failures. For example, a rational mechanism can be designed to terminate the drug release once the desired level of a marker (related to the treated pathological condition) is reached. Of course, when considering the complex (biological) operating environment of most drug delivery systems, accomplishing such a behavior requires the development of a well-programmable and tunable mechanism. Notably, the established mechanism must also be compatible with the physiological processes in the body and with the pharmacokinetics of the drugs to be administered [148].

The delivery strategies discussed in this chapter aim at offering mechanisms to initiate drug/drug carrier release events only under desired conditions and in a well-controlled manner.

4.1. Engineering a DNA cascade mechanism for the sequential delivery of nanoparticles ‡‡

Ensuring efficient encapsulation of drugs into a carrier matrix is not sufficient for a well-designed drug delivery mechanism. In addition to delivering the correct dose to the right point (*i.e.*, spatial control), delivering the drugs *at the right time* (*i.e.*, temporal control) is one of the most important elements of a meticulously engineered delivery mechanism. To gain a rough control over maintaining the drug concentration within the therapeutic window, conventional approaches

‡‡ This section follows in part the publication: Kimna and Lieleg, Journal of Controlled Release (2019).

suggest repeated doses of drugs, and this leads to high local concentrations. However, such systems increase the likelihood of side effects to occur, and they can lead to reduced overall bioavailability. Alternatively, mechanical systems such as insulin pumps provide an automated release of drugs from embedded reservoirs [149]. However, in cases where patients need to take various medications, managing multiple administrations can become quite challenging.

Previously, DNA/nanoparticle (NP) clusters and DNA-loaded liposomes were employed to achieve controlled strand-displacement reactions from a host agarose hydrogel (**Fig 4.1 A**) [150]. In detail, the release events were initiated by generating an osmotic pressure gradient that entailed rupture of liposomes carrying single-stranded oligonucleotides (ssDNA). Then, the liberated DNA strands could displace from previously formed AuNP clusters and initiated the release of those Au NPs. However, this system was limited to releasing only one type of NP species, and it was highly dependent on a controlled build-up of osmotic pressure to prevent the premature release of displacement sequences. In this thesis, based on the binding specificity of DNA hybridization, a release mechanism capable of autonomously undergoing a complex series of activation cascades was designed (**Fig. 4.1 B**). In detail, the created DNA-based reaction network was engineered to sequentially release strands that can trigger the disintegration of aggregates in a logical order, thus allowing for a highly efficient release of NP species in tandem. Notably, based on the fundamental physical principle of Debye screening (*i.e.*, reduced electrostatic interactions due to the shielding effect of ions), the mechanism was designed in such a way that the activation of the cascade is initiated when the host hydrogel matrix comes in contact with a physiological salt solution.

The NaCl concentration in body fluids and many tissues is somewhat similar, *i.e.*, around 150 mM [151]. This level could be sufficient to induce Debye screening to weaken the interactions between nanoparticulate systems that were electrostatically stabilized at lower ion concentrations: To enable sufficient electrostatic interactions with the negatively charged phosphate backbone of DNA oligonucleotides, NPs carrying a net positive charge were utilized [152,153]. Therefore, branched-polyethyleneimine (bPEI) coated AgNPs (100 nm particle size) carrying primary, secondary, and tertiary amine groups were chosen as the first type of NP species to be entrapped in the hydrogel matrix [154]. When (bPEI-coated) AgNPs were incubated with non functionalized, single stranded DNA strands, the ζ-potential value of the clusters dispersed in ddH_2O was reduced from strongly positive (39.2 ± 0.3 mV) to a moderate regime (23.0 ± 2.1 mV), which confirms that electrostatic interactions between the oppositely charged objects took place (**Fig. A9**). Additionally, the successful formation of AgNP/DNA clusters was confirmed by dynamic light scattering (DLS) as the hydrodynamic size of objects in this dispersion was measured as (2135 ± 640) nm. To confirm the reversibility of this cluster formation, the NaCl concentration of the medium was increased to 150 mM to weaken DNA/NP interactions through Debye screening effects. Indeed, after incubation with the NaCl trigger, changes in the average hydrodynamic size of the clusters were observed *via* DLS: The substantial size reduction to (259 ± 19) nm suggested that the high ionic concentration in the medium disintegrated the DNA/NP microaggregates.

Overall, these findings showed that the aggregation/disaggregation process of AgNP/DNA pairs can be well controlled.

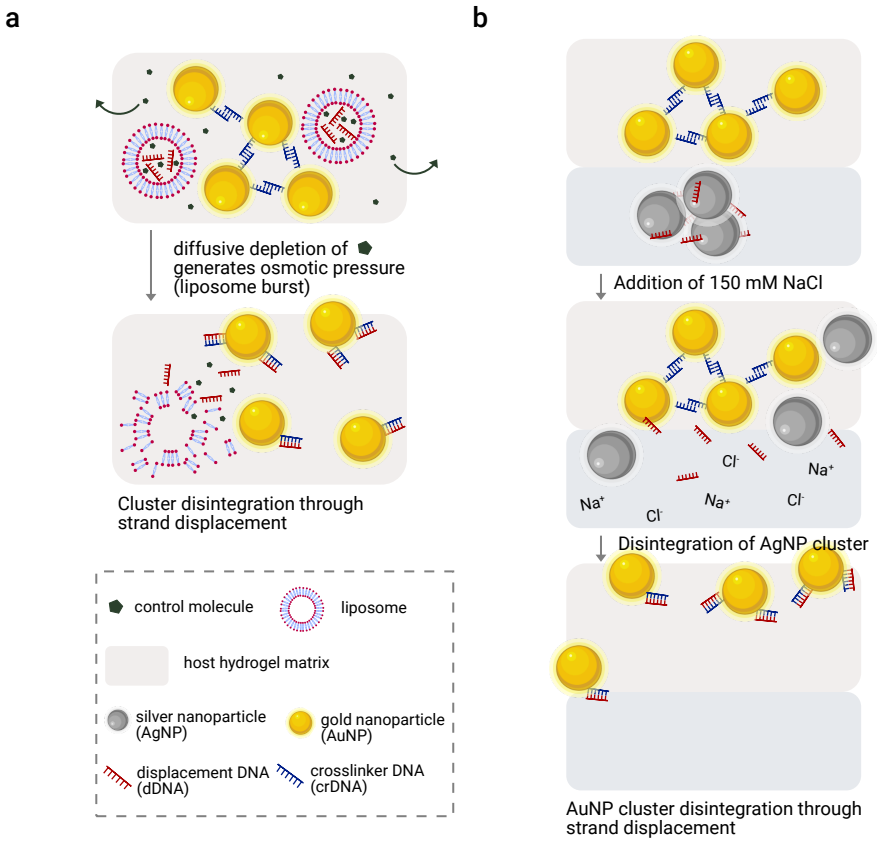

Figure 4.1: In the previous strategy, the osmotic balance was ensured by embedding a similar concentration of control molecules into the (dDNA containing) liposomes and into the host hydrogel matrix. Once the gel was incubated in a solution lacking this control molecule, the osmotic pressure gradient initiated the liposomal burst, liberating the dDNA to disintegrate AuNP clusters through strand displacement (**A**). In the current strategy, sequential release of NP species (here, AgNP and AuNP) from hydrogel layers was triggered by physiological NaCl concentrations. When the charge interactions were shielded by Debye screening effect, liberated dDNA diffuses to the upper layer of the agarose gel, fully hybridize with crDNA strands and thus cause the release of AuNPs (**B**).

After obtaining a controlled dispersal of NP aggregates, the next step was to install a control mechanism to enable consecutive release events. Therefore, a second type of DNA sequence was designed to form another DNA/NP depot by transiently crosslinking the NPs. The crosslinker DNA sequences (crDNA) used for this interaction had self-complementary domains (*i.e.*, two crDNA can partially hybridize through 8 base pairs), but they show complete complementarity to the 22 bases of the DNA strands that were liberated through the abovementioned Debye shielding induced disaggregation. Thus, those DNA strands liberated from AgNP clusters were denoted as displacement DNA (dDNA). For the second type of NP clusters, AuNPs were chosen; however here,

autonomous cluster formation was not possible due to their anionic charge, which repels DNA strands. To overcome this issue, thiol-functionalized crDNA sequences were used to form crDNA/AuNP clusters. Importantly, to enable good thiol-AuNP interactions, NaCl was added to the crDNA/AuNP mixture in a stepwise manner to screen negative charges of both, DNA strands and AuNPs. Finally, the obtained DNA/AuNP clusters were macroscopically observable, and could be collected and were embedded into the agarose hydrogel.

To test the rationality of the design, the first cluster species (AgNP/dDNA aggregates) was embedded into an agarose gel layer, and another layer carrying the second cluster (AuNP/crDNA aggregates) was placed on top. After adding a 150 mM NaCl solution on top of the hydrogel, the release of the two NP species was monitored for 24 days until both release profiles reached saturation (**Fig. 4.2 A**; see **Fig. A9** for photos of the host agarose gels at different DNA sequence and trigger conditions). It was found that, when DNA strands with a random sequence (coDNA; a control sequence that does not form any duplexes with the crDNA strands stabilizing AuNP clusters) were used for the complex formation of AgNPs, the AuNP release was negligible (**Fig. 4.2 B**). A similar effect was observed in the absence of dDNA, highlighting the necessity of correct sequence design to obtain a sequential release behavior (**Fig. 4.2 C**). Notably, control experiments performed without the NaCl trigger (**Fig. 4.2 D**) demonstrated that the NP clusters could remain stable in their reservoirs for ≈ 15 days even though the correct DNA pair was used to form NP aggregates. The small amount of released NPs (< 12 %) observed during this time frame can be attributed to the untriggered release of loosely bound dDNA from AgNP aggregates which was probably triggered by uncontrolled physical changes, *i.e.*, swelling and degradation, of the host gel matrix. Additionally, the similar levels of NP leakage (*i.e.*, ≈ 12 % for AgNPs and ≈ 9 % for AuNPs) observed for the different NP species showed that the leakage was not related to strand displacement reactions. Importantly, a sequential occurrence of two release events could only be achieved when both, the correct trigger and the rational DNA design were employed (**Fig. 4.2 E**). When the right combination of sequence and trigger was used, (36 ± 5) % of entrapped AgNPs were detected in the supernatant at t = 5 h. Afterwards, a similar level of AuNP release from the hydrogel reservoir (39 ± 3) % was achieved on the day 14th. This was made possible by first, salt-induced screening effects that initiated the dispersal of AgNP/dDNA clusters; second, by the diffusion of liberated dDNA molecules to the top layer of the gel. The latter started strand displacement reactions by forming thermodynamically more favorable dDNA/crDNA duplexes, thus triggering the liberation of individual AuNPs and their ensuing diffusive release from the host matrix.

The mechanism presented so far allows for the controlled, sequential release of two doses of NPs from a hydrogel network made of an uncharged, inert matrix, *i.e.*, agarose. Replacing or supplementing the agarose gel with a more complex macromolecular material could affect the release rate and release efficiency, but could also bring a "selectivity" function based on additional physicochemical interactions with the entrapped objects. However, it should be noted that choosing a matrix material carrying a highly cationic charge could impair the free diffusion of oligonucleotides and negatively charged NPs, which should be avoided.

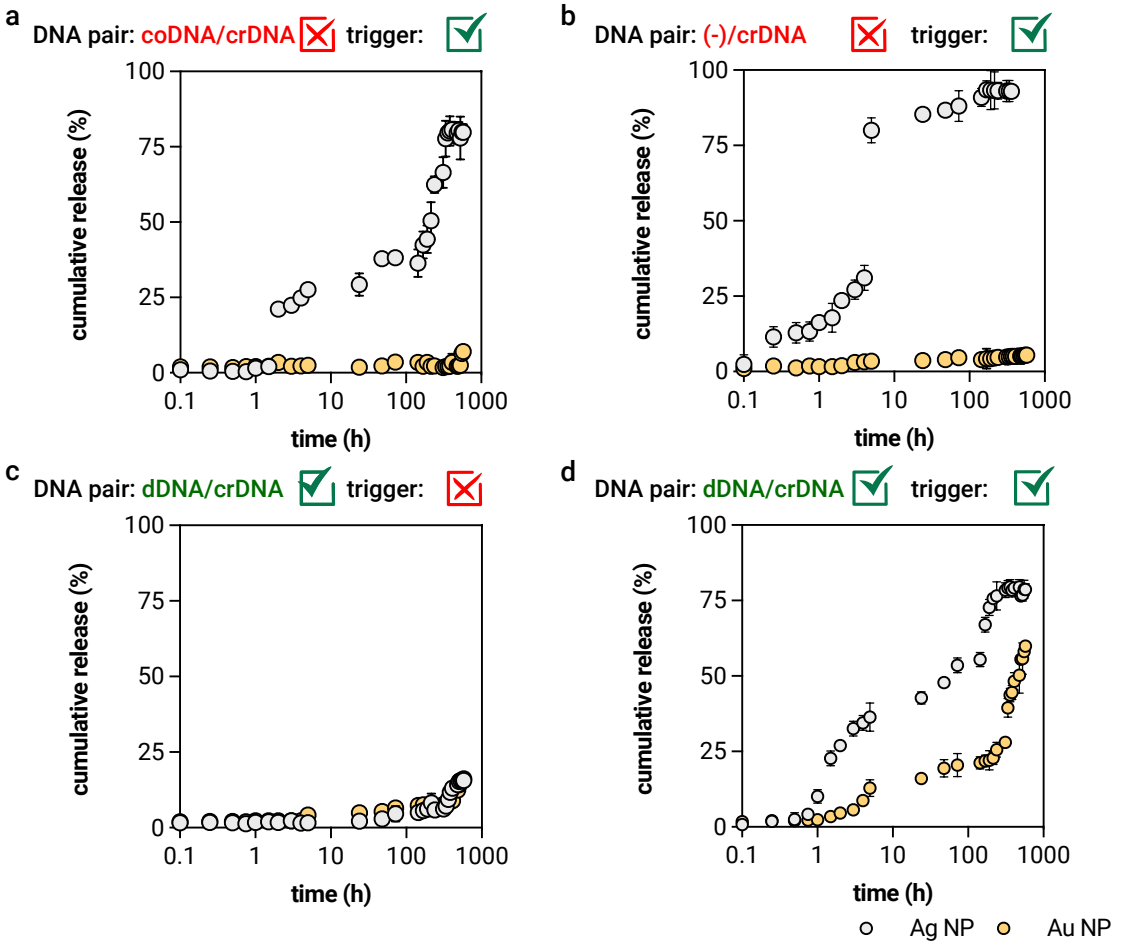

Figure 4.2: Cumulative release profiles of Ag- and Au-NPs are depicted in (a)–(d) for different conditions: AgNP clusters created with coDNA (no matching base pairs with crDNA in the AuNP aggregates) when the salt trigger present (**A**); free AgNPs (w/o dDNA) when the salt trigger present (**B**); dDNA/ crDNA aggregates, no salt trigger (**C**); Ag-NP/dDNA aggregates and 150 mM NaCl (salt trigger) (**D**). Data represent mean values, and the error bars show the standard deviation as obtained from n = 3 independent samples.

Mucin glycoproteins are promising biomacromolecules for such a complex gel component: Due to the polyanionic character of mucins, mucin gels were shown to possess selective permeability towards different molecules [115,155,156], and this property might be transferrable to a synthetic hydrogel when it is enriched with mucins [157]. Therefore, in the next step, a hybrid reservoir hydrogel made of mucin-agarose mixture was tested to obtain selective release properties for small molecules in addition to the DNA-controlled mechanism. Two fluorophores with similar molecular weight and hydrophobicity, but carrying different net charges (*i.e.*, neutral and cationic) were chosen as test molecules. As shown in **Fig. 4.3 A**, mucin-enriched agarose gels delayed the release of the cationic test molecules compared to their neutral counterparts. Also, after the release profiles reached to a saturation point ≈ 2 h, the cumulative release of molecules was

(91 ± 3) % for the neutral molecule (similar to the results obtained with the pure agarose gels), but (78 ± 2) % for the cationic molecule. This noticeable difference was attributed to the residual binding of the cationic molecules to sialic acids (pKa < 2.6) or sulfated sugars (pKa < 1) of the mucin macromolecules [115]. This finding suggested that, in addition to delaying the release, a mucin-enriched hybrid gel can also serve as a mid- or long-term depot, liberating another small dose of cationic molecules once the gel starts to degrade.

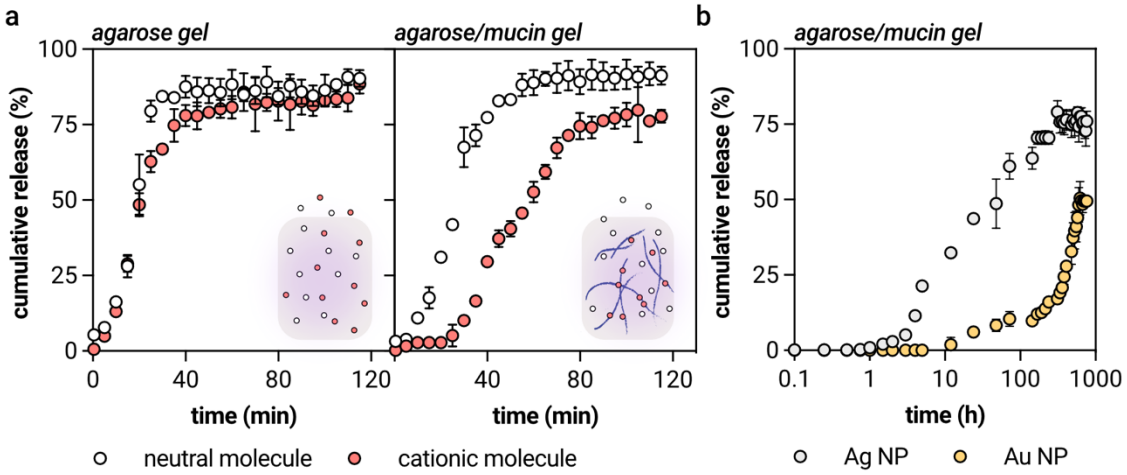

Figure 4.3: Cumulative release profiles of neutral and cationic small molecules from DNA/NP aggregates embedded agarose (left) and mucin/agarose (right) hydrogels (**A**). Cumulative release of AgNP and AuNP release from the mucin/agarose hydrogel in a sequential manner (**B**). Data represent mean values, and the error bars show the standard deviation as obtained from *n* = 3 independent samples.

Interestingly, the DNA-mediated NP release pattern and efficiency were not affected by the change in the host gel composition (**Fig. 4.3 B**). After 12 h, (32 ± 2) % of the AgNPs were detected in the buffer, whereas a similar level of AuNP release could be achieved on the 20th day. The changes observed in the release profiles could be associated with the interactions of NPs with charged moieties of mucin glycoproteins. Together, these results highlight that the DNA-mediated NP release mechanism can also be achieved in a more complex hydrogel environment, and it can be combined with other control strategies to obtain a selective/pre-defined release of both, NPs (model drug carriers) and molecules (model drugs). In addition, a hydrophobic/hydrophilic molecule pair might also be embedded into mucin-containing gels, as previously demonstrated by Duffy *et al.* [155]. Furthermore, the gel matrix hosting the particle reservoirs can be enriched with additional biomacromolecules to receive selective release properties towards embedded small molecules – without interfering with the designed order of the NP release process.

Having identified the fundamental requirements to control DNA-mediated NP release, the system was upgraded by introducing another step into the release cascade. To do so, all DNA sequences were re-designed to allow for the aggregation/disaggregation of three distinct NP species (**Fig 4.4**). In detail, electrostatic interactions were used to stabilize the first depot (AgNP/DNA clusters), and

second set of NP clusters was generated through covalent interactions between thiolated self-complementary DNA strands (crDNA) and AuNPs. A third NP species was introduced into the mechanism and designated as the second type of model object to be released. The underlying DNA-stabilization mechanism for this additionally introduced NP species was based on obtaining cage-like clusters, which was enabled by short palindromic bridge DNAs (brDNA) that connected DNA strands attached to the particle surface (pDNA). Here, the particle-DNA interactions were mediated by one of the most robust non-covalent interactions, *i.e.*, avidin/biotin. Each of the avidin-coated Fe_2O_3 NPs used for this strategy holds four binding sites for biotin-functionalized pDNAs, which enables their aggregation upon incubation with connecting brDNA strands. One of the critical boundary conditions for controlling the state of these clusters was to ensure the sufficient affinity of the brDNA sequence to pDNA to form stable clusters.

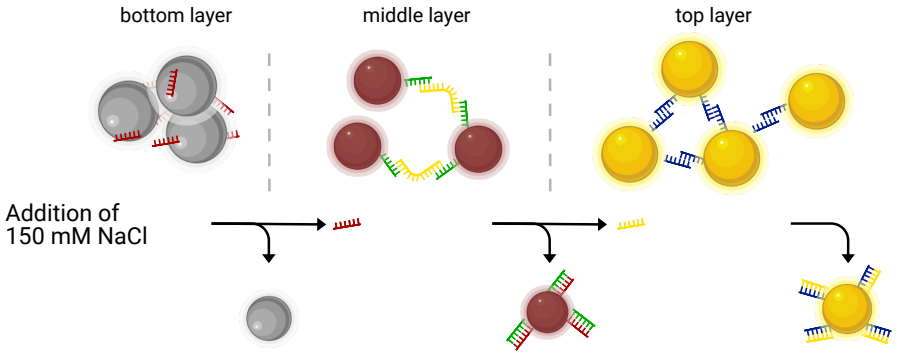

Figure 4.4: Envisioned interplay of the synthetic DNA sequences required for the three-stage nanoparticle release avalanche.

Importantly, the affinity of the brDNA sequence towards pDNA (forming the pDNA/brDNA/pDNA complex) must be lower than the affinity for dDNA (used for AgNP cluster formation) (**Fig. 4.5 A**). Then, dDNA released upon NaCl exposure can displace brDNA from Fe_2O_3 NP clusters. The boundary condition for the design of the second sequence was that the released brDNA strands, in turn, should act as displacement strands to break up AuNP clusters stabilized by self-complementary crDNA strands (in analogy to the two-step design introduced above).

To this end, individual NP clusters were integrated into a bulk agarose hydrogel matrix and exposed to physiological salt concentrations (**Fig. 4.5 B**). To define a burst-release threshold, the cumulative release detected for NP species for each time point was compared with the mean of three previously detected points. The first statistically significant different point was defined as the release onset. Starting with AgNPs and ending with AuNPs, the starting point for the release of the individual NP species was calculated as ≈ 1 h for AgNPs, ≈ 2 h for Fe_2O_3 NPs, and ≈ 12 h for AuNPs, respectively. Thus, the sequential release of the three NP species occurred in the correct order and was completed in ≈ 6 days.

a

# bps (T_m [°C])	$coDNA_2$	$dDNA_2$	pDNA	brDNA	$crDNA_2$
$coDNA_2$	2	3	2	3	3
$dDNA_2$	3	6	**20 (69)**	4	8
pDNA	2	**20 (69)**	2	**10 (53)**	5
brDNA	3	4	**10 (53)**	2	**25 (69)**
$crDNA_2$	3	8	5	**25 (69)**	**8 (39)**

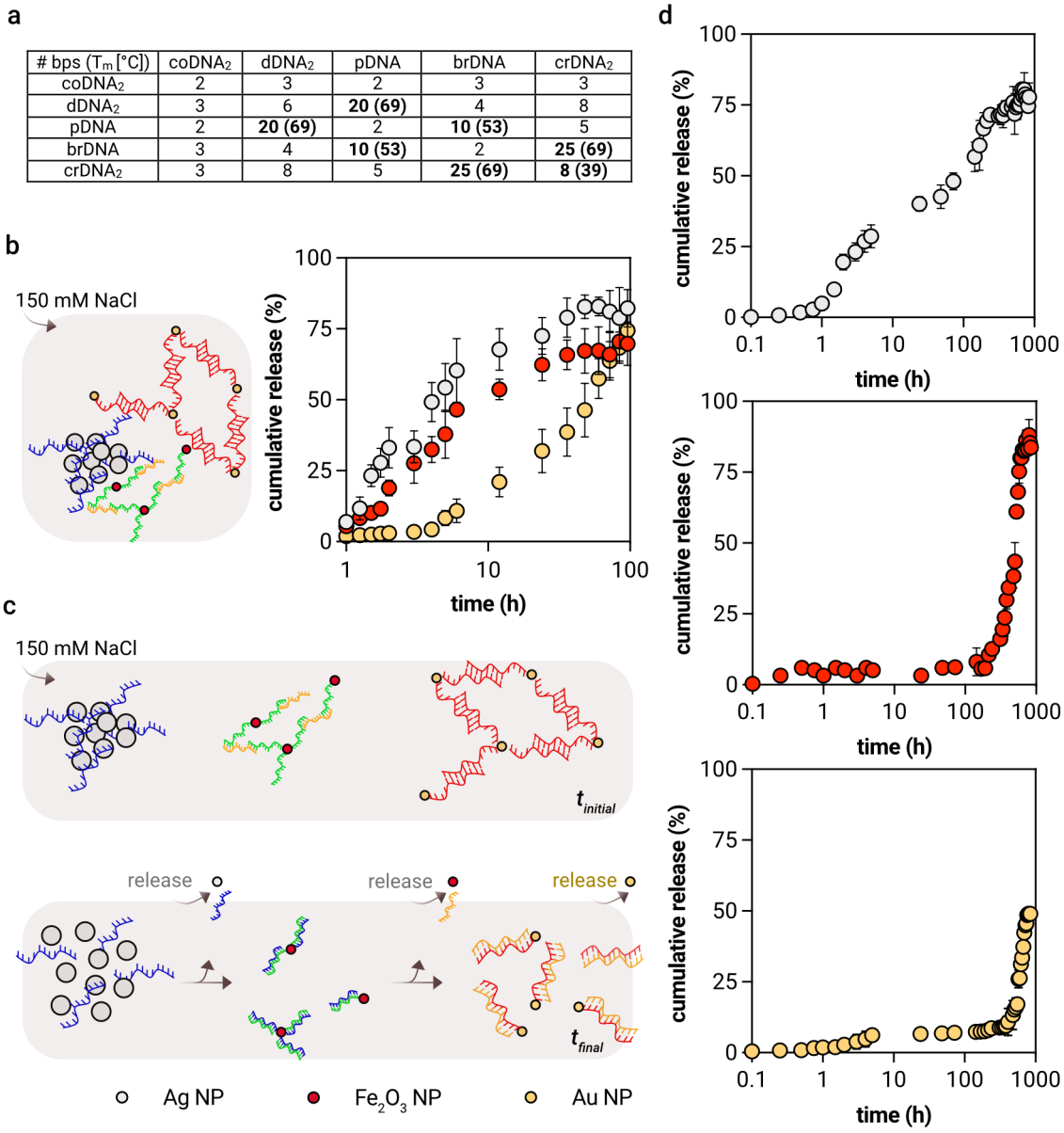

Figure 4.5: Number of matching base pairs and predicted melting temperatures of different polynucleotide pairings (**A**). Values depicted in bold print correspond to DNA pairings used in the experiments as the final design to obtain sequential release of three NP species. Schematic representation of a single-layered hydrogel into which three different types of NP/DNA aggregates are integrated (**B**, left). The cumulative release profiles of the individual NP species (**B**, right). Schematic representation of a three-layered hydrogel at the initial and final stages. Bottom layer: dDNA/AgNP complex (initial) and release of AgNPs are triggered by 150 mM NaCl (final); middle layer: Fe_2O_3 NPs clustered with pDNA/bDNA complex (initial) and due to $dDNA_2$ diffusion, consecutive strand displacement reaction forming (pDNA/$dDNA_2$); and release of Fe_2O_3 NPs (final); top layer: AuNP/crDNA clusters (initial) and liberated brDNA strands diffuse to the upper layer of the agarose gel, fully hybridize with $crDNA_2$ strands and thus cause the release of AuNPs (final) (**C**). The cumulative release profiles of the individual NP species liberated from three-layered hydrogels (**D**). Data represent mean values, and the error bars show the standard deviation as obtained from n = 3 independent samples.

In the next step, the hydrogel system was modified by integrating different aggregate species into individual agarose layers to test whether the saturation time interval could be adjusted. In detail, the NP cluster species were located from bottom to top as AgNPs, Fe_2O_3 NPs, and AuNPs, respectively (**Fig. 4.5 C**). In this setting, upon addition of the trigger solution, AgNPs left the gel after a few hours, followed by Fe_2O_3NPs after ≈ 200 h, and AuNPs were liberated last, *i.e.*, ≈ 550 h after the avalanche was initiated. The cumulative release efficiencies of Ag- and AuNPs as determined after 35 days were similar to those of the 2-step mechanism: (78 ± 5) % for AgNP, and (49 ± 1) % for AuNP (**Fig. 4.5 D**). For the newly introduced Fe_2O_3 NPs, the cumulative release was found to be highly efficient (84 ± 2) %. The release efficiency of this release mechanism was similar to that of single-layered host hydrogel. Still, the sequential release required an extended time span of ≈ 4 weeks to complete. This finding clearly demonstrated that the DNA-controlled hydrogel system could be tuned to obtain different lifetimes while maintaining its precision and accuracy.

In conclusion, the DNA-mediated mechanism developed here allows for temporal control over the consecutive disaggregation of NP cluster species. Although the strand displacement reactions take place autonomously, the initiation of this mechanism requires exposing the hydrogel to physiologically relevant salt concentrations suggesting that it could be a promising system compatible with physiological environments. Exposure to such a physiological salt concentration would occur automatically if the proposed mechanism comes into contact with a body fluid, for example, when applied onto a wound tissue. Importantly, the hydrogel can be stored in ddH_2O to retain the NP species embedded in the matrix until a future application of a salt solution. Especially when considering the well tunable lifetime of the gel (to achieve complete release of embedded objects), the system presented here can be very useful for administering multiple species requiring different dose intervals. In some cases, short- and long-term administration of the same drug is required: here, the biomacromolecule-enriched hydrogel design could be favorable to delay the release of later doses.

Importantly, the control over the release order of different species obtained here could minimize the risk of wrong medication usage by taking the administration duty off the hands of patients and caregivers. Such a tightly regulated order of drug administration is an essential demand for many cases: For example, studies showed that the continuous administration of antigens could enhance the immune response [158]. As the release period can cover ≈ 40 days (which can be extended to the desired duration by adjusting the embedded NP dose), the system developed here can, for example, be beneficial for vaccination formulations to release antigens twice a month. Furthermore, as the molecular clocks that control circadian rhythm are being revealed as essential regulators of physiology and disease, using this rhythm as a therapeutic target to deliver drugs at the most efficient time might increase their biological efficiency and safety [159,160]. Indeed, recent studies have revealed that a time-specific therapy increases the efficiency of some medications, such as anticoagulants and antihypertensive drugs, and reduces some adverse effects of chemotherapy drugs (*e.g.*, doxorubicin, cisplatin) [161,162].

Especially for cancer therapy, even a slight improvement in drug efficacy can significantly impact the treatment success. Thus, synchronizing the DNA-mediated time control to the biological rhythm of a patient can leverage maximum benefits. However, some fundamental questions must be answered before being able to design such a strategy. For instance, further research has to be done to reveal how pathological conditions affect the biorhythm or to identify ideal reporters of the circadian clock for chronotherapy [163].

Of course, the mechanism described here requires some modifications to become applicable in a real medical application. For example, the agarose matrix chosen here is not ideal for an implementation into a medical setting. However, as demonstrated by adding a second matrix component to the hydrogel, the host matrix can be altered without compromising the functionality of the DNA-based release cascade. In addition, flexibility in the choice of hydrogel material offers the possibility of obtaining an even more complex release mechanism capable of responding to other biological stimuli regulated by the hydrogel matrix components.

4.2. Stimuli-responsive coatings liberating cargo molecules from depots upon two independent triggers §§

Previous work presented a proof-of-concept mechanism for sequentially delivering therapeutic agents by employing a rational design of DNA-based strand displacement reactions [164]. However, to provide a therapeutic action by employing this mechanism, the model nanoparticles have to be replaced with drug carriers, or these particles have to be chemically modified to carry drug molecules on their surfaces [165-167]. Thus, applying a similar DNA-based release mechanism developed in this study to further control the structural state of biopolymer-based drug carrier materials was the next logical step.

Previously, Yan *et al.* [75] showed that, when exposed to glycerol, elongated mucin glycoproteins can be condensed into compacted, globular structures. By tuning the glycerol concentration in the medium, it was possible to produce mucin particles of different size, ranging from 90 to 800 nm. Theoretically, any molecule that exhibits binding interactions to mucins or is large enough to be sterically entrapped could be retained in condensed mucins upon glycerol-driven compaction. Importantly, the condensation of mucin particles with glycerol was shown to be fully reversible, *i.e.*, mucins quickly reverted to their original, elongated state when the glycerol in the environment was diluted or removed. With this dynamic behavior of mucins in mind, here, a DNA-mediated strategy was applied to surface-bound mucins to force them to remain condensed in a glycerol-free environment and to achieve control over their decondensation.

To do so, mucins were immobilized onto a PDMS surface using carbodiimide chemistry. Previously, this strategy was used to covalently stabilize mucins to form brush coatings on a broad

§§ This section follows in part the publication Kimna *et al.* Advanced Materials & Interfaces (2020) and the European patent application WO/2021/123126 (2019).

range of (medically relevant) polymeric surfaces to reduce biofouling events [56], and to improve the wettability and lubrication performance of coated biomaterials [168,169].

Here, when incubated with such a covalently attached mucin layer, partially self-complementary crDNA strands (carrying a thiol end-modification) spontaneously formed disulfide bonds with the cysteine-rich subdomains of the mucin glycoproteins [170]. In combination with an exposure to glycerol, crosslinker DNA hybridization allowed this brush coating to form a stable compacted layer - even when glycerol was removed from the environment (**Fig. 4.6 A**).

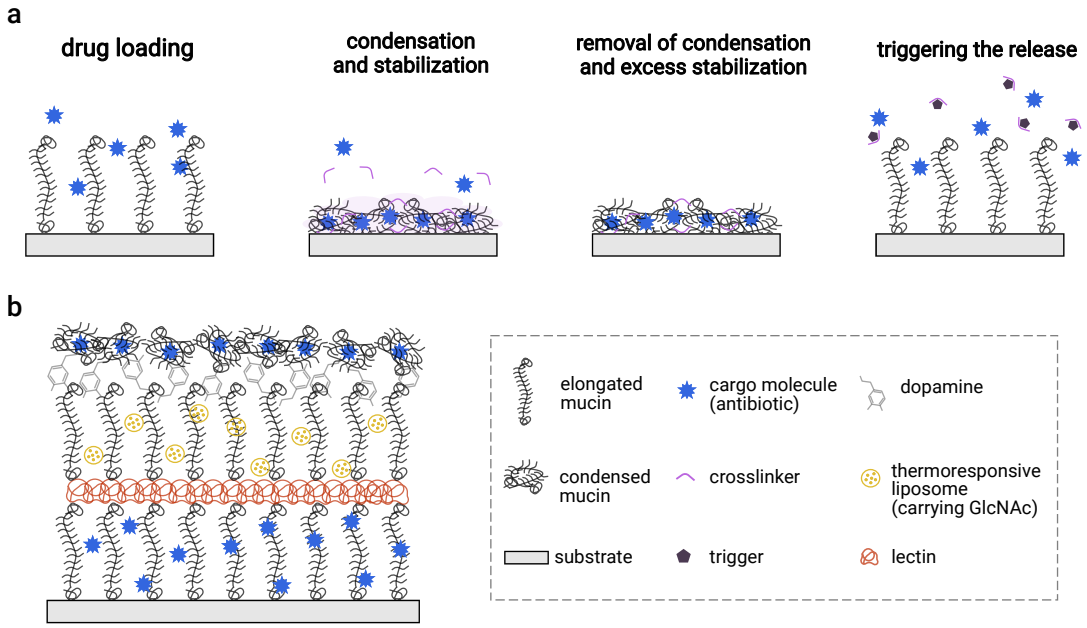

Figure 4.6: Schematic representation of the envisioned triggered release mechanism from macromolecular mucin coatings. The release mechanism from a surface-bound mucin layer comprises the loading of the layer with the drug, entrapment of the drug through condensation and stabilization of the mucin layer; after removal of the condensation and excess stabilization agent, the drugs stay trapped until contact with the trigger initiates their liberation **(A)**. Schematic representation of mucin-based multi-layers cross-linked with two types of connector molecules, that is, lectin and dopamine (**B**).

First, to prove the successful compaction of the polymer coating, surface-bound (fluorescently labeled) mucins were condensed with glycerol and crDNA, and then, their condensation was triggered with a dDNA solution. The acquisition of z-stacks using a confocal microscope revealed that the initial coating height (26.6 ± 4 µm) was reduced by 50 % upon exposure to glycerol, even after the glycerol was flushed away (**Fig. 4.7 A**). When this compacted layer was incubated with a solution containing dDNA strands, the coating height increased back to its original state, which illustrates the reversibility of the condensation upon function of a more favorable base pairing that cleaves the crDNA/crDNA crosslinks. Next, the ability of the condensed mucin layers to entrap desired molecules was visualized with a microfluidic setup. Therefore, mucins were immobilized

onto the inner surface of a PDMS microchannel. The successful implementation of the dDNA-triggered mechanism to a polymer-brush coating was observed using fluorescence microscopy: A fluorescent molecule (doxorubicin) was retained in the mucin layer *via* glycerol-driven condensation (**Fig. 4.7 B**). The fluorescent cargo remained in the surface coating when PBS was flushed to remove excessive glycerol and unbound drug molecules. In turn, when the dDNA solution was injected into the microchannel, a reduced fluorescence intensity was observed, which confirmed that strand displacement reactions initiated a drug release from the coating.

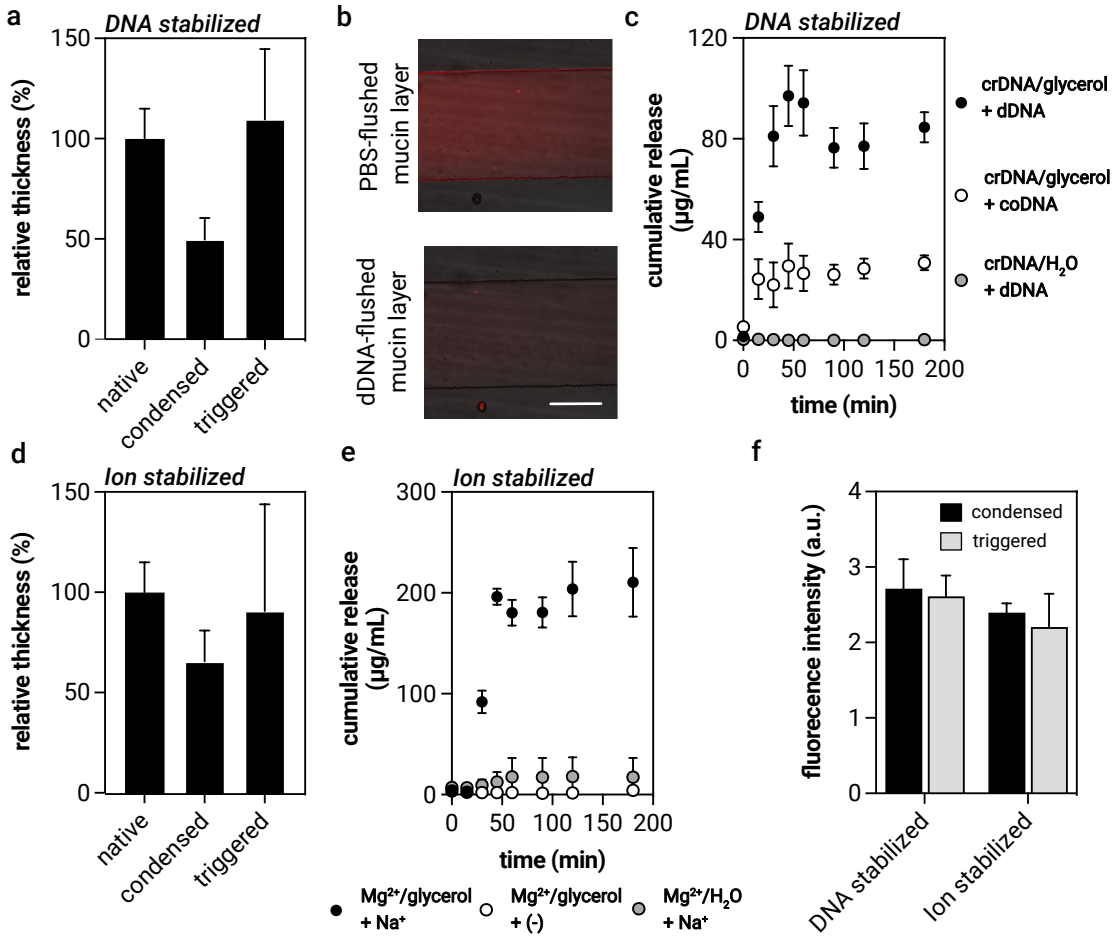

Figure 4.7: Glycerol-driven conformational changes of surface-bound mucin layers stabilized with crDNA remains after removal of glycerol (n = 5) (**A**). A trigger DNA can reverse the condensation step as evidenced with increased coating thickness. Optical visualization of DNA-triggered drug release in a microfluidics setup as indicated by the strongly reduced fluorescence signal of the entrapped drug (**B**). The scale bar represents 0.5 mm and applies to both images. Cumulative TCL release from DNA-stabilized mucin layer (n = 3) (**C**). Similar to DNA-stabilization, Mg^{2+} ions can remain mucins condensed until the system is exposed to 150 mM NaCl solution (**D**). Cumulative TCL release from Mg^{2+}-stabilized mucin layer (n = 3) (**E**). The fluorescence signals obtained from ELISA tests show that the surface bound mucin amount is not altered regardless of the condensation/decondensation strategy (n = 5) (**F**). Data represent mean values, and the error bars show the standard deviation.

In the next step, to be able to make a quantitative assessment of the drug release, Tetracycline hydrochloride (TCL) was chosen as a cargo molecule and loaded into the mucin coating generated in a polystyrene cuvette. TCL is a broad-spectrum antibiotic that is also used for catheter-associated urinary tract infections [171], which could be a potential application for the coatings developed here. As shown in **Fig. 4.7 E** (black symbols), TCL release was successfully initiated by the DNA trigger with a very short response time (≈ 15 min). In contrast, when a random DNA sequence (coDNA) was added, only a small amount of TCL release (open symbols) was detected.

Another control experiment, in which the coating was not condensed by glycerol, showed that TCL was not detectable during the experimental time frame and likely flushed away during the preparation steps. However, in a potential application such as coating a medical implant surface, it might be challenging to provide dDNA strands on-site, or it could even be necessary to implement another carrier vector to concentrate adequate amounts of the trigger on the coating. Thus, in the next step, the DNA-based control was replaced by another mechanism, which is a practically more convenient and physiologically compatible strategy.

Physiologically, mucin glycoproteins are often stored as condensed, globular structures that are unpacked when they are released from the secretory granules. The formation of these condensed structures in intragranular packaging is explained (for MUC5B) as the high Ca^{2+} concentration and low pH environment leads dimeric MUC5B to organize into head-to-head noncovalent tetramers where the von Willebrand D1 – D2 domains hooked into each other [172-174]. However, this structural organization is reversible upon their release during exocytosis, where the increase in pH and entry of Na^{+} ions displace Ca^{2+} ions and eventually trigger the rapid unfolding of the mucins through electrostatic and steric repulsions [175,176]. When divalent Ca^{2+} ions are exchanged by the monovalent Na^{+} and diffuse out of the mucin matrix, the effective cationic shield and ionic crosslinking weakens, and the mutual repulsion of the polyanionic charges can quickly drive the expansion of the mucin network [177]. Additionally, the rapid expansion of compacted mucin glycoproteins was previously explained by Kesimer *et al.* [178]: a dramatic increase in the Donnan potential due to rapid change of the environment from Ca^{2+}-rich to a Na^{+}-rich milieu drives mucin hydration. It was concluded that, together with the ion exchange, an ordering of the subunits enables the fast rate of mucin hydration and concurrent mucin expansion.

Thus, by implementing an artificial ion-exchange mechanism, it could be possible to obtain stable and condensed mucin layers even after removal of glycerol. Owing to its small atomic radius, Mg^{2+} ions can compete well with other divalent ions for binding sites, and Mg^{2+} has already been shown to form ion bridges between negatively charged macromolecules [179]. Thus, when the ionic strength of the medium that carries condensed mucins is increased to a certain Na^{+} concentration, the weakening of Mg^{2+}-crosslinking may be sufficient to induce mucin decondensation. Indeed, using confocal microscopy, Mg^{2+} ions were found efficient in keeping the mucin layer condensed (≈ 66% as calculated from the z-stack images), and this stabilization was reversible upon addition of a physiological NaCl solution (**Fig. 4.7 D**). Furthermore, when a TCL-loaded, condensed mucin layer stabilized by Mg^{2+} was exposed to a physiological NaCl solution, liberated drugs could be detected

after ≈ 30 min (**Fig. 4.7 E**). More importantly, the release efficiency was calculated as > 90 %, which demonstrated the excellent performance of the NaCl trigger. Control experiments also showed that, in the absence of the NaCl trigger, the Mg^{2+}-stabilized mucin layer showed negligible leakage of less than 2 %. This excellent stability significantly outperforms the result obtained with crDNA-stabilized coating. This observation could be related to a higher crosslinking density achieved with Mg^{2+} divalent ions, which can bind to all anionic groups along the mucin backbone. By comparison, crDNA can only bind to cysteine residues at the terminal ends of the glycoprotein, and these accessible cysteines are (at neutral pH) ≈ 6 times less frequent than the number of anionic residues along the mucin backbone [180]. In addition, another reason may be the smaller size of Mg^{2+} ions: Compared to the length of DNA crosslinks (each crDNA is ≈ 8.6 nm), Mg^{2+} ions may induce the formation of a more densely crosslinked mucin network that prevents an uncontrolled diffusion of drugs. Similar to the DNA-based strategy, a second control group without glycerol condensation showed almost no detectable signs of free drugs even when the correct trigger was used (**Fig. 4.7 E**). Again, this result can be rationalized by insufficient interactions between free TCL molecules and mucins.

To better understand the feasibility of this mechanism to be used in a clinical setting, a comparison between the doses of conventional systemic delivery and the ion-induced local release was performed with a focus on mild urinary tract infections, which are commonly obtained as a side effect of catheter implantation. Typically, a conventional TCL treatment comprises the systemic intake of 500 mg of TCL every 6 h for 10 days [181], which corresponds to serum and crevicular fluid concentrations of 3 – 4 µg/ml and 5 – 12 µg/ml, respectively [182]. With the Mg^{2+} stabilized mechanism achieved here, the TCL loading capacity per coated area can be calculated as 4.5 µg/mm^2, which corresponds to a local concentration of the released drug of ≈ 180 µg/ml [***] (see **Appendix A4.4**). This concentration exceeds the serum levels achieved by conventional routes and is also above the minimum inhibitory concentrations required to inhibit common bacterial pathogens responsible for urinary tract infections [183].

Importantly, the surface-immobilized mucin layers used in this approach can provide various functionalities in addition to drug release: reduced protein and bacteria adsorption, and reduced friction [184-187]. This can be very beneficial on the surface of short-term implants such as catheters. Of course, for these beneficial properties to present, the covalently attached mucin layer should remain on site after the drug release is triggered. An enzyme-linked immunosorbent assay showed that mucins were present at the same level before and after trigger exposure; this indicates that mucins remain stable on the surfaces to which they are conjugated [168,188], and this holds true when they are exposed to mechanical stress [37], or if they underwent a conformational change as shown here (**Fig. 4.7 F**). Furthermore, even after triggering their decondensation, surface-bound mucin layers maintained their lubricating properties (**Fig. A10**).

[***] The local drug concentration was estimated by assuming free diffusion of the drug in an aqueous environment.

An essential advantage of simplifying the mucin stabilization step by using ionic crosslinking is that the polymer coating does not require highly specific chemical interactions with the stabilizer as it was required for thiolated DNA and cysteine groups of mucins. To explore this idea, different macromolecules with diverse charge profiles and molecular weights were grafted onto a PDMS substrate. To do so, polyanionic carboxy-modified dextran (CM-dextran), polycationic chitosan, and polycationic end-functionalized alkynyl-poly(L-lysine hydrobromide) (aPLL) were used (see **Appendix A1**). Also here, by applying modifications to the covalent conjugation and condensation (in presence of divalent ion) steps, the TCL load entrapped in the condensed surface coatings could be released by adding a 150 mM NaCl trigger. After 1 hour, the drug concentration in the fluid reached a plateau value (**Fig. 4.8**). In all conditions, when the system was exposed to H_2O (simulation of storage conditions) instead of a NaCl solution, no remarkable drug release was observed within 3 h. However, when the incubation medium was changed to a NaCl solution at the 24th hour (grey symbols), release from these control groups was also found to be successful. Thus, in cases where different functionalities brought about by other polymers are needed (for example, a procoagulant function of chitosan), the presented strategy of drug release from surface-bound polymer layers can be easily transferred to other (bio)polymer coatings, thus, broadening the application range of the release mechanism.

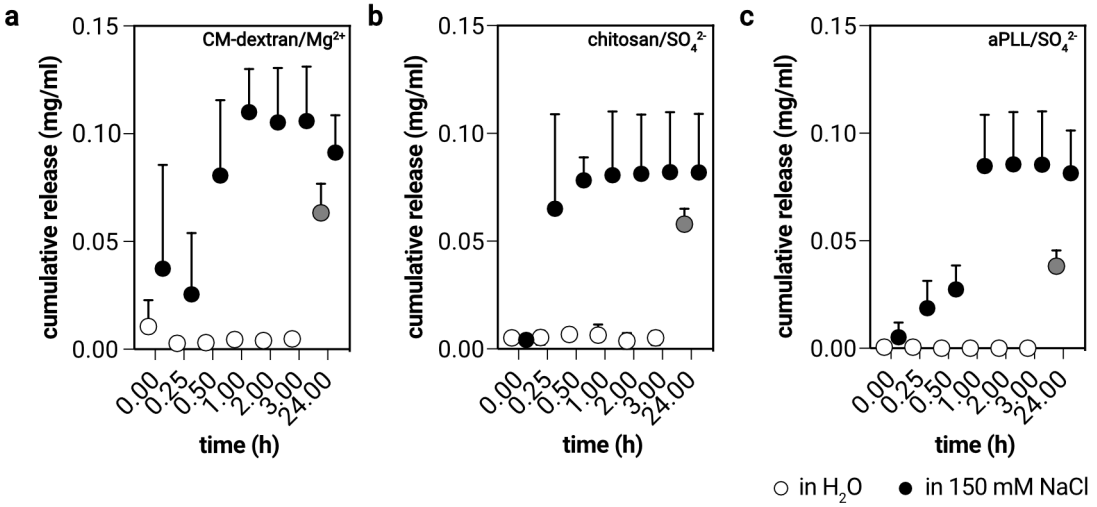

Figure 4.8: Cumulative TCL release from surface-bound CM-dextran (**A**), chitosan (**B**), and poly-L-lysine (**C**) layers. Drug release was initiated upon exposure to 150 mM NaCl solution (closed symbols). In contrast, samples incubated in water did not release their TCL load (open symbols) until the medium was exchanged with 150 mM NaCl at the 24th hour (grey symbols). Data represent mean values, and the error bars show the standard deviation as obtained from n = 3 independent samples.

When the the DNA-based cascade strategy (as described in the previous section) was employed, it was possible to enable multiple release events that were sequentially activated. Thus, a second and third dose was provided once the previous release event had taken place. In the problem

discussed here, drugs actively released from the implant surface upon exposure to a physiological salt concentration can help to prevent early, implantation-induced infections. However, a second dose might become necessary to suppress recurring infections and inflammation. In the following, control over the initiation of distinct release events was obtained to accomplish more complicated tasks such as providing the second drug dose *only if* demanded. Such multiple dosing was made possible by engineering a 3-layered mucin coating in which two independent stimuli controlled the release events (**Fig. 4.6 B**).

In the topmost layer, a Mg^{2+}-stabilized, condensed mucin layer was deployed as an initial drug reservoir; it will respond to a physiological salt concentration and will release the first dose of antibiotic. At the bottom, mucins were covalently attached to the substrate and passively loaded with the same drug to serve as a second drug depot (**Fig. 4.9 A**). Unlike in the previous strategy, this bottom layer required the removal of the top layer to enable the release of its cargo. Access to these molecules was controlled through a temperature-responsive logic that responds to an inflammatory state in the body: An elevated temperature does not only occur globally in the human body as fever (≈ 40°C) but also locally as a typical body reaction to inflammation, and an implant-mediated infection can trigger both situations [189,190]. With such a temperature-sensitive mechanism, the multi-layer drug release system can be alarmed that the second dose is required, and an elevated temperature will activate the antibiotic depot located in the bottom layer.

To obtain mucin multilayers, the base mucin coating was connected to a middle mucin layer *via* lectin. This molecule can drive the assembly of mucin multilayers *via* its affinity to sugar molecules found in mucins [79,191]. However, these lectins show a favorable binding to N-acetyl-D-glucosamine (GlcNAc). Exposure to such GlcNAc molecules would initiate lectin displacement through competitive binding, thus breaking up the connection between the layers [192,193]. Here, to avoid an external addition of such a trigger to the system, GlcNAc-loaded thermoresponsive liposomes were embedded into this middle mucin layer, which was sandwiched between the drug-carrying top and bottom layers. The liposome composition was chosen to obtain liposomes with an elevated membrane fluidity level above ≈ 39 °C (a temperature corresponding to an inflammation state; **Fig. 4.9 B**) [194]. When the membrane fluidity increases, the permeability of the lipid bilayer increases strongly, which leads to a diffusion of entrapped agents into the environment [195]. This phase transition temperature was confirmed by observing a drastic drop in the derived count rate in the light scattering data in response to an elevated temperature. After embedding this liposome-containing layer, the top-coating was attached *via* dopamine crosslinks to form the complete construct.

Successful multilayer assembly deposition was confirmed by QCM-D measurements in which a stepwise frequency shift was observed upon sequential injection of the layer-forming components (**Fig. 4.9 C, Fig. A11**). A slight, reversible frequency shift observed upon injection of a physiological NaCl solution was attributed to a conformational change of mucin molecules from an extended state to a denser state [196].

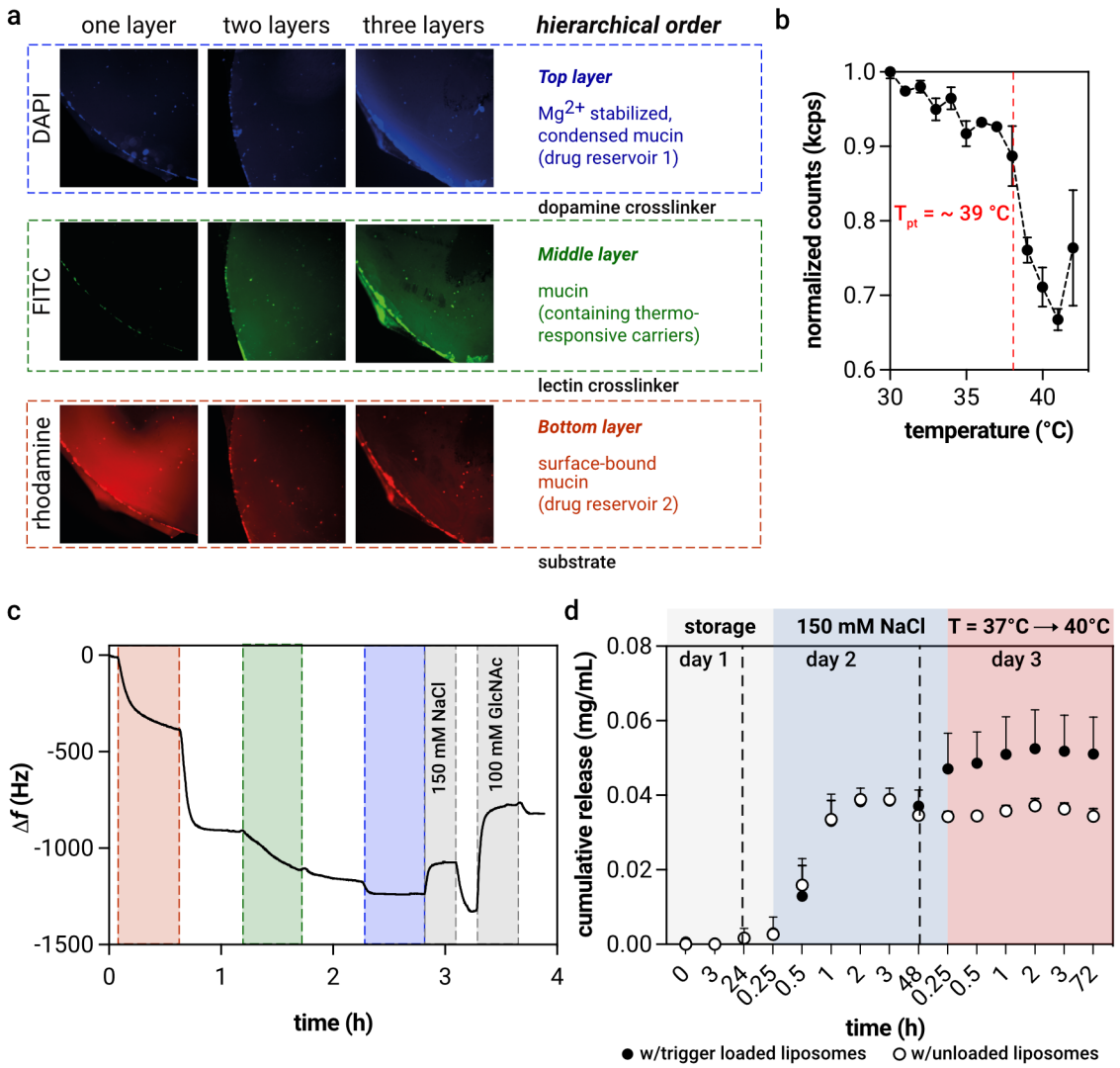

Figure 4.9: Layer-by-layer deposition of mucins with different fluorescent labels (bottom to top: red, green, and blue) was confirmed with epifluorescence microscopy imaging (left) (**A**). The hierarchical order of the multilayered structure with two types of crosslinking molecules is given on the right side of the panel. Phase-transition of liposomes at ≈ 39 °C as observed with a sharp drop in normalized counts when a temperature sweep was applied during DLS measurements (n = 3) (**B**). QCM-d measurement showing accumulation of multilayer forming components as well as partial disassembly in the presence of GlcNAc (**C**). Cumulative TCL release from multilayers when exposed to two independent stimuli (**D**). Filled symbols represent samples containing GlcNAc load whereas open symbols indicate data from a control group containing unloaded liposomes. The exposure time of the 150 mM NaCl trigger is shown with a blue background whereas the experimental conditions at 40 °C are shown with a red background. Data points in (**B**) and (**D**) represent mean values, and the error bars show the standard deviation as obtained from n = 3 independent samples.[†††]

[†††] I acknowledge Dr. Jian Song for the QCM-D measurements.

In addition, when the same construct was subsequently exposed to a GlcNAc solution, an irreversible increase in the recorded resonance frequency was detected, indicating a permanent loss of adsorbed mass. This result showed that the lectin/mucin crosslinks were cleaved by exposure to GlcNAc, and the middle and upper mucin layers were successfully detached. Furthermore, control experiments verified that the successful disassembly of the mucin multilayers by external GlcNAc results in the complete release of antibiotics from the mucin base layer (**Fig. A12-13**).

After confirming the successful deployment of mucin-based multilayers, the liberation of trapped drug depots from the individual layers was triggered by two independent stimuli: exposure to a physiological concentration of NaCl, and temperature increase, respectively. Before the initiation step, the entire construct was first incubated for 1 day at room temperature in a salt-free environment to demonstrate its stability in the absence of any trigger. No significant drug leakage was observed during this incubation period which highlights the excellent stability of the system under storage conditions.

Two-step reservoir activation was performed in the following days by exposure to a trigger solution (initiating decondensation of the mucin top layer) and increasing the incubation temperature to 40 °C (initiating the liberation of GlcNAc molecules to detach the top and middle mucin layers). A complete construct but without a GlcNAc load was used as a control group to investigate whether spontaneous detachment occurs upon temperature changes. For both conditions, TCL release from the condensed upper mucin layer was successfully initiated by exposing the system to a physiological saline solution, and the release event was completed within ≈ 2 h. The second release event of antibiotics entrapped in the base mucin layer was then triggered by increasing the incubation temperature from 37 °C to 40 °C (filled circles in **Fig. 4.9 D**). Importantly, this second release event did not occur in the control group as the embedded liposomes did not contain any GlcNAc cargo (open circles in **Fig. 4.9 D**). In a physiological setting, this second antibiotic reservoir would only get activated when the local temperature around the implant increases to fever-like levels; therefore, it would support overcoming tissue inflammation-related problems occurring at post-implantation stages.

Thus, different from the DNA-mediated cascade release mechanism, independent release events initiated by different stimuli were made possible by implementing different control strategies in the multilayer coating system. Now, the second release event does not necessarily occur right after the first one, but sets in only when it is demanded.

The most striking advantage of the mechanism presented here is the excellent flexibility brought about by the simplicity of the design. Due to their molecular structure, mucins can interact with a wide variety of molecules (*i.e.*, hydrophobic/hydrophilic, charged/uncharged) through electrostatic and hydrophobic interactions and hydrogen bond formation. Thus, antibiotics and other therapeutic molecules, as well as other nanocarriers, can be embedded into mucin coatings. Furthermore, utilizing the different functional groups of mucin molecules that allow for a wide range of modifications, the mechanism can be adjusted to respond to extracellular DNA, pH

changes, enzymatic attacks, or redox conditions that may be the consequence of a pathological condition. Furthermore, as the on-demand decondensation was also shown to work with other (surface-bound) macromolecules, combining different macromolecules during the layer-by-layer deposition may be a promising strategy for achieving different drug release kinetics or to obtain a multilayer construct responding to different stimuli. For such a setup, again, a non-specific dopamine crosslinking could be beneficial in connecting layers made of different macromolecules. Consequently, following the mechanism presented here, a wide variety of coating-cargo combinations can be applied to implant materials to combat device-associated infections and to prevent implant failure.

4.3. Shear-sensitive nanogels that deform upon contact with lumen obstruction ‡‡‡

As discussed in the *Introduction* chapter, stimuli-responsive mechanisms are designed to obtain control over the state of a material to achieve a desired, on-site therapeutic action. Most of these strategies use materials that are designed to be cleaved at the point of care due to a physicochemical alteration in the local environmental conditions. The most generic examples of these strategies employ pH, redox, or temperature-responsive control over the system.

However, one remarkable feature that has not been explored in depth yet is the geometric constraints of the pathological conditions. For example, alterations in the physical characteristics of blood vessels are typical markers for various diseases such as atherosclerosis, vascular intimal hyperplasia, and vasospasm. Although all vascular diseases require specific medications and treatment methods, they share the common problem of elevated wall shear stress levels due to vascular narrowing. Indeed, this effect represents a more specific signature condition than a shift in pH or enzymatic activity. At healthy conditions, the wall shear stress levels in human arteries remain in a range of 1 – 6 Pa. However, a pathological narrowing in stenotic vessels can generate abnormally high wall shear stress levels of > 100 Pa, requiring rapid intervention to prevent life-threatening outcomes such as myocardial infarction and stroke [197]. In the following study, a mechanosensitive nanogel system that exhibits a tunable degree of disintegration upon exposure to different levels of stenosis was developed.

In detail, the developed release mechanism responds to the physical microenvironment of atherosclerosis by on-site nanogel degradation, thus releasing the entrapped cargo molecules. PEGDA nanogels with varying polymer concentrations (10 – 40 v/v %) were prepared by water-in-oil emulsion followed by free radical polymerization technique as described by Anselmo *et al.* [65]. PEGDA droplets prepared in this concentration range formed nanogels with a low polydispersity index (< 0.2); however, their hydrodynamic size increased with an increase in the polymer concentration (**Fig. A14**). To avoid any size differences between particle groups (which would also potentially affect the particle response to different flow conditions), the volume of the continuous

‡‡‡ This section follows in part the publication: Kimna *et al.* (Manuscript in revision)

phase was proportionally increased with the increasing the polymer concentration. As a result, in all formulations, spherical nanogels with similar and monomodal size distributions (average: 249 ± 31 nm; PDI: < 0.25) were obtained (**Fig. 4.10 A, B**). Importantly, nanogels stored at 4 °C (under static conditions) showed only minor size fluctuations over 3 weeks, which shows their good stability (**Fig. A15**). Furthermore, the zeta potential of the nanogels was determined as (- 26 ± 2) mV, which is beneficial for their colloidal stability (**Fig. 4.10 C**).

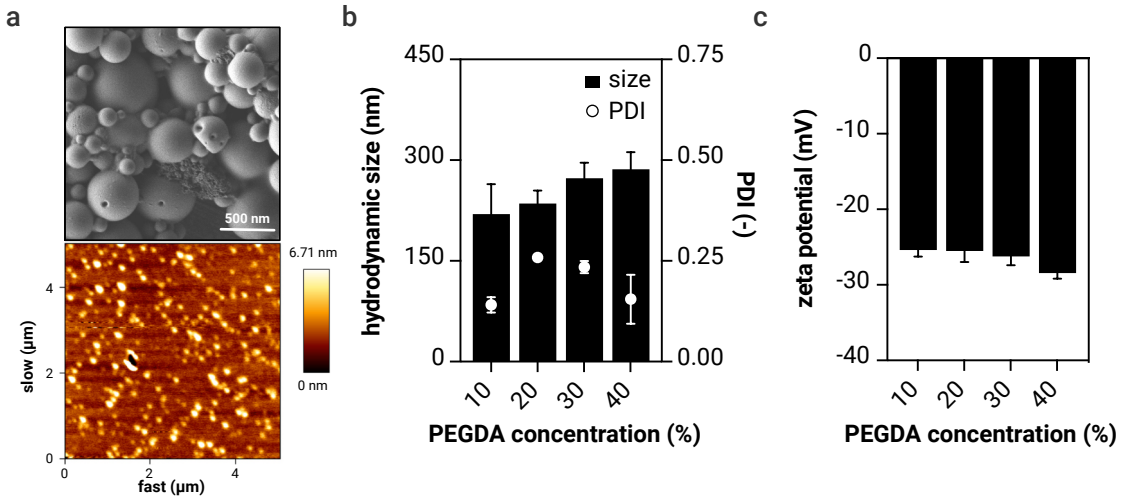

Figure 4.10: SEM and AFM images of the nanogels (30 % PEGDA) acquired at the dried state (**A**). Hydrodynamic size and the PDI values of the nanogels generated with different polymer concentrations (**B**). Zeta potential of the nanogels dispersed in ddH_2O (**C**). Data represent mean values, and the error bars show the standard deviation as obtained from n = 5 independent samples.

Bulk rheology (with a setup allowing for UV-crosslinking a PEGDA solution *in situ*) was used to investigate the viscoelastic properties of macroscopic PEGDA gels. Upon UV illumination, all samples (independent of the PEGDA concentration) showed an instant transition from a viscous solution into an elastically dominated gel. (**Fig. 4.11 A**). Notably, when probed at a constant frequency of f = 1 Hz, the recorded storage and loss moduli were proportional to the polymer concentration (**Fig. 4.11 B**). After this test, the viscoelastic moduli were measured while exposing the material to continuously increasing shear strain levels. This method, called Large Amplitude Oscillatory Shear (LAOS), indicates the critical strain level at which the linear response regime is left (**Fig. 4.11 C**). From an application point of view, beyond this critical strain level, the material is at risk of encountering permanent plastic deformations that often go along with irreversible material damage. With this analysis, it was observed that not only the gel stiffness but also the resilience of the gels towards mechanical failure were increased when tuning the polymer concentration (**Fig. 4.11 D**). Therefore, it was expected that nanogels produced at different polymer concentrations could exhibit a similar trend in their response to mechanical challenges as the tested bulk hydrogels.

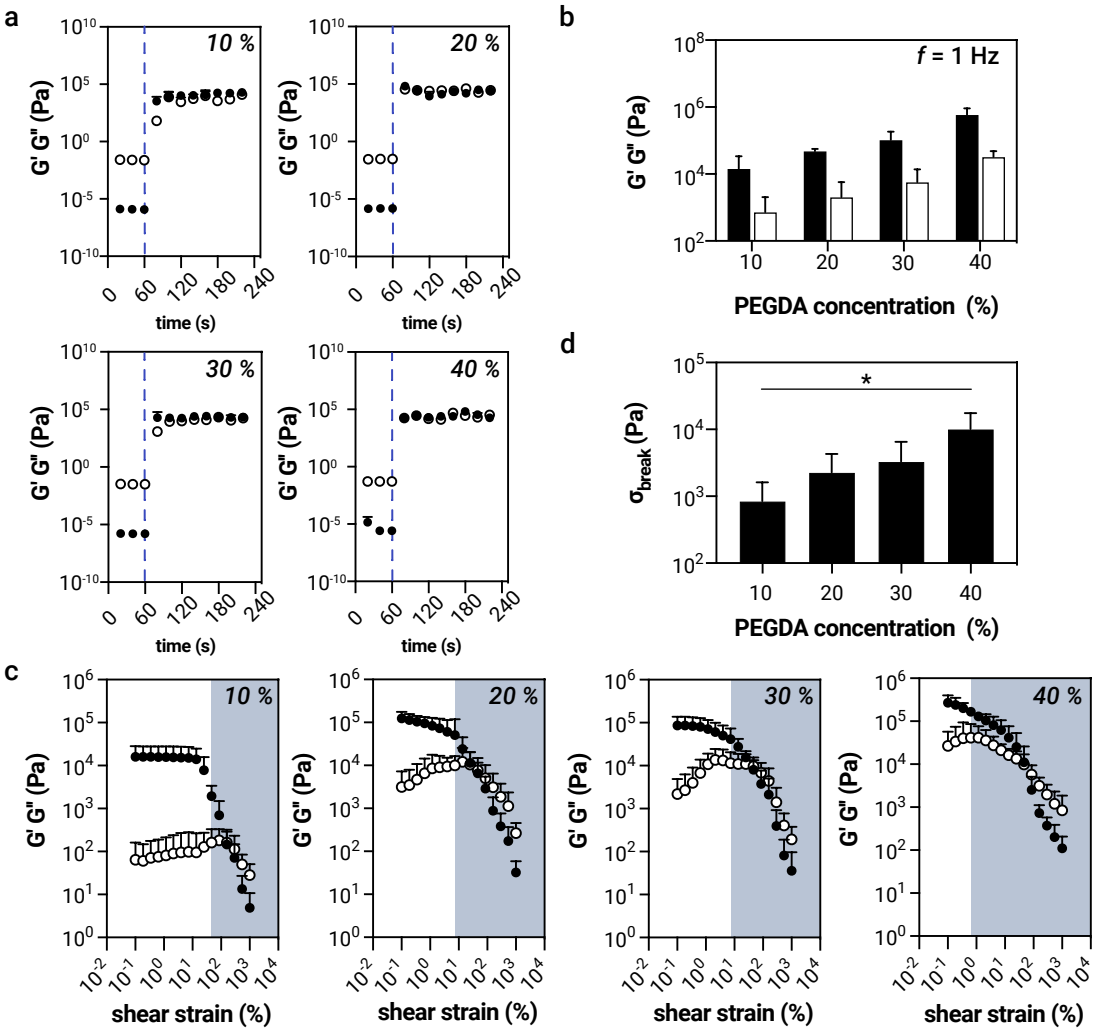

Figure 4.11: Gelation curves of macroscopic PEGDA gels. Dashed lines indicate t = 60 s at where the UV illumination was initiated (**A**). Viscoelastic moduli of the different hydrogel variants as obtained in the linear response regime after UV-crosslinking (f = 1 Hz) (**B**). Non-linear mechanical properties of the gels as determined by LAOS strain sweeps (n = 9) (**C**). The blue regions show the regime where the experimental data points start to significantly differ from the first measurement point, indicating the region where the linear regime was left. Calculated stress values determined at the end of the linear viscoelastic regime (**D**). Data represent mean values, and the error bars show the standard deviation as obtained from $n \geq 3$ independent samples. Asterisks mark statistically significant differences based on a p-value of 0.05.

In the following step, nanogels generated from those mechanically well-characterized polymer matrices were tested under different shear forces that mimic healthy (1.5 Pa) and two different stenotic flow conditions (moderate stenosis: 15 Pa, severe stenosis: 115 Pa) [24]. Control over the applied shear force was achieved by increasing the viscosity of the nanogel dispersion using glucose solutions (with a known viscosity). When a wall shear stress level of 1.5 Pa was applied to the particles, no significant change in particle size or polydispersity was observed. This finding

and the tests performed under storage conditions underline the good stability of the nanogel system in the absence of mechanical challenges. However, when exposed to pathological levels of shear stress, all nanogel formulations underwent significant size reduction (**Fig. 4.12 A**). Importantly, different levels of size reduction proportional to the shear stress level were observed, which shows the successful shear-responsiveness of the system.

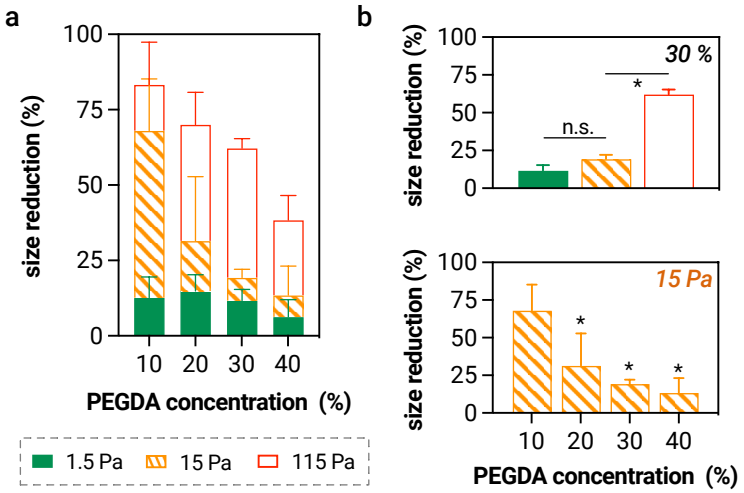

Figure 4.12: Size reduction of 10 – 40 % (v/v) PEGDA nanogels after the application of different macroscopic shear stress levels (n = 5) (**A**). Close up look at the size reduction behavior by keeping the polymer concentration constant as 30 % (v/v) and changing the applied wall shear stress (top); and by keeping the wall shear stress as 15 Pa and changing the polymer concentration (below) (n = 5) (**B**). Data shown represents mean values, error bars denote the standard deviation. Asterisks mark statistically significant differences based on a p-value of 0.05.

In detail, the size of stiff nanogels, *i.e.*, 40 % PEGDA, was reduced to ≈ 170 nm by application of 115 Pa, which corresponds to ≈ 40 % of their original size. On the other hand, for the softest nanogels with the lowest polymer concentration (10 % PEGDA), the percent size reduction under similar test conditions was ≈ 84 %, showing their remarkably higher disintegration level. Also, samples prepared with intermediate polymer concentrations (20 - 30 % PEGDA) showed a clear response (*i.e.*, size reduction) to elevated shear levels (**Fig. 4.12 B**). Additionally, increased PDI values further indicated that the PEGDA nanogels responded to the elevated shear stress values with an augmented size heterogeneity, *i.e.*, the presence of particle fragments.

Importantly, shear stress levels acquired at a moderate level of stenosis (*i.e.*, 15 Pa) returned different results: Now, the average size of the 40 % PEGDA particles was reduced by ≈ 14 % only, whereas the size of 10 % PEGDA nanogels was decreased by ≈ 70 % (**Fig. 4.12 B**). Compared to the response of soft nanogels (*i.e.*, 10 % PEGDA) to a “moderate” level of stenosis, all other nanogel variants showed a significantly different response. Overall, the size reduction response upon

pathological shear levels with respect to the increasing polymer concentration followed almost a linear trend.

To better probe the nanogel behavior in physiologically relevant conditions, a PDMS-based microfluidic setup was prepared to investigate the microscopic shear-response behavior of nanogels at the conditions mimicking the venous blood flow. First, the maximum wall shear stress (WSS) levels at the stenotic microchannels were calculated using computational fluid dynamics (CFD) simulations (**Fig. A16**). For example, in a 70 % stenotic channel, the maximum calculated WSS levels were around 40 Pa; in a 90 % stenotic channel, this value reaches 135 Pa, which agrees well with the findings reported for mildly- and critically stenotic blood vessels of patients diagnosed with atherosclerosis [24,198]. Thus, nanogels were flushed three times through microchannels with different obstruction levels (*i.e.*, no obstruction, 70 %, 90 %) to ensure that all particles in the dispersion were objected to the maximum WSS. No noticeable size reduction was detected in the reference channel (no obstruction), where the nanogels were exposed to a maximum WSS of ≈ 10 Pa only. When the conditions were changed to a pathologically relevant state, all nanogel variants showed increased size reduction in response to elevated shear stress levels. For instance, having passed through the 70 % stenotic microchannel, the size of the 10 % PEGDA nanogels was reduced by (47 ± 14) %. A similar response, *i.e.*, a size reduction by (42 ± 24) %, was observed for the 40 % PEGDA nanogels when the stenosis level was further increased to 90 %. In contrast, this high level of occlusion in microchannels resulted in (86 ± 7) % size reduction for 10 % PEGDA nanogels.

The shear-responsive behavior of the particles is reflected in the physical characteristics of the nanogel dispersion, such as nanoparticulate size, dispersion heterogeneity as well as the number of particles. To be able to count nanogels after being flushed through stenotic microchannels, PEGDA nanogels were labeled with a rhodamine tag and analyzed with an upright fluorescence microscope before and after exposure to the stenotic location (**Fig. 4.13**, **Fig. A17**).

Compared to nanogels passed through the reference channel, the number of 10 % PEGDA nanogels was increased by (46 ± 10) % and (80 ± 22) % after passing through the 70 % and 90 % constricted microchannels, respectively. For the 40 % PEGDA nanogels, the same set of microchannels caused an increase in particle number density by (12 ± 9) % and (35 ± 10) %, respectively. Thus, macroscopic and microscopic assays confirmed that the PEGDA nanogel system shows a tunable mechanosensitive response to different levels of shear stress. Furthermore, the response level can be tuned by adjusting the polymer concentration.

After characterizing the size change that nanogel variants undergo at different physical flow conditions, heparin was selected as a cargo molecule to test the drug release from nanogels upon exposure to pathologically relevant WSS levels. Heparin is one of the most commonly used anticoagulants; however, its free circulation in the body is not ideal due to the potential risk of bleeding complications [199]. Thus, the idea followed here was that a stenosis-driven, local release of heparin could minimize its dilution at the off-target location and thus prevent the potential risk of off-target effects.

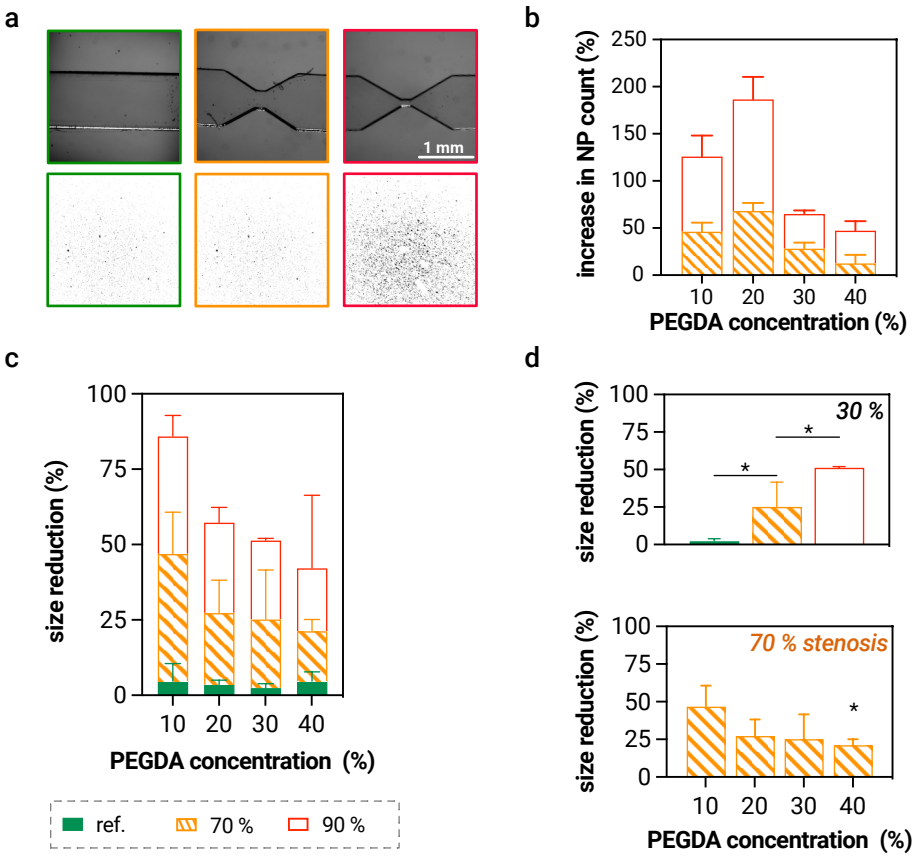

Figure 4.13: Brightfield microscopy images of the fabricated PDMS microchannels with no obstruction (green frame), 70 % stenosis (intermediate level; orange frame), and 90 % stenosis (severe level; red frame) and representative images of (fluorescently labeled) 30 % PEGDA nanogels after passing through abovementioned microchannels (**A**). Increase in number of (fluorescently labeled) nanogels after passing through stenotic microchannels as normalized to the reference channel (**B**). The number of nanogels was determined from 3 independent experiments by considering 5 images per experiment. Size reduction of 10 – 40 % (v/v) PEGDA nanogels after passing through the microchannels with different stenosis levels (n = 5) (**C**). Close up look at the size reduction behavior by keeping the polymer concentration constant as 30 % (v/v) and changing the stenosis level (top); and by keeping the stenosis level constant as 70 % and changing the polymer concentration (below) (n = 5) (**D**). Data shown represents mean values, error bars denote the standard deviation. Asterisks mark statistically significant differences based on a p-value of 0.05.

However, the polymeric matrix chosen for the nanogel formulation is not ideal for offering spontaneous binding to the selected cargo molecule. Although PEGDA matrices resist nonspecific adsorption, proteolytic degradation, low immunogenicity, and unspecific cellular uptake, similar reasons prevent the nanogels from spontaneously encapsulating desired molecules [61]. The 30 % PEGDA nanogels showed negligible, almost undetectable heparin encapsulation efficiency of (1.4 ± 3.1) % (**Fig. 4.14**). Thus, the nanogel formulation required either a chemical conjugation of the heparin, or an additional modification to the matrix to enable non-covalent interactions that entrap the cargo molecule during emulsification.

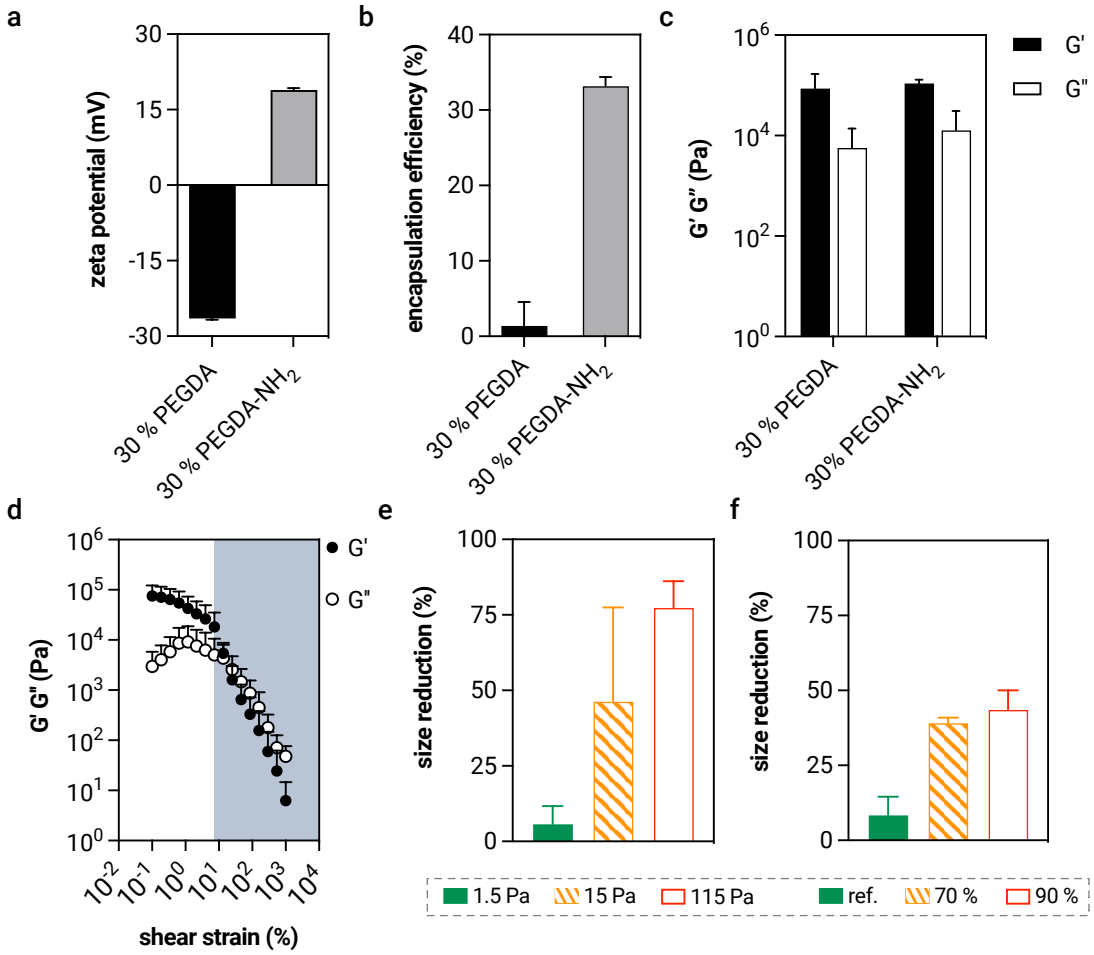

Figure 4.14: Zeta potential of 30 % PEGDA and 30 % PEGDA-NH_2 nanogels dispersed in ddH_2O (*n* = 5) (**A**). Heparin encapsulation efficiency of 30 % PEGDA and 30 % PEGDA-NH_2 nanogels (*n* = 5) (**B**). Viscoelastic moduli of macroscopic 30 % PEGDA and 30 % PEGDA-NH_2 gels at *f* = 1 Hz after UV exposure (*n* = 3) (**C**). Non-linear viscoelastic properties of macroscopic 30 % PEGDA and 30 % PEGDA-NH_2 gels as determined by LAOS strain sweeps (*n* = 3) (**D**). Size reduction of 30 % PEGDA-NH_2 nanogels upon application of varying shear stress levels using a rheometer (*n* = 3) (**E**). Size reduction of 30 % PEGDA-NH_2 nanogels upon exposure to varying shear stress levels in stenosed microfluidic channels (*n* = 3) (**F**). Data shown represents mean values, error bars denote the standard deviation.

To allow for better interactions between heparin and the PEGDA matrix, 2-aminoethyl methacrylate hydrochloride was incorporated into the PEGDA matrix. This molecule offers methacrylate groups that can readily get integrated into the PEGDA matrix upon free radical polymerization. Furthermore, it provides accessible amine groups that can give an overall cationic character to the particles, so they engage in electrostatic interactions with the polyanionic heparin. The hydrodynamic size of such modified particles was similar to those of unmodified 30 % PEGDA particles (270 nm ± 10 nm); however, the zeta potential was shifted to the positive region as (18.9 ± 0.4) mV at pH = 7.4. At the same time, the heparin encapsulation efficiency increased to

(33 ± 1) %. The loading capacity was calculated as (5.6 ± 0.1) µg heparin/mg NP, corresponding to approximately 0.04 ng heparin/NP.

After modifying the gel matrix with accessible amine groups to obtain favorable interactions with the heparin molecules, the mechanical functionality of the modified gels was also confirmed using both, bulk macroscopic gels and nanogels (**Fig. 4. 14 D**, **E**, **F**). The loss and storage moduli of both PEGDA variants after gelation (at f = 1 Hz) showed no difference. Similarly, strain weakening set in at the ≈ 8th measurement points of both PEGDA variants (with and without amine-modification). Thus, it was found that both materials show a similar response upon exposure to mechanical loads as well.

After being subjected to an occlusion level of 70 %, PEGDA-NH_2 nanogels released (73 ± 8) % of their payload. Furthermore, a cumulative release value of (89 ± 7) % was obtained when the same batch of nanogels was passed through a channel with 90 % stenosis. Notably, nanogels passed through the reference channel showed an average of 5 % (undesirable) cargo leakage, which indicates that flow-induced drug loss is very low. Given their good performance in holding their drug cargo during storage and healthy flow (*i.e.*, non-stenotic conditions), the nanogels produced here are likely to succeed in complex hemodynamic environments.

Thus, in the next step, the nanogels were dispersed in blood collected from healthy human donors to assess their hemocompatibility. First, nanogel dispersions (both unmodified and amine-modified variants of the 40% PEGDA formulation) were tested to evaluate any putative hemolytic effects. Hemolysis represents the level of destruction of red blood cells in response to contact with a foreign substance, and it is a fundamental parameter in the hemocompatibility testing of biomaterials [200,201]. Compared to the positive control (*i.e.*, a group in which an osmotic pressure gradient was created by diluting the blood sample with water, thereby triggering complete hemolysis), both nanogels showed no evidence of hemolysis (< 1 %) after 2 h of incubation (**Fig. 4.15 A**). Also, as demonstrated by a plasma recalcification test, neither nanogel variant induced blood coagulation. The average time required to initiate fibrin formation in the presence of nanogels (*i.e.*, 2010 ± 175 s) was considerably longer (*i.e.*, ≈ 20-fold when compared to the coagulated fibrin gel) that in control groups in which an instant fibrin formation was detected (**Fig. 4.15 B**). Thus, considering that the nanogels used here were made using the highest polymer concentration of 40 % (v/v), it was concluded that none of the other nanogel formulations should initiate any undesirable reaction either when they come in contact with blood.

Importantly, when nanogels dispersed in blood samples were exposed to stenotic locations in microfluidic channels, they showed the same disintegration profile as obtained in buffer (**Fig. A18**). This finding once again highlighted that the material response of the system can be well controlled under physiologically relevant conditions. Furthermore, *in vitro* cytotoxicity tests performed with human umbilical vein endothelial cells (HUVECs) showed that the nanogels do not cause any toxic effects. In the tested concentration range (4.8×10^4 – 6.1×10^6 NP/ml), cells incubated with nanogels (both, unfunctionalized and amine-modified variants) showed > 85 %

viability, which indicates good cytocompatibility (**Fig. 4.15 C**). However, a slightly decrease in viability was observed in a concentration-dependent manner.

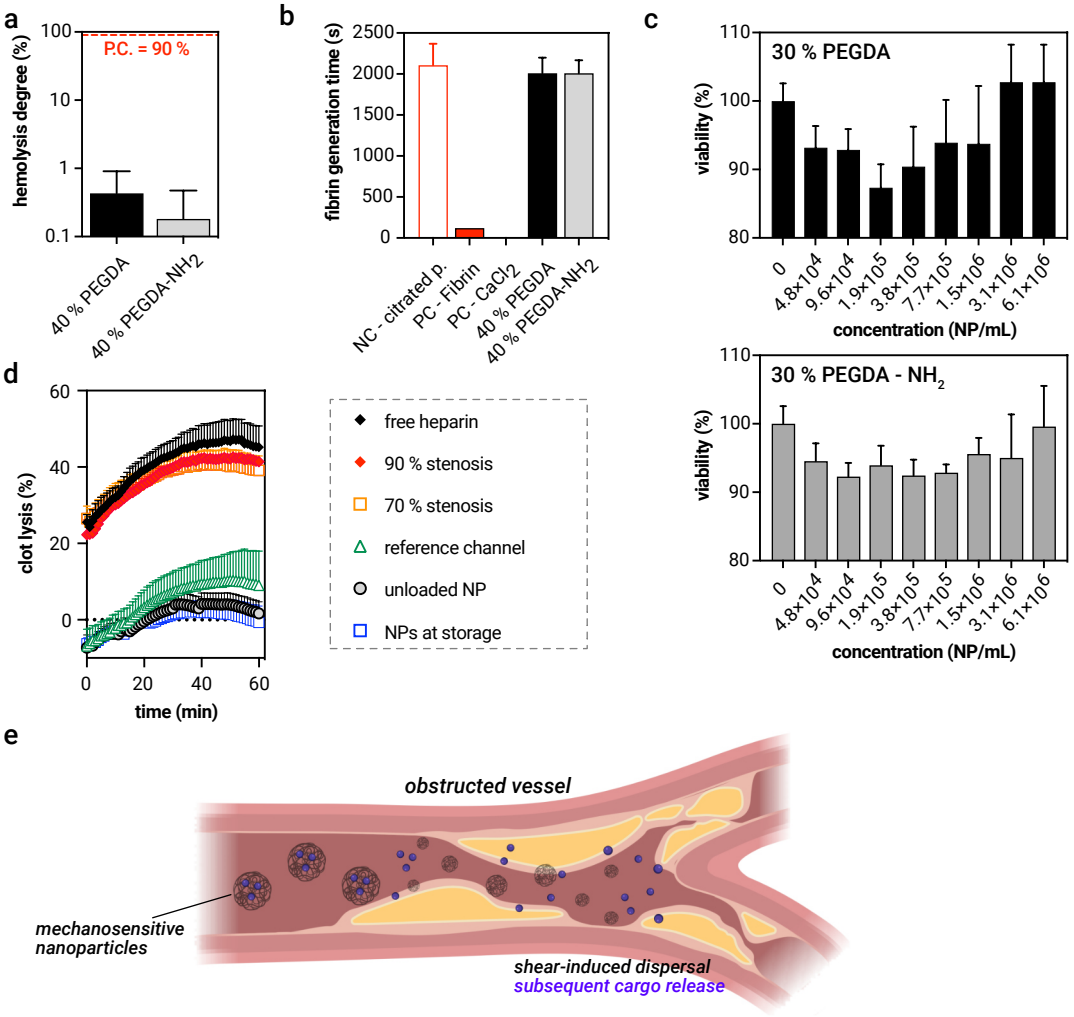

Figure 4.15: *In vitro* NP dose-dependent viability of HUVECs after incubation with 30 % PEGDA or 30 % PEGDA-NH_2 nanogels for 24 h (**A**). Nanogels do not induce hemolysis of whole blood samples (n = 3) (**B**). Plasma recalcification assay indicating the required time for fibrin formation (**C**). Time-dependent clot lysis in the halo human blood clot model after treatment with free heparin; NH_2-modified 30 % PEGDA nanogels flushed through stenosis levels of 90 %, 70 %, and the reference channel; nanogels without a heparin cargo; and the stagnant nanogels that are not flushed through any microchannel at 37 °C for 1 hour, respectively (**D**). Data represent average values as obtained by n = 5 individual clots. Schematic representation of mechanosensitive function of the nanogels in an obstructed vessel (**E**). Data shown represents mean values, error bars denote the standard deviation.[§§§]

§§§ I acknowledge Dario Arcuti for conducting the hemolysis and plasma recalcification tests, and Di Fan for the cytotoxicity test.

When the nanogel density per well exceeded a specific concentration (*i.e.*, 1.9 x 10^5 NP/ml for 30 % PEGDA and 7.7 x 10^5 NP/ml for 30 % PEGDA-NH_2 nanogels), the cellular viability was higher again. This effect obtained for two nanogel variants could be attributed to reduced interactions between the cells and nanogels that tend to agglomerate at excessive concentrations.

After demonstrating the *in-situ* drug release abilities and the excellent performance obtained with cells or blood, the antithrombotic performance of heparin molecules released from the nanogels was tested with an *in vitro* human blood clot model (**Fig. 4.15 D**). As a positive control, free heparin molecules (corresponding to the concentrations encapsulated into the nanogels) were tested, and their clot dissolution performance was measured as (45 ± 6) % within 60 min. Notably, the clot dissolution profiles obtained with nanogels exposed to stenotic channels (70 % and 90 % stenosis, respectively) showed a very similar trend with slightly reduced efficiencies of (39 ± 4) % and (42 ± 1) %. This finding confirmed that nanogel dispersal triggered by microfluidic shear stress initiates the release of free and, more importantly, functional cargo molecules available to dissolve blood clots. Additionally, heparin-loaded nanogels that were not forced to disintegrate (*i.e.*, nanogels flushed through the unconstructed reference microchannel and nanogels kept at storage conditions) did not show significant antithrombotic activity despite being drug loaded. Together, these findings demonstrated that the shear-responsive dispersal of nanogels triggers a burst release of their cargo without affecting the therapeutic functionality of the loaded drug.

Thus, by successfully addressing a pathological physical barrier, an intelligent drug release system that is not based on complex biochemical cues of the target region but its physical characteristics, *i.e.*, the degree of stenosis of the target location, was established (**Fig. 4.15 E**). In this study, two stenotic levels representing moderate and severe atherosclerosis conditions (75 % and 90 %, respectively) were probed to show the mechanosensitive degradation of the nanogels. Especially when considering that no disease-specific, precise biomarker has been identified for atherosclerosis [202], applying such a drug release mechanism based on physical conditions holds significant promise to overcome the limitations of conventional delivery systems.

5. Intracellular delivery mechanisms controlled by strand displacement

An ideal drug carrier system should not only canalize the therapeutically active molecules to the target site, but also maintain their accumulation there to avoid sub-therapeutical dosing. By avoiding on-site dilution of drugs, smart drug carriers supply correct drug doses and, at the same time, prevent off-target tissues from putatively adverse effects. To achieve this goal, complex strategies employing, *e.g.*, changes in intracellular pH [8,9], enzyme levels [10,11], or redox conditions [12,13] as release triggers have been developed. However, most of these marker conditions can also be affiliated to non-target, and in some cases, non-pathological conditions; thus, limiting their use in highly specific release mechanisms. Thus, the key challenge of trigger-induced drug delivery systems remains the identification of a signature condition that satisfies two demands: first, these strategies have to be highly specific for the particular pathological condition; second, they have to guarantee the delivery of therapeutic doses. To overcome "false alert" incidents, logical gates combining different pieces of molecular information were developed to decide if and where the release of the cargo molecule should occur [87,203]. Additionally, autonomous self-activation of drugs/drug carriers was considered as an innovative approach as those sophisticated mechanisms possess higher specificity compared to simpler strategies [204].

In the following section, a synthetic DNA-guided nanoparticulate drug delivery system was developed to establish an on-demand intracellular delivery mechanism. The underlying strategy is based on an on-point activation of the therapeutics. This was made possible by obtaining a precise control over the conformational change of the carrier material, *i.e.*, mucin glycoproteins. Furthermore, to achieve an autonomous activation behavior, an endogenous indicator, *e.g.*, the overexpression of a specific miRNA sequence (which is a marker of the initial phases of specific cancer types) was used as a stimulus to initiate cytosolic drug release only in the target cells.

5.1. Intracellular drug release from DNA-stabilized mucin nanoparticles *via* controlled strand displacement reactions [****]

In general, the use of nanoparticulate drug carriers improves the bioavailability of drugs; those systems can reduce non-specific interactions of cargo molecules with other biological macromolecules and cells (*e.g.*, serum proteins, immune cells, etc.). However, keeping non-target sites unaffected while achieving efficient delivery to the target site requires further strategies as nanoparticles mostly tend to accumulate at off-target organs, especially in the liver and the spleen.

[****] This section follows in part the publication: Kimna *et al.* ACS Nano (2020).

Bringing therapeutical molecules to the proximity of the target might be sufficient in some cases; however, the mode of action of certain drugs, *e.g.*, a specific intercalation with the DNA double helix in the nucleus, requires the implementation of a more selective mechanism to overcome off-target drug activation. This problem is particularly evident in the field of tumor targeting: even when cells are actively targeted *via* the attachment of receptor-targeting ligands to the carriers, those carriers are typically distributed around the target, *i.e.*, they still get in contact wih healthy cells and tissues. Unfortunately, current strategies that are actively targeting malignant cells do not significantly improve the nanoparticle – cell interactions, and this is due to several key challenges in transporting nanoparticles across the tumor barriers. For example, a conceptual study revealed that only 0.7 % of intravenously administered, ligand-coated Au NPs can reach the tumor microenvironment. Importantly, only less than 14 out of 1 million NPs (*i.e.*, 0.0014 % of the injected dose) could enter the cytosol of cancer cells *in vivo* [205]. Furthermore, even if an adequate number of NPs reaches the target cytosol, subcellular challenges (*e.g.*, lysosomal degradation and clearance) might reduce the expected efficiency of internalized drugs [206]. Thus, rather than improving the targeting efficiency of nanoparticles, the following study relies on embedding a secure lock into the drug carrier structure which can be unlocked only in the target cytosol. To do so, due to their complex biochemical architecture and amphiphilic nature, mucin glycoproteins were selected as carrier matrices to allow for binding interactions with charged cargo molecules [155].

To form securely locked mucin nanoparticles, glycerol-driven mucin compaction as presented by Yan *et al.* [75] was used. However, to control the nanoparticle structure also in the absence of glycerol, mucins were functionalized with partially self-complementary ssDNA strands (*i.e.*, crosslinker DNA, crDNA). In detail, this modification allows crDNA strands to spontaneously bind to the cysteine groups of the mucin backbone. Due to their self-complementary domains (8 bps), these ssDNA oligonucleotides can partially hybridize, and thus enable the formation of a stable nanoparticulate system. To verify successful crDNA binding to mucins, mucin/DNA mixtures were loaded into the pockets of an SDS-PAGE gel (**Fig. 5.1 A**) and subjected to electrophoresis. It was confirmed that the thiol functionalization was indeed necessary to attach crDNA strands to mucins: functionalized crDNA strands were retained in the same location where the mucin glycoproteins were trapped. In contrast, a similar sequence without any modification was quickly separated from the mucin glycoproteins and left the gel pocket accordingly.

After confirming successful conjugation of crDNA strands to the mucin glycoproteins, NPs were formed through glycerol-driven condensation. When condensed in the presence of 30 % glycerol, the mucin-DNA conjugates successfully formed NPs with a hydrodynamic diameter of (310 ± 60) nm regardless of the functionalization applied to the crDNA sequences (**Fig. 5.1 B**). However, the subsequent removal of glycerol drastically shifted the hydrodynamic size of mucin/non-thiolated crDNA complex to the micron regime (943 ± 117 nm). Together with the observed PDI values over 0.5, this observation suggests that those condensed NPs turned back to their elongated shape when glycerol was removed. In contrast, conjugation with thiolated crDNA enabled mucin NPs to

retain their condensed state (380 ± 12 nm) after glycerol removal with a monomodal size distribution as indicated by a remarkably low PDI (0.19 ± 0.03).

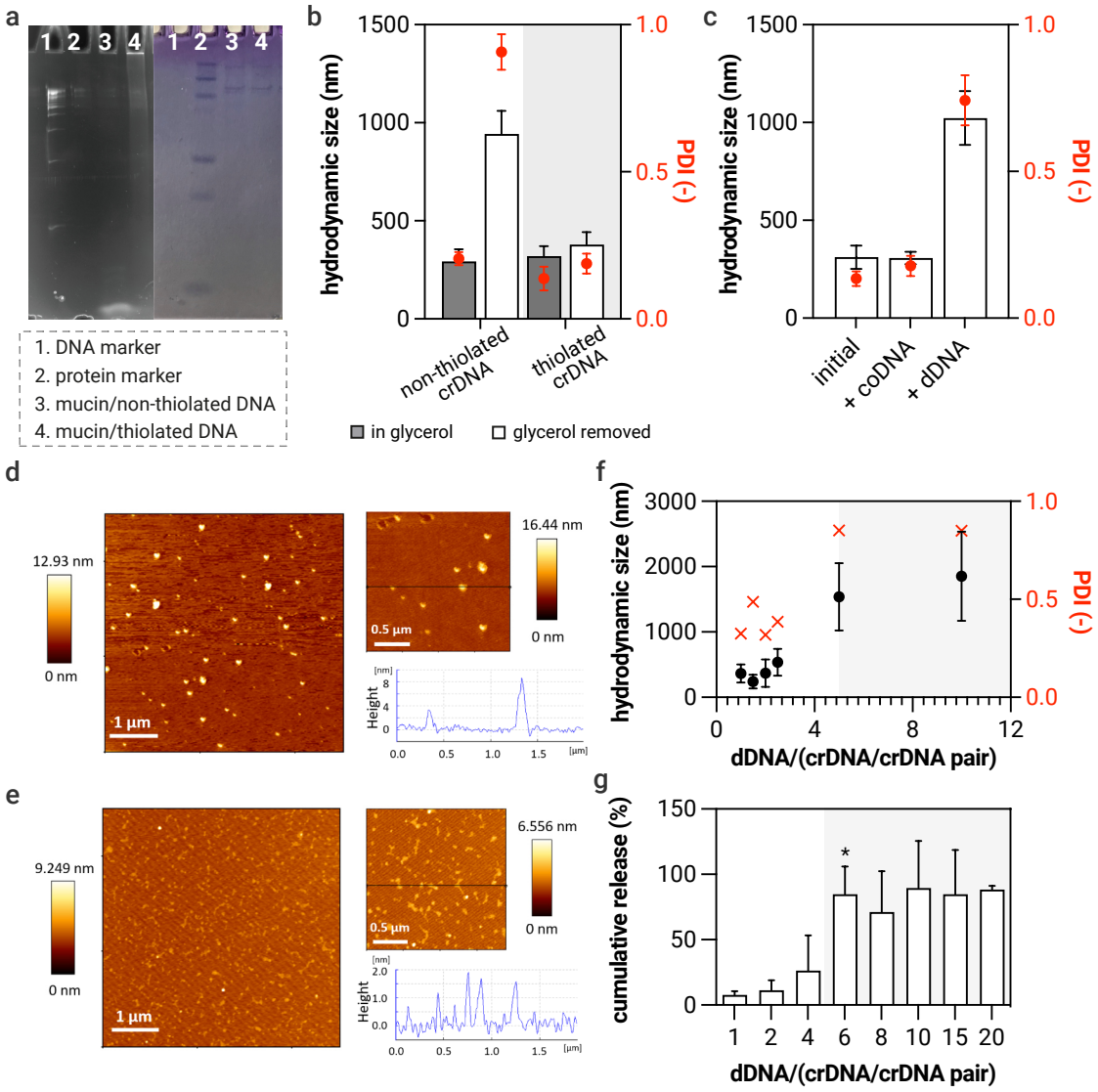

Figure 5.1: Electrophoretic separation of SYBR-Safe stained DNA/mucin mixtures (**A**). DLS measurements performed with mucin NPs incubated with thiolated and unmodified crDNA sequence during the glycerol incubation and after the dialysis step where the glycerol was removed (n = 5) (**B**). DLS measurements demonstrating the triggered conformational change upon incubation with the dDNA strands (**C**). Representative AFM images of DNA-crosslinked mucin NPs in a condensed state (**D**). Representative AFM images of mucin NPs after incubation with dDNA strands (**E**). DLS measurements of mucin NPs under a dDNA gradient showing the threshold dDNA concentration required to force the particulate structure to unfold (n = 5) (**F**). Cumulative cargo release from mucin NPs under a dDNA gradient showing the dDNA required to initiate the cargo release as an indication of conformational change (n = 5) (**G**). Data shown represents mean values, error bars denote the standard deviation.

In the next step, NP opening was triggered with a displacement DNA (dDNA) to displace the already existing thermodynamically favorable duplex, *i.e.*, the crDNA/crDNA pair that keeps the NPs stable in their condensed shape. Upon exposure to such dDNA, which was designed to be fully complementary to the crDNA strands, the hydrodynamic size of NPs was increased to micron-scale (≈ 1000 nm, PDI = 0.74 ± 0.09), again demonstrating that the condensation of mucins into NPs is reversible (**Fig. 5.1 C**). A control experiment, where a random DNA sequence (*i.e.*, control DNA, coDNA) was tested for its effect on the NP size, underscored the specificity of the dDNA binding: in the presence of a coDNA, the NP size remained unaffected. Together, these results showed that an on-demand decondensation of crDNA-stabilized NPs is possible only when the correctly designed DNA sequences are used for both, mucin crosslinking and unlinking.

It is noteworthy that the structural stability of the NPs must be maintained in storage and off-target conditions to avoid spontaneous destabilization and leakage of the entrapped cargo molecules. Accordingly, in the next step, the stability of the NPs was tested for an extended time period of 14 days under physiologically relevant pH levels and in the presence of extracellular enzymes (**Fig. A19**). The negligible size change and stable count rate obtained during this time interval indicated that the NPs remained stable throughout the experimental period, which is promising for their application in a physiological environment. After characterizing the hydrodynamic size of the NPs in their colloidal state, their controlled conformational change behavior was visualized using atomic force microscopy in air tapping mode (**Fig. 5.1 D**, **Fig. 5.1 E**). When glycerol was removed from the environment, crDNA-crosslinked mucin NPs were detected in a round shape, whereas dDNA incubation led to the formation of irregularly shaped, elongated objects. In addition, cross-sectional profiles of condensed mucin NPs suggested a particle diameter of ≈ 200 nm, which agrees with the DLS measurements and reported values for mucin NPs formed in glycerol [75,207] .

Up to now, an excess of trigger DNA was fed to the NP dispersions to demonstrate the control over the structural state of mucins. This excessive amount of dDNA was used to ensure that all accessible crDNA strands connected to the particle matrix could spontaneously bind dDNA, thus inducing a quick and full destabilization of intra- and intermolecular mucin crosslinks. In an attempt to understand the stoichiometry of the crDNA/mucin association, mucin-crDNA conjugates were analyzed spectrometrically. It was found that, ≈ 13 crDNA molecules could bind to a single mucin molecule [††††]. As the crDNA–mucin conjugation occurs through disulfide bonds between cysteine molecules of mucin and the thiolated 5' end of the crDNA, an estimate on the maximum number of available sites for DNA crosslinking can be obtained. Based on a given MUC5AC sequence (UniProt KB, Accession no. A0A287ANG4), a single mucin molecule comprises 270 cysteines; however, 109 of them are located in the glycosylated region, which is unlikely to interact with the crDNA due to electrostatic repulsion and steric effects, both originating from the

[††††] Here, the ssDNA content of lab-purified mucins (≈ 5 ng/µL) was substracted from the ssDNA amount of crDNA-conjugated mucin batch to obtain a rough estimation of number of crDNA molecules bound to mucins.

high density of partially anionic glycan residues in this area. The remaining cysteines are located in the terminal regions of the mucin (91 and 70 at each terminus). However, not all of them are accessible for disulfide bond formation due to the folding motifs (*i.e.*, vWF-C-like and vWF-D-like domains). If the cysteines in these folded domains are excluded for a more realistic approximation, the number of remaining accessible cysteines is reduced to 98. With the experimental assessment discussed above, a realistic crosslinking ratio of 13 crDNA/98 cysteines can be estimated, which corresponds to a functionalization efficiency of ≈ 13 %.

After this estimation, the threshold dDNA concentration required to induce a conformational change was investigated experimentally. In theory, each crDNA/crDNA pair requires one dDNA molecule to induce a structural alteration, however, both charged groups present in the mucin structure as well as possible steric effects might alter this expectation. Thus, NPs were exposed to increasing concentrations of dDNA equivalent to 1 – 10 dDNA strands per (crDNA/crDNA) pair present in the NPs, and the changes in NP size and PDI values were recorded (**Fig. 5.1 F**). Following this approach, NPs incubated with 2 or less dDNA strands per crosslink retained their size, whereas larger objects with a broader size distribution (and higher PDI) were detected at higher concentrations of dDNA. Especially after supplying > 5 dDNA molecules per crDNA/crDNA pair (grey zone at **Fig. 5.1 F**), the obtained picture was similar to experiments where excessive dDNA concentrations were fed to the dispersion. The observed hydrodynamic size changes clearly showed that the conformational change was initiated through dDNA addition. However, from an application point of view, it is also crucial to determine the minimum required dDNA to trigger cargo release from those NPs to secure the intended functionality, *i.e.*, controlled, on-site drug delivery. Accordingly, mucins were incubated with a test molecule which is detectable in the visible range of light (*i.e.*, tetracycline hydrochloride, TCL) before glycerol-driven compaction, and the required amount of dDNA trigger to initiate the opening of the NPs was tested by means of TCL release upon incubation with varying dDNA concentrations (1 – 20 dDNA per crDNA/crDNA pair). With this approach, the minimum amount of dDNA required to trigger drug release from mucin NPs was determined to be in the range of ≈ 4 – 6 dDNA strands per crDNA pair, which agrees well with the findings discussed above (**Fig. 5.1 G**). Nevertheless, these findings are hypothetical as the actual required number of DNA molecules may still be lower than these obtained values (due to the detection limit of the spectrometer). Probably, a higher un-linking efficiency is required to obtain a detectable drug release in the release medium and a noticeable morphological change in the NP ensemble.

To investigate whether the NPs can be efficiently taken up by eukaryotic cells (here, HeLa cells were chosen as a model cell line), fluorescently labeled NPs that reached the cytosol were detected using a flow cytometer. To accurately determine the signal obtained from internalized NPs, the fluorescence signal detected from membrane-bound NPs was quenched with trypan blue. However, only a slight increase in the fluorescence signal was detected over time (**Fig. 5.2 A**). One possible explanation for this result could be that the NPs did not interact sufficiently with the cellular membrane: in their present form, the NPs exhibited a strongly negative ζ-potential

of -41.5 ± 10.7 mV (**Fig. 5.2 B**), which was likely to give rise to electrostatic repulsion between the NPs and anionic components of the glycocalyx on the cellular membrane [208].

Indeed, previous studies have already shown that the ζ-potential of NPs is a crucial parameter that affects NP-cell interactions and consequently cellular uptake [209,210]. However, cells employing more active uptake mechanisms (*e.g.*, macrophages, neutrophils, dendritic cells) might even internalize these anionic NPs *via* phagocytic routes, pass them through biological barriers, and potentially shuttle the NPs to inflammatory sites. Preliminary studies performed in part of this study indeed showed that mucin NPs could be internalized by macrophages efficiently, and did not lead to any cytotoxic effects (**Fig. A20**). However, to improve cell membrane – NP interactions (which eventually led to an increased uptake into non-phagocytic cells), the surface properties of the NPs were altered by employing a second condensation step in the presence of cationic macromolecules (*i.e.*, PLL and chitosan). With this modification, the negative ζ-potential of the NPs was drastically shifted to the positive regime as (21.7 ± 12.2) mV and (2.3 ± 3.3) mV for CS- and PLL-coated NPs, respectively (**Fig. 5.2 B**).

Importantly, neither NPs in their unmodified and nor coated forms showed any perceivable cytotoxicity towards the tested cells (**Fig 5.2 C**). However, after 4 h of incubation, both coated NP variants showed significantly improved cellular internalization compared to their unmodified counterparts (**Fig. 5.2 D**). Furthermore, the dDNA-driven decondensation of the NPs was not affected by the application of the coating. However, this step increased the minimum dDNA amount required to initiate NP decondensation, which could be attributed to electrostatic interactions between the dDNA strands and the cationic surface coating (**Fig. A21**). This observation was especially pronounced for the strongly cationic CS-coated NPs. However, a positive surface charge might, in turn, facilitate 'fishing' the negatively charged dDNA from the environment. At least for the weakly charged PLL-coated variant, this might also improve the efficiency of the process and alter the kinetics of the decondensation process. Furthermore, results suggested that the slightly positive charge as brought about by the PLL coating might be sufficient to aid the NPs to the cellular membrane. Additionally, since they showed an only slightly positive zeta potential, permanent trapping of NPs at the cell membrane could be prevented. Therefore, all further experiments were conducted using PLL-coated mucin NPs.

After ensuring successful cellular internalization, the next issue potentially preventing an efficient intracellular delivery was identified as putative NP trapping in endosomal compartments. Stability tests performed under acidic environmental conditions and with intracellular enzymes already indicated that the NPs can survive under conditions they would encounter along the endosomal pathway; however, if the NPs cannot escape the endosomes, they are likely to be digested by hydrolytic enzymes upon fusion of late endosomes with lysosomes.

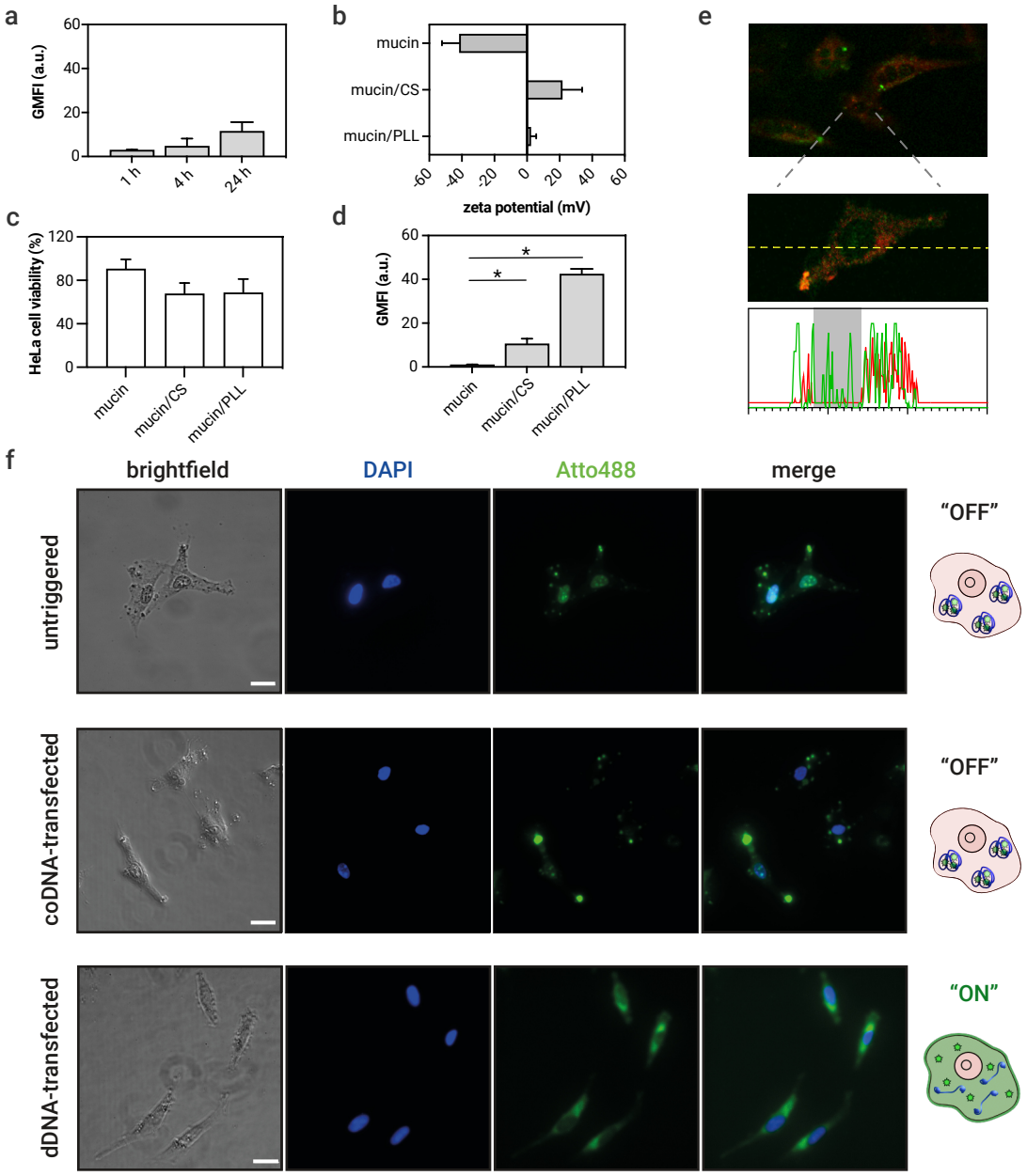

Figure 5.2: Geometric mean fluorescence intensity (GMFI) obtained by FACS evaluation of HeLa cells incubated with (fluorescently labeled) mucin NPs for 1 h, 4 h, and 24 h (n = 6) (**A**). Zeta potential measurements of mucin, mucin/CS, and mucin/PLL NPs at pH = 7.4 (n = 5) (**B**). *In vitro* viability of HeLa cells after incubation with mucin, mucin/CS, and mucin/PLL NPs for 24 h (n = 9) (**C**). GMFI of HeLa cells incubated with (fluorescently labeled) mucin, mucin/CS, and mucin/PLL NPs for 4 h (n = 6) (**D**). Confocal image of HeLa cells (endosomes: red, NPs: green). The profile denotes the fluorescence intensity variation measured along the yellow dashed line where the grey zone represents NPs out of endosomes (**E**). Representative fluorescent microscopy images of HeLa cells incubated with fluorescent cargo-loaded mucin/PLL NPs (cell nuclei: blue; NPs: green). Data shown represents mean values, error bars denote the standard deviation (**F**).

To test the endosomal escape of mucin NPs, the colocalization of NPs and endosomes was probed over time using a confocal fluorescence microscope. The green signal in **Fig. 5.2 E** represents (fluorescently labeled) NPs that were liberated from endosomes, whereas the signal obtained from NPs trapped in endosomes overlaps with the red endosomal marker and thus gives a yellow/orange color when the images are merged. It was observed that a considerable portion of NPs could successfully escape the endosome after 4 h of cellular internalization. In the endosomal compartment, where the environmental pH drops from 7.4 to ≈ 5.0 – 6.5, mucins become protonated, which (in combination with the cationic PLL coat) could be responsible from their escape [211].

Although control over the structural state of mucins was achieved successfully, the cytosolic microenvironment with its numerous ongoing biochemical reactions might still impair the controlled release of drugs from NPs. In the next step, to evaluate their cytosolic performance, NPs were loaded with a fluorescent dye (*i.e.*, Atto488). After 4 h of incubation, successful cellular uptake was confirmed using a fluorescence microscope: Here, the NPs could be visualized as dense fluorescent spots in the cytosol (**Fig. 5.2 F**, shown as "not triggered"). After confirming NP internalization, cell populations were transfected with either trigger dDNA, or control DNA (coDNA). Indeed, dDNA transfection resulted in a homogenous fluorescent cargo distribution within the cytosol as can be seen in **Fig. 5.2 F** (dDNA triggered). In contrast, NPs in coDNA-transfected cells could still be seen as localized spots (**Fig. 5.2 F**). This finding agrees with the picture above that only the correct strand displacement reaction can initiate NP dispersal and cargo release, even in the presence of cellular enzymes, proteins, and cytosolic oligonucleotides.

The precise control over the activation of the cargo delivery achieved here provides a great advantage over the regulation of the therapeutic function of a cargo molecule where off-target effects are highly undesirable. Owing to their molecular structure, mucins can engage in electrostatic and hydrophobic interactions with drugs. Additionally, they can form hydrogen bonds with the other molecules. Thus, the nanocarriers developed here should be able to carry drugs even in the absence of specific binding interactions. Indeed, first investigations showed that mucin NPs can entrap a broad range of antibiotics with a high loading capacity and concentrate them in the cytosol (**Fig. A20**). Furthermore, event when not coated with cationic macromolecules, NP uptake by macrophages as evidenced here can maybe be used to navigate the NPs to the actual point of care.

In the last step, to test the controlled intracellular delivery of drugs, the NPs were loaded with doxorubicin (DOX), which is a highly cytotoxic, anthracycline type molecule used in chemotherapy. DOX intercalates with DNA to inhibit the progression of an enzyme (*i.e.*, topoisomerase II) that relaxes supercoils in DNA for transcription, thereby stopping the replication process [212]. Thus, it is crucial to canalize a DOX therapy to the target cells to avoid highly toxic off-target side effects.

To test whether mucin NPs can be suitable carrier materials for DOX delivery, first, DOX loading to NPs was optimized in terms of encapsulation efficiency and drug loading capacity. Based on the

optimal encapsulation of (17 ± 2.4) % and the loading capacity of (8.6 ± 1.2) µg DOX/mg mucin, a formulation with a DOX feed concentration of 0.05 µg/ml was chosen for further experiments (**Fig. 5.3 A**). It was again confirmed by DLS measurements that (DOX-loaded) NP conformational change can be triggered only in the presence of dDNA (**Fig. 5.3 B**).

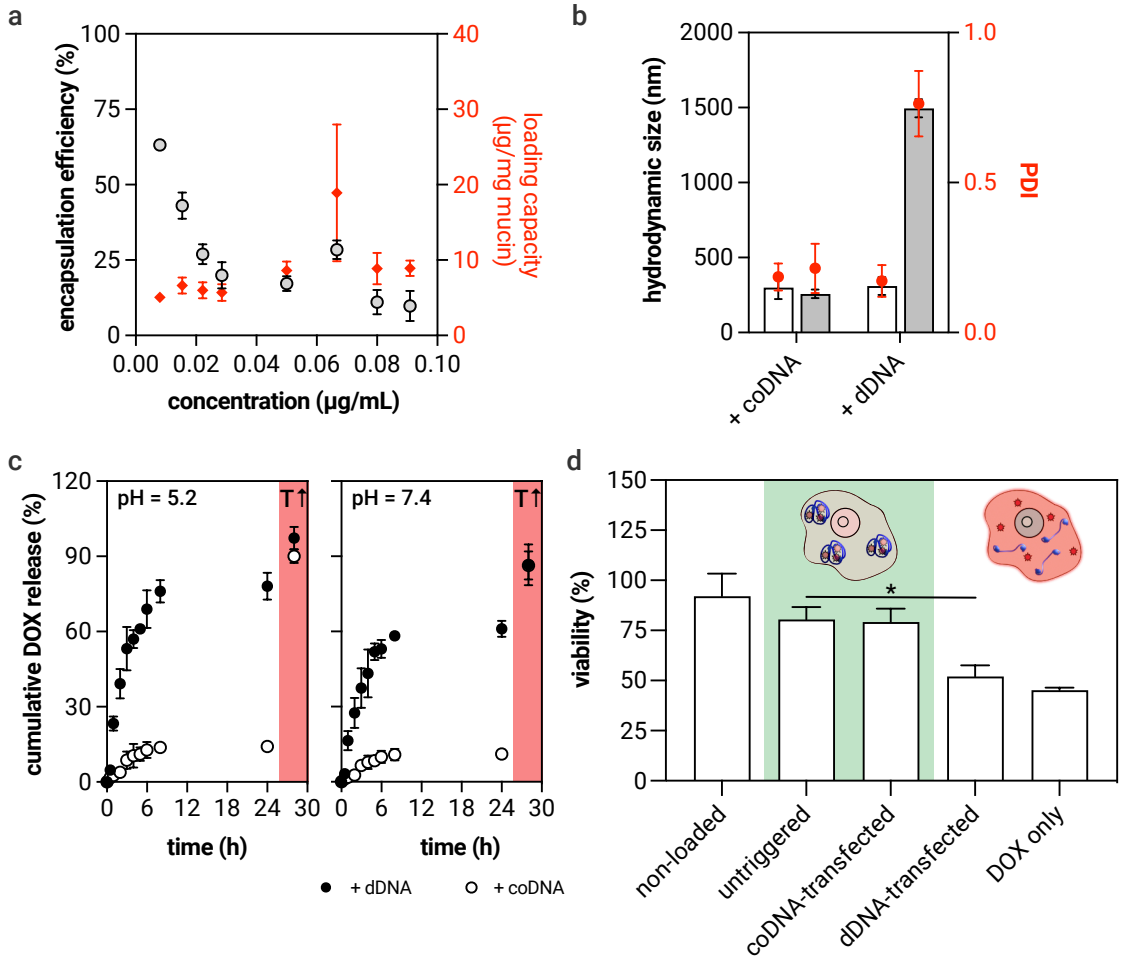

Figure 5.3: DOX encapsulation efficiency and loading capacity of PLL-coated mucin NPs (*n* = 3) (**A**). DLS measurements indicating on-demand opening of PLL-mucin NPs is possible only in presence of dDNA (*n* = 5) (**B**). The cumulative release profiles of DOX-loaded PLL-coated mucin NPs at pH = 5.2 and 7.4 (*n* = 3) (**C**). The data points at the red zone show the cumulative release after heating the NP dispersion to 75 °C. The viability of HeLa cells after incubation with non-loaded NPs, DOX-loaded NPs followed by a transfection step, and free DOX solution (*n* = 9) (**D**). Data shown represents mean values, error bars denote the standard deviation.

Incubation with dDNA at two pH conditions (7.4 and 5.2, representing the pH physiological range in the cellular compartments) resulted in a significant increase in DOX concentration in the medium which corresponds to > 60 % of the DOX loaded into the NPs. In contrast, coDNA incubation led to no considerable release but a minimal drug leakage of <15 % over 24 h

(**Fig. 5.3. C**). After the DOX release had reached a plateau, remaining DOX in the NP matrix was released by raising the temperature to 75 °C, which exceeds the melting temperature of the crDNA/crDNA structure (**Fig. 5.3. C,** red zones). Thus, it was confirmed that although NPs carry similar amounts of the drug, their cargo content can be assured despite different oligonucleotide and acidic pH conditions until their release is triggered.

Following the same conditions as described above, cytosolic drug release was confirmed by measuring the changes in cellular viability upon NP incubation for 4 h: when transfected with the correct trigger, the decrease in cell viability was similar to the result obtained for cell incubation with free DOX, demonstrating the high drug release efficiency of the NPs in their triggered state (**Fig. 5.3 D**). In contrast, no cytotoxic effects were observed for the groups that were not transfected with the correct dDNA trigger (*i.e.*, groups that were either not transfected or transfected with coDNA). This finding underscores that drug leakage from NPs was negligible.

Overall, by employing a secure DNA-lock to drug carrier mucin nanoparticles, a precise control over the state of the NPs (condensed vs. opened/elongated) was ensured. Importantly, the DNA-controlled activation step can prevent the premature release of cargo molecules which otherwise can lead to unwanted effects on off-target cells/tissues. Additionally, mucin NPs exhibit a stable structure over extended time periods which indeed is one of the most important requirements of a safe drug delivery system. Thus, these findings obtained with DNA-crosslinked mucins provide a major steppingstone towards the design of a well controllable intracellular drug delivery mechanism.

5.2. Autonomous strand displacement reactions triggered by endogenous markers to release drugs from DNA-stabilized mucin nanoparticles ‡‡‡‡

So far, the developed DNA-crosslinked mucin nanoparticles offer superior properties including good storage stability, favorable cellular uptake and endosomal escape profiles, high cargo encapsulation and release efficiency, and precise control over the cargo release. However, the requirement of a second transfection step to deliver the release initiator, *i.e.*, a trigger DNA, is not ideal in a physiological setting as target and non-target cells do not exist as separate populations. Thus, the presented mechanism, up to now, comes with the risk of transfecting non-target cells, which might lead to the activation of drug release in off-target cells.

To achieve a site-specific, precisely controlled drug delivery process, two key questions need to be addressed: Is there a specific difference between a healthy cell/tissue and its diseased counterpart? How can we make use of this difference to trigger the automatic release of therapeutically active agents while making sure that only the diseased cells/tissue receive the drug therapy?

‡‡‡‡ This section follows in part the publications: Kimna *et al.* ACS Nano (2020); Kimna and Lieleg, Biophysics Reviews (2021).

From a strategic point of view, keeping the mechanism as simple as possible by using minimal administration steps increases the chances of a therapeutic success. Thus, placing a DNA-logic gate mechanism or using a molecular trigger might be suitable for eliminating the second administration step [206,213]. However, the addition of a stimulus-sensitive component to the nanoparticulate matrix or the incorporation of a complex DNA logic gate might complicate the control over the conformational change. Unfortunately, overly engineered systems tend to work only at very specific *in vitro* conditions, which do not represent the level of complexity in the biological milieu. To avoid overengineering, the use of natural logic gates to implement a deterministic process was found to be the most rational strategy, and thus, was applied for the development of the next step: an autonomous cargo release driven by pathological miRNA expression of target cells.

Short, non-coding microRNAs (miRNAs) are cytosolic oligonucleotides that can interact with multiple mRNAs through complementary base pairing. Notably, about 50 % of the miRNA sequences discovered to date are predominantly located in cancer-associated genomic regions or at such sites where an unphysiological up- or downregulation negatively impacts immune responses modulating the physiological reaction to pathological conditions [214]. In the past decade, up- and downregulation of several miRNAs was related to the initiation phase of several diseases including cancer, viral infections, and cardiovascular diseases [215]. Accordingly, strategies to interfere with miRNA regulation have been developed in order to alter the biological fate of a cell: for instance, it is possible to suppress tumor growth, block cell invasion into neighboring tissues, prevent metastasis, and promote apoptosis [27]. Thus, repurposing a dysregulated miRNA overexpression as a modular drug release strategy might work without overengineering the carrier material.

Here, it was anticipated that a mucin crosslinking crDNA sequence responding to a specific cellular miRNA overexpression (by hybridization and thus strand displacement resulting in cross-linking opening) would initiate a NP conformational change, thus enabling the autonomous release of cargo molecules to the target cytosol. In this study, as HeLa cells were tested as a model cancer cell line, and the miRNA expression profile of this cell line was investigated to select a potential trigger sequence for such an autonomous drug release. In particular, miR-21 – an oncogenic miRNA overexpressed in many tumors [216,217], is reported to be one of the significantly overexpressed miRNA types in HeLa cells [87,218]. Indeed, miR-21 overexpression in HeLa cells was confirmed with qPCR experiments, where NIH/3T3 mouse fibroblast cells were selected as a control group due to their relatively low miRNA-21 expression profile (**Fig. 5.4 A**).

Based on the known target sequence of miR-21, the crDNA sequence was redesigned to comprise two main functions: First, it contains self-complementary domains (8 bps) to ensure good NP stability. Second, it shows a complementary region to miR-21 (*i.e.*, antimiR) with more bases (11 bps), and this can drive the thermodynamically favored state towards miR/crDNA complexes (**Fig. 5.4 B**). In detail, when antimiR-crosslinked NPs are delivered to miR-21 overexpressing cells, the projected base-pairing is expected to shift from crDNA/crDNA towards crDNA/miR-21. Thus,

following the same methodology as before, antimiR-21 strands were conjugated to mucin glycoproteins, and the mucins were condensed to form nanoparticles. Also here, all NPs received a cationic PLL coating to ensure efficient cellular uptake. Prior to testing their biological activity, the miR-21 driven dispersal of reengineered mucin NPs was verified using DLS (**Fig. 5.4 C**). Again, a strong increase in the heterogeneity and hydrodynamic size confirmed that the NPs can indeed be forced into an open state by the presence of a miR-21-mimicking sequence.

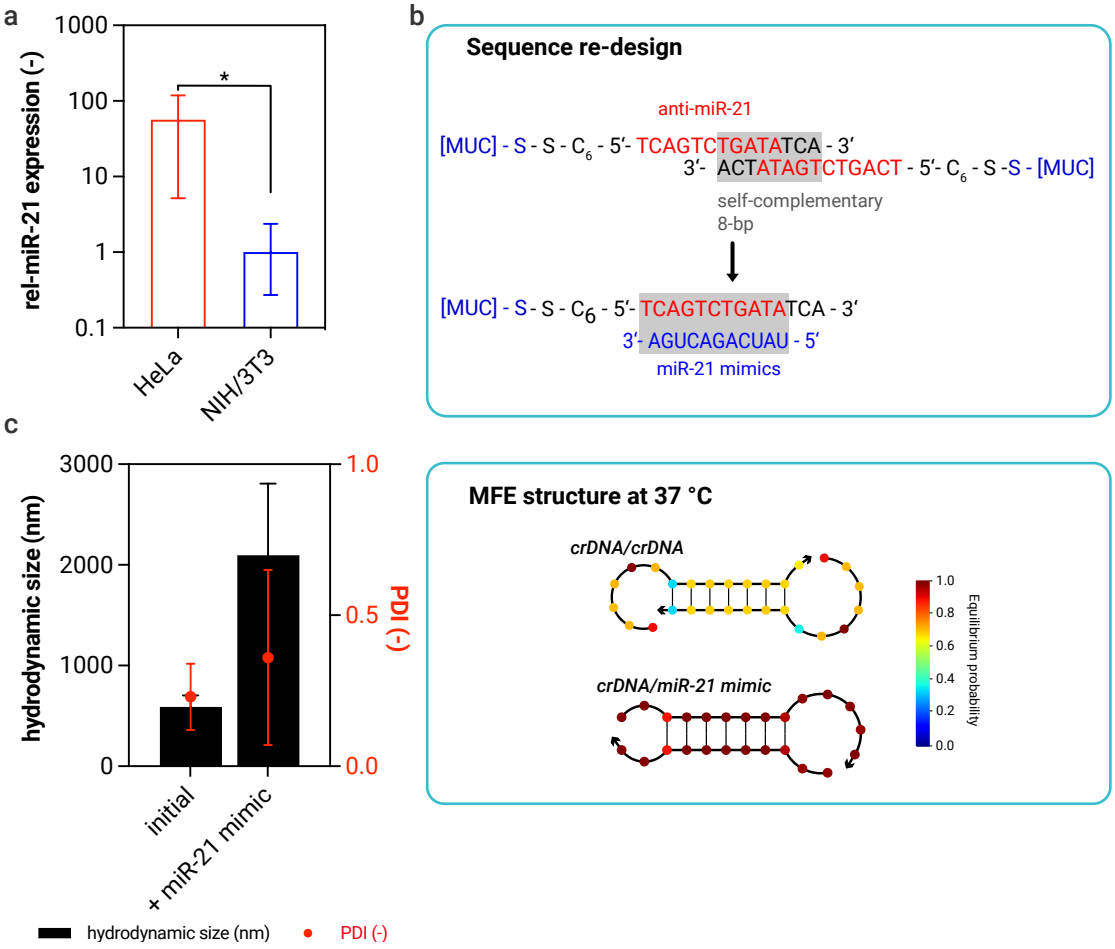

Figure 5.4: Quantitative real-time PCR analysis of miR-21 expression in HeLa and NIH/3T3 cells (*n* = 3 technical replicates; **A**). Re-designed crosslinker DNA sequence and the predicted minimum free energy structures at the equilibrium concentration at 37 °C (**B**). DLS measurements showing that miR-mimic sequence initiates the dispersal of antimir-locked NPs (*n* = 5) (**C**). Data shown represents mean values, error bars denote the standard deviation.

To test the performance of the intracellular miRNA-responsive sequence design without any transfection step, both target and off-target cells were imaged after incubation with fluorescent (dye-loaded) NPs. Notably, both cell lines internalized "anti-miR" conjugated mucin NPs, however, the NPs remained condensed in NIH/3T3 cells as shown by the localized fluorescent

signals (**Fig. 5.5 A**, left). In contrast, the fluorescent cargo was spread across the cytosol of HeLa cells (**Fig. 5.5 A,** right), indicating an autonomously triggered release of the model cargo.

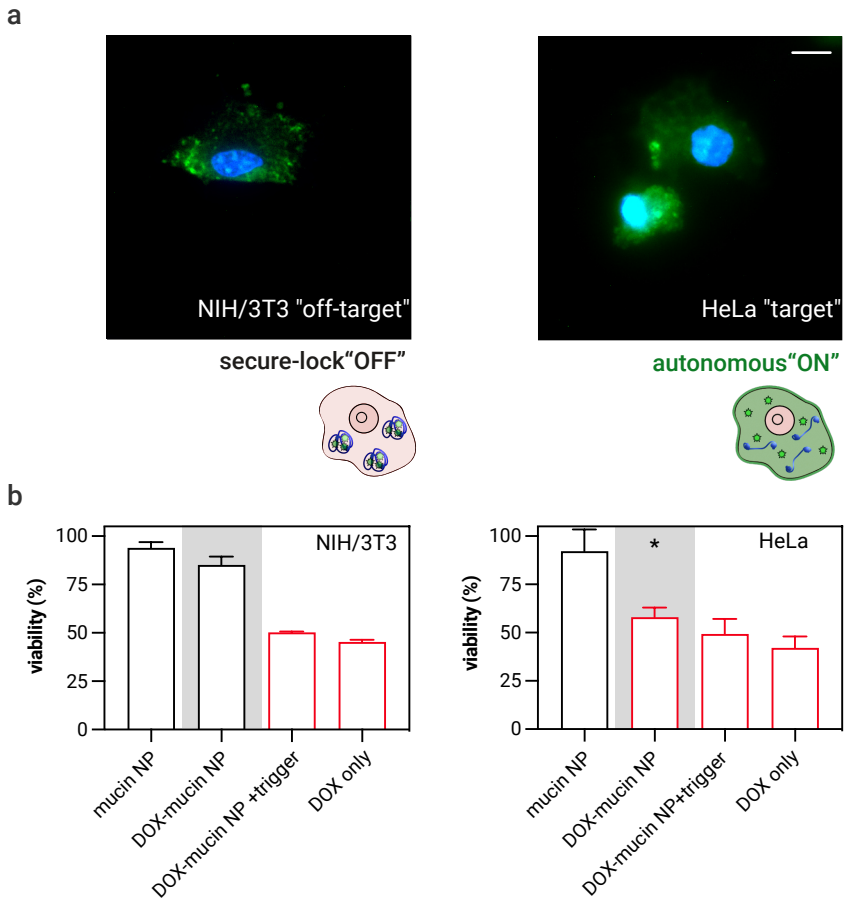

Figure 5.5: Fluorescence microscopy images of NIH/3T3 and HeLa cells showing autonomous fluorophore dispersal in the cytosol of HeLa cells (target), whereas NPs can be observed as concentrated spots at off-target NIH/3T3 (off-target) cells (**A**). Viability of NIH/3T3 (right) and HeLa (left) cells after incubation with unloaded nanoparticles, DOX-loaded nanoparticles (non-transfected and trigger DNA transfected cells), and a free DOX solution (**B**). Data shown represents mean values, error bars denote the standard deviation (n = 9).

In the last step, re-designed oligonucleotides were used to form DOX-loaded mucin NPs, and the resulting NPs were incubated with target and off-target cells (**Fig. 5.5 B**). When incubated with HeLa cells, DOX-carrying NPs exhibited a cytotoxic effect (*i.e.*, ≈ 50 % reduction of viability) regardless of addition of an external trigger. This result clearly shows that cellular overexpression of miR-21 was sufficient to induce a conformational change of mucin NPs, and to release their cargo. Notably, the cytotoxicity induced by the autonomous release from mucin NPs was found to be in a similar level for the cells that were incubated with free DOX. For NIH/3T3 cells, where the cellular level of miR-21 is significantly lower, it was necessary to provide an external trigger in

addition to mucin NPs to achieve a similar level of cytotoxicity. However, incubation with free DOX shows a similar cytotoxic effect on both, target and off-target cells. Together, these results strikingly demonstrated that the precise delivery mechanism employed here can be used to protect off-target cells from unfavorable drug delivery and enables a therapeutic action only at the required location.

5.3. Targeted miRNA therapy *via* mucin nanoparticles stabilized with gene silencing strands

In a healthy living organism, the maze of the intracellular metabolic pathways is tightly regulated: the body employs various mechanisms to ensure that each biochemical reaction occurs at the proper rate, time, and place. However, in recent years, abnormal expression levels of specific miRNA variants were found to be responsible for a cascade of cellular events in several pathological conditions including cancer [219]. Therapeutic nucleic acid delivery to specifically silence such signature miRNAs may be a promising treatment strategy that achieves both, a high efficiency and low side effects. To make this possible, a highly selective targeting mechanism is required that differentiates the "sick" cells from the surrounding healthy tissue. In previous work, a DNA-crosslinked mucin nanoparticle system was developed to undergo a dynamic conformational change when exposed to the correct trigger oligonucleotide strands (either a synthetic or intracellular miRNA) [220]. In the next step, synthetic DNA strands were designed to serve as therapeutic cargo molecules in addition to having an interactive, dynamic role that allows for the autonomous, cell-specific release of the NP cargo. This study aims at developing deliberately designed, mucin-based nanoparticles targeting the seed region of the cytosolic oligonucleotide to restore the non-malignant state of a cell. Therefore, the goal was to obtain a nanoparticle system capable of depleting and silencing the aberrantly expressed target miRNA, *i.e.*, miRNA-21, thus correct dysregulated functions. For example, miRNA-21 overexpression changes cellular behavior such as it stimulates migration and proliferation, and suppresses apoptosis [221,222].

Two types of sequences were designed to stabilize, and at the same time, enable a therapeutic action of mucin NPs. For both designs, a bridge DNA with a thiol functionalization was used to attach the DNA to the cysteines of mucins. Moreover, an antimiR sequence was designed to form a bridge/antimir/bridge complex in a stable state (**Fig. 5.6 A**). Importantly, the antimiR sequence was designed to silence the seed region of miR-21, which affects the expression of many of its targets through translational inhibition.

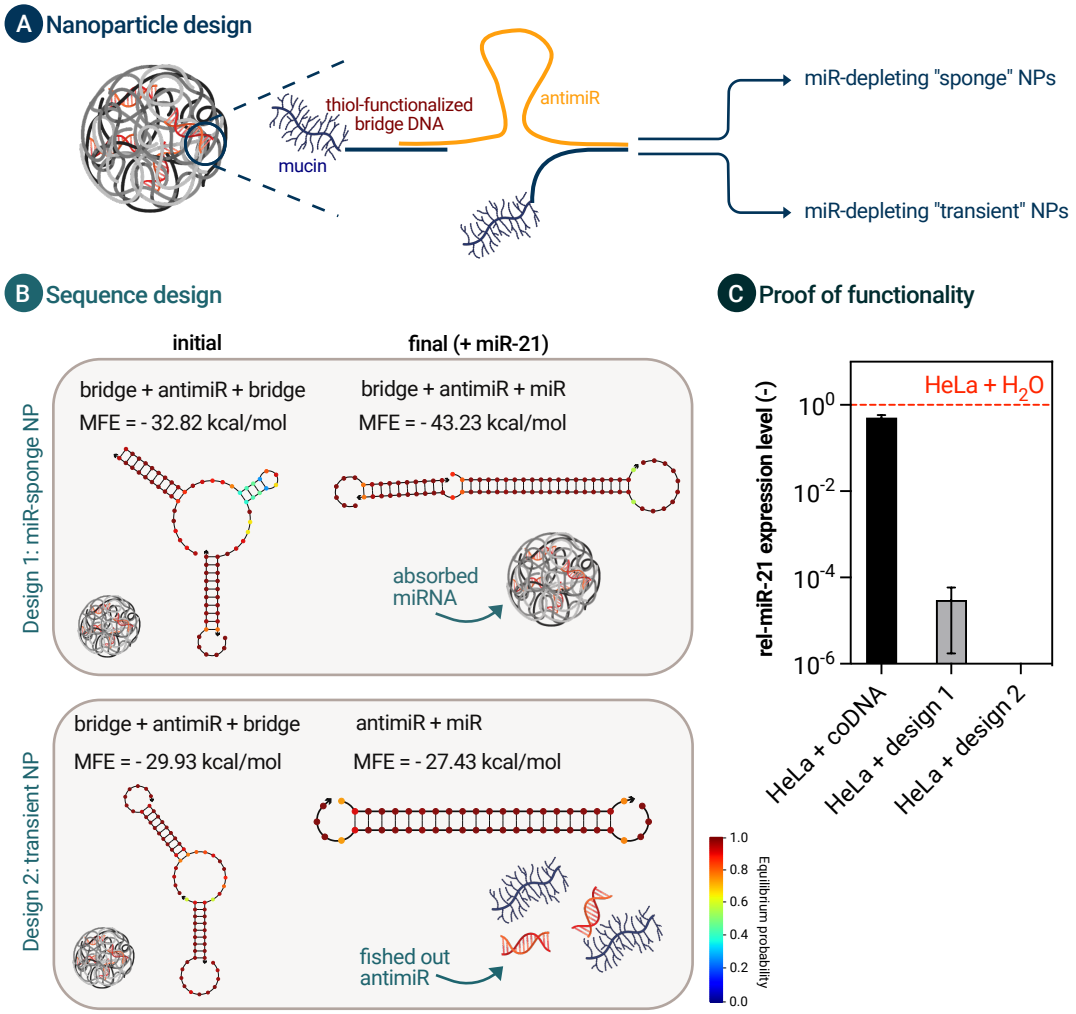

Figure 5.6: Nanoparticle design rationale (**A**), two set of DNA sequences designed to obtain different mode of actions, (**B**) and the miR-21 depletion activity of the antimiR strands as proven with qPCR measurements (**C**). For the qPCR measurements, data shown represents mean values, error bars denote the standard deviation as obtained from *N* = 3 independent biological replicates.[§§§§]

This strategy was employed by means of two different modes of action by locating the "miR-depleting region" to either dynamic or stable part of the entire sequence. In detail, two different sets of DNA-stabilized mucin NPs were designed to obtain the following mode of actions when internalized by target cells (**Fig. 5.6 B**):

i) **Design 1 – miR-sponge nanoparticles:** The stability of the nanoparticles (when the glycerol was removed) was ensured by a bridge/antimir/bridge complex. The miR-depleting region of the antimiR sequence was located in the middle of the sequence,

[§§§§] I acknowledge Dr. Matthias Marczynski for conducting qPCR measurements.

and was free to interact with cytosolic miRNAs upon cellular internalization. Thus, the nanoparticle can absorb excessive miRNA from the cytosol.

ii) **Design 2 – transient nanoparticles:** Again, a set of bridge/antimir/bridge was designed to keep the mucin NPs intact after glycerol removal. However, the antimiR sequence was designed in such a way that the miR-depleting region (of the antimiR sequence) had a base-pairing interaction with the bridge DNAs; this gave NPs the ability to switch their conformation: The NPs remain condensed unless exposed to pathologically high miRNA levels. If they are exposed to overexpressed miRNA, the cytosolic miRNA triggers a strand displacement reaction within the nanoparticle (by forming antimiR/miR complexes, thus, decondensing the NP structure into elongated mucins.

In both cases, antimiR strands were designed to silence the seed region of miR-21 to correct the dysregulated functions of the target cells. First, to confirm the miRNA-21 silencing activity of both antimiR sequences, the total RNA content of target cells was harvested, and the depletion of miR-21 was verified using qPCR (**Fig. 5.6 C**). As a control, a non-therapeutic crosslinker sequence was tested and shown to have no effect on relative miR-21 expression levels.

In the next step, mucin NPs were formed by condensing mucins and stabilizing the condensed structure using a bridge/antimir/bridge complex made of one of the two sets of sequence designs (*i.e.*, design 1, miR-sponge NPs; design 2, transient NPs). However, the glycerol concentration required for NP condensation was increased from 30 % (v/v) to 60 % (v/v) to obtain NPs with a smaller size than in the previous study [75]. Dynamic light scattering experiments showed that both groups formed uniform NPs (PDI < 0.25) with a hydrodynamic diameter of (215 ± 48) nm (**Fig. 5.7 A**). Importantly, when the NP variants were incubated with excessive miR-21 mimic strands, a strong change in the hydrodynamic size was observed only for the second NP species, proving the envisioned conformational change to occur only when expected. In contrast, no significant size change was observed for the miR-sponge NPs. Due to the overall anionic character of mucins, both NP species showed a negative zeta potential of - (20 – 30) mV, indicating good colloidal stability (**Fig. 5.7 B**). Furthermore, the stability of the mucin NPs was analyzed under storage conditions where the NPs were incubated at 4 °C for 14 days. As shown in **Fig. 5.7 C**, the hydrodynamic size of the NPs showed only a slight variation during this time span.

Previously, a second condensation step with cationic polymers was found to be necessary to improve the cellular uptake of mucin NPs. However, such a modification does not only improve the interaction with target cells but also enhances the NP uptake into off-target cells. To circumvent this issue and to canalize the NPs to the desired cells, the NPs were functionalized with folic acid. The folate receptor (FR) is a cell surface glycoprotein found in humans, and it has a high affinity for folic acid ($K_D < 10^{-9} – 10^{-10}$) [223]. Although FRs are not detectable in healthy cells, they are highly expressed in many malignant tumor cells. Targeting these FRs with folic acid conjugation to the NPs has several advantages such as high specific binding affinity and ease of conjugation.

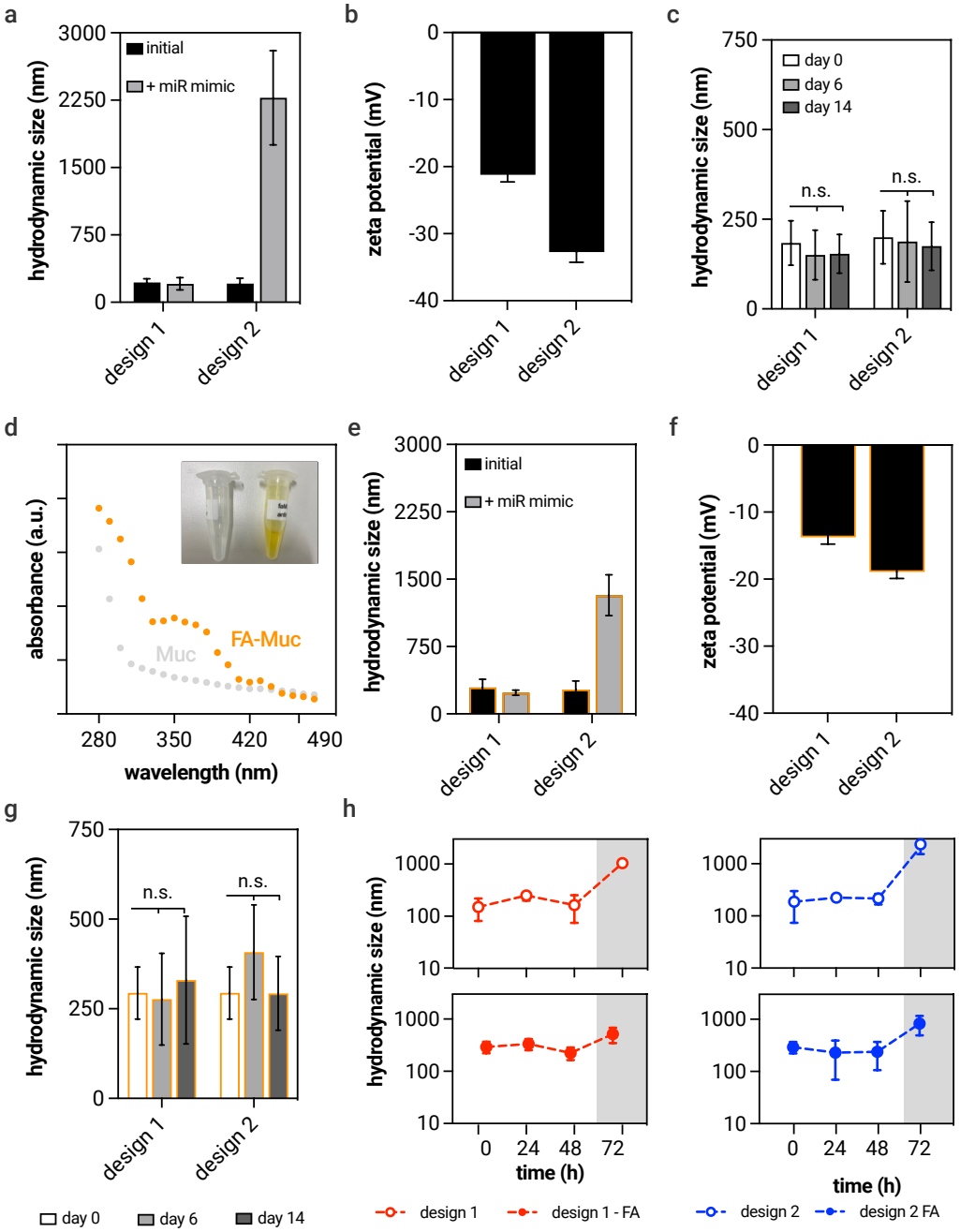

Figure 5.7: DLS measurements indicate that the miRNA-sponge NPs keep their shape when incubated with miRNA-mimic, whereas the transient NPs are triggered to destabilize (n = 5) (**A**). ζ-potential measurements of mucin NPs stabilized with one of two sets of DNA design (n = 3) (**B**). Both NP species are stable under storage conditions for 14 days (n = 5) (**C**). Folic acid conjugation to mucin glycoproteins as detected by a characteristic peak at 358 nm using a spectrometer (**D**). DLS measurements performed with folic-acid conjugated mucin NPs stabilized with one of two sets of DNAs (n = 5) (**E**). ζ-potential measurements of FA-conjugated mucin NPs stabilized with sets of DNA design (n = 3) (**F**). Both FA-conjugated NP species are stable under storage conditions for 14 days (n = 5) (**G**). Hydrodynamic size stability of mucin NPs in 10% FBS at 37 °C. Grey zones indicate where the size significantly deviates from the initial NP size (n = 5) (**H**). Data shown represents mean values, error bars denote the standard deviation.

Furthermore, when interacting with cell surface receptors, folic acid (and accordingly, the molecule it is conjugated to) is transported into the cytoplasm, which is advantageous compared to targeting a membrane marker that is not internalized into the cystosol [224]. To target the folate receptors of HeLa cells, folic acid was conjugated to the amine groups of mucins *via* carbodiimide chemistry, and the conjugation efficiency was spectrometrically determined as (40 ± 4) % (**Fig. 5.7 D**).

Having shown the efficient conjugation of folic acid to mucin glycoproteins, next, a set of NPs was prepared using such folic acid-mucin conjugates. Although the NP size was now found to be slightly larger (282 ± 87 nm) compared to the unmodified mucin NPs, a similarly strong increase upon miRNA-exposure could be observed for the transient NPs (**Fig. 5.7 E**). The zeta potential values of the NPs were in the negative regime, however, in the range of – (13 – 18) mV and thus less anionic than for unmodified mucin NPs (**Fig. 5.7 F**). This effect can be explained by the presence of positively charged groups in the folic acid structure. Notably, also folic acid modified NPs did not spontaneously degrade at storage (*i.e.*, stagnant conditions at 4 °C) over 14 days (**Fig. 5.7 G**). Importantly, neither particle species showed a significant sign of disintegration/aggregation propensity when incubated in 10 % FBS at 37 °C for 48 h (**Fig. 5.7 H**). These results together indicate that the NPs would not tend to instantly lose their stability when encountering a biologically relevant environment.

Having confirmed the functionality of the antimiR sequences and that these sequences can stabilize NPs in both, storage and biologically relevant environmental conditions, putative cytotoxic effects of the FA-conjugated NPs on target and off-target cells were investigated using a WST-1 assay. The WST-1 assay is based on the colorimetric detection of the conversion of the tetrazolium salt WST-1 to formazan by mitochondrial dehydrogenase activity, which directly correlates to the number of living cells. In the tested range, *i.e.*, 3.8×10^5 – 6×10^6 NP/mL, both NP types induced a slight reduction in the viability of the target (HeLa) cells in a concentration-dependent manner (**Fig. 5.8 A**). This effect was less evident with the off-target (NIH/3T3) cells when they were incubated with the miR-21 sponge NPs (design 1). Importantly, no apparent toxic effect on off-target cells was observed with the transient NPs (design 2). This effect can be related to the fact that two designs may require different threshold miRNA overexpression levels to deplete the target miR-21. For further *in vitro* tests, a dose of 3×10^6 NP/mL was selected since this concentration did not induce a remarkable viability reduction in off-target cells.

Selectively targeting the cell type of interest is crucial to avoid a depletion of the target RNA from the off-target cytosol. To check whether the folic acid functionalization has such an effect of cellular targeting through folate receptors, both cell groups were incubated with fluorescently labeled NPs and then analyzed using a flow cytometer in terms of their NP uptake efficiency (**Fig. 5.8 B**). Indeed, for all the tested time points (1 h, 4 h, and 24 h), the geometric mean fluorescence intensity (GMFI) indicating the NP uptake was significantly higher for the target cells compared to that of off-target cells. No remarkable difference was detected between the two NP

types in terms of uptake efficiency. This result clearly demonstrated that folic acid functionalization enhanced the targeting of FR-expressing cells.

When actively targeting the FRs, it was expected that the cellular internalization by receptor-mediated endocytosis is the governing mechanism responsible for transporting the NPs into the cytosolic compartments of target cells [225]. To identify the other contributing mechanisms driving mucin NP uptake, the effect of three endocytic inhibitors (*i.e.*, chlorpromazine, filipin, and amiloride) on NP uptake was studied (**Fig. 5.8 C**).

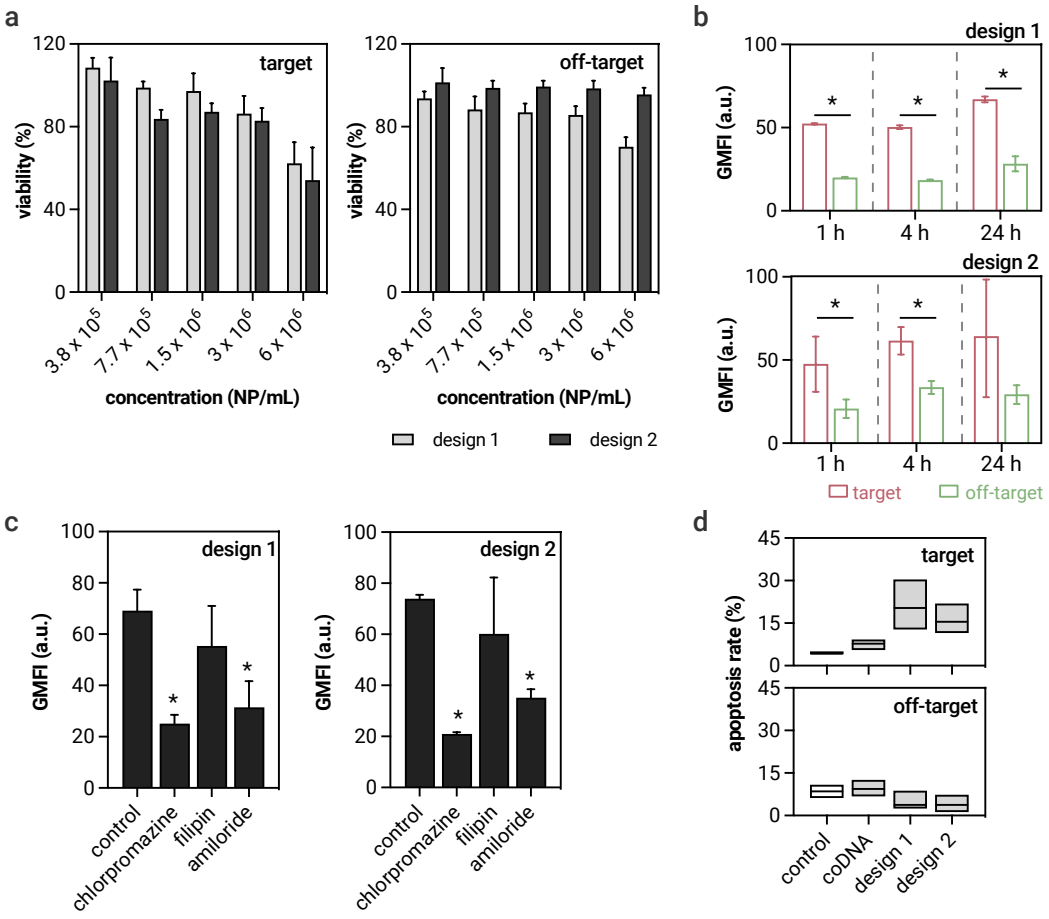

Figure 5.8: *In vitro* viability of target (HeLa) and off-target (NIH/3T3) cells incubated with mucin NP variants for 24 h (n = 6) (**A**). GMFI obtained by FACS evaluation of target and off-target cells incubated with fluorescently labeled mucin NP variants for 1, 4, and 24 h (n = 6) (**B**). Cellular uptake of mucin NP variants in the presence of different uptake pathway inhibitors (n = 6) (**C**). The effect of mucin NP treatment on the apoptosis rate of target and off-target cells after 4 h of incubation (n = 6) (**D**). Data shown represents mean values, error bars denote the standard deviation.

For both nanoparticle species, incubation with chlorpromazine (an inhibitor of clathrin-mediated endocytosis) significantly reduced the uptake of NPs compared to control conditions where no

pathway blocker was used. In the literature, it was reported that the maximum size of NPs undergoing clathrin-mediated endocytosis is ≈ 200 nm [226,227]. Since the NPs produced here cover a size distribution of 140 – 340 nm, it is likely that a fraction of NPs could follow this uptake pathway. Furthermore, incubation with amiloride, a specific inhibitor of the Na^+/H^+ exchange required for macropinocytosis, was also found to significantly reduce the mucin NP uptake for both cell lines. As cells typically take in large volumes of extracellular fluids *via* macropinosomes (which are in size of ≈ 5 µm [228]), it was very likely that NPs were internalized through this pathway as well. In contrast, exposing the cells to the caveolin-mediated transport inhibitor filipin did not significantly affect the NP uptake efficiency. Caveolae are typically 50 – 80 nm in size [228], which is considerably smaller than the average size of NPs used here. These findings were in full agreement with previous research that investigated the mechanisms responsible of mucin-based NP internalization***** [229].

As miRNAs often regulate multiple transcripts, they are involved in various biomolecular processes including protein secretion, metabolism, and cell differentiation [230]. Importantly, the upregulation of miRNA-21 induces a suppression of apoptosis [231]. Thus, to assess whether antimiR therapy with mucin NPs can restore natural cell death, in the next step, a PI/Annexin V double staining was applied to test for cellular apoptosis using a flow cytometer. The Annexin V signal allows for the detection of cellular apoptosis while propidium iodide is used to detect necrotic and late apoptotic cells, a state which is characterized by a loss of integrity of the plasma and nuclear membranes. First, the apoptosis rate, *i.e.*, total number of (early and late) apoptotic bodies over the total number of intact cells, was determined after treating the target and off-target cells with NPs (**Fig. 5.8 D**). When the target cells were analyzed in terms of their apoptotic activities, the control group that did not receive any NP treatment showed an apoptosis rate of (4.4 ± 0.4) % only. However, incubation with mucin NPs stabilized with DNA sequences of design 1 and design 2 significantly increased the apoptosis rate to (17.9 ± 5.5) % and (14.6 ± 2.3) %, respectively. As a control, cells treated with mucin NPs that were stabilized with a control DNA sequence (coDNA) showed a comparable response as the control group (7.6 ± 1.5) %, highlighting that the silencing miRNA sequence is indeed necessary to induce cellular apoptosis. In contrast, none of the NP variants induced apoptotic effects on off-target cells (< 10 %).

The picture obtained with the target population was further examined to gain a better understanding on whether the mucin NPs were successful in inducing apoptosis on the target cell population (See **Fig. 5.9 A** for the exemplary samples, and **Fig. 5.9 B** for the average values obtained from $N = 3$ biological replicates per group, and 6 separate wells were analyzed for each group per replicate). More than 94 % of the total population of the control group (group that did not receive any treatment) were found to be viable where the rest of this population was distributed as < 3 % early apoptotic, < 2 % late apoptotic and < 1 % necrotic (**Fig. 5.9 B**). Similarly, treatment with nanoparticles that were stabilized with non-therapeutical DNA crosslinkers

***** There, covalently crosslinked mucin nanoparticles were studied which had hydrodynamic sizes in the range of 60 – 300 nm.

(coDNA) did not induce a remarkable change in the population distribution as > 90 % viable, < 6 % early apoptotic, < 2 % late apoptotic, and < 3 % necrotic. However, mucin NPs carrying a therapeutical antimiR sequence led to a substantial enhancement of apoptosis compared to the untreated cells and the cells treated with coDNA (at same NP concentration only after 4 h of incubation): although the percentage of late apoptotic and necrotic cells were similar, the treatment with design 1 and design 2 increased the percentage of the early apoptotic population to 19 % and 14 %, respectively. Thus, blocking miRNA-21 overexpression using mucin NPs that can be selectively taken up by target cell population significantly induced the apoptosis. These findings suggest that silencing miR-21 plays an important role in the suppression of the progression of the malignancies and may become an important target for gene therapy.

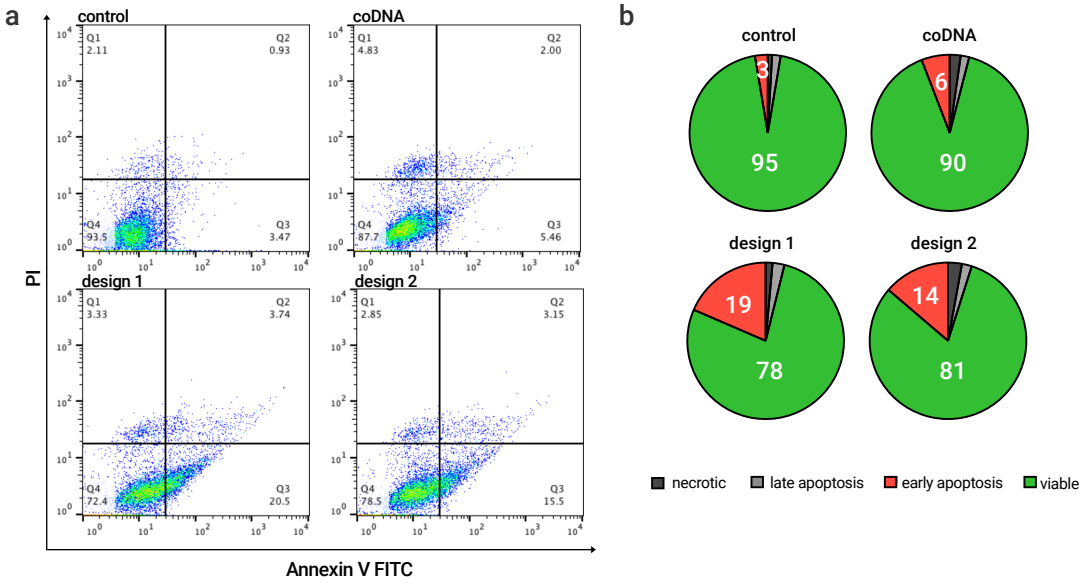

Figure 5.9: Representative flow cytometric analysis of HeLa cells after incubation with mucin NPs stabilized with coDNA, design 1, and design 2 sequences (**A**). Pie charts describing the mean percentage of necrotic, late apoptotic, early apoptotic and viable cells as obtained with Annexin V/PI double staining followed by flow cytometry analysis (**B**). Data shown in the pie charts represents mean values determined from *N* = 3 biological replicates per group (for each group, 6 separate wells were analyzed per biological replicate).

Overall, both antimiR-embedded mucin nanoparticles induced cellular apoptosis only in the target cell group whereas they did not affect the viability of off-target cells. Importantly, a mucin nanoparticle variant comprising a non-therapeutical crosslinker DNA (coDNA) did not show any toxic effect on both, target- and off-target cells, indicating the good cytocompatibility of DNA-crosslinked mucin nanoparticles themselves (**Table 5.1.**).

Table 5.1. Effect of stabilizer DNA sequences when internalized by target and off-target cells.

Design	Target	Off-target
Design 1	Dead	Alive
Design 2	Dead	Alive
coDNA	Alive	Alive

In conclusion, as shown in this chapter, the stabilizing DNA sequences used for mucin nanoparticle crosslinking can be tuned to achieve both a controlled release triggered by externally transfected synthetic DNA strands and by existing cytosolic overexpressed oligonucleotides (**Table 5.2.)**. Furthermore, since the functionality of the mucin nanoparticles is not affected by the attachment of other targeting molecules or further surface coatings, other cell types with known surface markers (*e.g.*, MUC1 overexpression) can be targeted. Thus, depending on the desired function, DNA-stabilized mucin nanoparticles can be tailored to match the requirements for a broad range of pharmacological applications.

Table 5.2. Summary of the features of DNA-stabilized mucin nanoparticles.

Design	Trigger	Transfection requirement	Targeted therapy	Action
Generation 1 (dDNA triggered)	Synthetic displacement DNA	Yes	No	Drug release
Generation 2 (miR-triggered)	Endogeneous miR-21	No	No	Drug release
Generation 3 (miR-triggered + miR-silencing)	Endogeneous miR-21	No	Yes	Silence seed region

6. Outlook

Although medication-based treatment strategies are generally well-standardized, there is considerable variability in the response of patients, which mainly stems from patient-specific factors. In fact, the successful response rate of patients to drug treatments varies between 25 – 80 %; and the lowest response rate was reported for cancer chemotherapies [232]. This dramatic fact mainly arises from the conventional healthcare approach, which is based on an extrapolation from population averages to treat diseases of individuals [233]. As factors such disease progression, presence of other pathological conditions, overall health state and inherited genetic variations are unique to individuals, a personalized healthcare approach may overcome treatment failures due to deviations from the average in patient profiles. Indeed, the realization for a need of customized healthcare dates back to the time of Hippocrates who stated, "*It is more important to know what sort of person has a disease than to know what sort of disease a person has*" [234]. Thanks to advances in molecular biology, medicine, and biomedical engineering, this approach has gained more importance over the centuries, has enabled the development of new therapeutic and diagnostic methods, and has provided a deeper understanding of the pathological conditions and their progression. With the growing sense for why drug therapies fail, the field of controlled and targeted drug delivery has emerged in recent decades as a feasible strategy to address this problem. Here, instead of trial-and-error based methods exploring different drug treatments, rational engineering approaches were developed where the materials (carrying therapeutic cargo molecules) follow a meticulously tailored, predetermined cues to safely and efficiently bring a therapeutical action to the point of interest.

The studies performed in the framework of this thesis aimed at approaching the problem of drug delivery from different aspects: by considering the complex characteristics of the biological site; by leveraging (patho)physiological markers of the point of care to initiate an on-demand release of drugs; and by making use of specific intracellular conditions at the molecular level for the autonomous liberation of cargo molecules from carriers. Accordingly, rational delivery strategies were implemented to the carrier materials to safely bring (a therapeutic level of) cargo molecules across biological barriers, to store these cargo molecules within the carrier structure until they are required to take a therapeutical action, and to liberate them with high efficiency. Furthermore, autonomous systems that comprise logical cues regulated by synthetic control tools were developed to enable an autonomous initiation of the drug release process once a molecular signature condition is present.

In the first chapter, tailored drug carrier materials were developed by considering the heterogeneous conditions of their biological routes and targets. In particular, carrier materials were developed to establish optimized asymmetric properties, such as a combination of high interactions with ocular mucosa (to avoid precorneal clearance) and the capability of traveling across the mucosal barrier (to reach the intraocular lumen). These functions were indeed

necessary to meet the demands of the biological environment which the drug carrier travels through (as in the case of polyelectrolyte complex nanoparticles) or contacts during its lifetime (as for Janus films). By adapting the physical properties of these carrier materials to the specific needs of the target tissues, a needleless administration of therapeutics can be considered, particularly for the pediatric population where injections are major stressors. Overall, these strategies are effective in delivering drugs to or across mucosal layers. Thus, they can help to overcome main disadvantages of existing mucosal drug delivery systems which are often affected by on-site dilution of drugs as well as low permeation efficiency.

Of course, the diseased state of a biological environment deviates from its healthy state, and the level of deviation is often highly specific to the progression of the condition. Therefore, tailoring a delivery system to meet the demands of complex biological environments might be, in some cases, insufficient to treat a target disease. Accordingly, the second chapter of the thesis aimed at developing drug delivery systems that are not only adapted to the target site but also respond to certain (patho)physiological triggers to release their loaded cargo molecules. To respond to certain environmental signature conditions (*e.g.*, physiological salt concentration, temperature elevation, or an increase in the wall shear stress), biopolymer-based materials were developed. Based on the requirements defined by the disease, the occurring environment, or the envisioned administration route, a single-dose drug depot (*e.g.*, shear-sensitive nanogels) or multiple drug depots (*e.g.*, mucin-based multilayer coatings) can respond to specific triggers. Alternatively, by programming the sequential release of substances through DNA strand displacement, the release of individual doses in a pre-determined order and at defined time points was made possible. Especially in the case of drug self-administration (*e.g.*, oral administration of antibiotics, insulin injections), missing a dose or not taking the medications in the prescribed fashion significantly affects the treatment success. Harnessing the high programmability of these stimuli- or self-driven release mechanisms, the efficacy of already existing drug formulations can be improved by delivering them at the right time, at well-defined intervals and over extended time windows. For example, a combination therapy of diabetic can by administrating hemostatic, antibacterial and angiogenic agents at distinct and pre-defined time points would prevent unwanted cross-interactions between different drugs [235].

Furthermore, embedding combination cancer therapies into a single-administration system could potentially reduce the drug resistance while providing therapeutic benefits. When considering that the process of developing a new anti-cancer drug is highly time consuming [236], new efficient drug delivery strategies reducing the need of multiple administrations can be considered as feasible and efficient steps before designing a new drug formulation. For example, a potential application could be to place such a release-cascade embedded hydrogel into the abdominal region of pancreatic cancer patients. As some drugs for the early treatment of peritoneal metastases (*i.e.*, cancer spreading to the peritoneum from other organs) proven to initiate a higher response rate when delivered sequentially [237], their metronomic, well-controlled, local delivery can maximize the therapeutic efficiency.

Although pathological conditions play a significant role in developing stimuli-responsive drug delivery systems, microlevel management is necessary for most intracellular treatments. Although numerous studies make use of certain pathological changes in the environment (*e.g.*, low pH, high temperature), these intrinsic stimuli are not precise enough to gain a high level of control. Especially when highly cytotoxic drugs such as chemotherapeutics are used, the importance of a control mechanism that can distinguish between target and healthy cells is pivotal. The mucin nanoparticles developed in the last chapter of this thesis showed a precise spatial control over the release of (highly cytotoxic) cargo molecules even in the cytosolic environment. In detail, the efficient release enabled by the displacement of oligonucleotides was accompanied by a robust control over the material state (*i.e.*, it provided a structural switch from condensed to elongated). This can protect the neighboring off-target cells and ensures the release of therapeutic molecules at the point of care. Due to positively and negatively charged groups and hydrophilic and hydrophobic domains, mucin-based nanocarriers can be loaded with a wide spectrum of molecules, making various combinational therapies possible for further steps. Notably, modifications applied to mucin nanoparticles (*e.g.*, conjugation of additional functional groups, polymeric surface coatings) do not affect their ability to undergo a conformational change that triggers drug release. Compared to other systems, one of the top features of DNA-stabilized mucin nanoparticles is their strong stability against (physiologically relevant) nuclease levels and environmental pH changes that naturally occur in the different locations of the body. Additionally, once the nanoparticles have completed their task, the remaining mucins and DNA strands can be processed by cell-secreted enzymes, thus leaving only biological byproducts that would also occur otherwise as a result of physiological processes.

Although the use of antisense oligonucleotides has been investigated in the last 20 years for a wide range of diseases, up to now, only one miRNA-based therapy (antimiR-122 therapy to suppress viral replication of hepatitis C) has entered human clinical trials [238,239]. By replacing the synthetic oligonucleotides which stabilize the mucin NPs with a therapeutically functional miRNA-silencing sequence which was attempted here for the first time, a pathological signature condition can serve both as a target and a trigger. Importantly, the tunability of the approach developed here allows for addressing other cancer types as well as other systemic diseases such as obesity and diabetes. However, to recreate a physiologically relevant microenvironment, *i.e.*, cell-to-cell contact and a proper spatial orientation of tissues, 3D models made of co-cultured target/off-target cells could be a reasonable intermittent step before translation to *in vivo*.

Of course, the perspectives discussed here should not only be considered as separate approaches. For example, a combination of NPs with different stability levels (or different crosslinks responding to separate trigger conditions) can be used as a first step to deliver disruptive agents to physical barriers (for example, those generated by cancer-associated fibroblasts) [240]. Then, a second set of NPs can deliver drugs to the tumor that is now stripped of its thick barrier, which otherwise would complicate the delivery process. Alternatively, combining controlled delivery cues with DNA-stabilized nanoparticles might enable the construction of dynamic architectures

which can rationally interfere with the metabolic activities at the sub-cellular compartments in an orchestrated manner [241]. For example, the release of lysosome-targeting nanoparticles followed by a mitochondria-targeting variant can enable the restoration of some physiological functions involved in the regulation of cellular events that are dysfunctional as a result of various pathological processes. As discovered recently, mammalian cells have evolved to repurpose viral retroelements in their genome to shuttle specific nucleic acids to neighboring cells [242]. Therefore, some of those retroelement-derived proteins may be harnessed to interfere with intercellular communication by amplifying or silencing nucleic acids, thus, providing new routes for therapeutics.

Furthermore, the delivery strategies presented here can be promising candidates for diagnostics, and combined diagnosis/treatment approaches. For example, the implementation of DNA strand displacement mediated logic gates has recently been found successful for developing cell-free biosensors which can detect various targets such as ions [243], pathogenic microorganisms [244], ATP [245], and viral DNA [246]. These logic operators can be engineered as disease assessment tools to respond to multiple conditions. For example, a DNA-based logic gate successfully detected the combined overexpression and downregulation of selected miRNA targets, which returns a positive signal for a malignancy and initiated the drug release [87].

Last but not least, many possibilities for future applications come to mind: in addition to searching for specific trigger conditions as discussed throughout this thesis, collecting personalized information from biological samples can help researchers to identify patterns in the disease development for further use as marker conditions. For example, fecal sampling might identify compositions of gut microbiome that contribute to diseases such as obesity; or collecting blood samples might enable the detection of circulating tumor cells or cancer-associated oligonucleotides that permit early detection of cancer [247]. Thus, by gathering a large scale of patient-specific information, developing a library that relates pathological conditions to the occurring diseases will be an important step for identifying unrevealed patterns and for planning personalized delivery strategies.

The conceptual strategies designed in this thesis showed that a precise control over targeted drug release is possible by engineering smart drug delivery systems. Although delivering drug molecules to a target location at the right time while ensuring a therapeutical function is still a complex task, it is by no means insurmountable. The wide range of stimuli able to trigger drug release at the right place and time, and the diversity of responsive materials that can be assembled into different architectures allow for great flexibility in the design of responsive carrier systems. However, translating these strategies from bench to bedside requires a broader view, including significant aspects such as the biodistribution propensity and the *in vivo* performance of the materials. Indeed, the *in vivo* performance of such materials still lacks an assessment gathered from multiple perspectives, and is typically limited to late readouts (such as the histological evaluation of tumor biopsies). Imaging technologies still have some restrictions regarding overlapping spectral bandwidths or poor light penetration into tissues [248], limiting the molecular

assessment of the therapeutic activity. The development of advanced tissue clearing and imaging technologies are the promising next steps to analyze the success of smart drug treatment strategies on intact organs at a single cell level [249]. By employing such a post-therapy assessment, targeted delivery strategies could be applied not only after the onset of certain pathological levels but even at early stages of disease progression.

While there is a great potential for designing smart drug delivery mechanisms with great precision, critical optimizations are necessary to ensure the function of a nano-size tailored material at whole organism. By successfully addressing biological barriers and biomolecular mechanisms in a controlled fashion, smart delivery strategies will indisputably represent an important modality within therapeutic and diagnostic applications, shaping the future of personalized medicine.

Appendix

Appendix A1: Additional methods

1. **Mucin purification**

Porcine gastric mucin MUC5AC was purified manually by following the protocol described in the reference with slight modifications [55]. First, mucus from pig stomachs was collected by gently scraping the inner surface of the gastric tissue, diluted 5-fold in 10 mM sodium phosphate-buffered saline (PBS, pH = 7.0) containing 170 mM NaCl and 0.04 % sodium azide (Carl Roth, Karlsruhe, Germany), and stirred at 4 °C overnight. Cellular debris was removed *via* basic filtration using a tea filter followed by ultracentrifugation (150,000·g at 4 °C for 1 h). Next, mucins were separated by size exclusion chromatography (SEC) using an ÄKTA purifier system (GE Healthcare, Munich, Germany) equipped with an XK50/100 column packed with Sepharose 6FF (GE Healthcare). The obtained mucin fraction was collected, NaCl concentration was increased to 1 M, and dialyzed against ddH_2O. The dialyzed mucin samples were concentrated by crossflow filtration (Xampler Ultrafiltration Cartridge, GE Healthcare; MWCO: 100 kDa). The resulting concentrate was lyophilized and stored at -80 °C until further use (**Fig. A1**).

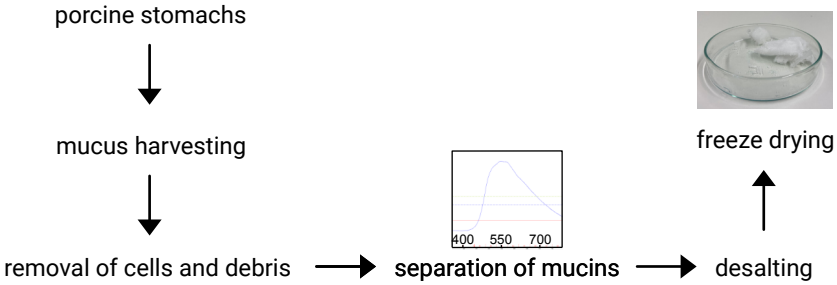

Figure A1: Purification steps of mucins harvested from porcine stomachs. After harvesting the crude mucus manually from the tissue surfaces, the cellular debris and coarse impurities were removed. After separation from other macromolecules *via* size exclusion chromatography, mucins are desalted, concentrated, and lyophilized to obtain a protein powder to be stored at – 80 °C.

2. **Polyacrylamide gel electrophoresis**

Polyacrylamide gel electrophoresis (PAGE) was employed to demonstrate binding interactions between mucins and thiolated crosslinker DNA strands. As a control, a similar DNA sequence but without thiol-modification was used. As a preparatory step prior to gel electrophoresis, 100 mM crDNA was incubated in the presence of 500 mM dithiothreitol (DTT) and 0.5 mM tris-(2-carboxyethyl)-phosphine hydrochloride (TCEP, Carl Roth, Karlsruhe, Germany) at room temperature (RT) for 2 h. Then, purified mucin was added to the DNA solution to a final mucin

concentration of 0.1 mg/mL and incubated overnight. The next day, 6× sample loading buffer (Sigma-Aldrich) was added, and the samples were loaded onto Mini-PROTEAN TBE Precast Gels (BIO-RAD, Munich, Germany). Electrophoresis was performed at 100 V in 0.5× Tris-Borat-EDTA (TBE) buffer (pH 8.0) containing 5 mM DTT. DNA staining was conducted by incubating the gel with an SYBR Safe solution (Sigma-Aldrich) in 0.5x TBE buffer for 1 h. Pictures were recorded on a Molecular Imager Gel Doc XR System (BIO-RAD). Protein bands were visualized by staining the gel with a Coomassie staining solution overnight, and gel imaging was conducted after destaining the gel with a 10% acetic acid solution.

3. **Quartz crystal microbalance (QCM-D)**

The adsorption properties of mucin multi-layers (as described in the chapter *4.2 Stimuli-responsive coatings liberating cargo molecules from depots upon two independent triggers*) on hydrophobic PDMS surfaces were studied by quartz crystal microbalance with dissipation monitoring (QCM-D) using a qcell T-Q2 platform (3T-Analytik, Tuttlingen, Germany) as described previously [196]. Since QCM-D is a very sensitive technique to detect adsorbed molecules [250], lower biomolecule concentrations were used here for conducting the coating process *in situ:* mucin (0.2 mg/mL) and lectin (0.1 mg/mL) solutions were prepared in 20 mm HEPES buffer (pH = 7.4). A dopamine solution (4 mg/mL) was prepared in 50 mm Tris buffer (pH = 8.5). Layers were formed by injecting the test solutions into the sample chamber and keeping them there for ~30 min each to allow for adsorption onto PDMS-coated Au chips. Chips were rinsed with HEPES buffer (pH = 7) for 2 min before injection of the next solution.

4. **Scanning Electron Microscope (SEM)**

The morphology of the materials was observed using Scanning Electron Microscopy (SEM, JEOL-JSM-6060LV, Jeol, Eching, Germany). Before analysis, a thin ~10 nm thick gold layer was sputtered onto the material under Argon gas using a MED 020 supper device (BAL-TEC, Balzers, Liechtenstein). To analyze the material properties such as diameter (of nanoparticles), thickness (of films), and mesh size (of nanofibrous mats), an average of 200 individual spots were evaluated from high magnification SEM images by using the software ImageJ.

5. **Atomic Force Microscopy (AFM)**

The morphology of mechanosensitive nanogels (*4.3 Shear-sensitive nanogels that deform upon contact with lumen obstruction*) and mucin nanoparticles (*5.1. Intracellular drug release from DNA-stabilized mucin nanoparticles via controlled strand displacement reactions)* were determined using NanoWizard II atomic force microscope (JPK Instruments, Berlin, Germany using an OMCL-AC160TS-R3 cantilever (Olympus, Tokyo, Japan) in air tapping mode at RT. Before imaging, the AFM was thermally equilibrated for 30 min. A 20 µL drop of the sample solution was pipetted onto a freshly cleaved mica slide, incubated for 5 min, and then rinsed with ddH2O and dried with

compressed air. From the obtained height images, representative cross-sectional profiles were analyzed using the SPM image processing software (v.3.3.20, JPK).

6. **Light profilometry**

To perform a topographical assessment whether the JFs leave any residues or surface damage on wet tissues, *ex vivo* porcine cornea samples were selected. In detail, each sample was evaluated before and after having been in contact with the adhesive side of a JF for 3 days.

After eliminating the eye samples which exhibited visible, macroscopic defects, profilometric images of the corneal surfaces were obtained using a laser scanning microscope (VK-X1000, Keyence, Oberhausen, Germany) equipped with a 20× lens. Image quantification was then performed using the µsoft analysis extended software (version 7.2.7568, NanoFokus AG, Oberhausen, Germany). Prior to data analysis, a Gaussian filter (according to ISO 16610–61) with a cutoff wavelength of 80 µm was applied. For each topographical image, the following metrological parameters were calculated: the root-mean-square height (S_q), the developed interfacial area ratio (S_{dr}), the isotropy of the surface (S_{tr}), the maximum peak height (S_p), the root mean square gradient (S_{dq}), the arithmetic mean peak curvature (S_{pc}), the peak material volume (V_{mp}), and the dale void volume (V_{vv}); those parameters are all defined in ISO 25178-2. From those assessments, the set of eye samples was further narrowed down by eliminating those which showed noticeable microscopic defects; in detail, those samples that returned a surface roughness parameter (S_q) smaller than 0.3 µm were selected. With this procedure, it could be ensured that the population of cornea samples had comparable, well-defined initial properties. Then, JFs were placed onto the hydrated surfaces of the cornea samples, and the eyes were immersed in STF (supplemented with 0.2% TCL) at 4 °C for 3 days until the bilayer films were fully degraded. As a control, similar incubation conditions were applied to a control group (eye samples without any JF treatment). After 3 days of incubation, profilometric images were acquired again, and the same metrological parameters described above were calculated to quantify the effect of bilayer film treatment. To compare the surfaces of untreated and bilayer film-treated cornea tissues, the following additional metrological parameters (which are also defined in ISO 25178-2) were used:

- The maximum peak height (S_p): This parameter describes the height of the highest peak within the analyzed area.

$$S_p = \max z(x, y) \tag{A.1}$$

- The root mean square gradient (S_{dq}): This value represents the root mean square of slopes determined at all points in the analyzed area.

$$S_{dq} = \sqrt{\frac{1}{A}\iint_A \left[\left(\frac{\partial z(x,y)}{\partial x}\right)^2 + \left(\frac{\partial z(x,y)}{\partial y}\right)^2\right] \mathrm{dxdy}} \tag{A.2}$$

- The arithmetic mean peak curvature (S_{pc}): This parameter quantifies the arithmetic mean of the principal curvature of the peaks on the surface.

$$S_{pc} = -\frac{1}{2}\frac{1}{n}\sum_{k=1}^{n}\left(\frac{\partial^2 z(x,y)}{\partial x^2}\right) + \left(\frac{\partial^2 z(x,y)}{\partial y^2}\right) \quad \text{(A.3)}$$

- The peak material volume ($V_{m(p)}$): This value represents the material volume of peaks at an areal material ratio of p = 10 %.

$$\text{Vm (p)} = \int_0^p \big(z(x) - z(p)\big)dx \quad \text{(A.4)}$$

- The dale void volume (V_{vv}): This value represents the void volume of dales at an areal material ratio between p = 80 % and 100 %.

7. **Surface coating process for other polymers**

The ion exchange mechanism applied to mucin layers (as described in the chapter *4.2 Stimuli-responsive coatings liberating cargo molecules from depots upon two independent triggers*) was implemented in the other macromolecular layers with slight modifications.

CM-dextran: CM-dextran coating was performed similarly to mucin-coating as described in the *Materials and methods* section, only by replacing mucin solution with 1% (w/v) carboxy-modified dextran (150 kDa, TdB Consultancy, Uppsala, Sweden) solution.

Chitosan: The coupling reaction was performed as described in the *Materials and methods* section except for the last step: After the carboxyl groups of the silanes were activated, the EDC-NHS solution was replaced by 2 % acetic acid containing 0.1 % (w/v) of chitosan (95/3000, Heppe Medical Chitosan GmbH, Halle, Germany) and stored at 4 °C overnight. Amine groups of the chitosan macromolecule were then allowed to react with the EDC-activated silane groups to form a stable covalent bound. Afterwards, the surface-bound chitosan layer was incubated with 0.5 mg/ml of TCL at 4 °C overnight and then condensed by adding a 30 % glycerol solution. To stabilize glycerol-induced compaction, coatings were incubated with 50 mM of $MnSO_4$ for 1 h to stabilize the compacted layer.

Poly-L-lysine: PDMS preparation and surface activation was performed as described before. Then, an azide-modified surface was generated by covalently bonding 6-azidosulfonyl-hexyltriethoxysilane (ASH-TES, abcr GmbH) to the activated surface. To do so, ASH-TES was diluted to 0.13 % (v/v) in methanol, and acetate buffer (pH = 4.5) was slowly added to obtain a 3:1 (MeOH: HOAc) solution with a final ASH-TES concentration of 0.1 % (v/v). The ASH-TES solution was then transferred into the cuvettes and allowed to react at 60 °C for 5 h. Afterwards, the samples were washed in 80 % ethanol for 1 h and placed in an oven at 60 °C for 1 h. To coat this surface with another polycationic molecule, an end-functionalized alkynyl-poly(L-lysine hydrobromide)

molecule (aPLL, Alamanda Polymers) was used. To covalently attach aPLL to the PDMS surface, 1,3-dipolar cycloaddition is used. Here, a mixture of 1,4-diazabicyclo-[2,2,2]-octane (DABCO), glacial acetic acid (AcOH), and Cu(I) ions is prepared according to Sarode *et al.* [251]. Therefore, 0.03 mmol copper sulphate pentahydrate (CuSO4 x 5H2O), 0.12 mmol sodium ascorbate (NaAsc), and 0.06 mmol 1,4-diazabicyclo[2.2.2]octane (DABCO, Carl Roth) were dissolved in 2 ml ddH_2O. Then, 0.06 mmol AcOH was added to the mixture, and 5 mg aPLL was added to this solution to obtain an aPLL concentration of 0.1 %. As before, the reaction was allowed to occur at 4 °C overnight. The surface-bound PLL layer was incubated with TCL solution (0.5 mg/ml) at 4 °C overnight and was condensed by adding a 30 % glycerol solution. Afterwards, 50 mM of $MnSO_4$ was added to stabilize the condensed layer, and the system was allowed to incubate for an additional 1 h.

8. **Tribological measurements**

For friction measurements, a commercial shear rheometer (MCR 302, Anton Paar, Graz, Austria) was equipped with a tribology unit (T-PTD 200, Anton Paar), and the measurements were performed using a ball-on-cylinder geometry. As friction partners in this tribology setup, PDMS cylinders and steel spheres with a diameter of 12.7 mm (1.4301, S_q < 0.2 µm, Kugel Pompel, Vienna, Austria) were chosen. This material pairing is common in biotribological studies. It was selected as it approximates a hard-on-soft interface as it frequently occurs in the human body (*e.g.*, between tongue and palate or between an implant and tissue). Pins were generated with a diameter of 6.2 mm by mixing PDMS (SYLGARD 184) in a 10:1 ratio with the curing agent and exposing the mixture to vacuum for 1 h to remove air bubbles. The mixture was then filled into a custom-made aluminum mold before curing the silicone at 80 °C for 1 h and tempering the samples at 100 °C for another 2 h. The specimens were cleaned with 80 % ethanol and ultrapure water before experiments.

To evaluate the mechanical robustness of the Janus films (as described in the chapter *3.2 Multifunctional bilayer films for unidirectional drug release into wound tissue*) under tribological stress, they were probed in an oscillatory tribology setup as described in Winkeljann *et al.* [252] and subsequently examined optically. Here, both counterparts of the setup, *i.e.*, PDMS pins in the measuring head and kidney-shaped PDMS samples in the sample holder, were cast in custom-made molds, activated by exposure to atmospheric plasma in a SmartPlasma2 oven (plasma technology GmbH, Herrenberg, Germany; settings: 0.4 mbar, 30 W, 1.5 min) to become hydrophilic [253], and stored in ddH_2O until further use to avoid hydrophobic recovery [253,254]. d-HA and bilayer films were obtained as circular samples (Ø = 10 mm) and were first hydrated *in situ* by applying each onto a pre-wetted kidney-shaped PDMS sample. Then, PBS (40 µL) was added as a lubricant, and the friction response of the material pairing was recorded every 0.15 s in oscillatory mode (deflection angle, 17°; normal load, F_N = 0.6 N; sliding velocity, 0.7 mm/s; temperature, 37 °C). With those parameters, the resulting contact pressure is ≈ 0.028 MPa. A moisture trap was installed to avoid evaporation of the lubricant and film drying. As control samples, plasma-activated PDMS specimens were probed without any film (using PBS as a lubricant).

To evaluate the lubricity of mucin coatings (as described in the chapter *4.2 Stimuli-responsive coatings liberating cargo molecules from depots upon two independent triggers*), measurements were performed at a constant normal load of $F_N = 6$ N, which resulted in contact pressure of ≈ 0.31 MPa[255]. The coefficient of friction was determined at a sliding velocity of ≈1 mm/s; at this speed, and with the steel-on-PDMS pairing, boundary lubrication occurs[256]. Before measuring, the system was allowed to stabilize at ≈ 700 mm/s for 30 s. 600 µL of lubricant (20 mM HEPES buffer, pH = 7) was used for each measurement.

9. **miRNA expression levels**

Isolation of miRNA*:* MicroRNA (miRNA) was isolated from cells using the commercial High Pure miRNA Isolation Kit (F. Hoffmann-La Roche AG, Basel, Switzerland). For each isolation, ~10^6 cells were used. In brief, the cells were lysed by adding 150 µL of 20 % lysis buffer and passing the cell suspension 10x through a sterile 20-gauge needle (Ø = 0.9 mm, Sterican; B. Braun SE, Melsungen, Germany). For the isolation of small RNA (<100 nucleotides), the 2-column protocol provided by the manufacturer was followed. The RNA was eluted in PCR-grade water and immediately frozen at -80 °C. The purity of the isolated RNA was checked using a NanoDrop 2000c spectrophotometer (Thermo Fisher Scientific, Waltham, MA, USA).

cDNA synthesis*:* The isolated small RNA was reverse transcribed into single-stranded cDNA using the High Capacity cDNA Reverse Transcription Kit (Thermo Fisher Scientific). Per 20 µL reaction, 200 ng of isolated RNA was used. In brief, the RNA was mixed with the provided reverse transcription buffer, dNTPs (0.25 mM each), MultiScribe™ reverse transcriptase (50 U μL^{-1}), nuclease-free water, and suitable primers according to the manufacturer's specifications. Stem-loop primers (Invitrogen, Thermo Fisher Scientific) specific for miR-21 (*i.e.*, the gene of interest) as well as U6 (*i.e.*, the housekeeping gene) were designed as specified by Chen *et al.* [85] (**Table A1**).

The transcription reaction was performed in a three-step procedure: first incubation at 25 °C for 10 min followed by incubation at 37 °C for 2 h, and incubation at 85 °C for 5 min. The amounts of generated cDNA were quantified using a NanoDrop 2000c spectrophotometer, and the cDNA was stored at -80 °C until further use.

Detection of miRNA-21 expression levels*:* Following cDNA synthesis, the differences in the miR-21 expression levels between different cell lines (or in one cell line before and after administration of mucin nanoparticles) were quantified using real-time polymerase chain reaction (RT-PCR). The reaction was carried out using the KiCqStart® SYBR® Green qPCR ReadyMix™ (Sigma-Aldrich, St. Louis, MO, USA) and an 'Mx3005P Real-Time PCR System' (Agilent Technologies, Inc., Santa Clara, CA, USA) according to the manufacturer's specifications. In brief, 5 µg of the synthesized cDNA were mixed with 10 µL 'KiCqStart® SYBR® Green ReadyMix™', 1.8 µL of the primer mix (containing forward and reverse primers; final concentration: 300 nM), and nuclease-free water to a final volume of 20 µL per reaction.

For RT-PCR, the reactions were incubated in the thermal cycler in 8-tube PCR strips (Thermo Fisher Scientific) at 94 °C for 2 min for initial denaturation, followed by 40 cycles of 94 °C for 15 s and 60 °C for 1 min. Dissociation from 65 to 95 °C was conducted to confirm the specificity of the amplification products.

U6 was used as an internal control to normalize the expression level of target miRNAs. The relative expression of miR-21 was calculated using the $2^{-\Delta Ct}$ method with $\Delta Ct = Ct_{miR\text{-}21} - Ct_{U6}$. All RT-PCR reactions were performed at least in triplicates (n = 3).

The total RNA content of 2x 10^6 HeLa cells (which overexpress miR-21, target group) grown in a 2D cell culture was harvested in PCR-grade water using the 'High Pure miRNA Isolation Kit' following the 1-column protocol provided by the manufacturer. The amount of RNA in the collected fractions was quantified using a NanoDrop 2000c spectrophotometer, and 2 µg of RNA were incubated with antimiR ssDNA in a mass ratio of 1:1 at 37 °C for 1 h during gentle shaking. As a control, 2 µg of isolated RNA were incubated with PCR-grade water at identical conditions.

Afterwards, these reaction mixtures were subjected to the 2-column protocol described by the manufacturer of the 'High Pure miRNA Isolation Kit' to isolate only small RNAs (<100 nucleotides) in PCR-grade water. To verify the depletion of free miR-21 from the reaction mixture by base pairing with the provided antimir ssDNA strands, cDNA was synthesized as described above (as explained under *cDNA synthesis*) followed by quantification using qPCR as indicated before.

Table A1. Primers used to quantify miR-21 expression levels (Sequences from 5' to 3')

code	sequence from 5'to 3'
miR-21 stem loop	GTCGTATCCAGTGCAGGGTCCGAGGTATTCGCACTGGATACGACTCAACA
U6 stem-loop	GTCGTATCCAGTGCAGGGTCCGAGGTATTCGCACTGGATACGACAAAATA
miR-21 forward	GCCCGCTAGCTTATCAGACTGATG
miR-21 reverse	CAGTGCAGGGTCCGAGGT
U6 forward	CTCGCTTCGGCAGCACA
U6 reverse	AACGCTTCACGAATTTGCGT

Appendix A2: Calibration curves

Standard curves for the molecules were obtained by measuring the absorbances of serially diluted solutions made of tested molecules with a spectrophotometer (specord 210, Analytikjena, Jena, Germany) or spectrofluorometer (Victor 3, Perkin Elmer, Rodgaum, Germany). As a reference, the solvent that was used for dissolving the test molecule was selected and scanned at the same wavelength range. The wavelength at which the tested molecule gives the highest peak was selected for the preparation of a standard curve that relates the absorbance (or fluorescence) values with the concentration. In the concentration range tested, a linear relation between the absorbance (or fluorescence) values and the tested molecule concentration holds. The concentration range where the coefficient of determination (R^2) value over 0.95 acquired was selected to plot the standard curves to determine the concentration of the molecules in a solution with an unknown concentration.

- Standard curves used for the spectro(photo)metric detection of probe nanoparticles and probe molecules

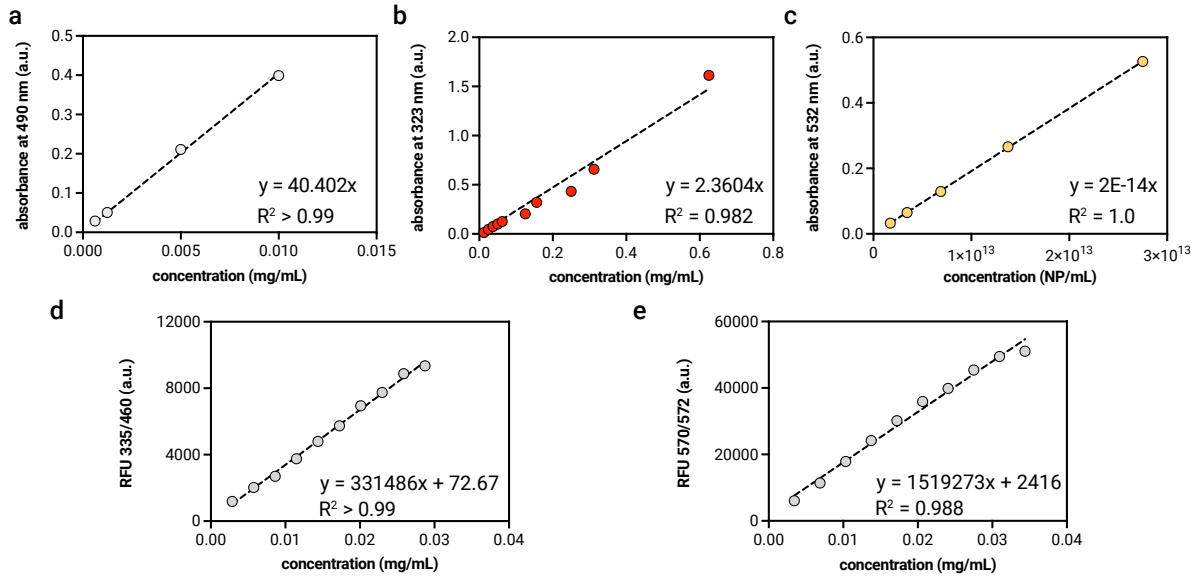

Figure A2: Calibration curves of test nanoparticles: Ag NPs **(A)**, Fe_2O_3 NPs **(B)**, Au NPs **(C)**, and test fluorophores: Atto550 **(D)** and Atto425 **(E)**.

- Standard curves used for the spectrometric confirmation of conjugation of functional molecules to the polymers

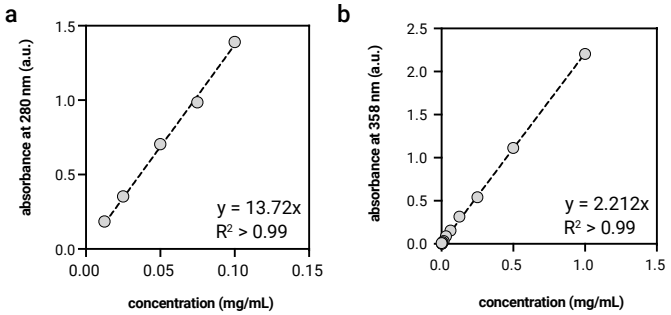

Figure A3: Calibration curves of functional molecules: dopamine standard curve used for the detection of its conjugation to hyaluronic acid (**A**), and folic acid curve used for the detection of its conjugation to mucin (**B**).

- Standard curves used for the spectrometric detection of drug release

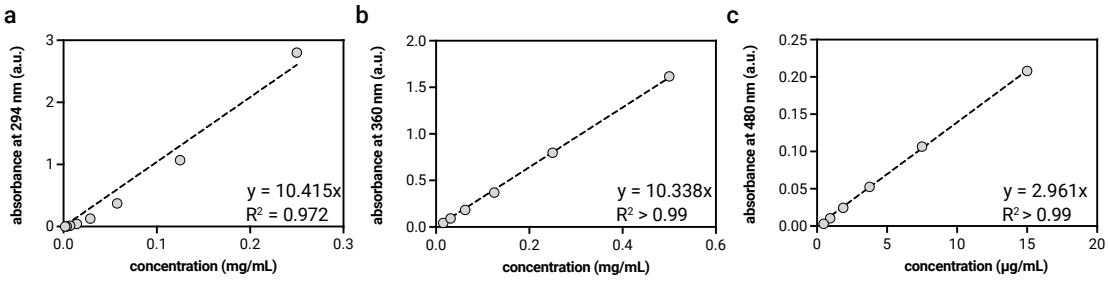

Figure A4: Calibration curves of therapeutically active molecules: timolol maleate **(A)**, tetracycline hydrochloride **(B)**, and doxorubicin hydrochloride **(C)**.

Appendix A3: Oligonucleotide design

1. Engineering a DNA cascade mechanism for sequential delivery of objects

Table A2. Designed oligonucleotide sequences for the release avalanche comprising three NP species.

code	**sequence from 5'to 3'**
$dDNA_2$	TGTACAAACGAATCAGCAAACAGGT
pDNA	TGATGTTTGCTGATTCGTTTGTAGT
brDNA	GCAAACATCAATCTAACTACAAACG
$crDNA_2$	AACGTTTGTAGTTAGATTGATGTTTGCAAA
$coDNA_2$	CCCTTCCCCGCTTCACCCCTATGCC

Table A3. The number of matching base pairs and predicted melting temperatures of different polynucleotide pairings. Values depicted in bold print correspond to DNA pairings used in the experiments described in the main text.

# bps (T_m [°C])	**$coDNA_2$**	**$dDNA_2$**	**pDNA**	**brDNA**	**$crDNA_2$**
$coDNA_2$	2	3	2	3	3
$dDNA_2$	3	6	**20 (69)**	4	8
pDNA	2	**20 (69)**	2	**10 (53.1)**	5
brDNA	3	4	**10 (53.1)**	2	**25 (69.5)**
$crDNA_2$	3	8	5	**25 (69.5)**	**8 (39.1)**

2. Dual stimuli-responsive coatings liberating cargo molecules from depots upon pathological triggers

Table A4. Designed oligonucleotide sequences. The table lists their dimerization energy, melting temperature and the possible number of hybridized base pairs when they interact with crDNA strands.

code	**sequence from 5' to 3'**	**ΔG (kcal/mol)**	**T_m (°C)**	**# of hybridized bp**	**modification at the 5' end**
crDNA	AAAAGAAGCAAAGACAACCCGGGTAA	-18.57	60.6	8	thiol-C6 capped poly(A)- tail
dDNA	TTACCCGGGTTGTCTTTGCTTC	-43.99	75.3	22	-
coDNA	AATGAGCACAACAGAAACGAAG	-3.61	N/A	2	-

3. Autonomous strand displacement reactions triggered by endogenous markers to release drugs from DNA-stabilized mucin nanoparticles

To initiate the drug release in the cells, two set of DNA designs were used in this study. First, for the system where the trigger DNA was supplemented to the cells *via* transfection agents, DNA set described in **Table A4** was used. For the second strategy where the release is autonomously initiated, experiments were performed with the sequences given in **Table A5**.

Table A5. Designed oligonucleotide sequences for the HeLa-cell specific release experiments. The table lists their dimerization energy, melting temperature and the possible number of hybridized base pairs when they interact with antimir-21 strands.

code	sequence from 5'to 3'	ΔG (kcal/mol)	T_m (°C)	# of hybridized bp	modification at the 5' end
antimiR-21	TCAGTCTGATATCA	-10.97	48.2	8	thiol-C6 capped poly(A)- tail
miR-21 mimics	TATCAGACTGA	-15.61	39.0	11	-
coDNA-2	GGAATTCCAAGTG	-1.95	N/A	2	-

4. Targeted miRNA therapy *via* mucin nanoparticles stabilized with gene silencing strands

Here, two different sets of DNA sequences were designed to obtain different mode of actions: The first set of DNA sequences were designed to stabilize mucin NPs that can adsorb excessive miRNA-21 from the environment without initiating a conformational change in the mucin NP structure whereas the stability of the second set of sequences were corrupted by the precense of excessive miRNA-21: Here, NP stability was achieved due to the base pairing interactions between the "miR-silencing" region of the antimiR and bridge DNA. When the cellular miRNA-21 or its synthetic counterpart was incubated with those NPs, a shift in the most favorable structure from bridge-antimiR to miR-antimiR induces a conformational change in the mucin NP structure.

Table A6. Designed oligonucleotide sequences.

abbreviation	sequence from 5'to 3'
design 1 – bridge DNA	TGGTCTAATTTGCGCG
design 1 - antimiR	CGCGCAAATTTCAACATCAGTCTGATAAGCTACGCGCAAATT
design 2 – bridge DNA	CCCTATGTTGACGCTAGCTTA
design 2 – antimiR	GCGTCAACATCAGTCTGATAAGCTAGCG
miR-mimic	TAGCTTATCAGACTGATGTTGA

Appendix A4: Supplementary data

A4.1. Nanoparticles with tunable mucoadhesion properties

- Estimation of the average travel duration of nanoparticles to pass the surface-bound ocular mucins

For sufficiently small molecules and nanoparticles that do not interact with the mucus network in any significant way, the nanoparticle movement can be considered as discrete random walk steps obeying Einstein-Stokes Brownian motion as dictated by:

$$D = \frac{k_B T}{6\pi\mu r} \qquad (A.5)$$

where D is the diffusion coefficient, k_B is the Boltzmann constant, T is the absolute temperature in kelvins, η is the dynamic viscosity and r is the particle radius.

The diffusive travel timespan of an object in a discrete travel distance ($<x^2>$) is related to its diffusion coefficient and the viscosity of the environment as:

$$t = \frac{< x^2 >}{2nD} \qquad (A.6)$$

Considering the viscosity of tear fluid as 0.0044 N·s/m^2 and the hydrodynamic diameter of the CS/A 1:1 NPs (≈ 250 nm), a diffusion coefficient of D = 0.40 µm^2·s^{-1} is obtained [257]. Assuming an average thickness of the surface-bound mucins as ≈ 500 nm, and the two-dimensional diffusion process (n = 2), the travel time for NPs to cross the surface-bound mucins was calculated as 0.16 s.

A4.2. Multifunctional Janus films to combat opposing tasks at the wound – healthy tissue interface

- Unidirectional release and degradation of Janus film in physiologically relevant fluids

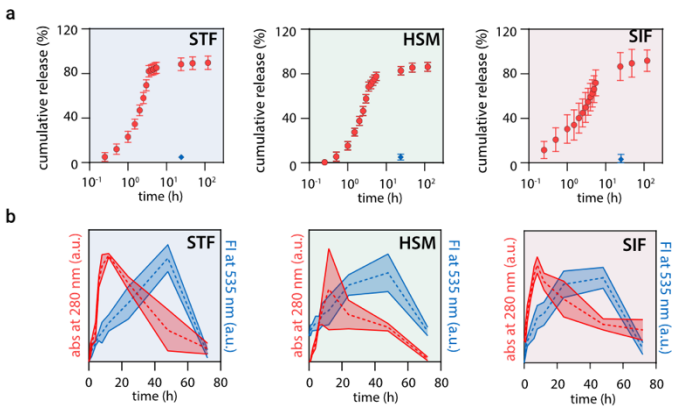

Figure A5: Cumulative drug release from bilayer films immersed in PBS, STF, HSM, and SIF, respectively. Diamond symbols (blue) denote the percentage of drug released into the donor chamber after 24 h (**A**). Degradation profiles of the two individual film layers when placed into physiologically relevant aqueous solutons (*i.e.*, STF, HSM, and SIF, respectively). Blue and red lines correspond to PVA/mucin and d-HA layers, respectively (**B**). Data shown represents mean values, error zones denote the standard deviation as obtained from *n* = 5 independent samples.

- Protein adsorption

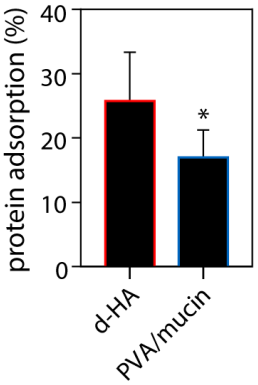

Figure A6: Protein adsorption onto d-HA and PVA/mucin layers. An unpaired t-test was used to detect the statistical significances between the groups. Error bars depict the standard deviation as obtained from *n* = 5 independent samples.

- *In vivo* wound healing performance

Prior to *in vivo* experiments, all film samples were sterilized by ethylene oxide exposure. The experimental protocol of the study was reviewed and approved by the Animal Experiments Local Ethics Committee of Bagcilar Training and Research Hospital (decision number: 2021/116). All procedures were applied according to the guide for the care and use of laboratory animals adopted by the National Institutes of Health (USA) and the Declaration of Helsinki. Tests were performed with Sprague-Dawley rats (body weight, 250 – 350 g, $N = 14$) at the University of Health Sciences, Bagcilar Training and Research Hospital Research Center, Istanbul, Turkey. The animals were housed in a controlled environment at a temperature of (24 ± 2) °C and at a humidity of 60 % under a 12 h light/dark cycle. The animals were given free access to water and standard nutrition. The rats were anesthetized by intraperitoneal administration of ketamine/xylazine (90/10 mg/kg), and all efforts were made to minimize animal suffering. Prior to the experiments, the backs of the rats were shaved; then, two full-thickness skin defects (including epidermis and dermis) were created on the dorsal side of each rat using a 12 mm biopsy punch. One of the such created wounds was covered with a Janus-type bilayer film (either plain or antibiotic loaded, $N = 7$ each), and the defects were covered with a bandage to avoid uncontrolled animal reactions such as scratching or biting. On the 3rd, 7th and 14th day of wound regeneration, a tissue sample was taken from both, the wound areas and a healthy skin tissue area using a 3 mm biopsy punch; those samples were fixed with paraformaldehyde (4 % v/v) and then subjected to further histopathological examinations (**Fig. A7**).

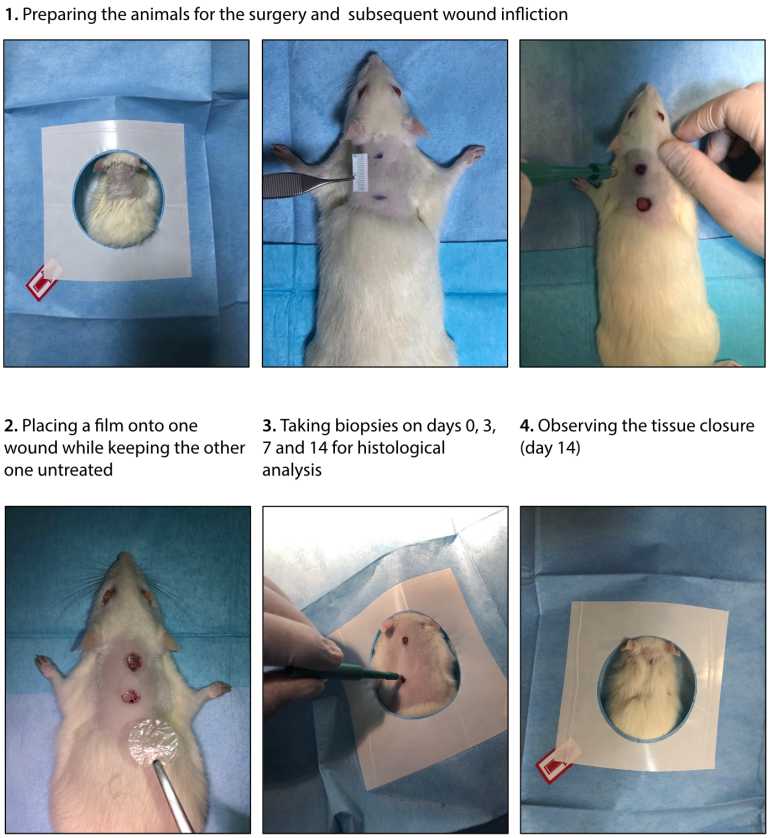

Figure A7: Macroscopic photographs documenting the procedure of the *in vivo* wound healing experiments.

For the histological examinations, 5 µm thick sections from paraffin-embedded tissue samples were stained with Harris hematoxylin/eosin and Masson trichrome (both obtained from Bio-Optika S.p.A, Milan, Italy) using routine procedures and afterwards examined under a light microscope (Olympus BX53, Melville, NY, USA). The maximal epidermis thickness per image, the total number of hair follicles, and the average collagen density per image were calculated using the software ImageJ by analyzing $n = 10$ images per animal ($N = 6$) at each day of observation (day 0, 3, 7 and 14). Findings obtained with film treated samples were compared to untreated wounds and healthy skin tissue using a paired t-test; significant differences were marked with an asterisk if based on a p-value of $p \leq 0.05$.

- Topographical assessment

The metrological parameters were calculated for each group, *i.e.*, for untreated (= control group) and film-treated eyes, and both, before and after 3 days of incubation. The obtained results are compiled in **Table A7** and **Fig. A8**.

Table A7. Metrological parameters used to quantify the effect of bilayer film treatment on the surface integrity of porcine cornea samples. Data shown represent mean values and error bars denote the standard deviation as obtained from *n* = 5 independent samples.

Parameters analyzed		Control group		Film treated group	
		before	after	before	after
S_q	[µm]	0.21 ± 0.06	0.24 ± 0.04	0.16 ± 0.06	0.20 ± 0.04
S_p	[µm]	3.4 ± 1.6	3.1 ± 0.8	2.3 ± 0.9	3.1 ± 0.8
S_{dr}	[%]	0.01 ± 0.01	0.01 ± 0.01	0.002 ± 0.01	0.01 ± 0.01
S_{dq}	[-]	0.11 ± 0.04	0.14 ± 0.04	0.06 ± 0.02	0.12 ± 0.02
S_{pc}	[1/µm]	228 ± 110	281 ± 102	103 ± 63	205 ± 58
V_m	[µm^3 /µm^2]	0.02 ± 0.01	0.02 ± 0.01	0.01 ± 0.01	0.01 ± 0.01
V_{vv}	[µm^3 /µm^2]	0.03 ± 0.01	0.03 ± 0.01	0.02 ± 0.01	0.02 ± 0.01

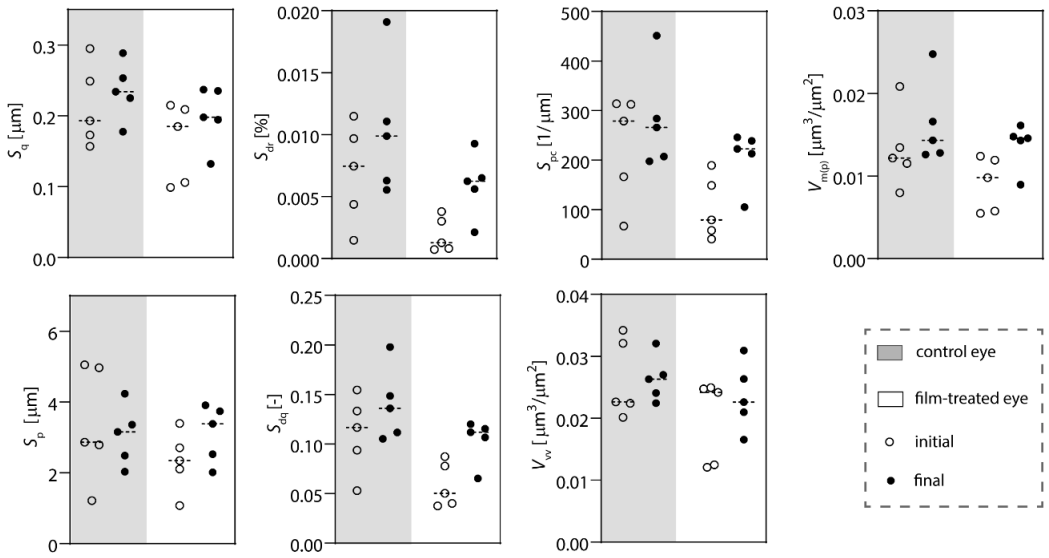

Figure A8: Topographical analyses of eye samples after JF treatment for 3 days. The horizontal lines represent the mean values; open and closed circles represent the average value of N = 5 individual measurements conducted per sample.

A4.3. Engineering a DNA cascade mechanism for sequential delivery of objects

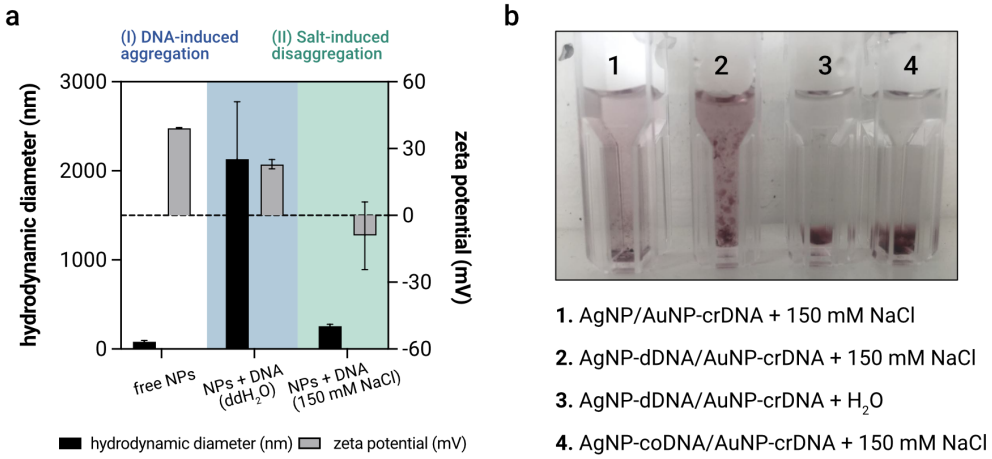

Figure A9: Hydrodynamic size and zeta potential measurements of BPEI-Ag NPs under different environmental conditions. Data shown represents mean values, error bars denote the standard deviation as obtained from *n* = 3 independent samples (**A**). Photographs of different particle – DNA combinations incubated in either H_2O or 150 mM NaCl solution (**B**).

A4.4. Dual stimuli-responsive coatings liberating cargo molecules from depots upon pathological triggers

- Lubrication function

The lubrication abilities of both triggered coatings were virtually identical to those of freshly generated (uncondensed) mucin coatings (**Fig. A10**). This indicated that triggered the drug release processes did not compromise the lubricity of the remaining mucin coating.

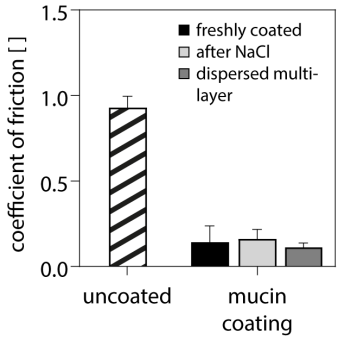

Figure A10: When lubricated with simple buffer solution, the friction coefficient obtained for a steel on PDMS pairing is quite high. However, when the PDMS surface is freshly coated with a mucin layer, the friction coefficient drops by a factor of ≈ 5. Both a decondensed mucin monolayer (first condensed by glycerol and stabilized with Mg^{2+} ions, and then decondensed by exposure to 150 mM NaCl) and a disassembled multilayer system show comparable lubricating properties. Error bars depict the standard deviation as obtained from *n* ≥ 3 independent samples.[†††††]

[†††††] I acknowledge Dr. Benjamin Winkeljann for the tribological measurements.

- Estimating the local drug concentration released from a mucin layer

The local drug concentration that can be achieved in proximity of a mucin-coated surface was estimated by assuming free diffusive spreading of the drug in an aqueous environment (η_{water} = 1 mPa·s). Here, free diffusion mimics the "worst-case scenario" as it describes the fastest possible way drug molecules could escape from the surface of the coating.

For the drug tetracycline (TCL), based on the molecular structure of the molecule, a molecular radius was estimated as 0.5 nm. According to the Stokes-Einstein relation, the diffusion coefficient for a TCL molecule at physiological body temperature of 37 °C (310 K) was calculated.

$$D_{TCL} = \frac{k_B \cdot T}{6\pi \cdot \eta_{water} \cdot r_{TCL}} \tag{A.7}$$

where k_B = 1.380649·10^{-23} J/K denotes the Boltzmann-constant. By further assuming a one-dimensional diffusional escape process orthogonal to the implant surface (d = 1, again mimicking the worst-case scenario), the maximal (average) distance a drug molecule can escape as a function of time t to be R was calculated with:

$$< R(t)^2 > = 2 \cdot d \cdot D_{TCL} \cdot t \tag{A.8}$$

To be able to compare the local drug concentration to a typical systemic dosing applied during the day (*i.e.*, within 6 h), the diffusive escape distance $R(t)$ for t = 6 h was calculated. With the other parameters given above, an average escape distance of R = 1 mm (measured from the surface of the coating) was obtained.

With the mucin monolayer coating, an antibiotic loading capacity on the model surface was calculated as 4.5 µg/mm^2. With this value, the concentration of released TCL in a cuboid volume above the coated surface was estimated to be 180 µg/mL after 6 h.

- Additional QCM-d measurements

The formation of dopamine or lectin crosslinked mucin double layers were indicated by the corresponding shifts in the resonance frequency (**Fig. A11 B**). When the dopamine crosslinked construct was exposed to 150 mM NaCl, the observed frequency shift was fully reversible, *i.e.*, it returned to its initial value when the NaCl was removed by rinsing with water. The transient change in the frequency shift was affiliated to the combination of osmotic and Debye screening effects inducing the conformational changes in the mucin layers and affecting their hydration state. In contrast, a controlled disintegration of the lectin crosslinked structure was possible by exposing the system to a 100 mM GlcNAc solution. Here, the frequency shift did not return to its original value when the GlcNAc molecules were removed by washing.

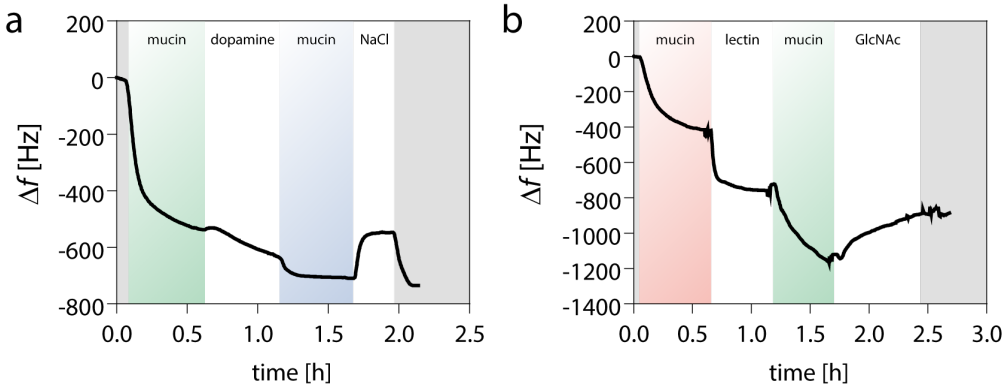

Figure A11: QCM-d measurements showing the layer-by-layer assembly of dopamine (**A**) or lectin (**B**) crosslinked mucin double layers. Grey zones depict time intervals where the system is rinsed with ultrapure water.

- Control drug release experiments

The successful disassembly of the mucin multi-layer by GlcNAc results in a release of TCL from the bottom mucin layer: First, the covalently bound mucin layer was incubated with a TCL solution (0.5 mg/mL) for 2 h to load this layer with the drug. Then, a mucin-based multi-layer (comprising 5 layers, *i.e.*, mucin/lectin/mucin/dopamine/mucin) was generated as described in the *Materials and Methods* section of the main text. The samples were incubated at 40 °C to be consistent with the protocol described before, but without integrating liposomes into the middle mucin layer. The purpose of this control is to show that, *i*) adding the top four layers onto the bottom mucin layers is sufficient to stably trap the TCL in the bottom mucin layer; *ii*) external addition of GlcNAc to the system triggers release of TCL from the bottom mucin layer by lifting off the top layers. Drug release from the multi-layer construct was initiated by adding 2 mL of the trigger solution (150 mM NaCl and 100 mM GlcNAc in 20 mM HEPES buffer, pH = 7.4) to the multi-layer system. The amount of cumulative drug release was determined spectroscopically. As a reference, a multiple layer coating assembled from the same components but without TCL molecules was used. The addition of free GlcNAc induced the release of TCL, which completed after ~1 h (**Fig. A12**).

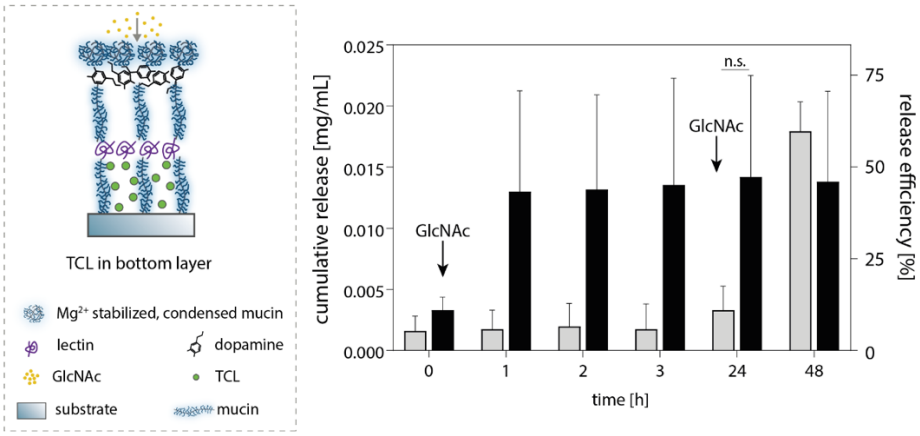

Figure A12: TCL release from the bottom mucin layer of the multi-layer construct triggered by the external supply of GlcNAc. Error bars depict the standard deviation as obtained from *n* = 3 independent samples.

In contrast, in the absence of GlcNAc addition (*i.e.*, if only 150 mM NaCl is used as a 'trigger' solution), only minor leakage was observed. However, when the trigger was added at later time points, *i.e.*, after 24 h of storage, similarly high final release levels occurred as when drug release was triggered at the beginning of the experiment.

The temperature increase triggers lift-off of the top mucin layers by inducing leakage of the embedded thermoresponsive liposomes: Here, the GlcNAc trigger molecules were encapsulated into thermoresponsive liposomes, and those liposomes were embedded into the middle mucin layer of the construct. The purpose of this experiment was to verify the efficiency of drug release from the bottom mucin layer when lift-off of the two upper mucin layers is triggered by a temperature increase that induces GlcNAc leakage from liposomes; as a control, the same multi-layer was constructed, but empty liposomes were added. Both groups were incubated at 37 °C for 24 h. Afterwards, the incubation temperature was increased to 40 °C (which exceeds the phase transition temperature of the liposomes). The temperature driven drug release was then followed spectrophotometrically as described before. For both groups, when incubated at 37 °C, almost no drug release was detected **(Fig. A13)**. However, when the temperature was increased to 40 °C, TCL was released from the samples carrying GlcNAc-loaded liposomes – but not from the control.

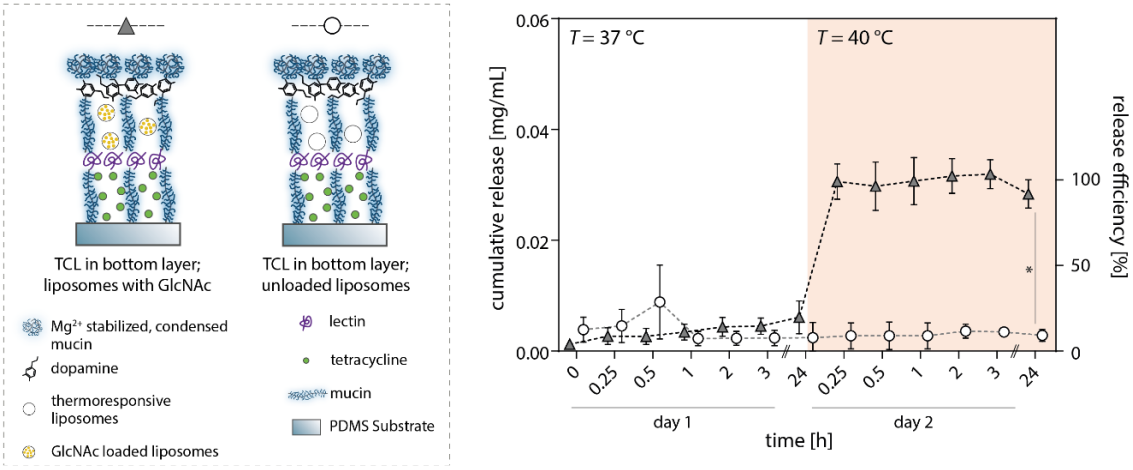

Figure A13: TCL release from the bottom mucin layer of the multi-layer construct triggered by an increase in temperature. Error bars represent the standard deviation as obtained from *n* = 3 independent samples. Asterisks denote statistically significant differences based on a *p*-value of 0.05.

A4.5. Shear-sensitive nanogels that deform upon contact with lumen obstruction

- Adjusting the size of the nanogels

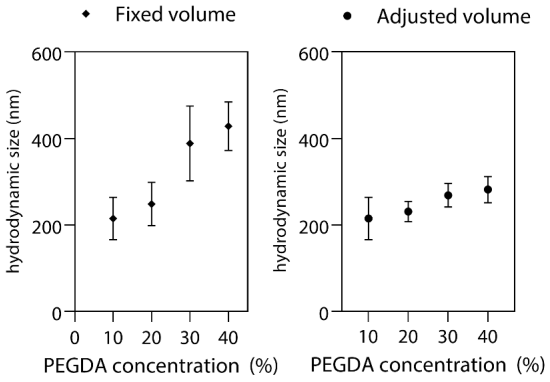

Figure A14: Dynamic Light Scattering (DLS) measurements demonstrate that the nanogel size can be tuned by adjusting the volume of the continuous phase. Data shown represents mean values, error bars denote the standard deviation as obtained from *n* = 5 independent samples.

- Storage stability of the PEGDA nanogels

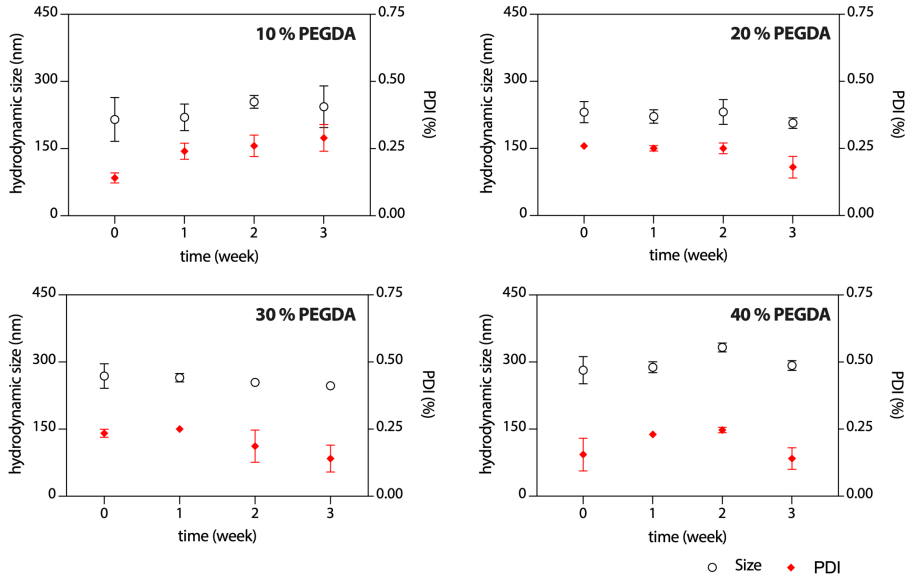

Figure A15: Hydrodynamic size of PEGDA nanogels measured over 21 days at storage conditions. Data shown represents mean values, error bars denote the standard deviation as obtained from *n* = 5 independent samples.

- Computational Fluid Dynamics (CFD) simulations

To find the proper geometries corresponding to pathophysiological-relevant levels of elevated shear stress, the Computer-Aided Design (CAD) software Autodesk Inventor (Autodesk Inc., San Rafael, CA, USA) was employed. These CAD models were then employed to conduct simulative predictions using the Computer Fluid Dynamics software Ansys Fluent (Ansys Inc., Canonsburg, PA, USA) and to produce microfluidic channels (by soft lithography) that mimic stenotic blood vessels.

Blood vessels were modeled as rectangular prisms with a width of 1 mm. This dimension is in the range of vessels found in the human circulatory system. Overall, three different geometries (0 %, 70 %, and 90 % stenosis) were created. The stenosis levels were calculated as follows:

$$\text{stenosis } \% = \left[1 - \left(\frac{w_{\text{stenosis}}}{w_{\text{reference}}}\right)^2\right] \times 100 \tag{A.9}$$

where *w* denotes the width of the channel.

Right after each stenotic narrowing, a wide collection pool was integrated into the channel design to allow for further on-chip analysis (*e.g.*, *via* optical microscopy) of particles that have passed the stenosis. The CAD geometry of the designed channels was imported into the CFD software, and the parameters for the flow simulations were defined according to **Table A8**.

Table A8. Parameters values used to conduct simulations on Ansys Fluent.

Parameter	Value
Fluid density	1000 kg/m^3
Fluid viscosity	1 mPa·s
Element size (mesh)	500 µm
Flow velocity	0.16 m/s

Since the experimental microfluidic tests are intended to be conducted with water, the fluid density and viscosity in the numerical model were chosen to be those of water, *i.e.*, 1000 kg·m^3 and 1 mPa·s, respectively. The walls of the channels were defined to be non-deformable and stationary. In addition, no-slip conditions were selected for the liquid flow at the wall regions. The flow velocity was chosen to be on a similar order of magnitude as blood flux in the human body [258]. All other parameters were kept at the standard configuration. For each simulation, the standard initialization was used; each calculation was run over 50 iterations, after which the solutions converged.

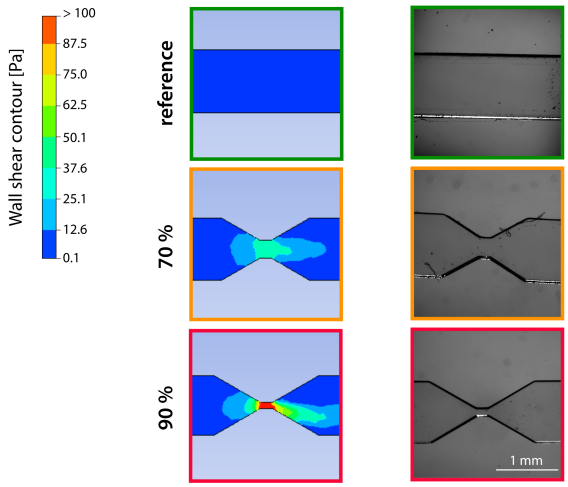

Figure A16: Computational fluid dynamics (CFD) simulations of wall shear stress values in unconstricted (reference), 70 % stenotic, and 90% stenotic channels models (left); brightfield microscopy images of the fabricated microfluidic channels with two different levels of stenosis (right). Scale bars denote 1 mm.‡‡‡‡‡

CFD simulations showed that the wall shear stress significantly increases before the actual stenotic location. In a 70 % stenotic channel, the maximum wall shear stress levels are around 40 Pa; in a 90 % stenotic channel, this value reaches 135 Pa (**Fig. A16**). These values agree well with findings reported for mildly- and critically stenotic blood vessels [24,198] and cover a similar range as the shear stress levels created on a macroscopic level using rheology. Thus, to assess the

‡‡‡‡‡ I acknowledge Bernardo Miller Naranjo for conducting the CFD simulations.

stress-induced disintegration behavior of different nanogel formulations at varying levels of stenosis, a set of unconstricted and constricted microchannels were generated using PDMS-based soft lithography.

- Number of fluorescently labeled nanogels after exposure to stenotic channels

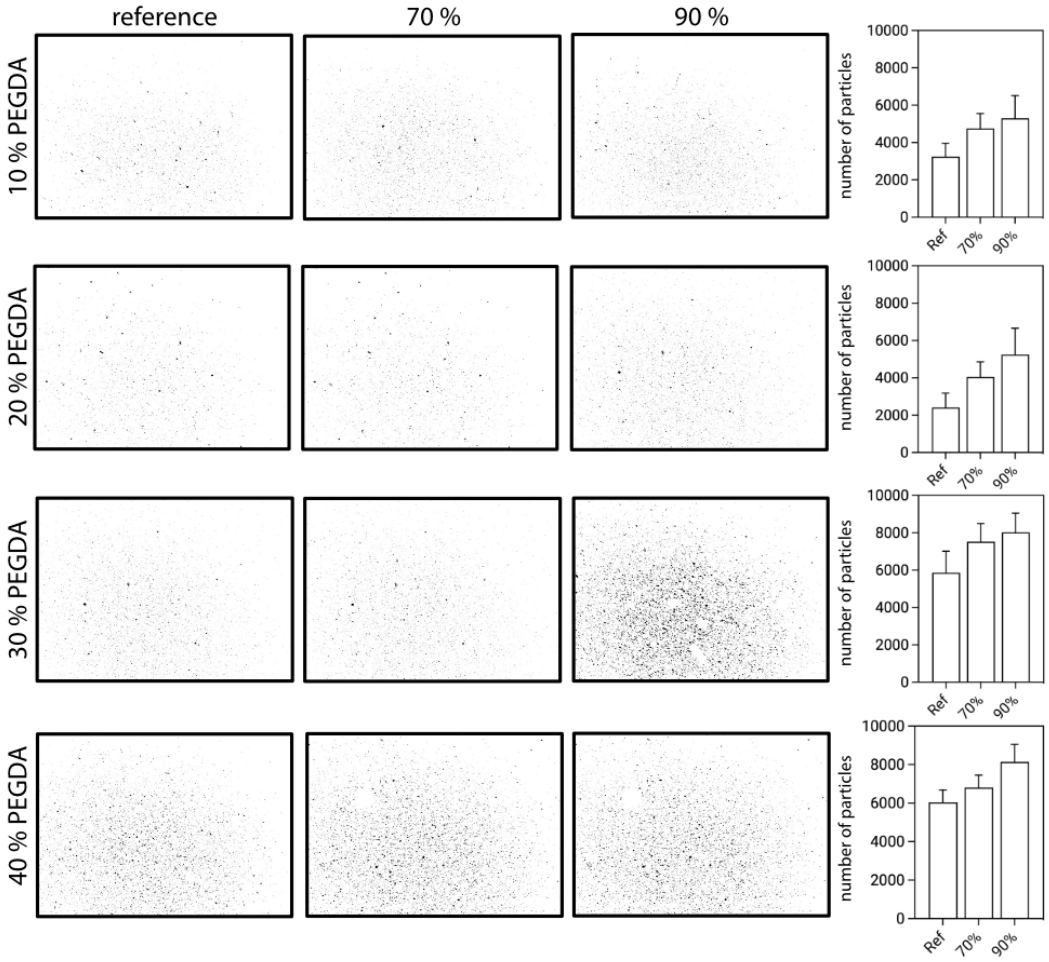

Figure A17: Representative images and the determined number of fluorescently labeled nanogels after they passed through microchannels of different stenosis levels. The number of nanogels shown in the bar plots was determined from 3 independent experiments; in each experiment, 5 images obtained from different locations of the collected sample were analyzed. Data shown represents mean values, error bars denote the standard deviation.

- Shear-responsive behavior of nanogels when dispersed in whole blood

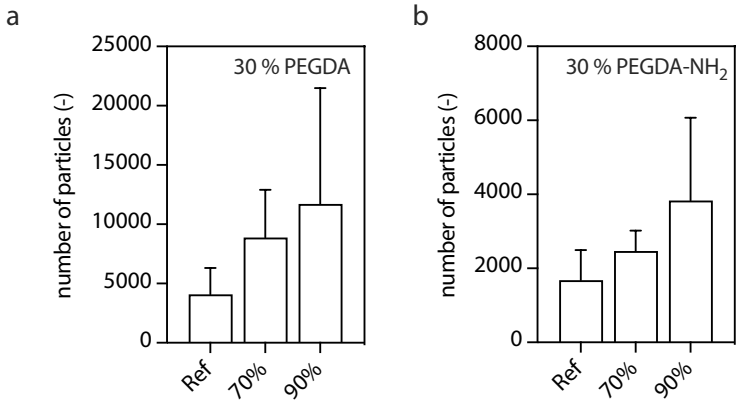

Figure A18: Number of fluorescently labeled 30 % PEGDA **(A)** and 30% PEGDA-NH_2 nanogels **(B)** dispersed in a human blood sample after they passed through microchannels of different stenosis levels. The number of nanogels was determined from 3 independent experiments; in each experiment, 10 images obtained from individual experiments were analyzed. Data shown represents mean values, error bars denote the standard deviation.

A4.6. Intracellular delivery mechanisms controlled by strand displacement reactions

- Stability of the mucin nanoparticles at different pH levels and in the presence of enzymes

The average hydrodynamic size and the derived count rate (a parameter that is function of the number of intact nanoparticles) were tracked to analyze the stability of the nanoparticles. An incubation pH of 7.4 and 5.2 were selected as they represent cytoplasmic and endosomal pH levels, respectively. It was found that the nanoparticles maintain their condensed configuration and count rate with a minimal fluctuation in the polydispersity index (PDI). After exposure to trypsin, a slow decrease in the derived count rate was observed over time. This observation can be attributed to the fact that trypsin treatment of mucins removes the terminal domains of the glycoprotein [259].When nanoparticles were exposed to high concentration of DNaseI (50 µg/mL), a rapid size change was observed indicating the nanoparticle deformation. However, under physiological DNaseI concentration of 0.025 µg/mL, nanoparticles were found stable over time.

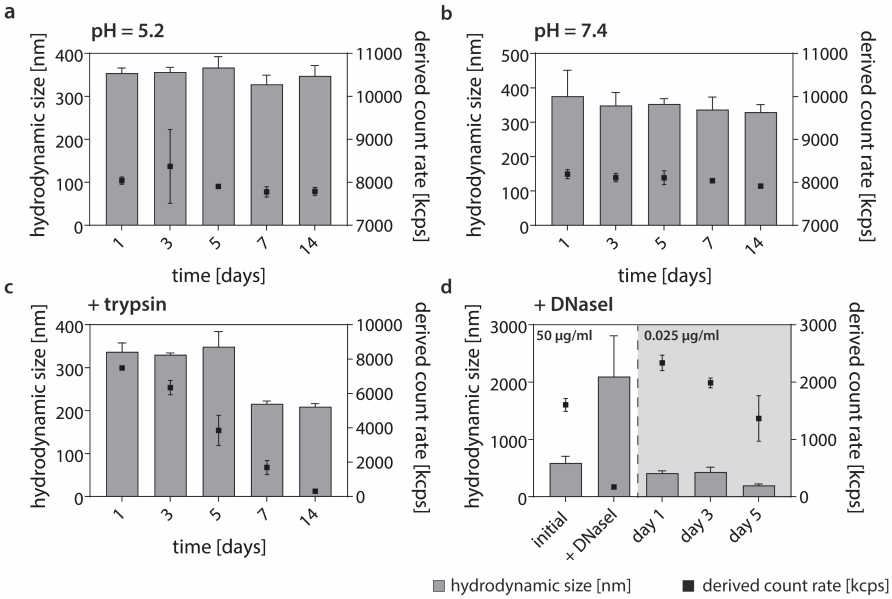

Figure A19: Hydrodynamic size of mucin nanoparticles measured at different environmental conditions over time. Data shown represents mean values, error bars denote the standard deviation as obtained from *n* = 5 independent samples.

Table A9. PDI values of mucin nanoparticles that were incubated at different environmental conditions up to 14 days.

incubation condition	PDI (-)				
	Day 1	Day 3	Day 5	Day 7	Day 14
pH = 7.4	0.15	0.17	0.21	0.35	0.24
pH = 5.2	0.10	0.13	0.12	0.17	0.16
trypsin	0.18	0.19	0.32	0.41	0.48
DNase I (c=0.025 µg/mL)	0.19	0.26	0.61	-	-
DNase I (c = 50 µg/mL)	0.21	0.81*	-	-	-

*data was taken after 4 h

NPs as antibiotic carriers to combat cellular infections

NPs developed here can be evaluated as an antibiotic delivery agent to combat intracellular infections such as those induced by *Listeria monocytogenes*, or *Pseudomonas aeruginosa* which are challenging to treat. These bacteria lead to severe diseases such as listeriosis, pneumonia, endocarditis, and meningitis, mainly targeting macrophages and epithelial cells [260,261]. In these cases, the bacterial pathogens hide in the macrophages, where they are protected from systemic antibiotic administration, and persistent infection of macrophages can lead to further spreading of the infection and infection recurrence. [262] With the strategy developed here, mucin NPs can be evaluated to target macrophages: even without a cationic polymer coating step, macrophages could quickly internalize mucin NPs in 2 h, possibly due to their active uptake mechanism as confirmed with confocal imaging and FACS, without causing any cytotoxic effects (**Fig. A21**).

Additionally, NPs can also be efficiently loaded with different groups of antibiotics possessing different overall charges, and their release can be triggered with a dDNA trigger. In the preliminary experiments of this study, when the membrane and cytosol fractions of the NP-treated cells were analyzed separately, it was found that the NPs can concentrate the drugs in the cytosol compared to the cells incubated with free drugs possessing ≈ 12 times less drug concentration. Importantly, the delivered dose *via* mucin NPs exceeds the subtherapeutic levels (*i.e.*, higher than corresponding MIC values) for various bacterial species, including *Staphylococcus spp*., some Streptococcus groups, and *P. aeruginosa* [183,263]. Therefore, these findings showed that NPs developed here might act as efficient vectors to overcome the diffusion-related rapid clearance of drugs from the extracellular environment.

However, although these experiments show that the cytosolic accumulation of drugs is facilitated *via* a mucin NP system, the setup does not allow for quantifying the liberated TCL upon a trigger DNA transfection. In all cases (*i.e.*, no transfection, coDNA, and dDNA transfection), 0.30 – 0.45 mM of TCL was detected at cytosol fractions, regardless of their liberated or entrapped state. Thus, to examine whether the drug was successfully liberated under desired conditions, these fractions were subjected to dialysis, allowing free drug molecules to diffuse out while keeping the mucin NP-entrapped drug retained in the membrane. After 2 days of dialysis, a significant decrease in TCL was detected for cytosol fractions transfected with the dDNA – but not for the other two populations. This finding demonstrated that the dDNA transfected cytosols contain liberated TCL molecules, which is consistent with previous observations. From those tests, it can be concluded that the DNA-based release strategy is applicable for different types of drugs in the subcellular microenvironment and that cytoplasmic components do not compromise the mechanism.

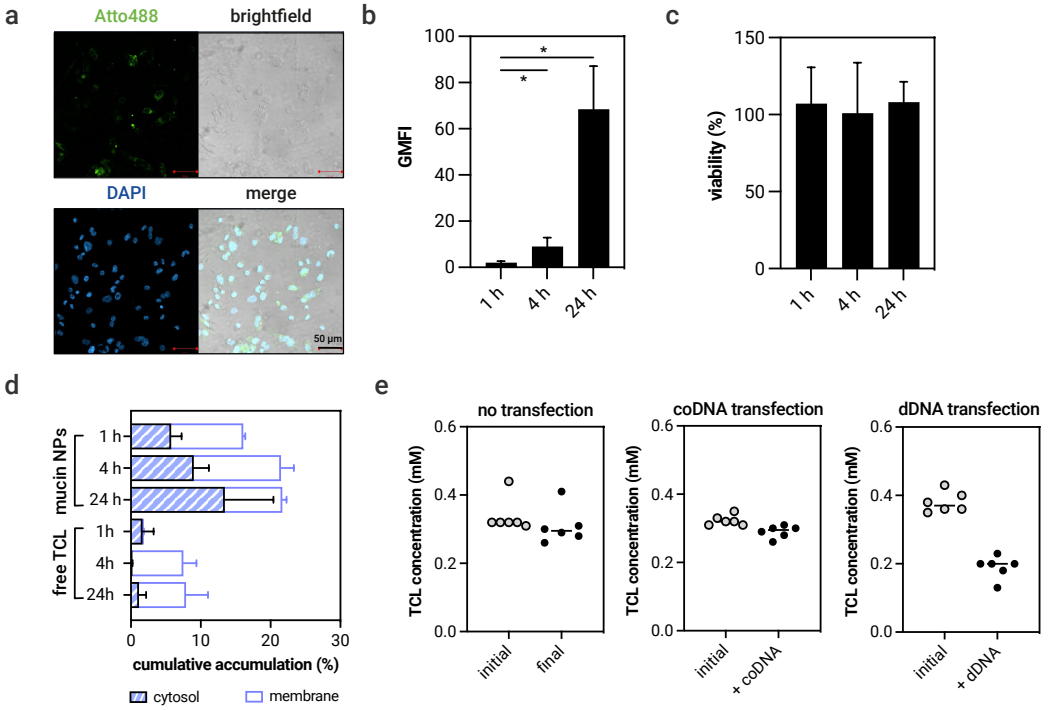

Figure A20: Differential interference contrast and fluorescent confocal laser scanning microscope images demonstrate the successful uptake of (uncoated) mucin NPs by THP-1 derived macrophages (M0) after 24 h of incubation. The scale bar represents 50 µm and applies to all images (**A**). Geometric mean fluorescence intensity of macrophages incubated with fluorescently labeled (uncoated) mucin NPs for 1 h, 4 h, and 24 h (n = 6) (**B**). Viability of macrophages after 1 h, 4 h, and 24 h of incubation with mucin NPs (n = 6) (**C**). Quantification of NP entrapped and free antibiotics (TCL) in cytosol and membrane fractions of HeLa cells after incubation of 1 h, 4 h, and 24 h showing that the mucin NPs facilitate the cytosolic concentration of drugs. At both conditions, the total administrated drug concentration was adjusted to 5 mM (n = 6) (**D**). TCL concentration in the cytosol fractions of non-transfected, coDNA- and dDNA-transfected HeLa cells before (grey dots) and after (black dots) dialysis (n = 6) (**E**). Data represent mean values and error bars denote the standard deviation.

Threshold trigger DNA amount required to trigger cationic polymer coated mucin NPs

To investigate whether addition of a cationic polymer coating to the NP formulation step rendered the dDNA induced decondensation of NPs, PLL-coated NPs were incubated with a concentration series of dDNA solutions which corresponds to 1 – 10 dDNA per cDNA/crDNA pair. In parallel, a similar set of conditions (however, in the range of 1 – 20 dDNA per crDNA crosslink) were tested to detect the minimum dDNA concentration that initiates a remarkable drug release from mucin NPs.

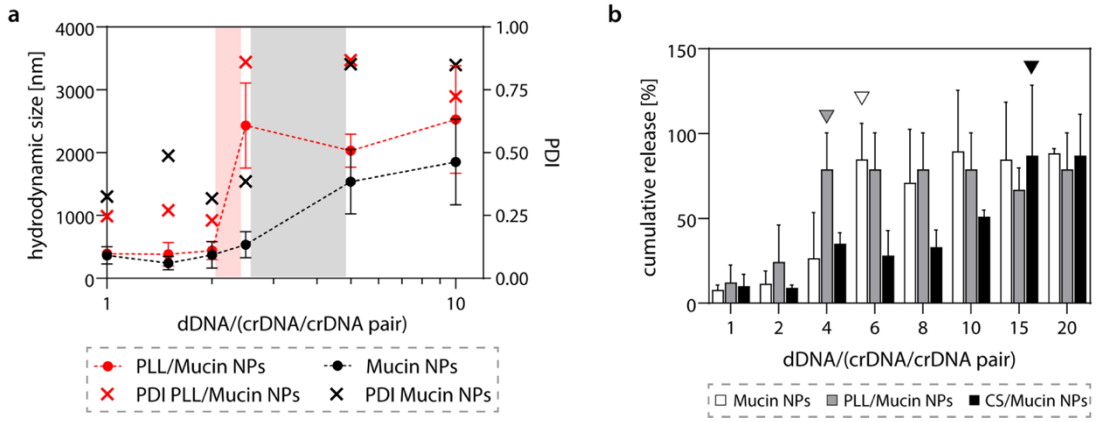

Figure A21: DLS measurements of PLL/mucin NPs under a dDNA gradient showing the threshold dDNA concentration required to force the particulate structure to unfold (*n* = 5) (**A**). Cumulative cargo release from coated mucin NPs under a dDNA gradient showing the amount of dDNA required to initiate a detectable cargo release as an indication of conformational change (*n* = 5) (**B**). Data shown represents mean values, error bars denote the standard deviation.

References

1 Increasingly translational delivery. *Nature Biomedical Engineering* **5**, 947-948 (2021).

2 Cohrs, R. J., Martin, T., Ghahramani, P., Bidaut, L., Higgins, P. J., & Shahzad, A. (2015). Translational medicine definition by the European Society for Translational Medicine.

3 Fröhlich, E. The role of surface charge in cellular uptake and cytotoxicity of medical nanoparticles. *International journal of nanomedicine* **7**, 5577 (2012).

4 Akinc, A., Thomas, M., Klibanov, A. M. & Langer, R. Exploring polyethylenimine-mediated DNA transfection and the proton sponge hypothesis. *The Journal of Gene Medicine: A cross-disciplinary journal for research on the science of gene transfer and its clinical applications* **7**, 657-663 (2005).

5 Aiyelabegan, H. T. & Sadroddiny, E. Fundamentals of protein and cell interactions in biomaterials. *Biomedicine & Pharmacotherapy* **88**, 956-970 (2017).

6 Langer, R. New methods of drug delivery. *Science* **249**, 1527-1533 (1990).

7 Giritligil, S., Cesur, S. & Kuryel, B. Overview of planning and scheduling of batch process operations. *IFAC Proceedings Volumes* **31**, 455-460 (1998).

8 Zhang, Q. *et al.* Dual-functionalized liposomal delivery system for solid tumors based on RGD and a pH-responsive antimicrobial peptide. *Scientific reports* **6**, 19800 (2016).

9 Ramírez-García, P. D. *et al.* A pH-responsive nanoparticle targets the neurokinin 1 receptor in endosomes to prevent chronic pain. *Nature nanotechnology* **14**, 1150-1159 (2019).

10 Lang, T. *et al.* Tumor microenvironment-responsive docetaxel-loaded micelle combats metastatic breast cancer. *Science Bulletin* **64**, 91-100 (2019).

11 Cao, M. *et al.* Enzyme-triggered morphological transition of peptide nanostructures for tumor-targeted drug delivery and enhanced cancer therapy. *ACS applied materials & interfaces* **11**, 16357-16366 (2019).

12 Chen, D. *et al.* Biodegradable, hydrogen peroxide, and glutathione dual responsive nanoparticles for potential programmable paclitaxel release. *Journal of the American Chemical Society* **140**, 7373-7376 (2018).

13 Luo, Z. *et al.* Intracellular redox-activated anticancer drug delivery by functionalized hollow mesoporous silica nanoreservoirs with tumor specificity. *Biomaterials* **35**, 7951-7962 (2014).

14 Guo, X., Chang, R.-K. & Hussain, M. A. Ion-exchange resins as drug delivery carriers. *Journal of pharmaceutical sciences* **98**, 3886-3902 (2009).

15 Huo, M., Yuan, J., Tao, L. & Wei, Y. Redox-responsive polymers for drug delivery: from molecular design to applications. *Polymer Chemistry* **5**, 1519-1528 (2014).

16 Guo, X. *et al.* Advances in redox-responsive drug delivery systems of tumor microenvironment. *Journal of Nanobiotechnology* **16**, 1-10 (2018).

17 Heo, Y. J., Shibata, H., Okitsu, T., Kawanishi, T. & Takeuchi, S. Long-term in vivo glucose monitoring using fluorescent hydrogel fibers. *Proceedings of the National Academy of Sciences* **108**, 13399-13403 (2011).

18 Yu, J. *et al.* Glucose-responsive insulin patch for the regulation of blood glucose in mice and minipigs. *Nature biomedical engineering* **4**, 499-506 (2020).

19 Hu, Q., Katti, P. S. & Gu, Z. Enzyme-responsive nanomaterials for controlled drug delivery. *Nanoscale* **6**, 12273-12286 (2014).

20 Karimi, M. *et al.* Smart micro/nanoparticles in stimulus-responsive drug/gene delivery systems. *Chemical Society Reviews* **45**, 1457-1501 (2016).

21 Alkekhia, D., LaRose, C. & Shukla, A. β-Lactamase-Responsive Hydrogel Drug Delivery Platform for Bacteria-Triggered Cargo Release. *ACS Applied Materials & Interfaces* (2022).
22 Bordat, A., Boissenot, T., Nicolas, J. & Tsapis, N. Thermoresponsive polymer nanocarriers for biomedical applications. *Advanced drug delivery reviews* **138**, 167-192 (2019).
23 Abulateefeh, S. R. *et al.* Thermoresponsive polymer colloids for drug delivery and cancer therapy. *Macromolecular bioscience* **11**, 1722-1734 (2011).
24 Korin, N. *et al.* Shear-activated nanotherapeutics for drug targeting to obstructed blood vessels. *Science* **337**, 738-742 (2012).
25 Molloy, C. P. *et al.* Shear-sensitive nanocapsule drug release for site-specific inhibition of occlusive thrombus formation. *Journal of thrombosis and haemostasis* **15**, 972-982 (2017).
26 Schmaljohann, D. Thermo-and pH-responsive polymers in drug delivery. *Advanced drug delivery reviews* **58**, 1655-1670 (2006).
27 Conde, J., Edelman, E. R. & Artzi, N. Target-responsive DNA/RNA nanomaterials for microRNA sensing and inhibition: The jack-of-all-trades in cancer nanotheranostics? *Advanced Drug Delivery Reviews* **81**, 169-183 (2015).
28 Kapadia, C. H. *et al.* Polymer nanocarriers for microRNA delivery. *Journal of applied polymer science* **137**, 48651 (2020).
29 Whitehead, K. A., Langer, R. & Anderson, D. G. Knocking down barriers: advances in siRNA delivery. *Nature reviews Drug discovery* **8**, 129-138 (2009).
30 Shin, C.-H. *et al.* Cytosolic microRNA-inducible nuclear translocation of Cas9 protein for disease-specific genome modification. *Nucleic Acids Research* (2022).
31 Peters, D. *et al.* Targeting atherosclerosis by using modular, multifunctional micelles. *Proceedings of the National Academy of Sciences* **106**, 9815-9819 (2009).
32 Pacifici, N., Bolandparvaz, A. & Lewis, J. S. Stimuli-Responsive Biomaterials for Vaccines and Immunotherapeutic Applications. *Advanced therapeutics* **3**, 2000129 (2020).
33 Anselmo, A. C. & Mitragotri, S. Nanoparticles in the clinic: An update. *Bioengineering & translational medicine* **4**, e10143 (2019).
34 Mura, S., Nicolas, J. & Couvreur, P. Stimuli-responsive nanocarriers for drug delivery. *Nature materials* **12**, 991-1003 (2013).
35 Brenner, J. S. *et al.* Red blood cell-hitchhiking boosts delivery of nanocarriers to chosen organs by orders of magnitude. *Nature communications* **9**, 1-14 (2018).
36 Akolpoglu, M. B. *et al.* High-Yield Production of Biohybrid Microalgae for On-Demand Cargo Delivery. *Advanced Science* **7**, 2001256 (2020).
37 Choi, J. *et al.* Use of macrophages to deliver therapeutic and imaging contrast agents to tumors. *Biomaterials* **33**, 4195-4203 (2012).
38 Jester, B. W. *et al.* Development of spirulina for the manufacture and oral delivery of protein therapeutics. *Nature biotechnology*, 1-9 (2022).
39 Poon, W., Kingston, B. R., Ouyang, B., Ngo, W. & Chan, W. C. A framework for designing delivery systems. *Nature nanotechnology* **15**, 819-829 (2020).
40 Cortez-Jugo, C., Czuba-Wojnilowicz, E., Tan, A. & Caruso, F. A Focus on "Bio" in Bio–Nanoscience: The Impact of Biological Factors on Nanomaterial Interactions. *Advanced Healthcare Materials* **10**, 2100574 (2021).
41 Sykes, E. A. *et al.* Tailoring nanoparticle designs to target cancer based on tumor pathophysiology. *Proceedings of the National Academy of Sciences* **113**, E1142-E1151 (2016).
42 Blanco, E., Shen, H. & Ferrari, M. Principles of nanoparticle design for overcoming biological barriers to drug delivery. *Nature biotechnology* **33**, 941-951 (2015).
43 Champion, J. A., Walker, A. & Mitragotri, S. Role of particle size in phagocytosis of polymeric microspheres. *Pharmaceutical research* **25**, 1815-1821 (2008).

44 Win, K. Y. & Feng, S.-S. Effects of particle size and surface coating on cellular uptake of polymeric nanoparticles for oral delivery of anticancer drugs. *Biomaterials* **26**, 2713-2722 (2005).
45 Salvati, A. *et al.* Transferrin-functionalized nanoparticles lose their targeting capabilities when a biomolecule corona adsorbs on the surface. *Nature nanotechnology* **8**, 137-143 (2013).
46 Lundqvist, M. *et al.* Nanoparticle size and surface properties determine the protein corona with possible implications for biological impacts. *Proceedings of the National Academy of Sciences* **105**, 14265-14270 (2008).
47 Garbuzenko, O. B. *et al.* Inhibition of lung tumor growth by complex pulmonary delivery of drugs with oligonucleotides as suppressors of cellular resistance. *Proceedings of the national academy of sciences* **107**, 10737-10742 (2010).
48 Vargason, A. M., Anselmo, A. C. & Mitragotri, S. The evolution of commercial drug delivery technologies. *Nature Biomedical Engineering* **5**, 951-967 (2021).
49 Kormann, M. S. *et al.* Expression of therapeutic proteins after delivery of chemically modified mRNA in mice. *Nature biotechnology* **29**, 154-157 (2011).
50 Coles, J. M., Chang, D. P. & Zauscher, S. Molecular mechanisms of aqueous boundary lubrication by mucinous glycoproteins. *Current Opinion in Colloid & Interface Science* **15**, 406-416 (2010).
51 Song, D., Cahn, D. & Duncan, G. A. Mucin biopolymers and their barrier function at airway surfaces. *Langmuir* **36**, 12773-12783 (2020).
52 McGuckin, M. A., Lindén, S. K., Sutton, P. & Florin, T. H. Mucin dynamics and enteric pathogens. *Nature Reviews Microbiology* **9**, 265-278 (2011).
53 Bansil, R. & Turner, B. S. Mucin structure, aggregation, physiological functions and biomedical applications. *Current Opinion in Colloid & Interface Science* **11**, 164-170 (2006).
54 Marczynski, M. *et al.* Structural Alterations of Mucins Are Associated with Losses in Functionality. *Biomacromolecules* (2021).
55 Schömig, V. J. *et al.* An optimized purification process for porcine gastric mucin with preservation of its native functional properties. *RSC Advances* **6**, 44932-44943 (2016).
56 Winkeljann, B. *et al.* Covalent Mucin Coatings Form Stable Anti-Biofouling Layers on a Broad Range of Medical Polymer Materials. *Advanced Materials Interfaces* **7**, 1902069 (2020).
57 Hemshekhar, M. *et al.* Emerging roles of hyaluronic acid bioscaffolds in tissue engineering and regenerative medicine. *International Journal of Biological Macromolecules* **86**, 917-928 (2016).
58 Burdick, J. A. & Prestwich, G. D. Hyaluronic acid hydrogels for biomedical applications. *Advanced materials* **23**, H41-H56 (2011).
59 Croisier, F. & Jérôme, C. Chitosan-based biomaterials for tissue engineering. *European polymer journal* **49**, 780-792 (2013).
60 Augst, A. D., Kong, H. J. & Mooney, D. J. Alginate hydrogels as biomaterials. *Macromolecular bioscience* **6**, 623-633 (2006).
61 Rogers, C. I., Pagaduan, J. V., Nordin, G. P. & Woolley, A. T. Single-monomer formulation of polymerized polyethylene glycol diacrylate as a nonadsorptive material for microfluidics. *Analytical chemistry* **83**, 6418-6425 (2011).
62 Rogers, C. I. *et al.* Microfluidic valves made from polymerized polyethylene glycol diacrylate. *Sensors and Actuators B: Chemical* **191**, 438-444 (2014).
63 Yang, F. *et al.* The effect of incorporating RGD adhesive peptide in polyethylene glycol diacrylate hydrogel on osteogenesis of bone marrow stromal cells. *Biomaterials* **26**, 5991-5998 (2005).

64 Zhang, X., Yang, D. & Nie, J. Chitosan/polyethylene glycol diacrylate films as potential wound dressing material. *International journal of biological macromolecules* **43**, 456-462 (2008).
65 Anselmo, A. C. *et al.* Elasticity of nanoparticles influences their blood circulation, phagocytosis, endocytosis, and targeting. *ACS nano* **9**, 3169-3177 (2015).
66 SantaLucia, J. A unified view of polymer, dumbbell, and oligonucleotide DNA nearest-neighbor thermodynamics. *Proceedings of the National Academy of Sciences* **95**, 1460-1465 (1998).
67 SantaLucia, J., Allawi, H. T. & Seneviratne, P. A. Improved nearest-neighbor parameters for predicting DNA duplex stability. *Biochemistry* **35**, 3555-3562 (1996).
68 Jeon, B.-j. *et al.* Salt-dependent properties of a coacervate-like, self-assembled DNA liquid. *Soft Matter* **14**, 7009-7015 (2018).
69 Lin, C., Liu, Y., Rinker, S. & Yan, H. DNA tile based self-assembly: building complex nanoarchitectures. *ChemPhysChem* **7**, 1641-1647 (2006).
70 Seeman, N. C. & Kallenbach, N. R. Design of immobile nucleic acid junctions. *Biophysical journal* **44**, 201-209 (1983).
71 Simmel, F. C., Yurke, B. & Singh, H. R. Principles and applications of nucleic acid strand displacement reactions. *Chemical reviews* **119**, 6326-6369 (2019).
72 Owczarzy, R. *et al.* IDT SciTools: a suite for analysis and design of nucleic acid oligomers. *Nucleic acids research* **36**, W163-W169 (2008).
73 Zadeh, J. N. *et al.* NUPACK: analysis and design of nucleic acid systems. *Journal of computational chemistry* **32**, 170-173 (2011).
74 Lesch, H. P., Kaikkonen, M. U., Pikkarainen, J. T. & Ylä-Herttuala, S. Avidin-biotin technology in targeted therapy. *Expert opinion on drug delivery* **7**, 551-564 (2010).
75 Yan, H. *et al.* Reversible condensation of mucins into nanoparticles. *Langmuir* **34**, 13615-13625 (2018).
76 Kim, O. V. & Dunn, P. F. Controlled production of droplets by in-flight electrospraying. *Langmuir* **26**, 15807-15813 (2010).
77 Pawar, A., Thakkar, S. & Misra, M. A bird's eye view of nanoparticles prepared by electrospraying: advancements in drug delivery field. *Journal of controlled release* **286**, 179-200 (2018).
78 Nguyen, D. N., Clasen, C. & Van den Mooter, G. Pharmaceutical applications of electrospraying. *Journal of pharmaceutical sciences* **105**, 2601-2620 (2016).
79 Crouzier, T., Beckwitt, C. H. & Ribbeck, K. Mucin multilayers assembled through sugar–lectin interactions. *Biomacromolecules* **13**, 3401-3408 (2012).
80 Bhattacharjee, S. DLS and zeta potential–what they are and what they are not? *Journal of controlled release* **235**, 337-351 (2016).
81 Missana, T. & Adell, A. On the applicability of DLVO theory to the prediction of clay colloids stability. *Journal of Colloid and Interface Science* **230**, 150-156 (2000).
82 Lieleg, O. & Bausch, A. R. Cross-linker unbinding and self-similarity in bundled cytoskeletal networks. *Physical review letters* **99**, 158105 (2007).
83 Ptaszek, P. in *Advances in food rheology and its applications* 87-123 (Elsevier, 2017).
84 Wallin, R. F. & Arscott, E. A practical guide to ISO 10993-5: Cytotoxicity. *Medical Device and Diagnostic Industry* **20**, 96-98 (1998).
85 Chen, C. *et al.* Real-time quantification of microRNAs by stem–loop RT–PCR. *Nucleic acids research* **33**, e179-e179 (2005).
86 Xu, X. M. *et al.* Expression of miR-21, miR-31, miR-96 and miR-135b is correlated with the clinical parameters of colorectal cancer. *Oncology letters* **4**, 339-345 (2012).

87 Zhang, P. *et al.* In situ amplification of intracellular microRNA with MNAzyme nanodevices for multiplexed imaging, logic operation, and controlled drug release. *ACS nano* **9**, 789-798 (2015).
88 Gladysz, M. Z., Stevanoska, M., Włodarczyk-Biegun, M. K. & Nagelkerke, A. Breaking through the barrier: Modelling and exploiting the physical microenvironment to enhance drug transport and efficacy. *Advanced Drug Delivery Reviews*, 114183 (2022).
89 Marczynski, M., Kimna, C. & Lieleg, O. Purified mucins in drug delivery research. *Advanced Drug Delivery Reviews* **178**, 113845 (2021).
90 Burgalassi, S., Chetoni, P. & Saettone, M. F. Hydrogels for ocular delivery of pilocarpine: preliminary evaluation in rabbits of the influence of viscosity and of drug solubility. *European journal of pharmaceutics and biopharmaceutics* **42**, 385-392 (1996).
91 Mathiowitz, E., Chickering III, D. E. & Lehr, C.-M. *Bioadhesive drug delivery systems: fundamentals, novel approaches, and development*. (CRC Press, 1999).
92 Di Prima, G. *et al.* Mucoadhesive PEGylated inulin-based self-assembling nanoparticles: In vitro and ex vivo transcorneal permeation enhancement of corticosteroids. *Journal of Drug Delivery Science and Technology* **49**, 195-208 (2019).
93 Prosperi-Porta, G., Kedzior, S., Muirhead, B. & Sheardown, H. Phenylboronic-acid-based polymeric micelles for mucoadhesive anterior segment ocular drug delivery. *Biomacromolecules* **17**, 1449-1457 (2016).
94 Ding, D. *et al.* Design of mucoadhesive PLGA microparticles for ocular drug delivery. *ACS Applied Bio Materials* **1**, 561-571 (2018).
95 Cuggino, J. C., Tártara, L. I., Gugliotta, L. M., Palma, S. D. & Igarzabal, C. I. A. Mucoadhesive and responsive nanogels as carriers for sustainable delivery of timolol for glaucoma therapy. *Materials Science and Engineering: C*, 111383 (2020).
96 Zhang, X. *et al.* Design and intestinal mucus penetration mechanism of core-shell nanocomplex. *Journal of controlled release* **272**, 29-38 (2018).
97 Watchorn, J. *et al.* Untangling Mucosal Drug Delivery: Engineering, Designing, and Testing Nanoparticles to Overcome the Mucus Barrier. *ACS Biomaterials Science & Engineering* (2022).
98 Marczynski, M. & Lieleg, O. Forgotten but not gone: Particulate matter as contaminations of mucosal systems. *Biophysics Reviews* **2**, 031302 (2021).
99 Janagam, D. R., Wu, L. & Lowe, T. L. Nanoparticles for drug delivery to the anterior segment of the eye. *Advanced drug delivery reviews* **122**, 31-64 (2017).
100 Tsai, C.-H. *et al.* Ocular drug delivery: Role of degradable polymeric nanocarriers for ophthalmic application. *International journal of molecular sciences* **19**, 2830 (2018).
101 Wang, L., Khor, E., Wee, A. & Lim, L. Y. Chitosan-alginate PEC membrane as a wound dressing: Assessment of incisional wound healing. *Journal of Biomedical Materials Research: An Official Journal of The Society for Biomaterials, The Japanese Society for Biomaterials, and The Australian Society for Biomaterials and the Korean Society for Biomaterials* **63**, 610-618 (2002).
102 Iwasaki, N. *et al.* Feasibility of polysaccharide hybrid materials for scaffolds in cartilage tissue engineering: evaluation of chondrocyte adhesion to polyion complex fibers prepared from alginate and chitosan. *Biomacromolecules* **5**, 828-833 (2004).
103 Venkatesan, J., Bhatnagar, I. & Kim, S.-K. Chitosan-alginate biocomposite containing fucoidan for bone tissue engineering. *Marine drugs* **12**, 300-316 (2014).
104 Mi, F.-L., Sung, H.-W. & Shyu, S.-S. Drug release from chitosan–alginate complex beads reinforced by a naturally occurring cross-linking agent. *Carbohydrate Polymers* **48**, 61-72 (2002).

105 Khong, T. T., Aarstad, O. A., Skjåk-Bræk, G., Draget, K. I. & Vårum, K. M. Gelling Concept Combining Chitosan and Alginate⊠ Proof of Principle. *Biomacromolecules* **14**, 2765-2771 (2013).
106 Wadhwa, S., Paliwal, R., Paliwal, S. R. & Vyas, S. Nanocarriers in ocular drug delivery: an update review. *Current pharmaceutical design* **15**, 2724-2750 (2009).
107 Zhou, H.-Y., Hao, J.-L., Wang, S., Zheng, Y. & Zhang, W.-S. Nanoparticles in the ocular drug delivery. *International journal of ophthalmology* **6**, 390 (2013).
108 Souza, J. G., Dias, K., Pereira, T. A., Bernardi, D. S. & Lopez, R. F. Topical delivery of ocular therapeutics: carrier systems and physical methods. *Journal of Pharmacy and Pharmacology* **66**, 507-530 (2014).
109 Sah, A. K. & Suresh, P. K. Medical management of glaucoma: focus on ophthalmologic drug delivery systems of timolol maleate. *Artificial cells, nanomedicine, and biotechnology* **45**, 448-459 (2017).
110 Jung, H. J., Abou-Jaoude, M., Carbia, B. E., Plummer, C. & Chauhan, A. Glaucoma therapy by extended release of timolol from nanoparticle loaded silicone-hydrogel contact lenses. *Journal of controlled release* **165**, 82-89 (2013).
111 Popov, A. Mucus-penetrating particles and the role of ocular mucus as a barrier to micro-and nanosuspensions. *Journal of Ocular Pharmacology and therapeutics* **36**, 366-375 (2020).
112 Gipson, I. K. & Inatomi, T. Cellular origin of mucins of the ocular surface tear film. *Lacrimal Gland, Tear Film, and Dry Eye Syndromes 2*, 221-227 (1998).
113 Cuggino, J. C., Blanco, E. R. O., Gugliotta, L. M., Igarzabal, C. I. A. & Calderón, M. Crossing biological barriers with nanogels to improve drug delivery performance. *Journal of Controlled Release* **307**, 221-246 (2019).
114 Schopf, L., Enlow, E., Popov, A., Bourassa, J. & Chen, H. Ocular pharmacokinetics of a novel loteprednol etabonate 0.4% ophthalmic formulation. *Ophthalmology and therapy* **3**, 63-72 (2014).
115 Marczynski, M. *et al.* Transient binding promotes molecule penetration into mucin hydrogels by enhancing molecular partitioning. *Biomaterials science* **6**, 3373-3387 (2018).
116 Lieleg, O., Vladescu, I. & Ribbeck, K. Characterization of particle translocation through mucin hydrogels. *Biophysical journal* **98**, 1782-1789 (2010).
117 Menchicchi, B. *et al.* Structure of chitosan determines its interactions with mucin. *Biomacromolecules* **15**, 3550-3558 (2014).
118 Sharma, R., Ahuja, M. & Kaur, H. Thiolated pectin nanoparticles: Preparation, characterization and ex vivo corneal permeation study. *Carbohydrate Polymers* **87**, 1606-1610 (2012).
119 Cheng, H. *et al.* Mucoadhesive versus mucopenetrating nanoparticles for oral delivery of insulin. *Acta Biomaterialia* **135**, 506-519 (2021).
120 Han, L. *et al.* Mussel-inspired adhesive and tough hydrogel based on nanoclay confined dopamine polymerization. *ACS nano* **11**, 2561-2574 (2017).
121 Lee, H., Dellatore, S. M., Miller, W. M. & Messersmith, P. B. Mussel-inspired surface chemistry for multifunctional coatings. *science* **318**, 426-430 (2007).
122 Han, L. *et al.* Mussel-inspired tissue-adhesive hydrogel based on the polydopamine–chondroitin sulfate complex for growth-factor-free cartilage regeneration. *ACS applied materials & interfaces* **10**, 28015-28026 (2018).
123 Park, H.-J. *et al.* Catechol-functionalized hyaluronic acid hydrogels enhance angiogenesis and osteogenesis of human adipose-derived stem cells in critical tissue defects. *Biomacromolecules* **17**, 1939-1948 (2016).

124 Colombo, P., Bettini, R., Santi, P., De Ascentiis, A. & Peppas, N. Analysis of the swelling and release mechanisms from drug delivery systems with emphasis on drug solubility and water transport. *Journal of controlled release* **39**, 231-237 (1996).
125 Shi, L., Liu, X., Wang, W., Jiang, L. & Wang, S. A self-pumping dressing for draining excessive biofluid around wounds. *Advanced materials* **31**, 1804187 (2019).
126 Janairo, R. R. R., Zhu, Y., Chen, T. & Li, S. Mucin covalently bonded to microfibers improves the patency of vascular grafts. *Tissue Engineering Part A* **20**, 285-293 (2014).
127 Song, J., Lutz, T. M., Lang, N. & Lieleg, O. Bioinspired Dopamine/Mucin Coatings Provide Lubricity, Wear Protection, and Cell-Repellent Properties for Medical Applications. *Advanced Healthcare Materials*, 2000831 (2020).
128 Crouzier, T., Jang, H., Ahn, J., Stocker, R. & Ribbeck, K. Cell patterning with mucin biopolymers. *Biomacromolecules* **14**, 3010-3016 (2013).
129 Yan, H. *et al.* Immune-informed mucin hydrogels evade fibrotic foreign body response in vivo. *Advanced Functional Materials* **29**, 1902581 (2019).
130 Junter, G.-A., Thebault, P. & Lebrun, L. Polysaccharide-based antibiofilm surfaces. *Acta biomaterialia* **30**, 13-25 (2016).
131 Carlson, G. A. *et al.* Bacteriostatic properties of biomatrices against common orthopaedic pathogens. *Biochemical and biophysical research communications* **321**, 472-478 (2004).
132 Percival, S. L., McCarty, S. M. & Lipsky, B. Biofilms and wounds: an overview of the evidence. *Advances in wound care* **4**, 373-381 (2015).
133 Chen, G. *et al.* Bioinspired multifunctional hybrid hydrogel promotes wound healing. *Advanced Functional Materials* **28**, 1801386 (2018).
134 Boehler, R. M., Graham, J. G. & Shea, L. D. Tissue engineering tools for modulation of the immune response. *Biotechniques* **51**, 239-254 (2011).
135 Chung, L., Maestas Jr, D. R., Housseau, F. & Elisseeff, J. H. Key players in the immune response to biomaterial scaffolds for regenerative medicine. *Advanced drug delivery reviews* **114**, 184-192 (2017).
136 Rayahin, J. E., Buhrman, J. S., Zhang, Y., Koh, T. J. & Gemeinhart, R. A. High and low molecular weight hyaluronic acid differentially influence macrophage activation. *ACS biomaterials science & engineering* **1**, 481-493 (2015).
137 Saleh, B. *et al.* Local immunomodulation using an adhesive hydrogel loaded with miRNA-laden nanoparticles promotes wound healing. *Small* **15**, 1902232 (2019).
138 Li, Z. & Bratlie, K. M. The Influence of Polysaccharides-Based Material on Macrophage Phenotypes. *Macromolecular Bioscience*, 2100031 (2021).
139 Yan, H. *et al.* Glyco-modification of mucin hydrogels to investigate their immune activity. *ACS applied materials & interfaces* **12**, 19324-19336 (2020).
140 Shin, J. *et al.* Tissue Tapes—Phenolic Hyaluronic Acid Hydrogel Patches for Off-the-Shelf Therapy. *Advanced Functional Materials* **29**, 1903863 (2019).
141 Ma, Y. *et al.* Liquid bandage harvests robust adhesive, hemostatic, and antibacterial performances as a first-aid tissue adhesive. *Advanced Functional Materials* **30**, 2001820 (2020).
142 Xu, B. *et al.* Elastic Janus film for Wound Dressings: Unidirectional Biofluid Transport and Effectively Promoting Wound Healing. *Advanced Functional Materials* **31**, 2105265 (2021).
143 Ni, Z. *et al.* Polyphosphazene and Non-Catechol-Based Antibacterial Injectable Hydrogel for Adhesion of Wet Tissues as Wound Dressing. *Advanced Healthcare Materials* **11**, 2101421 (2022).
144 Jung, H., Kim, M. K., Lee, J. Y., Choi, S. W. & Kim, J. Adhesive hydrogel patch with enhanced strength and adhesiveness to skin for transdermal drug delivery. *Advanced Functional Materials* **30**, 2004407 (2020).

145 Zhou, D. *et al.* Dopamine-modified hyaluronic acid hydrogel adhesives with fast-forming and high tissue adhesion. *ACS Applied Materials & Interfaces* **12**, 18225-18234 (2020).
146 Fan, X. *et al.* Mussel foot protein inspired tough tissue-selective underwater adhesive hydrogel. *Materials Horizons* **8**, 997-1007 (2021).
147 Freedman, B. R. *et al.* Enhanced tendon healing by a tough hydrogel with an adhesive side and high drug-loading capacity. *Nature Biomedical Engineering*, 1-13 (2022).
148 Kohane, D. S. & Langer, R. Biocompatibility and drug delivery systems. *Chem Sci* **1**, 441-446 (2010).
149 Bergenstal, R. M. *et al.* Effectiveness of Sensor-Augmented Insulin-Pump Therapy in Type 1 Diabetes. *New Engl J Med* **363**, 311-320 (2010).
150 Nowald, C., Käsdorf, B. T. & Lieleg, O. Controlled nanoparticle release from a hydrogel by DNA-mediated particle disaggregation. *J Control Release* **246**, 71-78 (2017).
151 Molas, M., Bartrons, R. & Perales, J. C. Single-stranded DNA condensed with poly-L-lysine results in nanometric particles that are significantly smaller, more stable in physiological ionic strength fluids and afford higher efficiency of gene delivery than their double-stranded counterparts. *Bba-Gen Subjects* **1572**, 37-44 (2002).
152 Boussif, O. *et al.* A Versatile Vector for Gene and Oligonucleotide Transfer into Cells in Culture and in-Vivo - Polyethylenimine. *P Natl Acad Sci USA* **92**, 7297-7301 (1995).
153 Baker, A. *et al.* Polyethylenimine (PEI) is a simple, inexpensive and effective reagent for condensing and linking plasmid DNA to adenovirus for gene delivery. *Gene Ther* **4**, 773-782 (1997).
154 El Badawy, A. M. *et al.* Impact of Environmental Conditions (pH, Ionic Strength, and Electrolyte Type) on the Surface Charge and Aggregation of Silver Nanoparticles Suspensions. *Environ Sci Technol* **44**, 1260-1266 (2010).
155 Duffy, C. V., David, L. & Crouzier, T. Covalently-crosslinked mucin biopolymer hydrogels for sustained drug delivery. *Acta biomaterialia* **20**, 51-59 (2015).
156 Vladescu, I., Lieleg, O., Jang, S. & Ribbeck, K. An adsorption chromatography assay to probe bulk particle transport through hydrogels. *J Pharm Sci-Us* **101**, 436-442 (2012).
157 Nowald, C. *et al.* A Selective Mucin/Methylcellulose Hybrid Gel with Tailored Mechanical Properties. *Macromol Biosci* **16**, 567-579 (2016).
158 Wise, D. L., Trantolo, D. J., Marino, R. T. & Kitchell, J. P. Opportunities and challenges in the design of implantable biodegradable polymeric systems for the delivery of antimicrobial agents and vaccines. *Advanced Drug Delivery Reviews* **1**, 19-40 (1987).
159 Crnko, S., Du Pré, B. C., Sluijter, J. P. & Van Laake, L. W. Circadian rhythms and the molecular clock in cardiovascular biology and disease. *Nature Reviews Cardiology* **16**, 437-447 (2019).
160 Wang, C., Lutes, L. K., Barnoud, C. & Scheiermann, C. The circadian immune system. *Science Immunology* **7**, eabm2465 (2022).
161 De Giorgi, A., Menegatti, A. M., Fabbian, F., Portaluppi, F. & Manfredini, R. Circadian rhythms and medical diseases: does it matter when drugs are taken? *European journal of internal medicine* **24**, 698-706 (2013).
162 Hrushesky, W. Circadian timing of cancer chemotherapy. *Science* **228**, 73-75 (1985).
163 Sulli, G., Manoogian, E. N., Taub, P. R. & Panda, S. Training the circadian clock, clocking the drugs, and drugging the clock to prevent, manage, and treat chronic diseases. *Trends in pharmacological sciences* **39**, 812-827 (2018).
164 Kimna, C. & Lieleg, O. Engineering an orchestrated release avalanche from hydrogels using DNA-nanotechnology. *Journal of Controlled Release* **304**, 19-28 (2019).

165 Austin, L. A., Mackey, M. A., Dreaden, E. C. & El-Sayed, M. A. The optical, photothermal, and facile surface chemical properties of gold and silver nanoparticles in biodiagnostics, therapy, and drug delivery. *Arch Toxicol* **88**, 1391-1417 (2014).
166 Duncan, B., Kim, C. & Rotello, V. M. Gold nanoparticle platforms as drug and biomacromolecule delivery systems. *J Control Release* **148**, 122-127 (2010).
167 Liong, M. *et al.* Multifunctional inorganic nanoparticles for imaging, targeting, and drug delivery. *Acs Nano* **2**, 889-896 (2008).
168 Rickert, C. A., Wittmann, B., Fromme, R. & Lieleg, O. Highly transparent covalent mucin coatings improve the wettability and tribology of hydrophobic contact lenses. *ACS Applied Materials & Interfaces* **12**, 28024-28033 (2020).
169 Rickert, C. A., Bauer, M. G., Hoffmeister, J. C. & Lieleg, O. Effects of Sterilization Methods on the Integrity and Functionality of Covalent Mucin Coatings on Medical Devices. *Advanced Materials Interfaces* **9**, 2101716 (2022).
170 Bernkop-Schnürch, A., Kast, C. & Guggi, D. Permeation enhancing polymers in oral delivery of hydrophilic macromolecules: thiomer/GSH systems. *Journal of Controlled Release* **93**, 95-103 (2003).
171 Koc, H., Kilicay, E., Karahaliloglu, Z., Hazer, B. & Denkbas, E. B. Prevention of urinary infection through the incorporation of silver–ricinoleic acid–polystyrene nanoparticles on the catheter surface. *Journal of Biomaterials Applications* **36**, 385-405 (2021).
172 Ridley, C. *et al.* Assembly of the respiratory mucin MUC5B: a new model for a gel-forming mucin. *Journal of Biological Chemistry* **289**, 16409-16420 (2014).
173 Trillo-Muyo, S. *et al.* Granule-stored MUC5B mucins are packed by the non-covalent formation of N-terminal head-to-head tetramers. *Journal of Biological Chemistry* **293**, 5746-5754 (2018).
174 Hughes, G. W. *et al.* The MUC5B mucin polymer is dominated by repeating structural motifs and its topology is regulated by calcium and pH. *Scientific reports* **9**, 1-13 (2019).
175 Holstein, T. & Tardent, P. An ultrahigh-speed analysis of exocytosis: nematocyst discharge. *Science* **223**, 830-833 (1984).
176 Pollack, G. H. The cell as a biomaterial. *Journal of Materials Science: Materials in Medicine* **13**, 811-821 (2002).
177 Liron, N., Ostfeld, E., Priel, Z. & Roth, Y. *Cilia, mucus, and mucociliary interactions*. (CRC Press, 1998).
178 Kesimer, M., Makhov, A. M., Griffith, J. D., Verdugo, P. & Sheehan, J. K. Vol. 298 L15-L22 (American Physiological Society Bethesda, MD, 2010).
179 Wolf, F. I. & Trapani, V. Cell (patho) physiology of magnesium. *Clinical science* **114**, 27-35 (2008).
180 UniProt. A worldwide hub of protein knowledge. *Nucleic acids research* **47**, D506-D515 (2019).
181 Rosenstock, J. *et al.* Comparison of single-dose tetracycline hydrochloride to conventional therapy of urinary tract infections. *Antimicrobial agents and chemotherapy* **27**, 652-654 (1985).
182 Winkelhoff, A. J. V., Rams, T. E. & Slots, J. Systemic antibiotic therapy in periodontics. *Periodontology 2000* **10**, 45-78 (1996).
183 *The European Committee on Antimicrobial Susceptibility Testing, Breakpoint tables for interpretation of MICs and zone diameters, version 9.0*, <http://www.eucast.org/clinical_breakpoints/> (2019).
184 Sandberg, T., Carlsson, J. & Ott, M. K. Mucin Coatings Suppress Neutrophil Adhesion to a Polymeric Model Biomaterial. *Microscopy Research and Technique* **70**, 864-868 (2007).
185 Shi, L., Ardehali, R., Caldwell, K. D. & Valint, P. Mucin coating on polymeric material surfaces to suppress bacterial adhesion. *Colloids and Surfaces B: Biointerfaces* **17**, 229-239 (2000).

186 Co, J. Y., Crouzier, T. & Ribbeck, K. Probing the Role of Mucin-Bound Glycans in Bacterial Repulsion by Mucin Coatings. *Advanced Materials Interfaces* **2**, 1500179 (2015).
187 Winkeljann, B., Boettcher, K., Balzer, B. N. & Lieleg, O. Mucin Coatings Prevent Tissue Damage at the Cornea–Contact Lens Interface. *Advanced Materials Interfaces* **4**, 1700186 (2017).
188 Marczynski, M. *et al.* Structural alterations of mucins are associated with losses in functionality. *Biomacromolecules* **22**, 1600-1613 (2021).
189 Schierholz, J. & Beuth, J. Implant infections: a haven for opportunistic bacteria. *Journal of Hospital Infection* **49**, 87-93 (2001).
190 Wardlow, R. *et al.* Targeted antibiotic delivery using low temperature-sensitive liposomes and magnetic resonance-guided high-intensity focused ultrasound hyperthermia. *International Journal of Hyperthermia* **32**, 254-264 (2016).
191 Polak, R. *et al.* Sugar-mediated disassembly of mucin/lectin multilayers and their use as pH-Tolerant, on-demand sacrificial layers. *Biomacromolecules* **15**, 3093-3098 (2014).
192 Schwefel, D. *et al.* Structural basis of multivalent binding to wheat germ agglutinin. *Journal of the American Chemical Society* **132**, 8704-8719 (2010).
193 Crouzier, T., Beckwitt, C. H. & Ribbeck, K. Mucin multilayers assembled through sugar-lectin interactions. *Biomacromolecules* **13**, 3401-3408 (2012).
194 Nowald, C. *et al.* A selective mucin/methylcellulose hybrid gel with tailored mechanical properties. *Macromolecular bioscience* **16**, 567-579 (2016).
195 Mouritsent, O. G. & Jørgensen, K. Micro-, nano-and meso-scale heterogeneity of iipid bilayers and its influence on macroscopic membrane properties. *Molecular membrane biology* **12**, 15-20 (1995).
196 Song, J., Winkeljann, B. & Lieleg, O. The lubricity of mucin solutions is robust toward changes in physiological conditions. *ACS Applied Bio Materials* **2**, 3448-3457 (2019).
197 Korin, N., Gounis, M. J., Wakhloo, A. K. & Ingber, D. E. Targeted drug delivery to flow-obstructed blood vessels using mechanically activated nanotherapeutics. *JAMA neurology* **72**, 119-122 (2015).
198 Zhang, Y., Yu, J., Bomba, H. N., Zhu, Y. & Gu, Z. Mechanical force-triggered drug delivery. *Chemical reviews* **116**, 12536-12563 (2016).
199 Mitragotri, S. & Kost, J. Transdermal delivery of heparin and low-molecular weight heparin using low-frequency ultrasound. *Pharmaceutical research* **18**, 1151-1156 (2001).
200 Kakavand, M., Yazdanpanah, G., Ahmadiani, A. & Niknejad, H. Blood compatibility of human amniotic membrane compared with heparin-coated ePTFE for vascular tissue engineering. *Journal of tissue engineering and regenerative medicine* **11**, 1701-1709 (2017).
201 Krajewski, S. *et al.* Hemocompatibility evaluation of different silver nanoparticle concentrations employing a modified Chandler-loop in vitro assay on human blood. *Acta Biomaterialia* **9**, 7460-7468 (2013).
202 Saxer, T., Zumbuehl, A. & Müller, B. The use of shear stress for targeted drug delivery. *Cardiovascular research* **99**, 328-333 (2013).
203 Amir, Y. *et al.* Universal computing by DNA origami robots in a living animal. *Nature nanotechnology* **9**, 353-357 (2014).
204 Saw, W. S. *et al.* Delivery of nanoconstructs in cancer therapy: challenges and therapeutic opportunities. *Advanced Therapeutics* **4**, 2000206 (2021).
205 Dai, Q. *et al.* Quantifying the ligand-coated nanoparticle delivery to cancer cells in solid tumors. *ACS nano* **12**, 8423-8435 (2018).
206 Pei, H. *et al.* Reconfigurable three-dimensional DNA nanostructures for the construction of intracellular logic sensors. *Angewandte Chemie International Edition* **51**, 9020-9024 (2012).

207 Marczynski, M. *et al.* Charged Glycan Residues Critically Contribute to the Adsorption and Lubricity of Mucins. *Colloids and Surfaces B: Biointerfaces*, 110614 (2019).
208 Weiss, L. in *International review of cytology* Vol. 26 63-105 (Elsevier, 1969).
209 He, C., Hu, Y., Yin, L., Tang, C. & Yin, C. Effects of particle size and surface charge on cellular uptake and biodistribution of polymeric nanoparticles. *Biomaterials* **31**, 3657-3666 (2010).
210 Dante, S. *et al.* Selective targeting of neurons with inorganic nanoparticles: revealing the crucial role of nanoparticle surface charge. *ACS nano* **11**, 6630-6640 (2017).
211 Varkouhi, A. K., Scholte, M., Storm, G. & Haisma, H. J. Endosomal escape pathways for delivery of biologicals. *Journal of Controlled Release* **151**, 220-228 (2011).
212 Pigram, W., Fuller, W. & Hamilton, L. Stereochemistry of intercalation: interaction of daunomycin with DNA. *Nature New Biology* **235**, 17-19 (1972).
213 Jhaveri, A., Deshpande, P. & Torchilin, V. Stimuli-sensitive nanopreparations for combination cancer therapy. *Journal of controlled release* **190**, 352-370 (2014).
214 Calin, G. A. *et al.* Human microRNA genes are frequently located at fragile sites and genomic regions involved in cancers. *Proceedings of the National Academy of Sciences* **101**, 2999-3004 (2004).
215 Garzon, R., Calin, G. A. & Croce, C. M. MicroRNAs in cancer. *Annual review of medicine* **60**, 167-179 (2009).
216 Pan, X., Wang, Z.-X. & Wang, R. MicroRNA-21: a novel therapeutic target in human cancer. *Cancer biology & therapy* **10**, 1224-1232 (2010).
217 Si, M. *et al.* miR-21-mediated tumor growth. *Oncogene* **26**, 2799 (2007).
218 Neilson, J. R., Zheng, G. X., Burge, C. B. & Sharp, P. A. Dynamic regulation of miRNA expression in ordered stages of cellular development. *Genes & development* **21**, 578-589 (2007).
219 Calin, G. A. & Croce, C. M. MicroRNA signatures in human cancers. *Nature reviews cancer* **6**, 857-866 (2006).
220 Kimna, C. *et al.* DNA Strands Trigger the Intracellular Release of Drugs from Mucin-Based Nanocarriers. *ACS Nano* (2020).
221 Yan, L.-X. *et al.* MicroRNA miR-21 overexpression in human breast cancer is associated with advanced clinical stage, lymph node metastasis and patient poor prognosis. *Rna* **14**, 2348-2360 (2008).
222 Barger, J. F. & Nana-Sinkam, S. P. MicroRNA as tools and therapeutics in lung cancer. *Respiratory medicine* **109**, 803-812 (2015).
223 Elnakat, H. & Ratnam, M. Distribution, functionality and gene regulation of folate receptor isoforms: implications in targeted therapy. *Advanced drug delivery reviews* **56**, 1067-1084 (2004).
224 Stella, B. *et al.* Design of folic acid-conjugated nanoparticles for drug targeting. *Journal of pharmaceutical sciences* **89**, 1452-1464 (2000).
225 Reddy, J. A. & Low, P. S. Folate-mediated targeting of therapeutic and imaging agents to cancers. *Critical Reviews™ in Therapeutic Drug Carrier Systems* **15** (1998).
226 Rejman, J., Oberle, V., Zuhorn, I. S. & Hoekstra, D. Size-dependent internalization of particles via the pathways of clathrin-and caveolae-mediated endocytosis. *Biochemical journal* **377**, 159-169 (2004).
227 Panariti, A., Miserocchi, G. & Rivolta, I. The effect of nanoparticle uptake on cellular behavior: disrupting or enabling functions? *Nanotechnology, science and applications* **5**, 87 (2012).
228 Hillaireau, H. & Couvreur, P. Nanocarriers' entry into the cell: relevance to drug delivery. *Cellular and molecular life sciences* **66**, 2873-2896 (2009).

229 Lutz, T. M., Kimna, C. & Lieleg, O. A pH-stable, mucin based nanoparticle system for the co-delivery of hydrophobic and hydrophilic drugs. *International Journal of Biological Macromolecules* **215**, 102-112 (2022).
230 Liu, M. *et al.* miR-21 targets the tumor suppressor RhoB and regulates proliferation, invasion and apoptosis in colorectal cancer cells. *FEBS letters* **585**, 2998-3005 (2011).
231 Pfeffer, S. R., Yang, C. H. & Pfeffer, L. M. The role of miR-21 in cancer. *Drug development research* **76**, 270-277 (2015).
232 Spear, B. B., Heath-Chiozzi, M. & Huff, J. Clinical application of pharmacogenetics. *Trends in molecular medicine* **7**, 201-204 (2001).
233 Harvey, A. *et al.* The future of technologies for personalised medicine. *New biotechnology* **29**, 625-633 (2012).
234 Egnew, T. R. Suffering, meaning, and healing: challenges of contemporary medicine. *The Annals of Family Medicine* **7**, 170-175 (2009).
235 Guo, C., Wu, Y., Li, W., Wang, Y. & Kong, Q. Development of a Microenvironment-Responsive Hydrogel Promoting Chronically Infected Diabetic Wound Healing through Sequential Hemostatic, Antibacterial, and Angiogenic Activities. *ACS Applied Materials & Interfaces* (2022).
236 Mokhtari, R. B. *et al.* Combination therapy in combating cancer. *Oncotarget* **8**, 38022 (2017).
237 Assenat, E. *et al.* Sequential first-line treatment with nab-paclitaxel/gemcitabine and FOLFIRINOX in metastatic pancreatic adenocarcinoma: GABRINOX phase Ib-II controlled clinical trial. *ESMO open* **6**, 100318 (2021).
238 Askari, F. K. & McDonnell, W. M. Antisense-oligonucleotide therapy. *New England Journal of Medicine* **334**, 316-318 (1996).
239 Gebert, L. F. *et al.* Miravirsen (SPC3649) can inhibit the biogenesis of miR-122. *Nucleic acids research* **42**, 609-621 (2014).
240 Duan, H. *et al.* Sequential Delivery of Quercetin and Paclitaxel for the Fibrotic Tumor Microenvironment Remodeling and Chemotherapy Potentiation via a Dual-Targeting Hybrid Micelle-in-Liposome System. *ACS Applied Materials & Interfaces* **14**, 10102-10116 (2022).
241 Li, F. *et al.* Dynamic assembly of DNA nanostructures in living cells for mitochondrial interference. *Journal of the American Chemical Society* **144**, 4667-4677 (2022).
242 Segel, M. *et al.* Mammalian retrovirus-like protein PEG10 packages its own mRNA and can be pseudotyped for mRNA delivery. *Science* **373**, 882-889 (2021).
243 Jung, J. K., Archuleta, C. M., Alam, K. K. & Lucks, J. B. Programming cell-free biosensors with DNA strand displacement circuits. *Nature chemical biology* **18**, 385-393 (2022).
244 Dai, S., Wu, S., Duan, N. & Wang, Z. A luminescence resonance energy transfer based aptasensor for the mycotoxin Ochratoxin A using upconversion nanoparticles and gold nanorods. *Microchimica Acta* **183**, 1909-1916 (2016).
245 Zhao, J. *et al.* Upconversion luminescence-activated DNA nanodevice for ATP sensing in living cells. *Journal of the American Chemical Society* **140**, 578-581 (2018).
246 Funck, T., Nicoli, F., Kuzyk, A. & Liedl, T. Sensing picomolar concentrations of RNA using switchable plasmonic chirality. *Angewandte Chemie International Edition* **57**, 13495-13498 (2018).
247 Collins, F. S. & Varmus, H. A new initiative on precision medicine. *New England journal of medicine* **372**, 793-795 (2015).
248 Roxbury, D. *et al.* Hyperspectral microscopy of near-infrared fluorescence enables 17-chirality carbon nanotube imaging. *Scientific reports* **5**, 1-6 (2015).
249 Zhao, S. *et al.* Cellular and molecular probing of intact human organs. *Cell* **180**, 796-812. e719 (2020).

250 Jordan, J. L. & Fernandez, E. J. QCM-D sensitivity to protein adsorption reversibility. *Biotechnology and bioengineering* **101**, 837-842 (2008).
251 Sarode, P. B., Bahekar, S. P. & Chandak, H. S. DABCO/AcOH jointly accelerated copper (I)-catalysed cycloaddition of azides and alkynes on water at room temperature. *Synlett* **27**, 2681-2684 (2016).
252 Winkeljann, B., Bussmann, A. B., Bauer, M. G. & Lieleg, O. Oscillatory tribology performed with a commercial shear rheometer. *Biotribology* **14**, 11-18 (2018).
253 Tan, S. H., Nguyen, N.-T., Chua, Y. C. & Kang, T. G. Oxygen plasma treatment for reducing hydrophobicity of a sealed polydimethylsiloxane microchannel. *Biomicrofluidics* **4**, 032204 (2010).
254 Eddington, D. T., Puccinelli, J. P. & Beebe, D. J. Thermal aging and reduced hydrophobic recovery of polydimethylsiloxane. *Sensors and Actuators B: Chemical* **114**, 170-172 (2006).
255 Winkeljann, B., Leipold, P.-M. A. & Lieleg, O. Macromolecular coatings enhance the tribological performance of polymer-based lubricants. *Advanced Materials Interfaces* **6**, 1900366 (2019).
256 Käsdorf, B. T. *et al.* Mucin-Inspired Lubrication on Hydrophobic Surfaces. *Biomacromolecules* **18**, 2454-2462 (2017).
257 Tiffany, J. M. The viscosity of human tears. *International ophthalmology* **15**, 371-376 (1991).
258 Klarhöfer, M., Csapo, B., Balassy, C., Szeles, J. & Moser, E. High-resolution blood flow velocity measurements in the human finger. *Magnetic Resonance in Medicine: An Official Journal of the International Society for Magnetic Resonance in Medicine* **45**, 716-719 (2001).
259 Kaẗsdorf, B. T. *et al.* Mucin-inspired lubrication on hydrophobic surfaces. *Biomacromolecules* **18**, 2454-2462 (2017).
260 Del Porto, P. *et al.* Dysfunctional CFTR alters the bactericidal activity of human macrophages against Pseudomonas aeruginosa. *Plos One* **6**, e19970 (2011).
261 Schmiedl, A., Kerber-Momot, T., Munder, A., Pabst, R. & Tschernig, T. Bacterial distribution in lung parenchyma early after pulmonary infection with Pseudomonas aeruginosa. *Cell and tissue research* **342**, 67-73 (2010).
262 Proctor, R. A. *et al.* Small colony variants: a pathogenic form of bacteria that facilitates persistent and recurrent infections. *Nature Reviews Microbiology* **4**, 295 (2006).
263 Li, X.-Z., Livermore, D. M. & Nikaido, H. Role of efflux pump (s) in intrinsic resistance of Pseudomonas aeruginosa: resistance to tetracycline, chloramphenicol, and norfloxacin. *Antimicrobial agents and chemotherapy* **38**, 1732-1741 (1994).

Author contributions

This thesis follows a total number of 5 research articles, 1 review article, and 1 European patent applications to which I contributed during my time as doctoral candidate. Those publications, which built the fundament of the individual chapters, are marked in the beginning of every sub-chapter as a footnote. My individual contribution to these publications that are listed according to the occurrence order in the thesis is described below:

1 **C. Kimna**, B. Winkeljann, J. Hoffmeister and O. Lieleg, Biopolymer-based nanoparticles with tunable mucoadhesivity efficiently deliver therapeutics across the corneal barrier, Materials Science and Engineering: C, 121, 111890 (2021)

Individual contribution: I contribute to the conception of this study, the design and performance of the experiments, the data analysis, and writing of the manuscript.

2 **C. Kimna**, M. G. Bauer, T. M. Lutz, S. Mansi, E. Akyuz, Z. Doganyigit, P. Karakol, P. Mela and O. Lieleg, Multifunctional 'Janus-type' bilayer films combine broad-range tissue adhesion with guided drug release, Advanced Functional Materials, (2022)

Individual contribution: I contribute to the conception of this study, the design and performance of the experiments, the data analysis, and writing of the manuscript.

3 **C. Kimna** and O. Lieleg, Engineering an orchestrated release avalanche from hydrogels using DNA-nanotechnology, Journal of Controlled Release, 304, 19-28 (2019)

Individual contribution: I contribute to the conception of this study, the design and performance of the experiments, the data analysis, and writing of the manuscript.

4 **C. Kimna**, B. Winkeljann, J. Song and O. Lieleg, Smart biopolymer-based multilayers enable consecutive drug release events on demand, Advanced Materials Interfaces, 7, 2000735 (2020)

Individual contribution: I contribute to the conception of this study, the design and performance of the experiments, the data analysis, and writing of the manuscript.

5 **C. Kimna**, B. Winkeljann and O. Lieleg, Controlled release of therapeutical agents from polymer brush coatings by employing reversible polymer condensation using ionic cross-linkers, European patent application, EP19217921.6 (2019)

Individual contribution: I contributed to the conception of this invention, the design and performance of experiments, data analysis, and writing of the text.

6 **C. Kimna**, B. M. Naranjo, F. Eckert, D. Fan, D. Arcuti, P. Mela and O. Lieleg, Tailored mechanosensitive nanogels release drugs upon exposure to different levels of stenosis, (in peer review)

Individual contribution: I contribute to the conception of this study, the design and performance of the experiments, the data analysis, and writing of the manuscript.

7 **C. Kimna** and O. Lieleg, Molecular micromanagement: synthetic DNA strands establish spatio-temporal control for precision medicine, Biophysics Reviews, 1(1), 011305 (2020)

Individual contribution: I contributed to the conception, the literature review, and writing of the manuscript.

8 **C. Kimna**, T. M. Lutz, H. Yan, J. Song, T. Crouzier and O. Lieleg, DNA strands trigger the intracellular release of drugs from mucin-based nanocarriers, ACS Nano, 15.(2), 2350-2362 (2020)

Individual contribution: I contribute to the conception of this study, the design and performance of the experiments, the data analysis, and writing of the manuscript.

List of publications

1 **C. Kimna**, S. Deger, S. Tamburaci, and F. Tihminlioglu, “Microfluidic-assisted preparation of nano and microscale chitosan based 3D composite materials: Comparison with conventional methods”, Journal of Applied Polymer Science, (2022).

2 T. M. Lutz, **C. Kimna**, and O. Lieleg, “A pH-stable, mucin based nanoparticle system for the co-delivery of hydrophobic and hydrophilic drugs”, International Journal of Biological Macromolecules, (2022).

3 **C. Kimna**, M. G. Bauer, T. M. Lutz, S. Mansi, E. Akyuz, Z. Doganyigit, P. Karakol, P. Mela and O. Lieleg, Multifunctional ‘Janus-type’ bilayer films combine broad-range tissue adhesion with guided drug release, Advanced Functional Materials, (2022)

4 T. Lutz, **C. Kimna** and O. Lieleg, Bio-based and bio-inspired adhesives from animals and plants for biomedical applications, Materials Today Bio, 100203 (2022)

5 **C. Kimna** and T. Fafal, Evaluation of the phenolic compounds and the antioxidant potentials of Vitex agnus-castus L. leaves and fruits, Turkish Journal of Biochemistry (2021)

6 M. Marczynski, **C. Kimna** and O. Lieleg, Purified mucins in drug delivery research, Advanced Drug Delivery Reviews, 113845 (2021)

7 **C. Kimna**, B. Winkeljann, J. Hoffmeister and O. Lieleg, Biopolymer-based nanoparticles with tunable mucoadhesivity efficiently deliver therapeutics across the corneal barrier, Materials Science and Engineering: C, 121, 111890 (2021)

8 **C. Kimna** and O. Lieleg, Molecular micromanagement: synthetic DNA strands establish spatio-temporal control for precision medicine, Biophysics Reviews, 1(1), 011305 (2020)

9 **C. Kimna**, B. Winkeljann, J. Song and O. Lieleg, Smart biopolymer-based multilayers enable consecutive drug release events on demand, Advanced Materials Interfaces, 7, 2000735 (2020)

10 **C. Kimna**, T. M. Lutz, H. Yan, J. Song, T. Crouzier and O. Lieleg, DNA strands trigger the intracellular release of drugs from mucin-based nanocarriers, ACS Nano, 15.(2), 2350-2362 (2020)

11 A. Palaveniene, K. Songailiene, O. Baniukaitiene, S. Tamburaci, **C. Kimna**, F. Tihminlioglu and J. Liesiene, The effect of biomimetic coating and cuttlebone microparticle reinforcement on the osteoconductive properties of cellulose-based scaffolds, International journal of biological macromolecules, 152, 1194-1204 (2019)

12 **C. Kimna**, S. Tamburaci and F. Tihminlioglu, Novel zein-based multilayer wound dressing membranes with controlled release of gentamicin, Journal of Biomedical Materials Research Part B: Applied Biomaterials, 107 (6), 2057-2070 (2019)

13 S. Tamburaci, **C. Kimna**, and F. Tihminlioglu, Bioactive diatomite and POSS silica cage reinforced chitosan/Na-carboxymethyl cellulose polyelectrolyte scaffolds for hard tissue regeneration, Materials Science and Engineering: C, 100, 196-208 (2019)

14 **C. Kimna** and O. Lieleg, Engineering an orchestrated release avalanche from hydrogels using DNA-nanotechnology, Journal of Controlled Release, 304, 19-28 (2019)

15 **C. Kimna**, S. Deger, S. Tamburaci and F. Tihminlioglu, Chitosan/montmorillonite composite nanospheres for sustained antibiotic delivery at post-implantation bone infection treatment, Biomedical Materials, 14 (4), 044101 (2019)

16 A. Palaveniene, S. Tamburaci, **C. Kimna**, K. Glambaite, O. Baniukaitiene, F. Tihminlioğlu and J. Liesiene, Osteoconductive 3D porous composite scaffold from regenerated cellulose and cuttlebone-derived hydroxyapatite, Journal of biomaterials applications, 33 (6), 876-890 (2019)

17 S. Tamburaci, **C. Kimna** and F. Tihminlioglu, Novel phytochemical Cissus quadrangularis extract–loaded chitosan/Na-carboxymethyl cellulose–based scaffolds for bone regeneration, Journal of Bioactive and Compatible Polymers, 33 (6), 629-646 (2018)

Patent applications

1 O. Lieleg**, C. Kimna**, and B. Winkeljann, Controlled release of compounds, European patent application, WO/2021/123126 (2019)

Acknowledgements

First, I would like to thank my supervisor, Prof. Dr. Oliver Lieleg, for supporting me throughout my time in his lab, for always being open to new ideas and for sharing all the excitement. Working in your lab grew me up and converted me from an excited student to an ambitious researcher. I also thank you for your great patience with my missing articles :)

Special thanks to all of my colleagues whom I listed in the thesis that contributed to the experiments yielded to our publications, but also to those colleagues who made the daily work great fun. First group members that I have met in this group helped me a lot to feel home in Munich. Caro and Jian, being a PhD student was a total fun when you, my best friends were my colleagues. Thank you, dear Dr. Matsi for being always there for a liquid break anywhere and anytime (and of course, curing all of those diseases meanwhile); Dr. MG for all of your chocolate support and setting a new low level of dark humor everyday; Berny for your *great* jokes, your great dance moves and your company in the U6; Theresa for all your helps in the lab and lifting up the mood with your music (paint it black!); Maria for being my drinking mate and performing all those emergency experiments; Ricky for always listening me and forcing me to do social activities; and, Ufuk for being the bro that I have found late but will never loose. Thank you again for all of your supports I had during my dissertation, we all found something here where the magic happens.

I would like to thank TUM media office for spreading our work to both, scientific and non-scientific audience. Additionally, I would like to thank all of my students; Julia, Helena, Franzi and Manuel, and of course to Tofulicious for his assistance in mucin purification.

I also would like to thank all of my friends from Izmir; Damla, Dicle, Gizem, and friends from Munich; Laura, Michal, Hatice, Nergis who were always there to support me and witness all phases of my PhD life with a great patience, I feel so lucky to have you as my friends!

Benji bebek, I do not know how I can thank you. Thank you for all those brainstorming sessions, for sharing all of your expertise to improve my work, bringing always positivity to the working environment, and supporting me. My gratitude, of course, goes beyond work aspects, thank you for being yourself, standing by my side unconditionally, being my mimo. I love you to the moon and back. Without you and my emotional support cats Bulut and Midas, I would not even be close to where and who I am now.

Ich möchte der Familie Winkeljann, Toni, Gitti, Joshi und Nadine für ihre endlose Unterstützung in dieser Zeit danken. Ihr habt mir sehr geholfen, kein Heimweh zu verspüren und mich in eurer Familie aufgenommen.

Bana kontrollu ilac salimi ve doku muhendisligi alanini tanitan Prof. Dr. Funda Tihminlioglu ve Dr. Sedef Tamburaci'ya bir kez daha tesekkur etmek istiyorum. Bana kendime güvenen, kendi ayakları üzerinde güçlü bir birey olmayı öğreten herkese, her deneyime; aynı zamanda beni destekleyen, zor duruma düştüğüm zaman omuzlarına tutunup ayağa kalkmamı sağlayan her güzel insana çok teşekkür ederim. Siz olmasaydınız bunların hiçbiri olmazdı. Ailem; oncelikle canım annem, Gizocum, teyzem,

dedem, anneannem, dayım, Yarkın, Çınar, sizleri seviyorum. Mutlu olun, hayata guzel gozlerle baktikca o size hep neşeyle ve bol enerjiyle gelsin. Bu yoluculuk süresince aramızdan fiziken ayrılanlar; Emrah abim, babaannem, canım babam, Çileğim, siz hep benimle berabersiniz; bu hayatı sizin için bir kez daha yaşıyor, tadını çıkarıyor ve deneyimlemeye devam ediyorum. Sizleri çok seviyorum…